Geomorphic impacts of rapid sediment-laden flows through computational modelling

Mingfu Guan

Submitted in accordance with the requirements for the degree of doctor of philosophy

The University of Leeds
School of Civil Engineering

January, 2014

The candidate confirms that the work submitted is his own and that appropriate credit has been given where reference has been made to the work of others.

This copy has been supplied on the understanding that it is copyright material and that no quotation from the thesis may be published without proper acknowledgement.

The right of *Mingfu Guan* to be identified as Author of this work has been asserted by him in accordance with the Copyright, Designs and Patents Act 1988.

Acknowledgements

Abstract

Outburst floods are one of the most catastrophic natural hazards for populations and infrastructure. They are usually generated from storm runoff, rapid melting of glacial ice or man-made and natural dam breaks, such as river dikes, volcanic debris dams and landslide dams etc. Such high-magnitude sudden onset floods generally comprise of an advancing intense kinematic water wave that can induce considerable sediment transport. Therefore, the exploration and investigation of sediment-laden outburst floods cannot be limited solely to water flow but must also include the flood-induced sediment transport. Understanding the complex flow-bed interaction process in large (field) scale outburst floods is still limited, not least due to a lack of well-constrained field data, but also because consensus on appropriate modelling schemes has yet to be decided. In recent years, attention has focussed on the numerical models capable of describing the process of erosion, transport and deposition in such flows and they are now at a point at which they provide useful quantitative data. Although the "exact" measure of bed change is still unattainable the numerical models enhance and improve insights into large outburst flood events.

In order to model and better understand heavily sediment-laden flows and resulting geomorphic impacts, this thesis adopts a layer-based conceptual model which separates the system into an active bed layer, a water-sediment mixed sheet flow layer and a suspension layer. Correspondingly, a layer-based hydro-morphodynamic model is proposed fully considering both bedload and suspended load based on shallow water theory. The model system is primarily composed of a combination of three modules: (1) a hydrodynamic module; (2) a sediment transport module; and (3) a morphological evolution module. In the thesis, firstly, a robust hydrodynamic model is proposed and tested including addressing the source terms and wetting/drying issues for application to irregular beds. Then based on the robust hydrodynamic model, a layer-based morphodynamic model is developed and solved numerically by an advanced second-order Godunov-type finite volume method. A series of theoretical and experimental tests are applied to validate the model in terms of both hydrodynamic and morphodynamic aspects. The results of these tests show that the developed models can predict the hydrodynamic and morphodynamic process

effectively with good agreement with theoretical and experimental results. To demonstrate a real application, a full-scale volcano-induced jökulhlaup or glacial outburst flood (GLOF) at Sólheimajökull, Iceland is reproduced by the proposed model. The simulation of the sediment-laden outburst flood is shown to perform well, with further insights into the flow-bed interaction obtained from the modelling output. These results are beneficial to flood risk management and hazard prevention and mitigation.

Author's publications

Journal Publications:

[1] **Guan M**; Wright NG; Sleigh PA. A Robust 2D Shallow Water Model for Solving Flow over Complex Topography using Homogenous Flux Method. International Journal for Numerical Methods in Fluids, 73(3), pp.225-249. 2013. This paper contributes to Chapter 3 of the thesis.

[2] **Guan M**; Wright NG; Sleigh PA. 2D process based morphodynamic model for flooding by non-cohesive dyke breach. Journal of Hydraulic Engineering, 10.1061/(ASCE)HY.1943-7900.0000861, in press.

Conference Proceedings:

[3] **Guan M**; Wright NG; Sleigh PA. Applicability of entrainment formulas to modelling of geomorphic outburst flows in: Hinkelmann R; Nasermoaddeli MH; Liong SY; Savic D; Fröhle P; Daemrich KF (editors) Proceedings of the 10th International Conference on Hydroinformatics (2012). This paper contributes to Chapter 2 of the thesis.

[4] **Guan M**; Wright NG; Sleigh PA; Carrivick JL; Stanies K. A layer-based morphodynamic model for unsteady outburst geomorphic floods: application in real world events in: Parsons DR; Ashworth PJ; Best JL; Simpson CJ (editors) Proceedings of the 10th International Conference on Fluvial Sedimentology (2013), pp.130-131.

[5] **Guan M**; Wright NG; Sleigh PA. Modelling and understanding multiple roles of sediment transport in floods in: Wang Z; Lee JH-W; Gao J; Cao S (editors) Proceedings of the 35th IAHR World Congress (2013). Tsinghua University Press. This paper contributes to Chapter 5 and Chapter 6 of the thesis.

[6] **Guan M**; Wright NG; Sleigh PA. Effects of vegetation on morphological change caused by rapid flood events in: A Report of Conference Proceedings of the Water Quality, 2012, pp.18-19.

Table of Contents

List of Tables

List of Figures

Preface

Computational modelling of rapid sediment-laden floods is important for flood risk management and is also a challenging task. Focused on this, this project was carried out in the School of Civil Engineering, University of Leeds, aiming to develop an advanced hydro-morphodynamic model for heavily-sediment laden flows and to better understanding of outburst floods and geomorphic impacts.

This thesis has been prepared in 7 chapters, which gives a detailed description of current research progress, the development of the computational model, and a full-scale application of the developed model, as well as discussion about the uncertainty factors for the modelling of sediment-laden flows. Hereby, this thesis provides further understanding of interactions between sediment transport and rapid outburst flows from both small-scale and large-scale hydro-morphodynamic events. The proposed model could be further developed for solving the practical engineering issues and it will be beneficial to flood risk management and disaster assessment.

Mingfu Guan
October 2013
Leeds, UK

Chapter 1
Introduction

1.1 Background

Flooding is one of the most catastrophic natural hazards the world can experience for both populations and infrastructures. For example, 1998 Yangtze River flood in China resulted in 3,704 dead, 15 million homeless and $26 billion in economic loss and a staggering 100,000 km^2 were evacuated, 13.3 million houses were damaged or destroyed [1]. Cumbria floods of 2009 in UK damaged a total of 253 footbridges and 51 paths, and an estimated cost of £2.5m to tourism businesses was lost [2]. People as individuals cannot avoid the disaster once it occurs, but the preventative measures which mitigate the inevitable situation may be accepted as benefit to protect people and infrastructure from damage. Therefore, it becomes necessary for hydraulic engineers to better understand flooding behaviours.

In a typical inundation, the outburst floods are more powerful and have a peak discharge that is several orders of magnitude greater than the perennial flows. Outburst floods are characterised by being sudden, short-lived and containing high energy. They are usually generated from storm runoff, rapid melting of glacial ice or man-made and natural dam breaks, such as river dikes, volcanic debris dams and landslide dams etc. [3-8]. Such kinds of outburst floods generally comprise of an intense advancing water wave which can induce considerable sediment loads, thereby resulting in rapid landscape change [5, 9, 10]. In recent years, flood modelling is considered as an effective tool for risk management and disaster mitigation, however, unfortunately, most of the previous flood models preferred to consider the water flow solely as a result of the simplicities, omitting the effects of sediment transport. The approach must be open to question in terms of predicting and understanding the physical flood behaviours. Therefore, an appropriate hydro-morphodynamic model for rapid sediment-laden flows and geomorphic impacts is particularly important. Consequently, a plethora of sediment transport models emphasising the erosion and deposition caused by outburst flows emerged in large numbers [11-18]. However, these models have various issues when it comes to application because of the simplifications and assumptions; most of the models were mainly focused on the investigations, consisting of theoretical analysis or

modelling small-scale laboratory experimental cases. Therefore, the understanding obtained from the theoretical analysis or small-scale experiments may possibly mislead our insights into large-scale flood events. All of these leave much room to improve such numerical models.

The commonly-seen flood models are mostly based on the 1D or 2D Shallow Water equations. The 3D models can give more detailed information and are attractive, but at the cost of high computational time. In particular for large-scale events, it seems to be prohibitive. One-dimensional models are applicable to the narrow and long channels; however, they are not enough to represent the complex flows in wider domains, thereby reducing the accuracy of modelling results. For these reasons the use of 2D computational models based on shallow water theory are widespread and have been investigated in a lot of research [19-23]. Amongst the techniques used, those based on finite volume Godunov-type Riemann Solvers are robust and accurate in solving the rapid outburst flows and have been used successfully in commercial as well as academic contexts. With these and other methods, the treatment of source terms and the numerical difficulties associated with wetting and drying are problematic and in view of their influence on numerical accuracy for flows over complex and irregular topography. Therefore, these problems must be treated thoroughly in solving the 2D shallow water model.

1.2 Sediment Transport Modelling in Regular Flows

Previous investigations on sediment transport have been carried out for more than a century [24-26]. With the advancement of computer technology, a plethora of mathematical or numerical models have become increasingly attractive and developed to simulate the fluvial process in regular flows, e.g. two-phase flow model, multi-layer based model, shallow water theory based model etc. Kobayashi and Seo [27] worked with a complete 1D two-phase model for fluid and sediment interaction in an erodible channel based on the conservation of mass and momentum of fluid and sediment using six governing equations: two for the mass balance of each phase and four for the momentum balance of each phase in the wall-normal as well as the stream wise directions. Armanini and Di Silvio [28] developed a 1D multi-layer mathematical model to simulate the morphological changes in regular flows. This model adopted a multi-layer conceptual framework which divided

the flow system into three layers: water stream layer, bottom layer and mixing layer below the bottom surface. The non-stationary one-dimensional continuity equations were used to describe the process in each layer. In the water stream layer, sediment is conveyed in suspension; the longitudinal motion of the sediment by the water prevails over the vertical motion due to turbulence fluctuation and particle fall-velocity. The bed-load transport primarily occurs in the bottom layer by sliding, rolling and saltation. In this layer the longitudinal transport rate depends on the local composition of the bottom sediments and on the local water flow conditions. No longitudinal motion of particles occurs in the mixing layer which plays a role in providing the particles upward lift and receiving the deposition particles downward. Figure 1.1 shows the multi-layer conceptual framework. This is a pioneering work for multi-layer based sediment transport modelling and provided a specific insight in describing the sediment transport phenomenon. However, the applications are restricted by the complexity necessary to distinguish suspended load and bedload and the need to quantify many parameters.
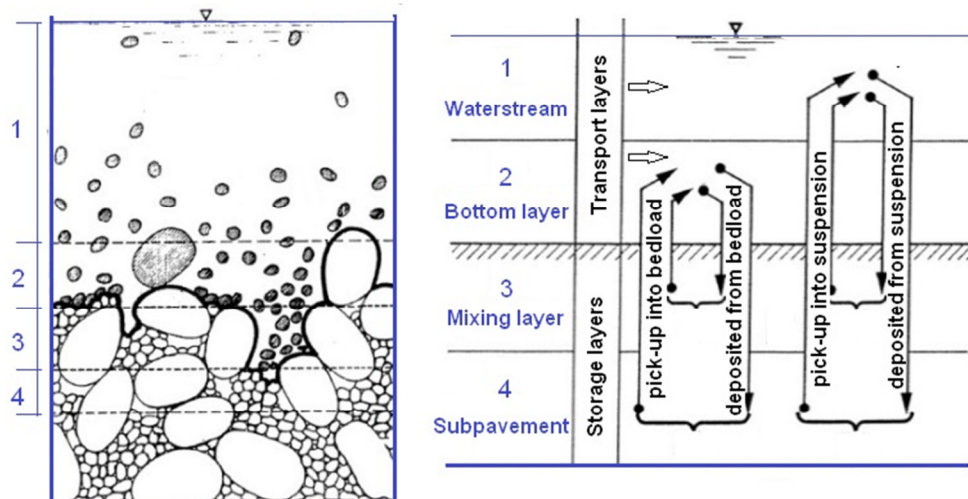
Figure 1.1 Multi-layer conceptual model in regular flow-sediment model

Spasojevic and Holly [29] generalized a two-dimensional mathematical model to simulate unsteady water flow over the mobile bed in the natural shallow watercourse fully considering suspended sediment transport and bedload transport. Similarly, the conceptualization of the governing physics is on the basis of different flow region layer and mechanism of exchange between them, see Figure 1.2. In this conceptual model, several important aspects of sediment-laden flows were considered: suspended load transport, bedload transport, and interaction between the two; bed level changes; hydraulic armouring; interaction between the flow and changes in bed elevation and bed surface size distribution.
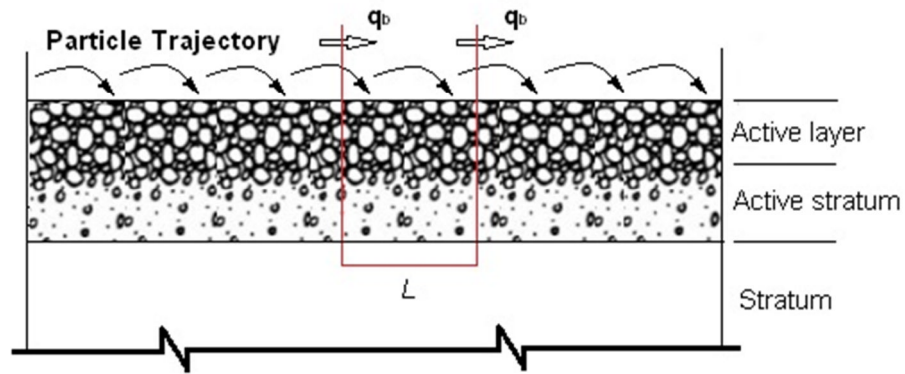
Figure 1.2 Schematic diagram of bed material division layers

Wu [30, 31] respectively proposed a depth-averaged two dimensional numerical model using finite volume method and a three dimensional numerical model governed by full Reynolds-averaged Navier-Stokes equations with the k-ε turbulence model to simulate unsteady flow and non-uniform sediment transport in open channels. In both models, both suspended load and bedload transport are accounted for, and the bedload transport is modelled with a non-equilibrium method. Abderrezzak and Paquier [32] presented and tested a one-dimensional numerical model for simulating unsteady flow and sediment transport by comparison with experiments, and the model is applied to simulate morphological changes in one real case. Papanicolaou et al. [33] presented an excellent review of these models.

1.3 Dam-break Flows over Movable Bed

Dam-break flows have been always the subject of scientific and technical research for many hydraulic scientists and engineers in the past century. Currently, many 1D, 2D and 3D hydrodynamic models have been developed for predicting dam-break flows with the advancement of computer technology and numerical solution methods. However, the majority of these models are only applicable to dam-break flows over fixed beds. In the natural environment, the dam-break flows can induce severe sediment motion in various forms, such as debris flows, mud flows, floating debris and sediment-laden currents [34]. In recent years, researchers have begun to address this issues with publications on simulation of dam-break over movable beds [11, 12, 16, 35-38].

Experiments in small-scale laboratory and field measurements can provide effective supporting data for validating the numerical models. However, it is

difficult to collect field measurements in real-world events of interest, therefore, most dam-break flows investigations incorporating sediment transport [12, 38-42] have been conducted in small-scale experiments. Chen and Simons [43] carried out the first experimental study on the morphological impacts of a dam-break flow, in which they concluded that the presence of easily erodible sediments deposited upstream of the dam can significantly increase the flood discharge due to the increase in local slope and the decrease in resistance to flow. The first idealized systematic experiments were performed by Capart and Young, Ferreira and Leal [12, 38] in a typical dam-break configuration. They carried out the experiments using different sediment material in different hydraulic conditions of downward and upward on both sides of the dam. Afterwards, a series of experiments were further investigated systematically on dam-break flow over movable beds using distinct bed material and different particle size by Spinewine [37]. Carrivick [42, 44] performed some experimental tests which quantified a range of flows and sediment phenomena within outburst floods. He indicated that suspended sediment dampens turbulence and causes energy loss, that increased sediment concentration increases momentum and shear stress, and that bed roughness effects vary non-linearly with flow stage. Experiments are limited due to the scale is very small, however, they clearly highlighted the physical process of dam-break flows over erodible beds and provided first-hand available data for validation of later numerical studies.

In terms of numerical modelling of dam-break flows over movable beds, Capart and Young [12] firstly described the shock feature associated with the scouring of a horizontal granular bed by a dam-break wave from the standpoint of shallow water theory through experimental and numerical approaches. Then Capart [45] initially proposed a two-layer model to simulate dam-break flow over movable beds similarly by small-scale experiment. In this model, he divided the flow of interest into upper clear water layer and mixture of water-sediment in the lower layer, and erosion and deposition are resulted from mass exchange between the fixed bed and the transport layer. However, this model has a key assumption which renders it to be limited for practical application; it is the assumption that velocity of clear water and mixture layers are considered as unique. In summary, the two-layer description of flow and sediment provided new insights into the process of geomorphic dam-break flows over movable beds. A recent extension of the two-layer model [13] allows the velocity in each layer to be different. Fraccarollo and Capart [13] proposed an approximate

theoretical description of the formative stages of erosional dam-break flows based on a shallow-water approach extended to fast geomorphic phenomena based on two-layer model, but the problem of equal velocity and concentration in water and mixture layers was not improved further, and the effects of sediment particle size are not taken into consideration. Then, Spinewine [37] extended the initial two-layer model and developed a mathematical model to simulate dam-break over erodible bed. In recent years, some researchers have been dedicating to improving and extending the two-layer model of geomorphic dam-break flow [41, 46].
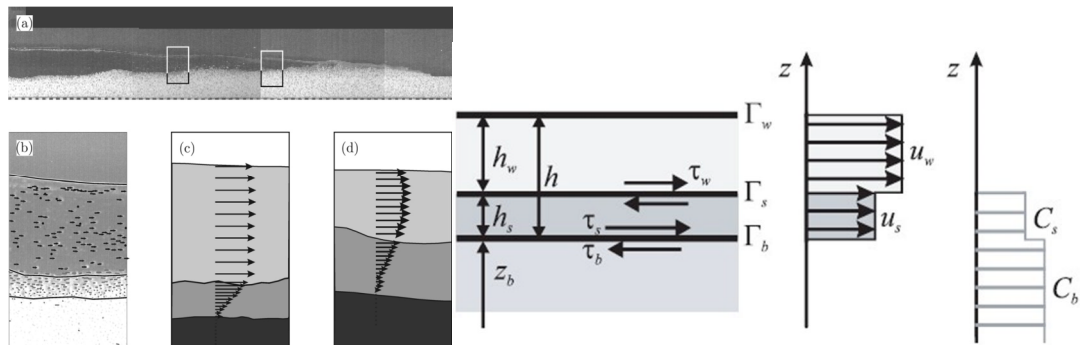
Figure 1.3 Two-layer conceptual model [37]

The two-layer transport model is complicated, but it provides a new insight into the dam-break induced geomorphic flows. Apart from research on two-layer description of flow and sediment, a plethora of other capacity models and non-capacity models [11, 12, 15, 16, 31, 47-52] have been developed in recent years, such as just considering bed load transport, suspended load or both as a total or separately in one regular single layer. Cao's non-capacity model is described briefly here which provides valuable descriptive and qualitative findings for dam-break fluvial processes. In the model, effects of sediment transport on the flow and non-equilibrium sediment transport approach are accounted for, and suspended load and bed load transport are considered as a total and the determination of exchange net flux of sediment is based on previous empirical formulas. The model's contribution is that it is one of the first dedicated studies of mobile-bed dam-break hydraulics, which is built up on the shallow flow conservative laws together with existing formulations for bed friction and sediment exchange between the water column and the bed. However, several shortcomings exist. Firstly, this model is a theoretical framework which is restricted to one-dimensional flow in a channel with rectangular cross sections of constant width, and over a mobile bed that is composed of uniform and non-cohesive sediment with particle diameter. Also, this model is only for lower shear stress and does not consider the condition of high shear stress that is usually triggered by dam-

break flows in the nature state. Recently they extended the analysis of the multiple time scales of sub-aerial (near-bed) sediment-laden flows over erodible bed to subaqueous turbidity currents, and proposed a fully coupled modelling study [53, 54]. Aiming at some shortcoming of Cao's model, Wu and Wang [15] established another one-dimensional model to simulate fluvial processes under dam-break flow over movable beds still on the basis of non-equilibrium assumption. The authors treat the total sediment as suspended load transport and bed load transport to be considered separately and their modified formulas about determining equilibrium bed load transport rate and near-bed suspended load concentration under high flow conditions. Also, that is the big difference from Cao's model. They got more precise results which are tested by experimental cases, with fairly good agreement between simulations and measurements. However, since the difficulties to collect data of field case, the validity of these models is still questionable due to the lack of any application to field cases and comparison with field measurements. Abderrezzak and Paquier [36] represented a one dimensional numerical model on dam break over movable beds based on Saint-Venant equations for shallow water waves, the Exner equation of sediment mass conservation and a spatial lag equation for non-equilibrium sediment transport. Interestingly, the model was tested on a field case. In the morphological models, an uncertainty comes from the empirical formulas about sediment transport which are developed in regular river flow; and because of the large differences in flow features of outburst dam-break flows, such empirical formulas may be not applicable to geomorphic dam-break flow. To investigate the influences of these formulas on simulation, Abderrezzak and Paquier [55] used the model developed in above literature and incorporated a variety of empirical sediment transport functions. By comparing with experimental data, they examined the performance of each formula. The models mentioned above are all one-dimensional. Currently, the majority of existing two-dimensional models used to simulate dam-break flows are only applicable to fixed beds, fewer to movable beds. Xia et al. [16] presents a 2D morphodynamic model for predicting dam-break flows over mobile beds based on non-equilibrium transport equations incorporating both suspended load and bed load, with consideration of the effects of bed material size distributions on the flood flow and bed evolution.

1.4 Modelling of Large-scale Outburst Floods

The research mentioned above predominantly focuses on sediment transport in ordinary open channel flow, small-scale experiments and ideal models of dam-break induced geomorphic flows. However, in the real world high-magnitude outburst floods exist in which sediment transport plays a significant role, for instance, glacial outburst floods and lahars are increasingly attracting the attention of hydraulic engineers. Such flows are characterized by huge flow discharge and high concentration of sediment so that morphology changes rapidly. The sediment particles in flows may vary from coarse (nominally > 250 mm by commonly > 1000 mm) to fine (sand) particles. Even though with respect to suspended load transport, its concentration may be also fairly high, it is not like that in ordinary channel flow. Mud flows, hyperconcentrated flood and debris flow all belong to this category. Hyperconcentrations refer to heavily sediment-laden flows in which the presence of fine sediments materially affects fluid properties and bed material transport. In general, the volumetric sediment concentration of hyperconcentrations is >20% and the concentration of debris flow is >40% by volume [34]. To model such kind of sediment problem, some particular flow features must be taken into consideration. In recent several years, Carling et al. [56] performed interesting 1D and 2D simulations of ice dam break unsteady flows of Quaternary megaflood, the discharge of which is several orders of magnitude larger than that of *ordinary* floods. The case they selected is an ice-dammed lake located in Altai Mountains, in Southern Siberia. Where the height of dam reach up to 600m, and the peak flow discharge is estimated up to 9 million to 11million m^3/s. Compared with ordinary floods, high energy and flow velocity render the modelling more difficult. Such kind of outburst flow often involves intense erosion and deposition which impose a crucial impact on flood routing [45, 57]. Unfortunately, the erosion and deposition effects, however, are not incorporated in their modelling. Another high outburst flood case of interest investigated is Glacial Lake Missoula whose discharge also is up to the order of 10 million m^3/s. Denlinger and O'Connell [58] developed the two dimensional numerical modelling for shallow water flow over rugged terrain to simulate Scabland flood routing just like the flood routing simulation in the case of Altai Mountains, in Southern Siberia. The reconstructions of the GLM flow processes based on a coupled approach of hydraulic modelling and geomorphic evidence have not been undertaken. In fact, high-magnitude outburst floods are catastrophic geological agents, transforming landscapes through erosion and deposition within a matter of hours. Alho et al. [59] used

TUFLOW 2D hydraulic modelling to understand the paleoflow conditions for different scenarios of draining GLM at its highest stands, where they included the geomorphic sediment load. Since the difficulties of direct measurement and field survey, the understanding of high-magnitude floods processes and mechanisms is still poor. Therefore, computer modelling, particularly 2D hydrodynamic models, has the potential to improve our understanding of hitherto unquantifiable processes and mechanisms in high-magnitude floods [60]. Carrivick [5, 61] applied hydrodynamic model, with fully integrated sediment transport, to reconstruct this kind of high-magnitude outburst floods of interest and then have an assessment of rapid landscape change induced erosion and deposition of sediment. The research provides a good mechanistic understanding of geomorphic change due to outburst floods.

1.5 Numerical Methods

1.5.1 Main Classifications

In the past more than half century, there are many numerical methods developed in practice to solve hyperbolic partial differential equations (PDEs). The differences among the methods mainly stem from different discretisation of the governing equations. Therefore, by virtue of the difference of discretisation type, the numerical methods which are widely applied are as follows: Finite difference method (FDM); Finite element method (FEM); Finite volume method (FVM). Finite volume method (FVM) is widely-used and has matured into powerful tools for the computation modelling of flow issues in recent years [62]. Of course, the research and improvement on this method is still going on. This method discretised the continuous equations into discrete equations around a finite volumes in each of which the integral equations are applied to obtain the exact conservation within each cell or grid (volume). It is particularly useful in cases like hydrodynamic modelling, where the equation is solved on basis of the principle of momentum conservation. By the discretization of the integral form of conservation equation, the mass and momentum remain conservation characteristics. The main advantage of FVM is that it combines the simplicity of FDM with the geometric flexibility of FEM [63]. Lomax et al. (1999) [64] stated that FVM have become popular in CFD as a result, primarily, of two advantages: 1. they ensure that the discretization is conservative, i.e., mass, momentum, and energy are conserved in a discrete

sense. While this property can usually be obtained using a finite difference formulation, it is obtained naturally from a finite volume formulation as well; and 2. Finite volume methods do not require a coordinate transformation in order to be applied on irregular meshes. As a result, they can be applied on unstructured meshes consisting of arbitrary polyhedral in three dimensions or arbitrary polygons in two dimensions. This increased capability can be used to great advantage in generating grids about arbitrary geometries.

1.5.2 Applications of FVM to Shallow Water Flows

In recent years, finite volume methods have attracted wide attention and achieved a series of successes in the numerical simulation of shallow water flows. Toro [65] presented an exact Riemann solver for the shallow water equations along with several approximate Riemann solvers and used the weighted average flux method (WAF) to solve two-dimensional shallow water problems. Alcrudo & Garcia-Navarro [66] presented a high-resolution Godunov-type scheme based on MUSCL variable extrapolation and slope limiters for the resolution of 2D free-surface flow equations and reported impressive results for rapidly varying inviscid flow. Sleigh et al. [22] presented an efficient finite volume based numerical algorithm for the solution of geometrically challenging two-dimensional river and estuary flows, based on an adaptive triangular tessellation of the flow domains of interest. The two dimensional governing shallow water equations were solved by using a finite volume approach embodying variable step time integrators, to yield a method that is second order accurate in both space and time. An approximate Riemann solver was used to determine flow directionality in conjunction with an effective means of dealing with wetting and drying at the boundaries. Recent applications have further extended the scope from pure water flow transients to mixtures of flows and sediment transport, such as mudflows, debris flow and dam-break induced geomorphic flows [67, 68]. Fraccarollo et al. [62] proposed a Godunov method for the computation of open-channel flows incorporating rapid bed erosion and intense sediment transport based on the HLL scheme with second-order accuracy solution using Strang splitting and MUSCL extrapolation. Afterwards, for computation of the case of flows over mobile bed, Rosatti and Fraccarollo [69] devised a new Godunov-type numerical approach for this kind of one-dimensional flows which are characterized by high concentration of sediment and strong interaction between flow and bed, as in hyper concentrated and debris flows. Rosatti [70] proposed a

generalized, well-balanced Roe solver without using the concept of a family of paths. In their research, two numerical schemes based on the same set of matrices were developed, one in terms of conserved variables and one in terms of primitive variables. In comparison with the AWB-3SRS mentioned in literature above [69], the main advantages of the proposed Roe schemes are simplicity and efficiency. On the other hand, the main drawbacks of the new methods are the lower accuracy as compared to AWB-3SRS and this method is one-dimensional with first-order accuracy. Apart from one-dimensional methods for flows incorporating sediment transport, based on the two phase description of mixture of flow and sediment, Armanini et al. [71] developed a set of two-dimensional depth-averaged motion equations to address the propagation of non-cohesive debris flows, in which the erosion and sedimentation processes play a significant role. An approximated Riemann solver of LHLL type mentioned in literature above is utilized, which takes the non-conservative terms and an implicit discretization of the bed shear stress source terms. Benkhaldoun [47, 72] delivered a two-dimensional morphodynamic model on unstructured triangular meshes using the finite volume methods. To solve the model, the authors utilised a modified Roe's scheme incorporating the sign of the Jacobian matrix to discretise the gradient fluxes in the morphodynamic system, and a well-balanced discretization is used for the treatment of source terms. The proposed method was the one that is second-order accurate, well-balanced, non-oscillatory, and simple to implement on unstructured triangular meshes. Furthermore, for the case of transient flow over erodible bed, Murillo and Garcia-Navarro [73] described two mathematical models: two-dimensional hydrodynamic model based on depth-averaged shallow water equations and the Exner equation which governs the bed load transport by a power law of the flow velocity and by a flow/sediment interaction parameter that varies in time and space. To solve the governing equations, a high-order Roe-type scheme was used on 2D triangular unstructured meshes. The proposed numerical scheme, following Rosatti et al. [70] as reviewed above, extended the sediment transport formulation of Grass to general formulations, focussing on the conservation of the bed material volume.

These models showed the robustness of FVM in such shallow water flows as water and sediment-laden flow. The successful applications provided a good basis for developing a morphodynamic model based on shallow water theory using FVM.

1.5.3 Treatment of Bed Slope Source Term

For application of FVM, source terms treatment usually imposes a significant impact on solutions of numerical results, especially, the source terms related to bed geometry, because they will cause numerical errors if an imbalance of flux gradient and source terms appears. The traditional method called the pointwise approach is considered as the simplest option to deal with source terms; however, the solution results are not satisfying, particularly in case of flow over irregular bed geometric and variable width. In recent years, a lot of attention has been paid to research on geometric source terms treatment.

To solve flow over variable bottom geometry, Nujic [74] suggested several methods to deal with water surface oscillations. Firstly he took the water elevation as an independent variable in the continuity equation instead of the water depth for eliminating numerical diffusion. Secondly, the $0.5gh^2$ term in the flux function was extracted and combined with the bottom slope term. However, this method could not solve the problem completely still exhibiting small amounts of numerical error.

LeVeque [75] introduced a discontinuous Riemann problem at the centre of each cell to incorporate source terms into the wave propagation algorithm so that the flux difference at grid cell exactly cancels source terms and avoid the need for fractional steps. However, LeVeque's approach is complicated to implement and shows less robustness and there are numeric errors in case of steady transcritical flows with shocks.

Bermudez and Vazquez [76] first proposed the upwind source terms treatment approach and have been widely used because of its accuracy compared with previous method. Garcia-Navarro and Vazquez-Cendon [77] presented an upwind source term treatment technique which was applied to 1D shallow water models for prismatic and non-prismatic rectangular channels. Compared with pointwise method, the upwind approach can get perfect balance of flux gradient and source terms in case of flows over irregular geometry. Thereafter, Hubbard and Garcia-Navarro (2000) extended the upwind approach to high-resolution TVD schemes which they applied to 1D and 2D shallow water flows to illustrate the effectiveness of this approach and. However, although the upwind source terms treatment approach shows very robust and accurate solutions, the main disadvantage of the upwind method is its complexity in implementation.

Zhou *et al.* [78] proposed a general scheme for treating source terms called the surface gradient method (SGM) in the shallow-water equations. The purpose of the SGM is to determine the accurate conservation variables at cell interfaces in order to achieve accurate calculation of the flux, At the cell centre, a piecewise linear relation of water surface was considered, and a slope limiter was used to avoid spurious oscillations occurring at the cell interfaces. The biggest advantage of this method is its simple implementation, and it can be applicable to steady and unsteady shallow water problems.

Most of the source term treatments mentioned above are difficult to implement or have some limitations for applying to unsteady flow. Lee and Wright [79] presented a novel simple and efficient technique for source terms treatment. They combined the source terms with flux gradient for balance between them to derive a homogeneous form of the shallow water equations which is straightforward to solve. In this method the source terms are automatically discretised and achieve perfect balance with flux terms without any special treatment. Several benchmarks tests solved by modifying several well-known Riemann solvers showed good agreement with analytical solutions. The advantages of this method lie in its simplicity, efficiency and applicability.

1.6 Classification of Morphodynamic Models

With the advancement of computer technology, mathematical modelling of sediment transport has been attracting and emerged in large numbers in last decades, involving one-dimensional models (1D), two dimensional models (2D) and fully three-dimensional models (3D) from the viewpoint of dimensions, as well as capacity models and non-capacity models, etc. Here, the sediment transport models are classified as purely theoretical-mathematical models and process-based numerical models considering the theoretical basis of models.

1.6.1 Purely Theoretical-mathematical Models

The principle of purely theoretical-mathematical models can be summarized as solving the coupled shallow water equations (SWE) and the Exner equation. A plethora of mathematical models and advanced numerical solvers have been developed, for example the research in the publications in

recent years [47, 48, 69, 80-87]. A main characteristic of these SWE-Exner morphodynamic models is that it quantifies the sediment movement by using an Exner equation based on the information from shallow water flow. The majority of the research on this type of morphodynamic model are focused on developing new algorithms or numerical solvers to solve the coupled SWE-Exner model system and on the accuracy and stability of numerical methods. In other words, the main concern of those models is a pure theoretical-mathematical problem with some vital simplifications for the real circumstances. In terms of sediment transport, an important assumption is that the sediment rate is assumed to be equal at any time to the sediment transport capacity, which is inherently unreasonable for most circumstances in reality, because there are spatial and temporal lags for sediment transport to adapt to the local flow conditions [53, 88, 89]. Also, suspended load is not usually considered as a contributor to bed deformation. This is bound to result in misrepresentation of the real fluvial process. This kind of model provides insight into the numerical algorithms. However, there is still much room for improvement in the application of these models to real engineering cases.

1.6.2 Process-based Numerical Models

Process-based numerical models of the fluvial process are increasingly and extensively used because they originate from the consideration of sediment transport mechanisms, such as the models by [11-16, 28, 31, 32, 37, 45, 49-51, 88, 90-94]. Likewise, these models involve capacity models and non-capacity models. The advantages and disadvantages of capacity models and non-capacity models have been investigated by many researches. Capacity models assume that sediment transport is always equal to at any time the sediment transport capacity under the local flow conditions. Whilst the non-capacity model, in converse, accounts for the spatial and temporal lags of sediment transport and determines the quantity based on evaluating the mass exchange of flow and bed. The non-capacity model is increasingly attractive and much more appropriate for the fluvial sediment transport because it represents the physical situation more reasonably. However, most of the numerous models are focused on academic basic research from the viewpoints of theoretical analysis or small-scale experiments, many lack sufficient validation. Nonetheless, although a lot of efforts have been paid in developing fluvial model of sediment transport, to attain accurate predicted results is still a distant hope based on current understanding. The fluvial

modelling is still uncertain and challenging because of the scarce understanding of sediment transport.

Most of existing morphodynamic models for the fluvial process stem from single-phase flow theory. In recent years, the conceptual model of two-phase flow has been investigated and suggested for sediment-laden flows and hyperconcentrated flows in open channels or coastal zones [95-101]. The motivations of these two-phase models are focused on assessing sediment flux, sediment concentration or sediment/fluid velocity variations for high concentrated suspended sediment or bed load dominant sheet flows. Yet, even though the two-phase flow model seems promising, its use and even the formulation of the governing equations in flow-sediment problems are still in the infancy; and the solution time of practical sediment problems for the two-phase flow model is relatively expensive even for the not-so-near future [94]. The two-phase concept for complete morphodynamic models is hardly presented in the literature. Recently, a rigorous theoretical derivation of a general two-phase morphodynamic model has also been introduced by Dewals et al. [96], but validation and applications have not yet been reported.

1.7 Uncertainty Factors for Morphodynamic Modelling

To date, computational modelling has become one of the most beneficial tools for providing quantitative decision-support in engineering design, planning and assessment. However, computational modelling has encountered a series of thorny issues as a result of the complexity of the physical situations and the significant uncertainties of some sediment-related parameters. In reality, the process of flow-sediment-geometry involves hydrodynamic phenomena, flow-sediment interactions, as well as particle-particle interactions. That makes the numerical modelling of fluvial sediment transport to be still a challenging topic of research today. Currently, a plethora of numerical models have been developed. Of course, all models can never represent the reality completely. Therefore, a lot of simplifications and approximations are inevitably assumed to be amenable to each simulation, resulting in the uncertainty of modelling results. Also, the scant understanding of complex fluvial process in reality leads to accurate prediction of such fluvial process being unattainable. According to the model development and applications in small- and large-scale hydraulic events, a series of uncertainty factors in the computational modelling of rapid fluvial

process are summarised; also some challenges are discussed in following sections.

The potential factors causing the uncertainties of modelling results can be summarised as: 1) numerical methods; 2) bed resistance; 3) sediment particles; 4) sediment transport capacity; 5) non-equilibrium adaptation length; 6) entrainment and deposition rate for suspended load; 7) channel cover condition; etc.

Table 1.1 Uncertainty factors for the morphodynamic modelling

No.	Uncertainty factors	Explanations	Issues
1	Numerical methods	(1) types (2) accuracy	
2	Bed resistance		difficulty to quantify in reality
3	Sediment particles	(1) uniform (2) non-uniform	difficulty to quantify in reality
4	Sediment transport capacity	For bedload dominant flow	All the existing formulas were derived based on small-scale experiments and have a limited scope of application.
5	Non-equilibrium adaptation length	For bedload dominant flow	It is empirical
6	Entrainment/deposition fluxes	For suspended load flow	Empirical functions
7	Channel cover	(1) types (2) distribution	difficulty to quantify in reality

1.7.1 Numerical Methods

To develop robust and accurate numerical solvers is one of the motivations of many researchers, looking forward to obtaining better predicted results, which is attractive theoretically. However, what is the implication of the numerical solver on the fluvial sediment transport modelling? In fact, the order and accuracy of numerical schemes are not a primary uncertainty factor for the modelling of rapid fluvial process. The important uncertainty issue in the numerical methods is how and when the sediment in the bed responds to the flow, because of the spatial and temporal scale of flow and sediment. For many computational models, the bed deformation is usually updated at each time step based on the evaluation of sediment entrainment and deposition fluxes; however, the bed response to the fluid flow in a natural flow-sediment event might be several, tens or hundreds of time steps

which are certainly unsure, particularly for the bedload dominant flow. Furthermore, from the viewpoint of model dimensions, 2D and 3D models can represent the physical situation in reality better and give the more detailed information we need, however, the computational time of detailed 2D and 3D models is also much more expensive. Of course, the rapid advancement of computer technology will provoke the development of full 3D models, such as Reynolds-Averaged Navier–Stokes (RANS), large eddy simulation (LES) or Smoothed Particles Hydrodynamics (SPH), etc. Nonetheless, the application of full 3D numerical models in large-scale flood events is still a big challenge. Most of them were only focused on small-scale experiments or academic theoretical research.

1.7.2 Hydraulic Resistance

Hydraulic resistance not only affects the flow properties, but also it can alter the bed shear stress which directly decides how much sediment can be entrained into movement. The estimation of it, however, is still full of uncertainty because of the complexity of physical situation in reality. Conventional resistance equations include those based on Chézy's resistance factor, Darcy–Weisbach friction factor and Manning's '*n*' which are widely used in hydraulic and sediment transport modelling [102-104]. Yet, these factors depend strongly on bed form, grain size, bed cover and flow conditions etc., which make it impossible to estimate them accurately. Also, the incorporation of sediment load probably increases or decreases the flow resistance, which has been a controversy in the last few decades. In addition, the approaches used to calculate the bed shear stress is numerous, such as the depth-slope product, or shear velocity-based method.

1.7.3 Input Sediment Particles

In reality, the river channel is often composed of different sediment grain size fractions; for example, as shown in Figure 7.1, where the sediment materials involve the fine gravel and coarse boulders. The fluvial sediment transport process is significantly affected by the grain size of sediment. Firstly, the hydraulic resistance is relative to the grain size; secondly the grain size can directly influence the bed shear stress which, in reverse, decides the entrainment and movement of sediment particles; also most of sediment transport equations are the functions of the size distribution of bed material. Inevitably, the sediment grain size is a vital input parameter for the fluvial-

geomorphic modelling. However, to estimate it in reality is rather arbitrary and likewise quite hard work because of the complexity of real riverbeds. For most modelling work, a common approach of treating this is just to incorporate an estimated median value for uniform model and several estimated diameters of each fraction for non-uniform model, which certainly brings about uncertainty of modelling results.

Figure 1.4 Sediment particles in river channel in reality

1.7.4 Empirical Sediment Transport Function

The sediment transport rate is, without exception, calculated by a variety of empirical formulae which were derived based on certain sediment material, certain hydraulic conditions and limited experimental conditions. Therefore, each formula has a limited scope of application. To estimate sediment transport capacity, the primary challenges involve the estimation of flow conditions, sediment material.

In many transport formulae, the flow shear stress is considered as the flow force acting per unit area of stream bed, and it is estimated from the flow discharge and bed and hydraulic roughness of the stream channel, yet It is difficult to estimate the correct value and as matter of fact, only part of the flow force exerted on the bed induces sediment into movement. Furthermore, sediment transport rate is closely related to grain size of sediment. Estimation of grain size of the stream channel in reality is rather arbitrary, and for a gravel bed the range of sizes is typically very broad. This makes it impossible to calculate sediment transport capacity accurately. Even more, the existing empirical formulae cannot be used to estimate the transport of very coarse boulder particles. In addition, it is also found that sediment transport rates are influenced significantly by bed slope, i.e. the empirical transport formulae derived in flat bed may cause deviation for the case of steep bed channel. In summary, the underlying reason why estimation of transport rate has such a large uncertainty is that the formulae

are strongly nonlinear. The significance of this is that if the input is slightly deviated, the calculated sediment transport rates can have a large error. For example, the formulae could calculate large sediment transport capacity when little transport actually occurs, or might predict no transport for the case when the actual transport is quite large.

For capacity models and non-capacity models for bedload dominant sheet flow, sediment transport capacity is a vital function to close the model system. To date, a plethora of sediment transport formulas have been developed [24-26, 105-112]; nevertheless, nearly all of these formulations were derived based on laboratory or fieldwork datasets under certain hydraulic conditions. Therefore, the resulting functions have their own scope of applications and none can be universally used for complex natural rivers. For example, these empirical formulae may be no longer appropriate for the case with very coarse boulders. Although it is claimed by many researchers that the sediment transport formulae they proposed can produce the results with good agreement with the measured data, the application of them in real situations is certainly different and no verification shows that these functions are suitable for all real events. In the past decades, the applicability of some popular formulations has been investigated by some research through comparing against the river data or computational application in experimental event [55, 113] and it has been found that the performance has significant differences for some functions in terms of the quantity. Research has been increasingly concerned with how to develop an accurate and universal sediment transport function, which has been unattainable so far. Sediment transport formulation is undoubtedly a primary source of uncertainty in the river fluvial modelling.

1.7.5 Non-equilibrium Adaption Length

In the computational models, bed deformation for the fluvial process is generally expressed by assessing the entrainment and deposition flux at certain cells or the non-equilibrium adaption length of sediment which represents the distance of sediment particles entrained from bed and re-deposited to bed. The non-equilibrium adaptation length L is related to the dimensions of sediment movements, bed forms, and channel geometry which are usually considerably different in laboratory and field situations. Similarly, this parameter is presented by laboratory-based empirical relationships [28, 31, 49, 89, 114, 115], and no universal formulation is available. Duc and Rodi [49] tested the performance of several empirical

formulations. It was found that the parameter influences the stability of morphodynamic model and the bed deformation in terms of quantity; however, the erosion and deposition has a similar distribution feature. In other words, the qualitative assessment for the fluvial sediment transport is still acceptable.

The non-equilibrium adaption length represents the distance over which sediment particles are entrained and then re-deposited to the bed, which influences the magnitude of geomorphic change. The non-equilibrium adaptation length L is generally related to the dimensions of sediment movements, bed forms, and channel geometry which are usually considerably different in laboratory and field situations. Similarly, this parameter is measured by laboratory-based empirical relationships. For example, Phillips and Sutherland (1989) [89] assumed that the average saltation step length can be expressed as a simple function of the Shields parameter θ, the critical value θ_{cr}, and mean grain size d_m. Based on the analysis of a number of flume data, the following equation was proposed for the average saltation step length:

$$L = \alpha_p (\theta - \theta_{cr}) d_m$$

where α_p=4000 as suggested by the authors. Van Rijn [114] proposed the average saltation step length of particles L as a function of the transport stage T and the particle parameter d_*, based on calibrating the numerical model for simple flow situations with plane bed using flume and field data. His derivation adopted the Lagrangian equations for the motion of particles.

$$L = 3 d_m d_*^{0.6} T^{0.9}$$

For sand dunes dominant bedform, van Rijn [114] suggested a simplified expression to determine the non-equilibrium adaption length L as a function of water depth based on the analysis of a large number of reliable flume and field data.

$$L = 7.3h$$

Apart from these, many other different relationships have been used to model the corresponding sediment transport problem [28, 31, 115]. However, no formula hitherto can be generally applicable.

1.7.6 Entrainment and Deposition Rates

For the fine sand bed, sediment particles are usually entrained into suspension by intense water flow and re-deposited somewhere water flow cannot support them anymore. In such circumstance, the fluvial process is often calculated by the entrainment and deposition rates of sediment particles in bed. How to quantify the entrainment and deposition rates naturally becomes a vital issue. However, a generic theoretical expression of them, unfortunately, does not exist. Once again, to be amenable to the numerical modeling, empirical formulas are suggested and many efforts have been taken to investigate the sediment entrainment and deposition rates. For example, for the entrainment flux, some typical and commonly-used formulas involve: Engelund & Fredsoe (1976) (EF), Smith & McLean (1977) (SM), van Rijn (1984) (VR), Garcia & Parker (1991) (GP), Zyserman & Fredsoe (1994) (ZF), Cao et al. (2004) (C), Sun & Parker (2005) (SP) [11, 52, 116-120]. These formulas can be catalogued into two types: (1) the direct expression S_E of the pick-up rate; (2) other formulas were expressed by multiplying near-bed equilibrium concentration by setting velocity of sediment as $S_E = w_f C_{ae}$. All these formulas were shown to agree well with the experimental dataset. However, is it appropriate to use them in numerical modeling for the fluvial sediment transport? According to an assessment of dam-break flow over a movable bed [121], it is found that the differences of simulated results are obviously significant. Qualitatively speaking, the trend of bed deformation and flow features are similar, whilst the quantified results are far away to be credible.

1.7.7 Quantification of Land Cover

Land cover of stream channel is case-dependent. For those cases with vegetation cover, the vegetation effects on morphodynamic process is non-negligible, because vegetation can significantly alter flow features and geomorphic change. However, the randomness of vegetation distribution and catalogue increases the difficulty of quantification of them.

(1) The presence of flexible vegetation increases the total resistance and the threshold of sediment entrainment meanwhile decreases sediment transport capacity, because its presence alters the flow velocity field. However, there is still only a few investigations on sediment transport capacity in presence of vegetation. Moreover, the experimental studies on vegetation effects are also very scarce, which limits the generation of reliable formulation of sediment transport capacity in presence of

vegetation.

(2) Treating vegetation appropriately is a challenging task; and most of the existing methods generally assume that the vegetation is artificial rigid cylinders with the same diameter. It is apparent that the diversity of plants in the natural environment limits the accuracy of such approaches in hydraulic models. In other words, the difficulty of quantifying the complex vegetation distribution causes hydraulic modelling is rather full of uncertainty.

Like this study many previous studies have also claimed that the roughness coefficient has a strong relationship with depth of flow, height of vegetation and discharge level [102, 122]. Numerous efforts have been made to quantify vegetation-flow resistance relationship; yet, the fact is that these methods themselves have some not inconsiderable uncertainty factors. Therefore, owing to the complexity of quantifying roughness, the value is usually assumed to be a constant according to the experienced estimation in most of real applications. But the constant value is bound to cause inaccurate predication results. That is a vital point for hydraulic modellers when simulating real flood case.

1.8 Research Questions and Objectives

According to the issues reviewed above, the existing numerical models for rapid sediment-laden flows have a series of problems, such as how to address the source terms and wetting/drying fronts for application in reality, how to better construct the conceptual model, how to apply it to large-scale event and also how to improve the further understanding of the flow-sediment interaction in rapid outburst flood. Based on these limitations, several research questions will be resolved and answered in this thesis and correspondingly the outputs attained.

1 How can irregular topography be better addressed when solving the 2D shallow water numerical model, including the issues of handling bed slope term and wetting/drying fronts?

2 What can be improved in the layer-based hydro-morphodynamic model and what significant advantages can be identified?

3 What understanding of flow-sediment transport interactions and unsteady sediment transport can be obtained through computational modelling of small-scale hydraulic events and large-scale rapid outburst floods?

3i) *what role does sediment grain size play in the flow-sediment interactions?*

3ii) *what are the implications of sediment transport on flood propagation?*

3iii) *how does the outburst flood affect the antecedent river bed?*
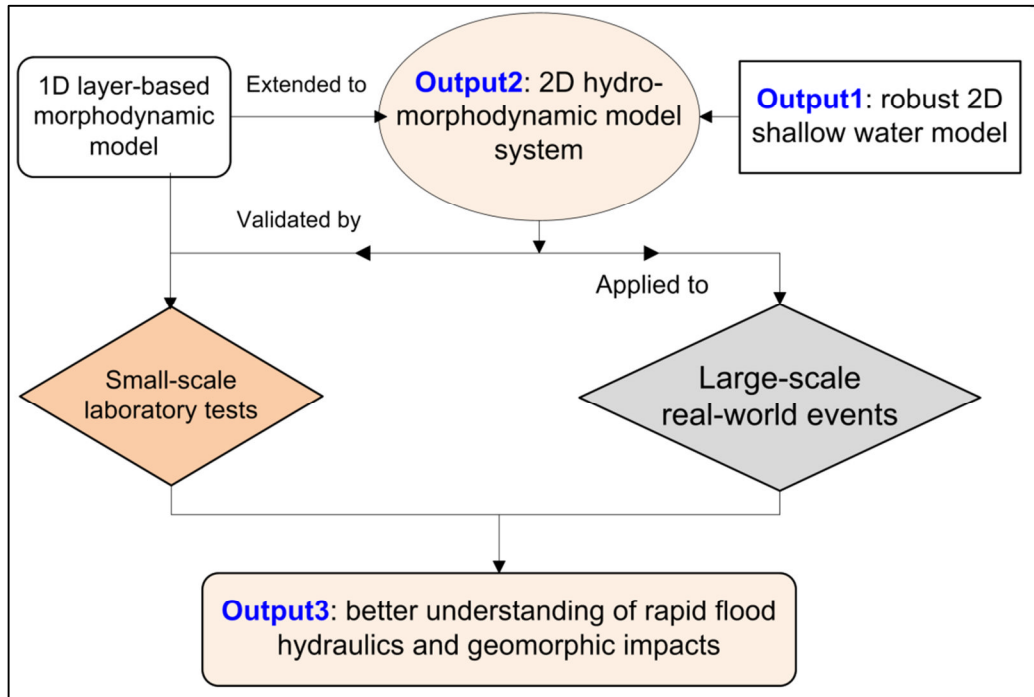
Figure 1.5 The research framework

In short, the motivation of this thesis is to develop a hydro-morphodynamic model applicable to rapid outburst floods with high magnitude unsteady sediment transport. Figure 1.5 illustrates the research framework. To attain the desired outputs, several objectives are formulated as follows:

- to present an easily-implemented approach to address the issues of flows over irregular topography in two dimensions;
- to develop a 1D layer-based hydro-morphodynamic model for unsteady sediment transport and validate it against a series of experimental cases;
- to extend the 1D model to two dimensions and test it against small-scale experimental cases;
- to apply the 2D computational model to a selected appropriate representation of full-scale outburst floods with rapid geomorphic change which differs from the long-term fluvial process by perennial flows in rivers or coastal areas; and
- to further understand rapid outburst flood hydraulics and unsteady sediment transport.

1.9 Outline of the Thesis

The thesis is organised as 3 Parts with 8 Chapters as following:

- **Chapter 1**: i.e. current chapter, to present literature review on the related research scope, including the morphodynamic modelling in regular flow and outburst floods, as well as the research progress of numerical methods in solving shallow water model and then to propose the research questions and objectives.
- **Chapter 2**: to give a theory introduction of sediment transport mechanisms used in the following model development and to present a 1D and 2D bed slope avalanching model with model tests.
- **Chapter 3**: to present a robust 2D shallow water model to solve pure water flows over complex, irregular topography, including the method of handling bed slope source term and wetting/drying fronts, and to validate the 2D hydrodynamic model in a series of benchmark tests.
- **Chapter 4**: to present a hydro-morphodynamic model framework and model assumptions, to develop a 1D layer-based hydro-morphodynamic model and then to test it by comparison with a series of experimental tests.
- **Chapter 5**: to extend the 1D computational model to two dimensions and to validate it against a series of related experimental tests, also to apply the model to a special complex flow-sediment event (dike breach caused by flow overtopping).
- **Chapter 6**: a full-scale rapid outburst flood with high magnitude sediment transport is reproduced using the developed model system for testing the applicability and importantly, obtaining further understanding of the outburst flood hydraulics and rapid geomorphic impacts.
- **Chapter 7**: some conclusions are drawn out and future works are recommended in this chapter.

Chapter 2
Parameterisation of Sediment Transport

In this chapter, the sediment transport properties and quantification of sediment transport parameters used for computational modelling are introduced. Also, an avalanching model is proposed for unstable sloped beds.

2.1 Sediment Transport Properties

2.1.1 Settling Velocity

Generally, for a single particle, the setting velocity ω_0 (m/s) is a function of particle Reynolds number, it is usually determined by their diameter and density, and the viscosity of the water. In recent years, a number of empirical formulae have been derived to calculate the setting velocity ω_0 of single grain based on the experimental works [27, 123]. Therein, van Rijn (1984) presented the following equations to calculate the settling velocity of natural non-cohesive sediment as:

$$\omega_0 = \begin{cases} \dfrac{(s-1)gd^2}{18v} & for\ 1 < d < 100\mu m \\[2mm] 10\dfrac{v}{d}\left[\left(1 + \dfrac{0.01(s-1)gd^3}{v^2}\right)^{1/2} - 1\right] & for\ 100 < d < 1000\mu m \\[2mm] 1.1\sqrt{(s-1)gd} & for\ d > 1000\mu m \end{cases} \quad (2.1)$$

where g = gravitational acceleration = 9.81 m/s^2

   s = relative density of sediment
   d = representative diameter of sediment (m)
   v = kinematic viscosity coefficient of water (m^2/s)

Soulsby (1996) derived the following formula for natural irregular gains:

$$\omega_0 = \frac{v}{d}\left[\sqrt{(10.36^2 + 1.049d_*^3)} - 10.36\right]\ for\ all\ d_* \quad (2.2)$$

where d$_*$ = dimensionless sediment grain size is calculated by

$$d_* = d\left[\frac{g(s-1)}{v^2}\right]^{1/3} \quad (2.3)$$

At high concentration mixtures, the settling velocity ω_0 of a single particle is reduced due to the presence of other particles. So this causes the hindered

settling velocity in a fluid-sediment mixture to be smaller than that at low concentration. A factor $(1-C)^{4.7}$ is incorporated into the formula (3.2) as [27]:

$$\omega_f = \frac{v}{d}\left[\sqrt{10.36^2 + (1-C)^{4.7}1.049d_*^3} - 10.36\right] \quad for\ all\ d_* \qquad (2.4)$$

where ω_f = effective settling velocity (m/s)

$\quad$ C = volumetric sediment concentration

2.1.2 Shields Parameter θ

The Shields parameter θ is the dimensionless bed shear stress exerting on the sediment particles, which can be expressed by:

$$\theta = \frac{\tau_b}{(\rho_s - \rho_w)gd_{50}} = \frac{u_*^2}{(s-1)gd_{50}} \qquad (2.5)$$

where τ_b = bed shear stress (N/m^2)

$\quad$ ρ_s = density of sediment (m^3/s)

$\quad$ ρ_w = density of water (m^3/s)

$\quad$ d_{50} = median diameter of sediment grain (m)

$\quad$ u_* = shear velocity

There are several methods available to calculate shear velocity u_*, but in this project, a Manning's coefficient-based approach is used. Therefore, the shear velocity u_* is calculated by

$$u_* = \sqrt{C_d\bar{u}^2} = \sqrt{\frac{gn^2}{h^{1/3}}\bar{u}^2} \qquad (2.6)$$

where C_d = drag coefficient

$\quad$ h = flow depth (m)

$\quad$ $\bar{u}$ = depth average velocity (m/s)

$\quad$ n = Manning's coefficient

2.2 Threshold of Incipient Motion

2.2.1 Critical Shields Parameter

The motion of sediment is a process where sediment is entrained from the bed, transported and then re-deposited on the bed. For the first stage, say, entrainment, it is decided by the relationship of the bed shear stress exerted by the flow mentioned above and the threshold of incipient motion of the sediment. This threshold condition results from the hydrodynamic moments

of force acting on the sediment balancing the resisting moments of force [124]. The critical value is the so-called Shields parameter or dimensionless bed shear stress θ_c, which can be written as

$$\theta_c = \frac{\tau_{b,c}}{(\rho_s - \rho_w)g d_{50}} \tag{2.7}$$

where $\tau_{b,c}$ = threshold bed shear stress (N/m^2)

In fact, no special relationships have been proposed for the threshold of initial sediment motion which is closely related to dimensionless sediment particle size. Most existing relationships are based on the experimental data. The pioneering empirical formulae by van Rijn (1984) and Soulsby (1997) are most widely used. Figure 2.1 illustrates the Shields curves of the two relationships, which indicates that there is no significant discrepancy. The relationship of Soulsby is applied in the following applications.

van Rijn (1984):

$$\theta_c = \begin{cases} 0.24 d_*^{-1} & d_* \leq 4 \\ 0.14 d_*^{-0.64} & 4 < d_* \leq 10 \\ 0.04 d_*^{-0.1} & 10 < d_* \leq 20 \\ 0.013 d_*^{0.29} & 20 < d_* \leq 150 \\ 0.056 & d_* > 150 \end{cases} \tag{2.8}$$

Soulsby (1997):

$$\theta_c = \frac{0.3}{1 + 1.2 d_*} + 0.055[1 - \exp(-0.02 d_*)] \tag{2.9}$$
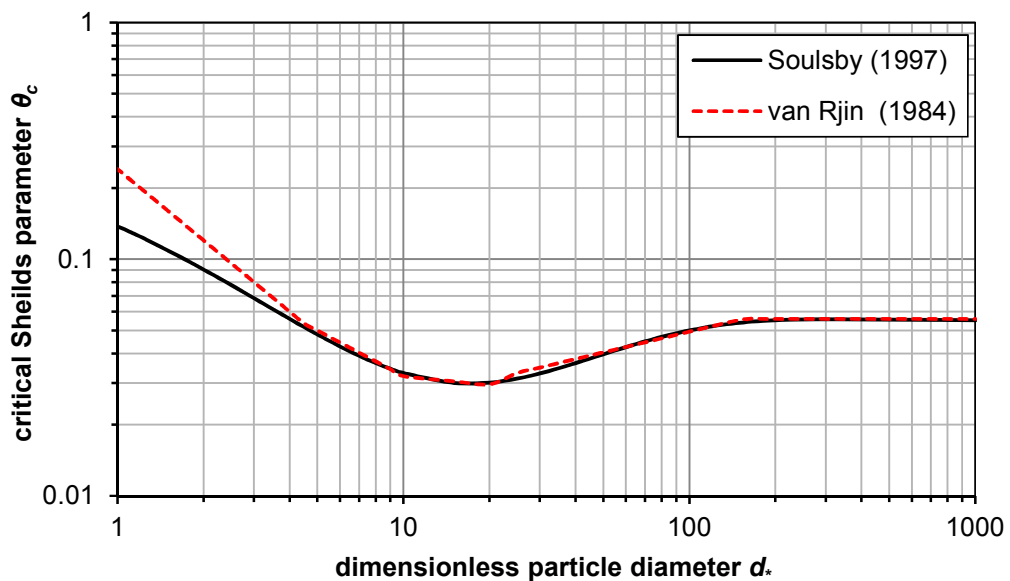
Figure 2.1 Shields curves by Soulsby (1997) and van Rijn (1984)

2.2.2 Hiding and Exposure Effects

For non-uniform sediment mixtures, as the sediment grain sizes are different, the coarser particles can easily generate an armour layer which shelters the finer particles, thereby preventing the finer sediment particles from being entrained, whereas the exposure of coarser particles on the bed causes them to be entrained more easily than uniform sediment of same size. For example, as illustrated in Figure 2.2, the movement of non-uniform sediment mixtures can involve no motion, partial motion and full motion, which one depends on the magnitude of bed shear stress.

(a) No motion   (b) Partial motion   (c) Full motion
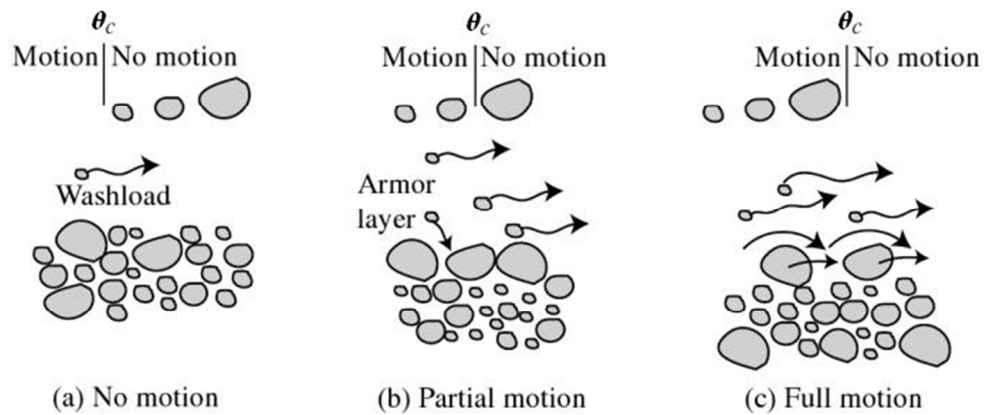
Figure 2.2 Bed surface for sediment mixtures [124]

Therefore, the critical Shields parameter will be slightly different for different sediment grain sizes because of the hiding and exposure effects. The critical dimensionless shear stress θ_{cHE} for the destruction of the armour layer are defined by Hunziker and Jäggi [125] as:

$$\theta_{cHE} = \theta_c k_1 = \theta_c \left(\frac{d_{90}}{d_m}\right)^{2/3} \qquad (2.10)$$

where θ_{cHE} = critical Shields parameter with hiding and exposure effects

k_1 = the coefficient corresponding to hiding/exposure

d_{90} = characteristic grain size for which 90% by weight is finer (m)

d_m = mean diameter (m)

2.2.3 Bed Slope Effects

One of the most important implications of bed slope is its effect on the critical shear stress for initial sediment motion. A number of studies have highlighted that variation in channel gradient has an influence over the mean bed shear stress at which sediment is entrained [112, 126, 127]. Smart and Jäggi [112] considered the influence of gravity on incipience of motion at steep slopes and derived an equation for the initiation of bedload transport:

$$\theta_{cs} = \theta_c \cos(\arctan S)\left(1 - \frac{S}{\tan\varphi}\right) \qquad (2.11)$$

Lamb et al. [126] obtained a trend of increasing critical Shields stress with channel slope by analysing a large set of experimental and field data from incipient motion studies.

$$\theta_c = 0.15 S^{0.25} \qquad (2.12)$$
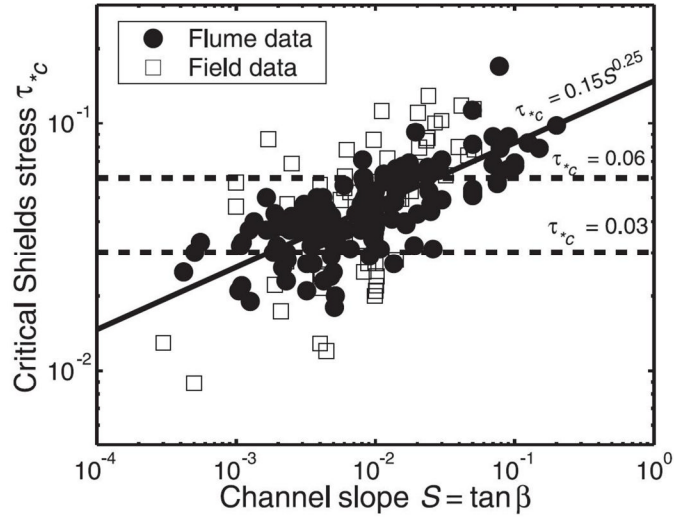
Figure 2.3 The slope dependency of the critical Shields stress [126]

However, bed slope S can be positive or negative; and the flow direction and slope direction can influence the revised critical shear stress. So according to the relation of flow and slope direction, we can improve Eq. (2.11) as follows:

$$\theta_{cs} = \theta_c k_2 = \theta_c \begin{cases} \cos(\arctan|S|)\left(1 - \dfrac{|S|}{\tan\varphi}\right) & u \cdot S < 0 \\[2mm] \cos(\arctan|S|)\left(1 + \dfrac{|S|}{\tan\varphi}\right) & u \cdot S > 0 \end{cases} \qquad (2.13)$$

where θ_{cs} = a corrected critical Shields parameter for high slopes

k_2 = the coefficient with consideration of bed slope effects

φ = the sediment angle of repose

$S = dz/dx$ = the bed slope

u = the depth-averaged velocity (m/s)

Therefore, in summary, considering hiding/exposure effects and bed slope effects, the critical Shields parameter is calculated by

$$\theta_{cr} = k_1 k_2 \theta_c \qquad (2.14)$$

where k_1, k_2 are the coefficients mentioned above. For uniform sediment, k_1 = 1; and for flat bed, k_2 = 1.

2.3 Sediment Transport Equations

In general, sediment transport can be catalogued into three modes: wash load transport, suspended load transport and bed load transport. Therein, wash load refers to the particles that are too fine to settle and are carried within the water column as part of the flow, and therefore moves with similar velocity to flow. The wash load is usually found in very small amount and does not affect geomorphic changes. Suspended load denotes the sediment that is conveyed in suspension supported by turbulence fluctuation in the lower to middle parts of the flow. Bedload transport is coarser sediment particles that moves by sliding, rolling and hopping over the bed and actively interacts with the bed. The bed load and the portion of suspended load entrained from the bed constitute the bed material load, which is often dominated by bed load, especially in gravel-bed rivers. As an important component of that, bedload transport plays a dominant role in controlling the geomorphic changes of channel. At high bed shear stress, the suspended load also plays an important role for the morphodynamic process.
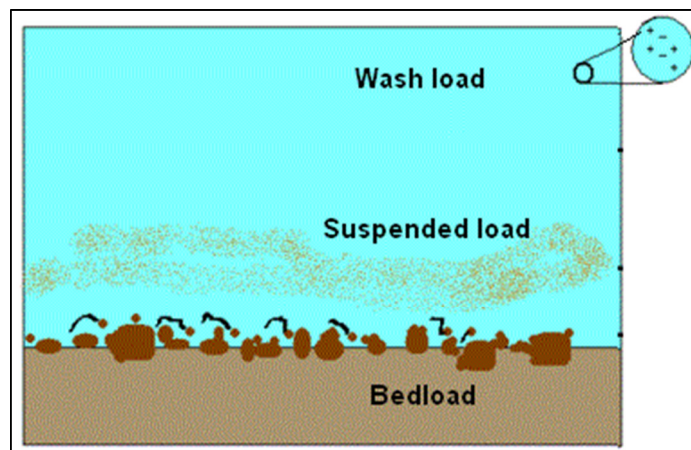
Figure 2.4 Sediment transport modes

2.3.1 Suspended Load Transport

According to the mass conservation of sediment, the suspended load transport can be governed by the three-dimensional advection-diffusion equation expressed by:

$$\frac{\partial c}{\partial t} + \frac{\partial uc}{\partial x} + \frac{\partial vc}{\partial y} + \frac{\partial (\omega - \omega_f)c}{\partial z} = \varepsilon_x \frac{\partial^2 c}{\partial x^2} + \varepsilon_y \frac{\partial^2 c}{\partial y^2} + \varepsilon_z \frac{\partial^2 c}{\partial z^2} \qquad (2.15)$$

where c = volumetric sediment concentration

u, v, ω = velocities in x, y and z directions (m/s)

ε_x, ε_y, ε_z, = eddy diffusivities of sediment in x, y and z directions (m²/s)

However, for a two-dimensional equation in x and y directions (plan view), it is easy to convert Eq.(2.15) to a depth-averaged formation by integrating it in vertical direction. Consequently, the 2D depth-averaged suspended load transport equation is written by

$$\frac{\partial hC}{\partial t} + \frac{\partial huC}{\partial x} + \frac{\partial hvC}{\partial y} = \frac{\partial}{\partial x}\left(\varepsilon_x h \frac{\partial C}{\partial x}\right) + \frac{\partial}{\partial y}\left(\varepsilon_y h \frac{\partial C}{\partial y}\right) + (S_E - S_D) \qquad (2.16)$$

where C = depth-averaged volumetric sediment concentration

h = water depth (m)

S_E = entrainment flux of sediment

S_D = deposition flux of sediment

For suspended load dominant transport, the geomorphic change of bed is closely related to the entrainment rate and deposition rate of sediment. However, a complete theoretical expression does not exist and it is nearly impossible. In recent decades, much efforts were taken to investigate the quantification of the entrainment rate and deposition rate of sediment. Firstly, for the entrainment flux, some typical and commonly-used formulae are selected and summarised, involving: Engelund & Fredsoe (1976) (EF), Smith & McLean (1977) (SM), van Rijn (1984) (vR), Garcia & Parker (1991) (GP), Zyserman & Fredsoe (1994) (ZF), Cao (1999) (C), Sun & Parker (2005) (SP) [52, 117, 118, 120, 123, 128]; as shown in Table 2.1. Generally, the formulae of entrainment flux can be catalogued into two types: (1) the direct expression S_E of the pick-up rate; (2) other formulae were expressed by multiplying near-bed equilibrium concentration by the settling velocity of sediment as $S_E = w_f C_{ae}$.

However, each formula mentioned above has a particular scope, and is not applicable to all circumstances. According to the assessment by the author [121], for the lower Shields parameter ($\theta < 2$) case, the typical empirical formulae of EF, SM, GP and ZF can achieve similar results with no big discrepancy. However, with increasing θ, their performance becomes unreliable, so they cannot be recommended for high shear stress cases. The uncertainty of empirical coefficients in the SP makes it too uncertain to be applied well; vR is based on bed shear stress related to grain skin friction that is the combination of bed grain and form shear stresses, importantly, it has fewer uncertain empirical parameters and the performance is stable in both low and high shear stress. It is recommended to apply only provided that it is satisfying its applicable scope.

Table 2.1. The empirical formulae of entrainment flux

Name	Entrainment formulae	Type
EF	$C_{ae} = \dfrac{0.65}{(1 + \lambda_b^{-1})^3}$; $\lambda_b = \sqrt{\dfrac{\theta - 0.06 - p\pi/6}{0.027\theta(\rho_s/\rho_w - 1)}}$	$S_E = \omega_f C_{ae}$
SM	$C_{ae} = \dfrac{0.65 \times 0.0024T}{1 + 0.0024T}$; $T = \dfrac{\theta - \theta_{cr}}{\theta_{cr}}$	
vR	$C_{ae} = 0.015\dfrac{d_{50}}{a}\dfrac{T^{1.5}}{d_*^{0.3}}$; $T = \dfrac{(u_*^2 - u_{*,cr}^2)}{u_{*,cr}^2}$; $a = \min(\max(2d_{50}; 0.01h), 0.2h)$	
GP	$C_{ae} = \dfrac{1.3 \times 10^{-7}Z_u^5}{1 + 1.3 \times 10^{-7}Z_u^5/0.3}$; $Z_u = \dfrac{u_* R_p^n}{v}$	
ZF	$C_{ae} = \dfrac{0.331(\theta - 0.045)^{1.75}}{1 + 0.331(\theta - 0.045)^{1.75}/0.46}$	
C	$S_E = \dfrac{160}{R^{0.8}}\dfrac{1 - p}{\theta_{cr}}\dfrac{(\theta - \theta_{cr})d_{50}}{h}\dfrac{7u}{6}$	S_E
SP	$S_E = \alpha_t \theta_{cr}^2 \left[\dfrac{u}{u_t} - 1\right]^{1.5\sim2}$; $u_t = \sqrt{\dfrac{(\rho_s/\rho_w - 1)gd_{50}\theta_{cr}}{C_f}}$	

Note: C_{ae} = near-bed equilibrium concentration

p = sediment porosity

u_* = bed shear velocity related to grain friction

u_{*cr} = critical bed-shear velocity for initial motion of sediment

v = kinematic viscosity of water

R_p = sediment particle Reynolds number

α_t = empirical coefficient

The deposition flux is represented as the product of effective sediment settling velocity and the near-bed concentration at reference level $S_D = \omega_f C_a$. Therein the near-bed concentration C_a is determined by $C_a = \delta C$. The coefficient δ is empirically specified by some authors [11, 129]. Furthermore, physically the near-bed concentration must not be larger than 1 minus sediment porosity p. The coefficient δ definition of Zhou and Li [129] can be slightly modified by:

$$\delta = \min\left\{\frac{\omega_f(h - a)}{\varepsilon_z}\left[1 - \exp\left(-\frac{\omega_f(h - a)}{\varepsilon_z}\right)\right]^{-1}, \frac{1 - p}{C}\right\} \tag{2.17}$$

where $\varepsilon_z = \kappa u_* h/6$ = vertical sediment diffusivity (m²/s)

a = reference level (m)

Cao et al. [11] treated δ as an empirical coefficient with the following relationship:

$$\delta = \min\left\{2.0, \frac{1-p}{C}\right\} \tag{2.18}$$

2.3.2 Bedload Transport

Bed particles enter motion as soon as the bed shear stress exerted on the bed material exceeds the critical shear stress. There are hitherto many formulae derived based on experiment data to calculate the bedload transport capacity. However, such bedload transport equations have a particular scope of application. Several frequently-used formulae are briefly introduced here.

2.3.2.1 Meyer-Peter and Müller (1948)

Meyer-Peter and Müller [26] derived a relatively simple bedload formula for gravels by conducting extensive experimental work in a laboratory flume. It is written by:

$$q_{b*} = 8(\theta - 0.047)^{1.5}\sqrt{(s-1)gd_{50}^3} \tag{2.19}$$

where q_{b*} = bedload transport capacity (m^2/s)

$s = \rho_s/\rho_w$ = ratio of densities of sediment and water

The scope of application is: d_{50} = 0.4 mm~29 mm; bed slope = 0.0004~0.02; Shields parameter θ < 0.25.

Wong and Parker [130] re-analysed the experimental data and modified the original MPM bed load equation as the following two equations:

$$q_{b*} = 4.93(\theta - 0.047)^{1.5}\sqrt{(s-1)gd_{50}^3} \tag{2.20a}$$

$$q_{b*} = 3.97(\theta - 0.0495)^{1.5}\sqrt{(s-1)gd_{50}^3} \tag{2.20b}$$

2.3.2.2 Van Rijn (1984)

Van Rijn (1984) [109] proposed a bedload transport equation based on a verification study using 580 flume and field data. The equation is expressed by several parameters related to the sediment particle as:

$$q_{b*} = 0.053\frac{T^{2.1}}{d_*^{0.3}}\sqrt{(s-1)gd_{50}^3} \tag{2.21}$$

where $T = \frac{(u_*^2 - u_{*,cr}^2)}{u_{*,cr}^2} = \frac{\theta - \theta_{cr}}{\theta_{cr}}$ = transport stage parameter

d_* = dimensionless particle diameter defined by Eq.(2.3)

The applicable scope of this equation is: sand of median diameter d_{50} = 0.1mm~2.0mm; bed slope < 0.005.

2.3.2.3 Smart and Jäggi (1983)

Both bedload transport equations mentioned above are only applicable to gentle slopes. To date, only a few bedload transport formulae have been developed for steep gravel bed channel [107, 111, 112]. Smart and Jäggi (1983) expanded the database obtained by Meyer-Peter and Müller (1948) for the steep slope range from 0.03 to 0.20. They performed flume experiments to estimate the maximum transport capacity of mountain streams.

$$q_{b*} = 4 \left(\frac{d_{90}}{d_{30}}\right)^{0.2} \frac{h^{1/6}}{n\sqrt{g}} \min(S_o, 0.2)^{0.6} \theta^{0.5}(\theta - \theta_{cr}) \sqrt{(s-1)g d_{50}^3} \qquad (2.22)$$

where d_{30}, d_{90} = grain sizes of 30% and 90% by weight is finer (m)

$q = hu$ = flow discharge rate per unit width (m²/s)

θ_{cr} = critical Shields parameter estimated according to Eq.(2.14)

The applicable range is: d_{50} = 0.4mm~29mm; bed slope = 0.03~0.2; Shields parameter θ = 0.1~3.3; $d_{90}/d_{30} \leq 10$; for uniform sediment, $d_{90}/d_{30} = 1.05$.

2.3.2.4 Rickenmann (1991, 2001)

For the steep bed slope, Rickenmann (1991) [111] developed the following dimensionless bedload transport equation by performing flume experiments for slopes ranging from 0.07 to 0.20 and by using a total of 252 experiments including flume data obtained by Meyer-Peter and Mueller (1948) and Smart and Jäggi (1983).

$$q_{b*} = \frac{3.1}{\sqrt{s-1}} \left(\frac{d_{90}}{d_{30}}\right)^{0.2} \theta^{0.5}(\theta - \theta_{cr}) \mathrm{F}^{1.1} \sqrt{(s-1)g d_{50}^3} \qquad (2.23)$$

where F = $v/(gh)^{0.5}$ = Froude number

v = characteristic velocity (m/s)

Rickenmann (2001) [107] modified Eq.(2.23) to the following expression by comparing with other formulas and with experimental observations with steep bed slope.

$$q_{b*} = \frac{3.1}{(s-1)^{1.5}} \left(\frac{d_{90}}{d_{30}}\right)^{0.2} S^{1.5}(q - q_{cr}) \sqrt{(s-1)g d_{50}^3} \qquad (2.24)$$

where q_{cr} = critical flow discharge (m²/s).

The applicable range is: d_{50} = 0.4 mm~29 mm; bed slope = 0.001~0.2; Shields parameter θ = 0.1~3.3; for uniform sediment, $d_{90}/d_{30} = 1.05$.

2.4 Unstable Bed Slope Avalanching

2.4.1 Derivation of Avalanching Equation

Due to the effects of gravity, an unstable bedform will collapse or avalanche to reach a stable state. In order to address this issue, the stability analysis of bed slope should be assessed. In this section, a simple mathematical avalanching model is proposed in one dimension and two dimensions. The principle of this method is based on the mass conservation of sediment and the restriction of stability relationship; more specifically, if the bed slope of a non-cohesive bed becomes larger than the angle of repose of sediment, then bed slope avalanching will occur to form a new bed with a slope approximately equal to the angle of repose. The process of avalanching is simulated by enforcing the real bed slope to be smaller than angle of repose i.e. $|\varphi_i|<\varphi$, and meanwhile maintaining mass continuity between adjacent cells. For the case with structured cells in two dimensions, there are eight cells around cell (i, j), therefore, the restriction in four directions (1, 2, 3 and 4 as shown in Figure 2.5) will be exerted.
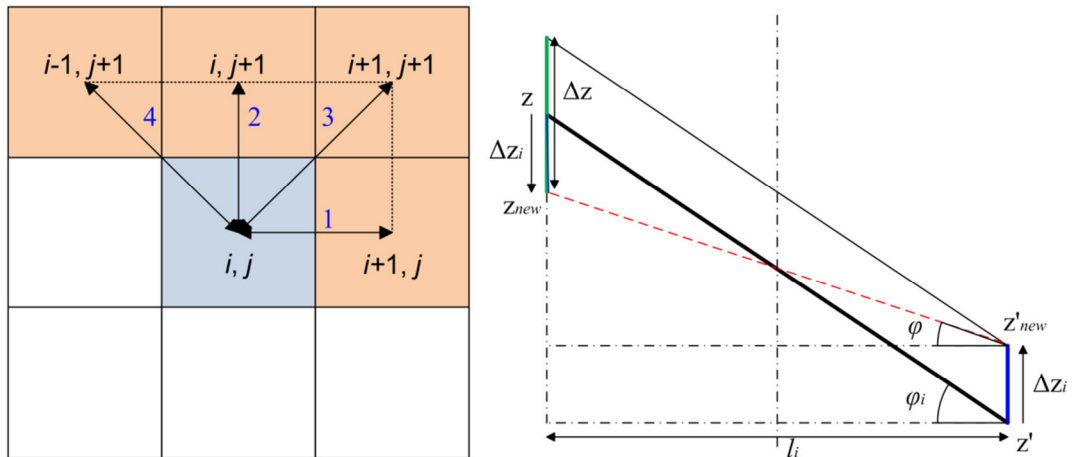
Figure 2.5 Schematic diagram of unstable bed slope re-forming; (a) the re-forming process in two-dimension; (b) the updating of two adjacent computational cells in x direction

Correspondingly, the avalanching is divided into four steps at each cell:

step 1: updating bed level in x direction, i.e. direction 1
step 2: updating bed level in y direction based on the first step
step 3: updating bed level in the 3rd direction based on the second step

step 4: updating bed level in the 4th direction based on the third step

For each step, a similar updating method is used.

The re-forming process of sediment in ith (i=1, 2, 3, 4) direction is taken as an example to derive the updating equation as follows. When $\varphi_i > \varphi$, the new angle of bed slope is approximately equal to the angle of repose by reducing the higher cell elevation and elevating the lower cell elevation. This is depicted in the schematic diagram Figure 2.5(b) where $\varphi_i > 0$.

$$\Delta z_i(i = 1, 2, 3, 4) = \frac{\Delta z}{2} \approx \frac{l_i(\tan \varphi_i - \tan \varphi)}{2} \tag{2.25}$$

where l_i = the length of two cells in the i direction (m)

φ_i = the real bed slope in the i direction

φ = the angle of repose

As the bed slope angle φ_i might be positive or negative, Eq.(2.25) is rewritten with consideration of the positive and negative values of φ_i by

$$\Delta z_i(i = 1, 2, 3, 4) = \begin{cases} \frac{\Delta z}{2} \approx sign(\varphi_i) \dfrac{l_i(\tan|\varphi_i| - \tan \varphi)}{2} & |\varphi_i| > \varphi \\ 0 & |\varphi_i| \leq \varphi \end{cases} \tag{2.26}$$

$$sign(a) = \begin{cases} 1 & a > 0 \\ 0 & a = 0 \\ -1 & a < 0 \end{cases}$$

Thus, the modified bathymetry in two-dimensions is finally calculated by

$$\begin{cases} z_{new(i,j)} = z_{i,j} + \sum_{i=1}^{4} \Delta z_i \\ z_{new(i,j+1)} = z_{i,j+1} - \Delta z_1 \\ z_{new(i+1,j)} = z_{i+1,j} - \Delta z_2 \\ z_{new(i+1,j+1)} = z_{i+1,j+1} - \Delta z_3 \\ z_{new(i-1,j+1)} = z_{i-1,j+1} - \Delta z_4 \end{cases} \tag{2.27}$$

Since the avalanching between two cells may induce new avalanching at neighbouring cells, the sweeping process is repeated using Eq.(2.27) until no avalanching occurs anymore. However, the re-forming process is time-consuming which increases the computational time, so during the computation, the stability analysis is implemented only at certain time steps. The updating interval depends on different simulated conditions.

2.4.2 1D Test on Avalanching Model

To demonstrate the avalanching process in case of unstable bed slope where the bed slope angle exceeds the critical value, a dune sliding case is

implemented. This is implemented by applying one direction of Eq.(2.27).The purpose of this test is to verify whether the proposed updating equation can accurately calculate the re-form process for an unstable bed. The initial state of this case is a semi-circular unstable dune with a radius of 2m located at the centre which is described by:

$$z_b = \sqrt{4 - x^2} \quad -2 \le x \le 2$$

The area is discretised with 1000 cells in one dimension. The critical sediment angle of repose is set at 27°, 31° and 35°, in recognising that sediment angle of repose might be different for different sediments. The calculation of the avalanching process was carried out according to the proposed Eq.(2.27) and the reformed bed profiles are shown in Figure 2.6. It is clear that the smaller the sediment angle of repose, the more severe the avalanching is (see Figure 2.6(b)). Further according to the comparison
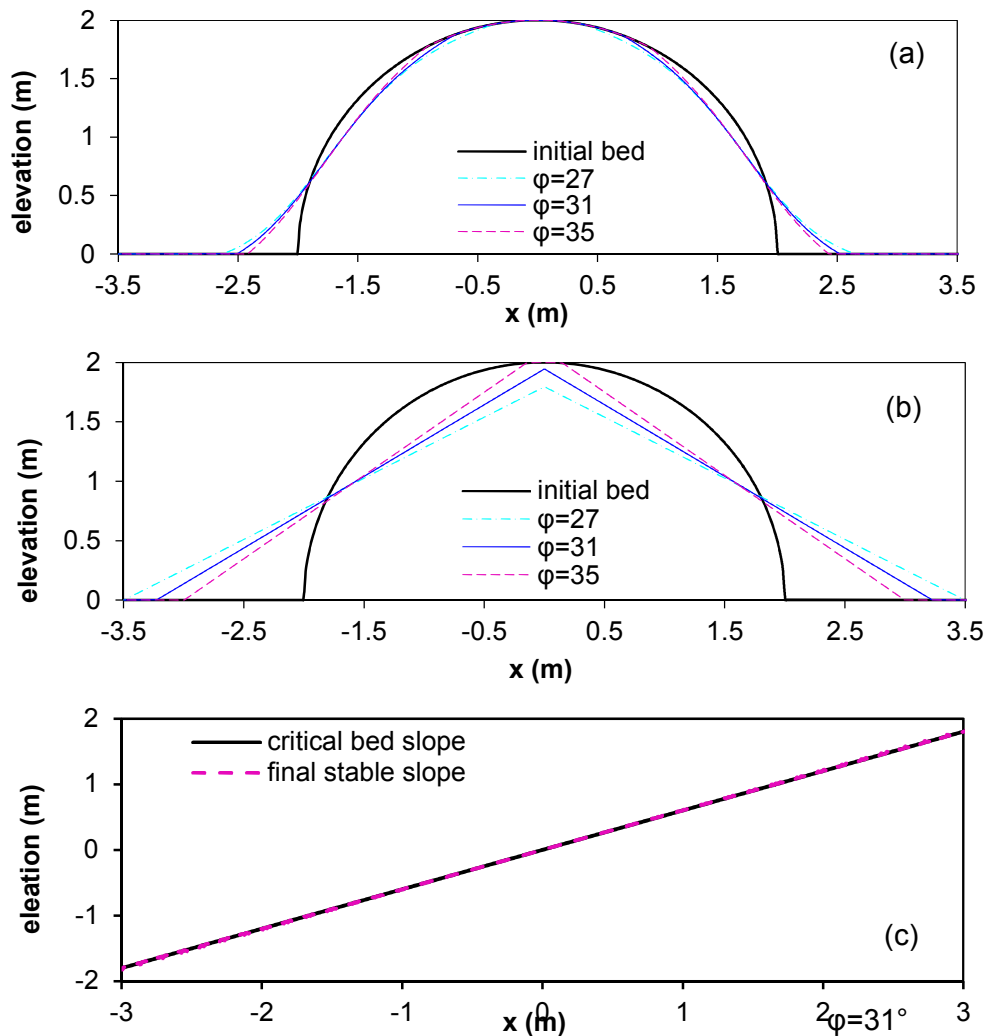
Figure 2.6 The reposing process due to avalanching; (a) bed profiles after 1000 steps; (b) final stability bed profiles; (c) the comparison between reposed final stable slope and critical bed slope

for φ=31° in Figure 2.6(c), the stable bed slope in final stage is approximately equal to the critical value of stable bed slope; besides, intuitively, the final stability of dune looks similar to a real stability dune case. This test demonstrates that the proposed updating equation for an unstable bed slope for non-cohesive sediment works qualitatively correctly.

2.4.3 2D Test of the Avalanching Model

For the 2D test of the avalanching model, a 1.5m radius hemispherical non-cohesive dune is located at the centre of a 3m×3m domain and is described as:

$$z_b = \max\{0;\ 1 - [(x - 1.5)^2 + (y - 1.5)^2]\}$$

The area is discretised by 300×300 cells. The sediment angle of repose is set to 31°. To demonstrate the result of Eq.2.27, the avalanching process of 2D dune is displayed in Figure 2.7. It shows that the unstable dune collapses with a reduction of the top level and slides to an expanded area, reaching a stable state progressively. Theoretically, the unstable dune will expand to the surrounding sides with the same rate, however, as the domain is discretised in rectangular grids, which limited the avalanching process to happen in four directions, the final stable bedform has slight difference to the ideal cone. Yet the results are good enough to accept qualitatively that the model is behaving correctly. The temporal evolution of one cross section as shown in Figure 2.8, the final stable bed profile has a constant slope whose angle is approximately equal to the angle of repose.
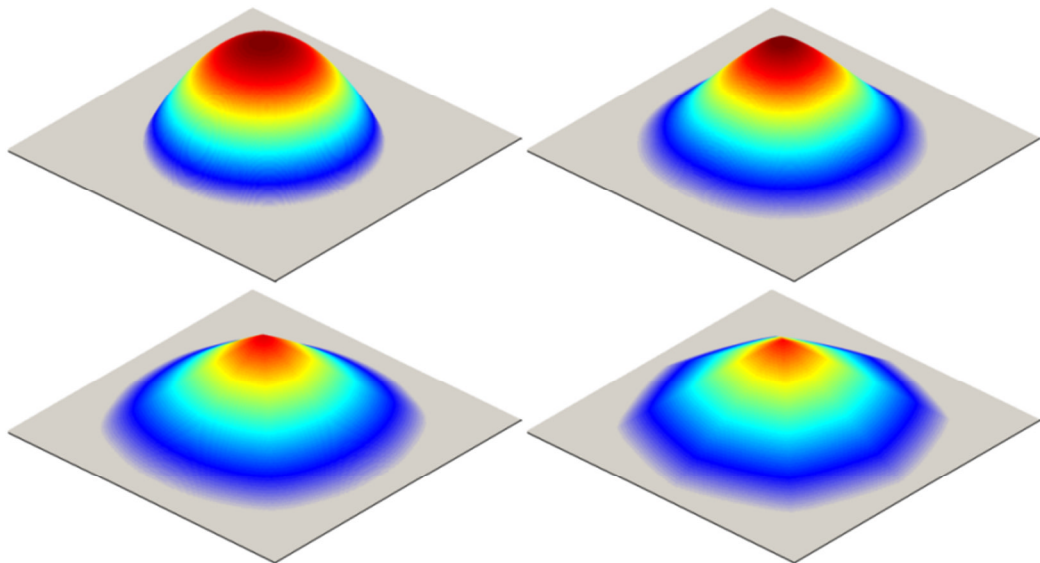
Figure 2.7 The avalanching process of 2D non-cohesive dune
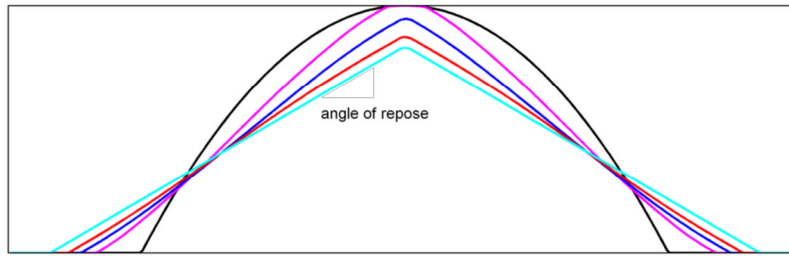
Figure 2.8 The temporal evolution of a cross section at the middle in x direction

In addition, a further implemented test is a square channel with vertical banks, and the inlet and outlet are assumed to be glass wall. Initially, the bank elevation is 4m and the static water level in the channel is 1.5m. The critical failure angles of wet beds and dry beds are considered as 61° and 31° respectively, and the reformation angle of both are 60° and 30° respectively. Figure 2.9 illustrates the topography of channel after being simulated by the bed slope avalanching model. It is shown that the final stable bank slopes above and below the water are the corresponding to critical angles.
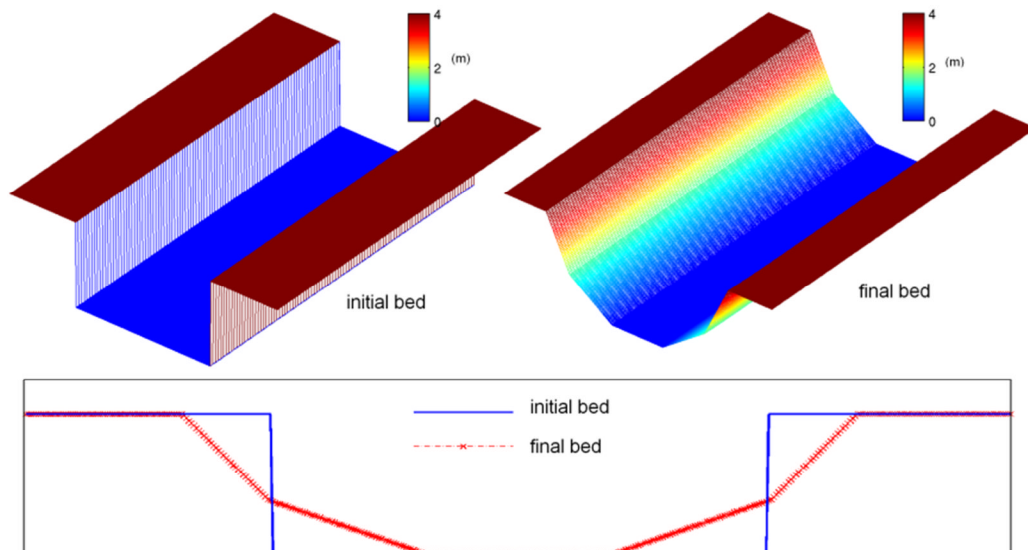
Figure 2.9 A square channel with vertical banks

2.5 Concluding Remarks

This chapter briefly described the parameterisation of sediment transport. These parameters will be used in the following model development and include critical bed shear stress, sediment transport capacity, bedload and suspended load transport equations etc. In order to update unstable bed

slope, this chapter also proposed a simple mathematical model in one and two dimensions. The model was tested in three non-cohesive bed sliding events. The modelling results implied that unstable bed can be effectively and reasonably updated by the model. The unstable bed slope avalanching could be used in such morphodynamic events of interest as dyke breach and river bank failure.

Chapter 3
Two-dimensional Hydrodynamic Model

In this chapter, a robust numerical method for solving the 2D shallow water model without sediment transport is proposed, including addressing the source terms, as well as handling the wetting and drying issues. The 2D hydrodynamic model is validated against a range of benchmark tests.

3.1 Introduction

Numerical techniques for the solution of the shallow water equations that represent flow in rivers and estuaries have developed considerably since they were first adopted in the seventies [131-133], and their use has become widespread. Amongst the techniques used, those based on finite volume Godunov-type Riemann Solvers [19, 22, 66] are robust and accurate and have been used successfully in commercial as well as academic contexts. However, with these and other methods, the treatment of source terms and the numerical difficulties associated with wetting and drying are problematic and in view of their influence on numerical accuracy researchers have sought to overcome these with some success.

For the first of these issues, the source term treatment is critical for robust and accurate application of the Finite Volume Method (FVM). This is especially true for the source terms relating to the bed geometry, because numerical errors will arise if an imbalance between the flux gradient and the bed-slope source terms is created. The traditional, simplest method is the pointwise approach, but this suffers severely with this imbalance. For flow over variable bottom geometry, many alternatives to the pointwise approach have been developed [74-78]. However, some limitations still exist in such methods. For example, Nujic's method [74] could not solve the problem completely and exhibited some numerical errors. LeVeque's approach [75] is complicated to implement and is not always robust with numerical errors in the case of steady transcritical flows with shocks. The upwind source term treatment from the Zaragoza school [76, 77] shows very robust and accurate solutions, but at the cost of complexity in implementation. The surface gradient method (SGM) proposed by Zhou *et al.*[78] is applicable to steady and unsteady problems and is simple to implement, but the steady flow simulation results are not as adequate as other methods, and additional special treatment must be implemented for the vertical bed step case [134].

Lee and Wright [79] proposed a novel, simple and efficient technique for source term treatment in one-dimensional Shallow Water equations by combining the source terms with the flux gradient in order to balance them. The advantages of this method lie in its simplicity, efficiency and range of applicability. The approach, however, was only described and demonstrated for one-dimensional modelling. The applicability of such a method to two-dimensional equations with second-order accuracy should also give significant advantages, but has not been proposed so far. In two-dimensional flows with complex, irregular topography the wetting/drying problem is a frequent source of instability and inaccuracy. In solving the non-linear Shallow Water equations, this problem must be considered thoroughly, as small naturally occurring water depths can cause unrealistic high velocities which will lead to numerical instabilities. A plethora of wetting/drying algorithms have been developed for the hyperbolic Shallow Water equations [19, 20, 135-138]. For example, Toro's method [138] proposed shock capturing schemes considering that a cell is dry if water depth is below a small critical value. Bradford and Sanders [20] suggested bypassing the incorrect estimation of pressure and body forces in partially wet cells by using Neumann extrapolation of the velocity. Brufau et al. [135] used an algorithm that modified the bed slope by enforcing the mass balance in the mass conservation equation, but it is only used for the first order accurate scheme. Liang and Borthwick's approach [136] modified the mass conservation in both fully and partially submerged cells during flooding and recession. A straightforward wetting/drying treatment is proposed in this Chapter and its application to a range of complex flows is demonstrated.

Based on the issues outlined above, the main objective in this Chapter is to propose a robust source term treatment in 2D, the so called Homogenous Flux Method (HFM) and thereby to develop a straightforward and efficient method for application to wet/dry fronts in irregular topography. The homogenous source terms treatment method of Lee and Wright [79] is extended to two-dimensions taking into account aspects that do not arise in 1D and the appropriate modified Godunov-type numerical schemes are defined. Following this the approach to deal with wet/dry fronts is described and several test case situations are analysed. Due to its simplicity and efficiency for shock-capturing problems with wet/dry fronts, the second-order TVD-WAF discretisation in conjunction with the HLLC Riemann solver is adopted. The scheme achieves second-order in space and time without performing data reconstruction just by solving the conventional Riemann problem associated with the first-order Godunov scheme.

3.2 Governing Equations

3.2.1 Modified Form of 2D Shallow Water Equations

The hydrodynamic model is governed by the 2D shallow water equations based on mass continuity and momentum balance. The diffusion terms due to viscosity and turbulence are not incorporated here, but could be if necessary. In vector form, the equations can be expressed as follows.

$$\frac{\partial \mathbf{U}}{\partial t} + \frac{\partial \mathbf{F}}{\partial x} + \frac{\partial \mathbf{G}}{\partial y} = \mathbf{S}_o + \mathbf{S}_f \tag{3.1}$$

$$\mathbf{U} = \begin{bmatrix} h \\ hu \\ hv \end{bmatrix} \quad \mathbf{F} = \begin{bmatrix} hu \\ hu^2 + \frac{1}{2}gh^2 \\ huv \end{bmatrix} \quad \mathbf{G} = \begin{bmatrix} hv \\ huv \\ hv^2 + \frac{1}{2}gh^2 \end{bmatrix} \quad \mathbf{S}_o = \begin{bmatrix} 0 \\ ghS_{ox} \\ ghS_{oy} \end{bmatrix} \quad \mathbf{S}_f = \begin{bmatrix} 0 \\ -ghS_{fx} \\ -ghS_{fy} \end{bmatrix}$$

where h = water depth (m)

$\quad$ g = acceleration due to gravity (m/s^2)

$\quad$ u, v = depth averaged velocity in the x and y directions (m/s)

$\quad$ S_{ox}, S_{oy} = bed slopes in x and y directions

$\quad$ S_{fx}, S_{fy} = frictional slopes in x and y directions.

The bed slopes and frictional slopes are defined by

$$S_{ox} = -\frac{\partial z_b}{\partial x}, S_{oy} = -\frac{\partial z_b}{\partial y} \tag{3.2}$$

$$S_{fx} = \frac{n^2 u \sqrt{u^2 + v^2}}{h^{4/3}}, S_{fy} = \frac{n^2 v \sqrt{u^2 + v^2}}{h^{4/3}} \tag{3.3}$$

in which, z_b is the bed level at (x, y) location (see Figure 3.1); the friction slopes S_{fx}, S_{fy} are defined based on Manning's roughness coefficient denoted by n.
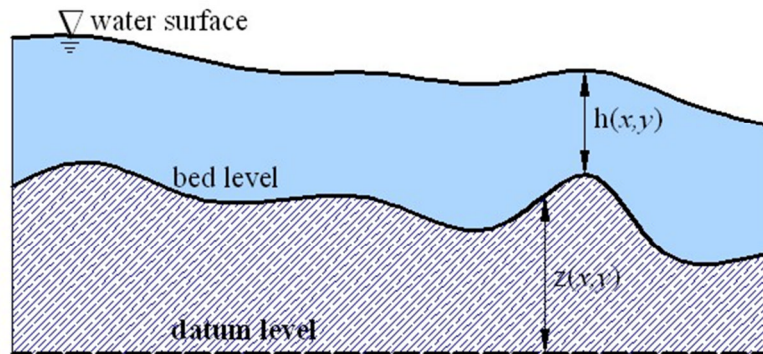
Figure 3.1 Sketch of shallow water flow over irregular bed

The integral form of Eq.(3.1) over a fixed volume Ω can be written by

$$\frac{\partial}{\partial t} \int_\Omega \mathbf{U} d\Omega + \int_\Omega (\nabla \cdot \mathbf{E}) d\Omega = \int_\Omega (\mathbf{S}_o + \mathbf{S}_f) d\Omega \qquad (3.4)$$

where $\mathbf{E}=[\mathbf{F}, \mathbf{G}]^T$ = the flux tensor

The application of the Gauss's divergence theory leads to the following conservation equation with surface integral:

$$\frac{\partial}{\partial t} \int_\Omega \mathbf{U} d\Omega + \oint_s (\mathbf{E} \cdot \mathbf{n}) ds = \int_\Omega (\mathbf{S}_o + \mathbf{S}_f) d\Omega \qquad (3.5)$$

where s = the surface boundary of control area Ω

$\mathbf{n}=[n_x, n_y]^T$ = the outward pointing normal vector

The Jacobian matrix, $\mathbf{J}_n$ of the normal flux can be expressed by

$$\mathbf{J}_n = \frac{\partial(\mathbf{E} \cdot \mathbf{n})}{\partial \mathbf{U}} = \frac{\partial \mathbf{F}}{\partial \mathbf{U}} n_x + \frac{\partial \mathbf{G}}{\partial \mathbf{U}} n_y \qquad (3.6)$$

$$\mathbf{J}_n = \begin{bmatrix} 0 & n_x & n_y \\ (gh - u^2)n_x - uvn_y & vn_y + 2un_x & un_y \\ (gh - v^2)n_y - uvn_x & vn_x & un_x + 2vn_y \end{bmatrix} \qquad (3.7)$$

The system for the governing equation can be defined using an averaged Jacobian matrix $\tilde{\mathbf{J}}_n$ with eigenvalues and eigenvectors by

$$\tilde{\lambda}_1 = \tilde{u}n_x + \tilde{v}n_y - \tilde{c}, \tilde{\lambda}_2 = \tilde{u}n_x + \tilde{v}n_y, \tilde{\lambda}_3 = \tilde{u}n_x + \tilde{v}n_y + \tilde{c} \qquad (3.8)$$

$$\tilde{\mathbf{e}}_1 = \begin{pmatrix} 1 \\ \tilde{u} - \tilde{c}n_x \\ \tilde{v} - \tilde{c}n_y \end{pmatrix}, \tilde{\mathbf{e}}_1 = \begin{pmatrix} 1 \\ -\tilde{c}n_y \\ -\tilde{c}n_x \end{pmatrix}, \tilde{\mathbf{e}}_1 = \begin{pmatrix} 1 \\ \tilde{u} + \tilde{c}n_x \\ \tilde{v} + \tilde{c}n_y \end{pmatrix} \qquad (3.9)$$

where $\tilde{c}$ = the celerity of small amplitude surface waves

The average values at the interface are calculated as:

$$\tilde{u} = \frac{u_R\sqrt{h_R} + u_L\sqrt{h_L}}{\sqrt{h_R} + \sqrt{h_L}}, \tilde{v} = \frac{v_R\sqrt{h_R} + v_L\sqrt{h_L}}{\sqrt{h_R} + \sqrt{h_L}}, \tilde{c} = \sqrt{\frac{g(h_R + h_L)}{2}}, \tilde{h} = \sqrt{h_R h_L} \quad (3.10)$$

where L, R = the left side and right side of the cell

$\tilde{h}, \tilde{u}, \tilde{v}$ = the average water depth, average velocities in x and y directions at the interface of cell

In the hydrodynamic case, the source terms are combined into the bed slope term S_o and friction slope term S_f. Generally, the source term relevant to

bottom geometry plays a significant role in maintaining flux balance [79]. Therefore, an approach addressing the bed slope term is adopted here by defining bed slope source flux **M**. More specifically, the bottom variation term S_o is quantified as a flux to be incorporated into flux terms, thereby automatically achieving the exact balance between flux gradient and bed slope. Thus

$$\int_\Omega (\nabla \cdot \mathbf{M}) d\Omega = \int_\Omega \mathbf{S}_o d\Omega$$

where **M** = the defined bed slope source flux vector

So the modified homogenous form of the two-dimensional shallow water equations can be obtained by incorporating bed slope source flux **M** into flux terms **E** and given by

$$\frac{\partial}{\partial t} \int_\Omega \mathbf{U} d\Omega + \int_\Omega [\nabla \cdot (\mathbf{E} - \mathbf{M})] d\Omega = \int_\Omega \mathbf{S}_f d\Omega$$

So system Eqs.(3.1) is rewritten by

$$\frac{\partial \mathbf{U}}{\partial t} + \frac{\partial \mathbf{H}}{\partial x} + \frac{\partial \mathbf{K}}{\partial y} = \mathbf{S}_f(x, y, \mathbf{U}) \tag{3.11}$$

in which, **H**, **K** are flux vectors incorporating source flux vectors $\mathbf{B}_1$, $\mathbf{B}_2$; **H=F-$\mathbf{B}_1$, K=G-$\mathbf{B}_2$**, where vectors $\mathbf{B}_1 = [0, R_1, 0]^T$ and $\mathbf{B}_2 = [0, 0, R_2]^T$ are the source flux vector corresponding to the bed slope term in the *x* and *y* directions respectively; therein, R_1 is the source flux relevant to bed slope S_{ox} in *x* direction and R_2 is the source flux relevant to bed slope S_{oy} in *y* direction. Source term **S$_f$** is the vector form relevant to friction component. Since the friction source term **S$_f$** is not often the cause of the imbalance problem of shallow water models, a simple pointwise method is used to discretise the friction vector **S$_f$** in this study. Based on the aforementioned points, Figure 3.2 illustrates the fluxes at corresponding cell interface.

For the modified vector form of the 2D shallow water equations, similarly, the explicit finite volume discretisation method is adopted to discretise the modified 2D conservation equation numerically. For a structured grid, the updating of conservation variables (**U**) is rewritten by

$$\mathbf{U}_{i,j}^{n+1} = \mathbf{U}_{i,j}^n - \frac{\Delta t}{\Delta x}\left(\mathbf{H}_{i+\frac{1}{2},j}^* - \mathbf{H}_{i-\frac{1}{2},j}^*\right) - \frac{\Delta t}{\Delta y}\left(\mathbf{K}_{i,j+\frac{1}{2}}^* - \mathbf{K}_{i,j-\frac{1}{2}}^*\right) + \Delta t \mathbf{S}_{f,i,j} \tag{3.12}$$

where $\mathbf{H}^*$, $\mathbf{K}^*$ = the numerical flux at the interface between adjacent cells

$\quad$ Δt = the time interval

$\quad$ Δx, Δy = the cell length in *x* and *y* direction
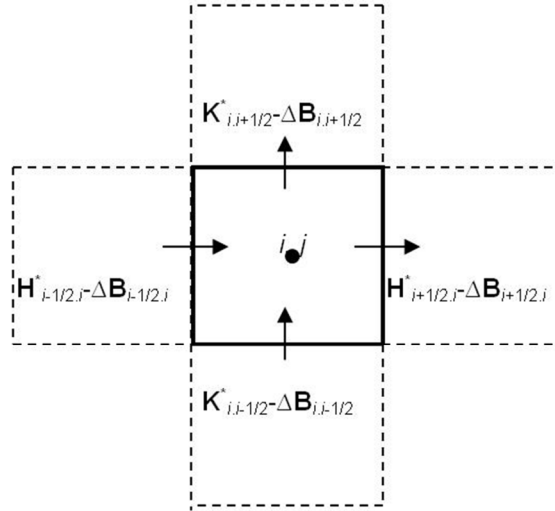
Figure 3.2 Fluxes inclusion of bed slope flux cross structural control cell

3.2.2 Bed Discretisation and Source Flux R$_1$, R$_2$

The source flux terms R_1 and R_2, which are the component of source flux vector **B**$_1$ and **B**$_2$, are related only to the bed slope term. A definition of the flux term related to these bed slope term is required. The approach incorporates the bed slope term into the flux terms effectively, that is to say, the non-homogenous form of system Eq. 3.1 is converted to homogenous form for the bed slope source term. Thus, all the external forces caused by bed slope in a cell are exerted by bed slope source flux at the interface of adjacent cells. To be compatible with this method, a proper bed reconstruction should be implemented. In this paper, the cell-centred piecewise linear bed reconstruction is applied in deriving the bed slope source flux at the interface of cells. Except for this, there is no need for any special treatment for bed slope source term. Taking ΔR_1 as an example, the definition of the source flux R_1 can be obtained by the following approach. Comparing Eq.3.1 and Eq.3.11, it can have:

$$\frac{\partial R_1}{\partial x} = -ghS_{ox} = -gh\frac{\partial z_b}{\partial x} = -gh\frac{\partial(\eta - h)}{\partial x} \tag{3.13}$$

where z_b = bed elevation at cell centre discretised by cell-centred approach

$\partial z_b/\partial x$ = slope of the bed elevation at two adjacent cells centre

η = water surface elevation

h = water depth at the discretised cell

The difference of the source flux, ΔR_1, at the boundary between the cell (i,j) and $(i+1,j)$ can be obtained by integrating the Eq.3.13 over the x direction face of the two cells interface.

$$\int_{x_i}^{x_{i+1}} \frac{\partial R_1}{\partial x}\, dx = \int_{x_i}^{x_{i+1}} g\left(-h\frac{\partial \eta}{\partial x} + h\frac{\partial h}{\partial x}\right) dx \qquad (3.14)$$

where x_i, x_{i+1} = the x value of the i th and $i+1$th cell centre

For the two discretised cells here, Eq.3.14 is approximately rewritten by

$$\frac{\Delta R_1}{\Delta x} = -\frac{1}{2}g\left(h_{i,j} + h_{i+1,j}\right)\left(\frac{\eta_{i+1,j} - \eta_{i,j}}{\Delta x}\right) + \frac{1}{2}g\left(\frac{h_{i+1,j}^2 - h_{i,j}^2}{\Delta x}\right) \qquad (3.15)$$

where $\eta_{i,j}$, $\eta_{i+1,j}$ = the water surface elevations at the (i,j) and $(i+1,j)$ cell-centre

Therefore, in x direction, ΔR_1 is then given by

$$\Delta R_{1(i+1/2,j)} = R_{1(i+1,j)} - R_{1(i,j)}$$

$$= -\frac{1}{2}g\left(h_{i,j} + h_{i+1,j}\right)\Delta\eta_{x(i+1/2,j)} + \frac{1}{2}g\left(h_{i+1,j}^2 - h_{i,j}^2\right) \qquad (3.16)$$

where $\Delta\eta_{x(i+1/2,j)}$ represents the difference of water elevation at i th and $i+1$ th cell centre in x direction. Define $\Omega_{ox(i+1/2,j)} = -0.5g\left(h_{i,j} + h_{i+1,j}\right)\Delta\eta_{x(i+1/2,j)}$; the equation (3.16) is simplified as

$$\Delta R_{1(i+1/2,j)} = R_{1(i+1,j)} - R_{1(i,j)} = [\Omega_{ox}]_{i+1/2,j} + \frac{1}{2}g\left(h_{i+1,j}^2 - h_{i,j}^2\right) \quad (3.17a)$$

Similarly, at the interface i-1/2, the source term flux is written by

$$\Delta R_{1(i-1/2,j)} = R_{1(i,j)} - R_{1(i-1,j)} = [\Omega_{ox}]_{i-1/2,j} + \frac{1}{2}g\left(h_{i,j}^2 - h_{i-1,j}^2\right) \quad (3.17b)$$
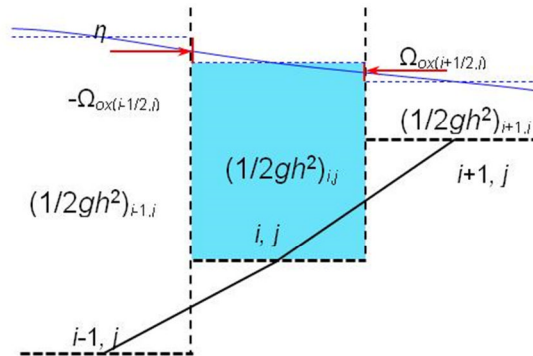
Figure 3.3 External force exerted by water elevation difference Ω_{ox} between two adjacent cells and hydrostatic pressure term $(1/2gh^2)$ in the cells

In Eqs.3.17, Ω_{ox} term represents the momentum flux due to the water level difference in x direction; and the second term $\Delta\left(\frac{1}{2}gh^2\right)$ illustrates the

difference of hydrostatic pressure term between left and right cells. Therefore, when splitting ΔR_1, the first terms in Eqs.3.17 are treated as an external force exerted by splitting into the neighbouring cells (see Figure 3.3), and the hydrostatic pressure term $\frac{1}{2}gh^2$ is split between each cell in order to balance the hydrostatic pressure term in momentum fluxes.

For updating the variables at cell (i,j), the source term R_1 in each neighbouring cell is calculated by:

$$R_{1(i-1,j)} = -[\Omega_{ox}]_{i-1/2,j} + \left(\frac{1}{2}gh^2\right)_{i-1,j} \tag{3.18a}$$

$$R_{1(i,j)} = \left(\frac{1}{2}gh^2\right)_{i,j} \tag{3.18b}$$

$$R_{1(i+1,j)} = [\Omega_{ox}]_{i+1/2,j} + \left(\frac{1}{2}gh^2\right)_{i+1,j} \tag{3.18c}$$

The momentum flux terms R_1, R_2 in each cell do not have an absolute value but a relative value. These three flux terms are calculated by decomposing Eqs.3.17. In other words, when updating $\mathbf{U}_{i,j}$, group Eqs.3.18 is adopted, however, when updating $\mathbf{U}_{i+1,j}$, the source flux terms $R_{1(i,j)}$, $R_{1(i+1,j)}$ and $R_{1(i+2,j)}$ are recomputed by a similar decomposition of $\Delta R_{1(i+1/2,j)}$ and $\Delta R_{1(i+3/2,j)}$. In fact, only the source term flux difference influences the updating $\mathbf{U}$ vector. For example, the interface flux of Roe's scheme in the x-direction generally can be expressed by

$$\mathbf{H}^*_{i-1/2,j} = \frac{1}{2}\left[\left(\mathbf{F}_{i-1,j} - \mathbf{B}_{1(i-1,j)}\right) + \left(\mathbf{F}_{i,j} - \mathbf{B}_{1(i,j)}\right)\right] - \tilde{\mathbf{J}}_n\Delta\mathbf{U}'_{i-1/2,j} \tag{3.19a}$$

$$\mathbf{H}^*_{i+1/2,j} = \frac{1}{2}\left[\left(\mathbf{F}_{i,j} - \mathbf{B}_{1(i,j)}\right) + \left(\mathbf{F}_{i+1,j} - \mathbf{B}_{1(i+1,j)}\right)\right] - \tilde{\mathbf{J}}_n\Delta\mathbf{U}'_{i+1/2,j} \tag{3.19b}$$

where $\mathbf{U'}_{i\pm1/2,j} = [\Delta h', \Delta(hu)', \Delta(hv)']^T_{i\pm1/2,j}$ = the modified difference of $\mathbf{U}$.

According to the updating equation (Eq.3.12), it is necessary to calculate the difference of left and right interface in a cell by:

$$\mathbf{H}^*_{i+1/2,j} - \mathbf{H}^*_{i-1/2,j}$$
$$= \frac{1}{2}\left[\left(\mathbf{F}_{i+1,j} + \mathbf{F}_{i,j}\right) - \left(\mathbf{F}_{i-1,j} + \mathbf{F}_{i,j}\right) - \left(\mathbf{B}_{1(i,j)} - \mathbf{B}_{1(i-1,j)}\right)\right.$$
$$\left. - \left(\mathbf{B}_{1(i+1,j)} - \mathbf{B}_{1(i,j)}\right)\right] + \tilde{\mathbf{J}}_n\Delta\mathbf{U}'_{i-1/2,j} - \tilde{\mathbf{J}}_n\Delta\mathbf{U}'_{i+1/2,j}$$
$$= \frac{1}{2}\left[\left(\mathbf{F}_{i+1,j} + \mathbf{F}_{i,j} - \Delta\mathbf{B}_{1\left(i+\frac{1}{2},j\right)}\right) - \left(\mathbf{F}_{i-1,j} + \mathbf{F}_{i,j} + \Delta\mathbf{B}_{1\left(i-\frac{1}{2},j\right)}\right)\right]$$
$$+ \tilde{\mathbf{J}}_n\Delta\mathbf{U}'_{i-1/2,j} - \tilde{\mathbf{J}}_n\Delta\mathbf{U}'_{i+1/2,j} \tag{3.20}$$

where $\Delta\mathbf{B}_{1(i-1/2,j)} = [0, \Delta R_{1(i-1/2,j)}, 0]^T$
$\Delta\mathbf{B}_{1(i+1/2,j)} = [0, \Delta R_{1(i+1/2,j)}, 0]^T$

$\Delta R_{1(i-1/2,j)}$ and $\Delta R_{1(i+1/2,j)}$, can be calculated by use of Eq.3.17(a) and (b). Therefore, the relative decomposing source term flux in Eqs.3.18 is sufficient for the scheme's solution. For other numerical scheme, it is easy to prove this. Similarly, in the y direction, the flux term R_2 is calculated by

$$R_{2(i,j-1)} = -\left[\Omega_{oy}\right]_{i,j-1/2} + \left(\frac{1}{2}gh^2\right)_{i,j-1} \qquad (3.21a)$$

$$R_{2(i,j)} = \left(\frac{1}{2}gh^2\right)_{i,j} \qquad (3.21b)$$

$$R_{2(i,j+1)} = \left[\Omega_{oy}\right]_{i,j+1/2} + \left(\frac{1}{2}gh^2\right)_{i,j+1} \qquad (3.21c)$$

3.3 Numerical Solution

3.3.1 Numerical Scheme

A wide range of numerical schemes have been proposed and an excellent review was written by Toro [138]. In this section, the modified equations with the source term fluxes are solved using the first-order HLLC scheme. Further, the second-order TVD-WAF is applied, there the intercell flux is obtained from an integral average of the flux function **E** across the complete wave structure of the local Riemann problem with piece-wise constant data (U_L, U_R) [94, 139, 140]. Here the TVD-WAF is used in conjunction with the modified first-order HLLC Riemann solver. As similar derivation method can be applied for other solvers.

3.3.1.1 The HLLC Solver Including Source Flux

The HLLC approximate Riemann solver is a modification of the basic HLL scheme that accounts for the influence of intermediate waves [138] and ensures greater accuracy. In the structure of HLLC solver, there are two distinct fluxes for the star region (see Figure 3.4), so there is a need to determine the intermediate waves as well as the left and right wave speed estimates.
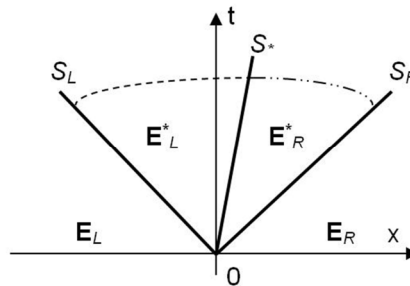
Figure 3.4 The structure of HLLC Riemann solver

Firstly, the modified intercell numerical flux vector $\mathbf{E}^*$ is derived with the incorporation of source fluxes as:

$$\mathbf{E}^*_{LR} = \begin{cases} \mathbf{E}_L & if\ S_L \geq 0 \\ \mathbf{E}_{*L} & if\ S_L < 0 \leq S_* \\ \mathbf{E}_{*R} & if\ S_* < 0 \leq S_R \\ \mathbf{E}_R & if\ S_R < 0 \end{cases} \tag{3.22}$$

where $\mathbf{E}_L = \mathbf{E}(\mathbf{U}_L, \mathbf{B}_L)$ = conserved variable vector at the left side of cell

$\quad\quad\mathbf{E}_R = \mathbf{E}(\mathbf{U}_R, \mathbf{B}_R)$ = conserved variable vector at the right side of cell

$\quad\quad\mathbf{E}_{*L}$ = numerical flux in left star region divided by the middle wave S_*

$\quad\quad\mathbf{E}_{*R}$ = numerical flux in right star region divided by the middle wave S_*

It is noted that the intermediate wave arising from the presence of the tangential momentum equation is always a shear wave, across which the tangential velocity component changes discontinuously whereas the perpendicular velocity component and water depth remain constant [138]. Taking calculation fluxes $\mathbf{H}_{*L}$ and $\mathbf{H}_{*R}$ in x direction as an example, they are calculated according to following expression.

$$\mathbf{H}_{*L} = \begin{bmatrix} H_{*1} \\ H_{*2} \\ v_L H_{*1} \end{bmatrix}, \mathbf{H}_{*R} = \begin{bmatrix} H_{*1} \\ H_{*2} \\ v_R H_{*1} \end{bmatrix} \tag{3.23}$$

where v_L, v_R are the initial velocity tangential to the interface of a local Riemann problem, which remain unchanged across the left and right waves, respectively. $[H_{*1}, H_{*2}, H_{*3}]^T = \mathbf{H}_*$ is the flux in star region according to modified HLL formula when evaluating fluxes in the x direction. For the y direction, a similar approach is applied. The modified HLL formula is calculated by the following equation in two-dimensions.

$$\mathbf{E}_* \cdot \mathbf{n} = \frac{S_R \mathbf{E}_L \cdot \mathbf{n} - S_L \mathbf{E}_R \cdot \mathbf{n} + S_R S_L \Delta \mathbf{U}'_{LR}}{S_R - S_L} \tag{3.24}$$

In Eq.(4.24), S_L and S_R are two wave speeds which are supposed to be selected carefully to avoid entropy violation. Einfeldt's method [141] was adopted here including dry-bed options from the two-rarefaction approximate Riemann solver, and Roe's average eigenvalues were used in this method. They are expressed by

$$S_L = \begin{cases} \min\left(\mathbf{q}_L \cdot \mathbf{n} - \sqrt{gh_L}, \tilde{\mathbf{u}}_\perp \cdot \mathbf{n} - \sqrt{g\tilde{h}} \right) & if\ h_L > 0 \\ \mathbf{q}_R \cdot \mathbf{n} - 2\sqrt{gh_R} & if\ h_L = 0 \end{cases} \tag{3.25a}$$

$$S_R = \begin{cases} \min\left(\mathbf{q}_R \cdot \mathbf{n} + \sqrt{gh_R}, \tilde{\mathbf{u}}_\perp \cdot \mathbf{n} + \sqrt{g\tilde{h}} \right) & if \; h_R > 0 \\ \mathbf{q}_L \cdot \mathbf{n} + 2\sqrt{gh_L} & if \; h_R = 0 \end{cases} \qquad (3.25b)$$

where $\mathbf{q}=[u, v]$

$\tilde{\mathbf{u}}_\perp = [\tilde{u}, \tilde{v}]$ is Roe's average velocity

$\sqrt{g\tilde{h}}$ is Roe's average wave speed

The middle wave speed S_* can be calculated in a variety of ways, but the following form is recommended by Toro (2001) [138].

$$S_* = \frac{S_L h_R (\mathbf{q}_R \cdot \mathbf{n} - S_R) - S_R h_L (\mathbf{q}_L \cdot \mathbf{n} - S_L)}{h_R (\mathbf{q}_R \cdot \mathbf{n} - S_R) - h_L (\mathbf{q}_L \cdot \mathbf{n} - S_L)} \qquad (3.26)$$

For the original HLL or HLLC scheme, $\mathbf{\Delta U'}$ in Eq.(24) should be equal to $\mathbf{U}_R$-$\mathbf{U}_L$, representing the conserved variables difference between left and right cell; however, the $\mathbf{\Delta U'}$ becomes net difference of conserved variables considering bed geometry effect in this Homogeneous Flux Method because of the inclusion of source flux into flux term $\mathbf{F}$. Therefore, the modified $\mathbf{\Delta U'}$ should be recalculated. According to Eq.(3.6) $\mathbf{J}_n = \frac{\partial (\mathbf{E \cdot n})}{\partial \mathbf{U}}$, the flux difference is expressed by Jacobian matrix multiplying the conserved variables difference as $\Delta \mathbf{E} \cdot \mathbf{n} = \mathbf{J}_n \Delta \mathbf{U}$. For the Roe's approximate Riemann solver, an approximate Jacobian $\tilde{\mathbf{J}}_{LR}$ at the edges of cell, analogous to $\mathbf{J}_n$, was constructed to satisfy the conservation property across discontinuities $\Delta \mathbf{E}_{LR} \cdot \mathbf{n} = \tilde{\mathbf{J}}_{LR} \Delta \mathbf{U}$. There $\tilde{\mathbf{J}}_{LR}$ is closely expressed by its eigenvalues. However, the solution structure of HLL approximate Riemann solver is different from that of Roe's solver. To satisfy the conservation property for HLL solver, the approximate Jacobian $\mathbf{J}_{LR}^{HLL}$ is approximately constructed based on Roe's Jacobian matrix by using the two alternative eigenvalues S_L and S_R calculated by Einfeldt's method [141] which is based on Roe's average eigenvalues. So the modified vector of $\mathbf{\Delta U'}$ satisfies the following equation.

$$\Delta \mathbf{E}_{LR} \cdot \mathbf{n} = \mathbf{J}_{LR}^{HLL} \Delta \mathbf{U'} \qquad (3.27)$$

where $\mathbf{\Delta U'} = [\Delta h', \Delta(hu)', \Delta(hv)']^T_{LR}$ = the difference of the modified conservative variables between two adjacent cells

$\mathbf{\Delta E}_{LR}$ = the difference of the flux vectors (that include the bed slope flux) at the cell interface.

More specifically, the Eq.(27) is rewritten by:

$$
\begin{bmatrix}
\Delta(hu)n_x + \Delta(hv)n_y \\
\Delta(hu^2) + \Delta(gh^2/2)n_x + \Delta(huv)n_y \\
\Delta(huv)n_x + \Delta(hv^2) + \Delta(gh^2/2)n_y
\end{bmatrix}_{LR}
-
\begin{bmatrix}
0 \\
\Delta R_1 n_x \\
\Delta R_2 n_y
\end{bmatrix}_{LR}
=
\mathbf{J}_{LR}^{HLL}
\begin{bmatrix}
\Delta h' \\
\Delta(hu)' \\
\Delta(hv)'
\end{bmatrix}_{LR}
\tag{3.28}
$$

To calculate the flux in *x*-direction, $n_x=1$ and $n_y=0$. As aforementioned, the Jacobian matrix for HLL approximate Riemann solver, $\mathbf{J}_{LR}^{HLL}$ constructed by using the two eigenvalues S_L and S_R is used instead of Roe's Jacobian matrix $\tilde{\mathbf{J}}_n$, referring to Lee and Wright [79].

$$
\mathbf{J}_{LR}^{HLL} =
\begin{bmatrix}
0 & 1 & 0 \\
-S_L S_R & S_L + S_R & 0 \\
-1/2(S_L + S_R)\tilde{v} & \tilde{v} & 1/2(S_L + S_R)
\end{bmatrix}
\tag{3.29}
$$

Taking Eq.3.29 into Eq.3.28 and solving it, the unknown conserved variable differences $\Delta h'$, $\Delta(hu)'$ and $\Delta(hv)'$ are derived as

$$
\Delta h'_{LR} = -\frac{\Delta(hu^2)_{LR} - \Omega_{ox} - (S_L + S_R)\Delta(hu)_{LR}}{S_L S_R}
\tag{3.30a}
$$

$$
\Delta(hu)'_{LR} = \Delta(hu)_{LR}
\tag{3.30b}
$$

$$
\Delta(hv)'_{LR} = \Delta(hv)_{LR} + \tilde{v}(\Delta h'_{LR} - \Delta h_{LR})
\tag{3.30c}
$$

There, Ω_{ox} is the momentum flux due to water surface difference between left and right cells in *x* direction. Similarly, for the calculation of the flux in *y* direction, $n_x=0$ and $n_y=1$. Taking n_x and n_y into Eq.3.28 and solving it, $\Delta h'$, $\Delta(hu)'$ and $\Delta(hv)'$ are expressed as

$$
\Delta h'_{LR} = -\frac{\Delta(hv^2)_{LR} - \Omega_{oy} - (S_L + S_R)\Delta(hv)_{LR}}{S_L S_R}
\tag{3.31a}
$$

$$
\Delta(hu)'_{LR} = \Delta(hu)_{LR} + \tilde{u}(\Delta h'_{LR} - \Delta h_{LR})
\tag{3.31b}
$$

$$
\Delta(hv)'_{LR} = \Delta(hv)_{LR}
\tag{3.31c}
$$

There, Ω_{oy} is the momentum flux due to water surface difference between left and right cells in *y* direction. Overall, the modified difference of conservative terms $\mathbf{\Delta U}'$ can be summarized by incorporating n_x, n_y into the derived expressions; therefore, the new equations are rewritten by

$$
\Delta h'_{LR} = -\frac{\Delta(h\mathbf{u}^2 \cdot \mathbf{n})_{LR} - \mathbf{\Omega} \cdot \mathbf{n} - (S_L + S_R)[\Delta(h\mathbf{u} \cdot \mathbf{n})_{LR}]}{S_L S_R}
\tag{3.32a}
$$

$$
\Delta(hu)'_{LR} = \Delta(hu)_{LR} + \tilde{u}(\Delta h'_{LR} - \Delta h_{LR}) \cdot n_y
\tag{3.32b}
$$

$$
\Delta(hv)'_{LR} = \Delta(hv)_{LR} + \tilde{v}(\Delta h'_{LR} - \Delta h_{LR}) \cdot n_x
\tag{3.32c}
$$

where, $\mathbf{u}^2 = [u^2, v^2]$, $\mathbf{\Omega} = [\Omega_{ox}, \Omega_{oy}]$, $\mathbf{u} = [u, v]$ *and* $\mathbf{n} = [n_x, n_y]^T$.

In general, it is vital that a scheme satisfies the *C*-property to maintain the correct balance between source terms and flux gradients. The *C*-property is the requirement for a well-balanced scheme [76, 142-144]. That is proved as follows (taking *x* direction as an example). In case of no flow motion, the flow property has

$$\eta = h + z_b \equiv \text{constant value}, \Delta\eta \equiv 0, u \equiv 0, S_{fx} \equiv 0$$

Therefore, the external force due to water surface difference $\Omega_{ox} \equiv 0$ and $R_{1(i-1,j)} = \left(\frac{1}{2}gh^2\right)_{i-1,j}, R_{1(i,j)} = \left(\frac{1}{2}gh^2\right)_{i,j}, R_{1(i+1,j)} = \left(\frac{1}{2}gh^2\right)_{i+1,j}$ in Eqs.3.18. Take the $\Omega_{ox} \equiv 0$ and $u \equiv 0$ into Eqs.3.30, the modified vector of $\mathbf{\Delta U'}$ satisfies $\mathbf{\Delta U'} \equiv$ null $[\Delta h' \equiv 0, \Delta(hu)' \equiv 0, \Delta(hv)' \equiv 0]$. Therefore, the momentum flux change at the cell (*i,j*) in *x* direction is calculated by

$$
\begin{aligned}
H_m &= H^*_{i+1/2,j} - H^*_{i-1/2,j} \\
&= \frac{1}{2}\{[(f_{i+1,j} - R_{1(i+1,j)}) + (f_{i,j} - R_{1(i,j)})] - [(f_{i,j} - R_{1(i,j)}) + (f_{i-1,j} - R_{1(i-1,j)})]\} \\
&= \frac{1}{2}\left\{
\begin{aligned}
&\left[\left(\frac{1}{2}gh^2_{i+1,j} - \frac{1}{2}gh^2_{i+1,j}\right) + \left(\frac{1}{2}gh^2_{i,j} - \frac{1}{2}gh^2_{i,j}\right)\right] \\
&-\left[\left(\frac{1}{2}gh^2_{i,j} - \frac{1}{2}gh^2_{i,j}\right) + \left(\frac{1}{2}gh^2_{i-1,j} + \frac{1}{2}gh^2_{i-1,j}\right)\right]
\end{aligned}
\right\} \\
&\equiv 0
\end{aligned}
\tag{3.33}
$$

Similarly, in *y* direction, the momentum flux change at the cell (*i,j*) has

$$K_m = K^*_{i+1/2,j} - K^*_{i-1/2,j} \equiv 0 \tag{3.34}$$

Therefore, the conserved variables (**U**) is updated at new time by

$$
\begin{aligned}
\mathbf{U}^{n+1}_{i,j} &= \mathbf{U}^n_{i,j} - \frac{\Delta t}{\Delta x}\left(\mathbf{H}^*_{i+\frac{1}{2},j} - \mathbf{H}^*_{i-\frac{1}{2},j}\right) - \frac{\Delta t}{\Delta y}\left(\mathbf{K}^*_{i,j+\frac{1}{2}} - \mathbf{K}^*_{i,j-\frac{1}{2}}\right) + \Delta t \mathbf{S}_{f,i,j} \\
&= \mathbf{U}^n_{i,j} - 0 - 0 + 0 = \mathbf{U}^n_{i,j}
\end{aligned}
\tag{3.35}
$$

As shown above, the numerical solution of the stationary flow problem by the proposed scheme is equal to the exact solution where the flow variables do not change with time i.e. the initial state is maintained. From the above analysis, the *C*-property is guaranteed by the proposed source term treatment method. The bed slope source term is well balanced with the flux gradient terms.

3.3.1.2 Second-order TVD-WAF Scheme

To compute the intercell numerical fluxes, the weighted average flux (WAF) method is employed. However, the basic WAF scheme without TVD modification is seldom used in practice because of its unphysical or spurious

oscillations that can occur. To avoid such oscillations, a total variation diminishing (TVD) constraint is enforced on the WAF scheme with a flux limiter function. The TVD-WAF scheme is second-order accurate in space and time by solving the conventional Riemann problem associated with the first-order Godunov scheme. A detailed description can be found in Toro (2001).The modified TVD-WAF scheme applied in this paper is described in the following; we take the calculation of *x*-direction flux as an example, the *y*-direction is treated in similar way. The modified TVD-WAF flux can be written as:

$$\mathbf{H}_{i+1/2}^{*} = \frac{1}{2}(\mathbf{H}_i + \mathbf{H}_{i+1}) - \frac{1}{2}\sum_{k=1}^{N} sign(c_k)\Phi_{i+1/2}^{k}\Delta\mathbf{H}_{i+1/2}^{k} \qquad (3.36)$$

$$sign(a) = \begin{cases} 1 & a > 0 \\ 0 & a = 0 \\ -1 & a < 0 \end{cases}$$

There, $\mathbf{H}_i$= H ($\mathbf{U}_i$, $\mathbf{B}_i$), $\mathbf{H}_{i+1}$ = H ($\mathbf{U}_{i+1}$, $\mathbf{B}_{i+1}$) are the conservative variable flux vectors at the left and right side of each cell interface; c_k is the Courant number for wave *k*, $c_k = \Delta t S_k/\Delta x$; S_k is the speed of wave *k* and N is the number of waves in the solution of the Riemann problem, *N*=3 in conjunction with HLLC approximate Riemann solver. $\Delta\mathbf{H}_{i+1/2}^{(k)} = \mathbf{H}_{i+1/2}^{(k+1)} - \mathbf{H}_{i+1/2}^{(k)}$, which is the flux jump across wave *k*; $\mathbf{H}_{i+1/2}^{(k)}$ is the value of the flux vector in the interval k; herein $\mathbf{H}_{i+1/2}^{(1)} = \mathbf{H}(\mathbf{U}_i,\mathbf{B}_i)$, $\mathbf{H}_{i+1/2}^{(2)} = \mathbf{H}(\mathbf{U}_i^{*},\mathbf{B}_i)$, $\mathbf{H}_{i+1/2}^{(3)} = \mathbf{H}(\mathbf{U}_{i+1}^{*}, \mathbf{B}_{i+1})$ and $\mathbf{H}_{i+1/2}^{(4)} = \mathbf{H}(\mathbf{U}_{i+1}, \mathbf{B}_{i+1})$ which are estimated by virtue of the modified HLLC approximate Riemann solver, $\Phi(r)$ is WAF limiter function whose function is to raise spatial order to second, while maintaining stability. There are various limiter functions available to choose from Toro [138].The WAF limiter used expressed through the well-known conventional flux limiters $\varphi(r)$ is the *minmod* limiter:

$$\Phi(r^k) = 1 - (1 - |c|)\varphi(r^k)$$
$$\varphi(r^k) = max[0, min(1, r^k)] \quad (minmod \text{ limiter})$$

where r^k is the ratio of the upwind change to the local change in the scalar quantity *q*, which can be written:

$$r^k = \begin{cases} \dfrac{\Delta q_{i-1/2}^{(k)}}{\Delta q_{i+1/2}^{(k)}} = \dfrac{q_i^{(k)} - q_{i-1}^{(k)}}{q_{i+1}^{(k)} - q_i^{(k)}} & if\ c_k > 0 \\[4mm] \dfrac{\Delta q_{i+3/2}^{(k)}}{\Delta q_{i+1/2}^{(k)}} = \dfrac{q_{i+2}^{(k)} - q_{i+1}^{(k)}}{q_{i+1}^{(k)} - q_i^{(k)}} & if\ c_k > 0 \end{cases} \qquad （3.37）$$

For the *x*-split two-dimensional shallow water equations we choose $q=h$ for the non-linear waves (waves S_L, $k=1$ and S_R, $k=3$) and $q=v$ the tangential velocity component for the shear wave (waves S_*, $k=2$).

3.3.2 Stability Criteria

The numerical scheme is explicit, so in order to restrict the instability of numerical model, the well-known Courant-Friedrichs-Lewy (*CFL*) stability condition is applied [145-147]. For a two-dimensional Cartesian cell, the time step Δt is determined by multiplying the Courant number by the smaller value of the time steps in *x*-and y-directions. This is expressed as

$$\Delta t = CFL \min \left(\min \frac{dx_i}{|u_i| + \sqrt{gh_i}}, \min \frac{dy_j}{|v_j| + \sqrt{gh_j}} \right)$$

where the Courant number 0<*CFL*<1.

3.4 Wetting and Drying

At the wetting and drying front, small water depths can cause unrealistically high velocities which in turn causes numerical instabilities. To overcome this, a water depth tolerance is introduced. If the water depth is smaller than the tolerance depth, it will be treated as a dry bed case whose velocity is set equal to zero; otherwise it is treated as a wet bed case. In addition, the source term is incorporated into flux term, so when handling wet/dry fronts, the source term flux should be considered. According to the treatment of wetting and drying mentioned above, four wetting and drying situations are accounted for and they are summarized in Figure 3.5.

Most hydraulic conditions can be included in these four situations. More specifically,

1) Both left and right cell are dry (Figure 3.5a). The flux is considered as zero.
2) Both left and right cell are wet (Figure 3.5b). The numerical flux at cell interface is calculated according to proposed numerical scheme without any special treatment.
3) One side cell is wet; another side cell is dry and the relation of the water surface elevation and bed elevation satisfy: $z_{bR} \geq \eta_L$ or $z_{bL} \geq \eta_R$ (Figure 3.5c). The flow flux at cell interface should have been regarded as zero,

but the source flux should still be calculated because it will be applied to balance the source flux at the former cell interface when updating the variables at left cell. In this circumstance, a water elevation η'_R at dry cell is temporarily replaced otherwise a non-physical flux will be predicted. The treatment is handled as:

$$\eta_R = z_{bR}$$
$$\Delta\eta = \eta_R - \eta_L$$
$$\eta'_R = \eta_R - \Delta\eta$$

Meanwhile, the wet cell component normal to dry cell interface is set to zero to ensure that the flow is in no-motion state.

4) One side cell is wet; another side cell is dry and the relation of the water surface elevation and bed elevation satisfy: $z_{bR} < \eta_L$ or $z_{bL} < \eta_R$ (Figure 3.5d). No special treatment is carried out; and the cell interface flux will be in the wet-to-dry direction according to the proposed numerical scheme.
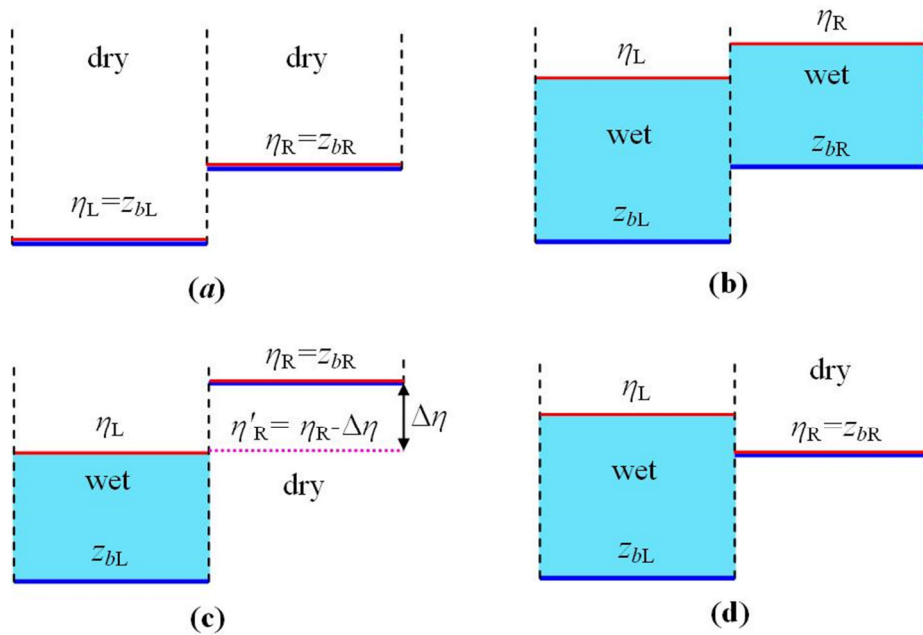
Figure 3.5 The scenarios of flow over variable topography

Furthermore, updating of water depth at each time step may cause a negative value to occur, which violates mass conservation law and will lead to a gain of water mass if just treating negative water depth as zero and also considering corresponding velocities as zero. Therefore, a special treatment handling the negative water depth problem should be implemented. In this Chapter, the following treatment is applied in terms of maintaining mass conservation referring to the publications [135, 136]. Firstly, the velocity components are treated as zero for any dry cells. In general, water is

subtracted from the adjacent cell with most water, where the conserved variables *hu* and *hv* are modified so that *u* and *v* remain the same as before in order to maintain the front velocity components; if there is no adjacent cell to provide adequate water to be subtracted, then the negative mass of water for maintaining conservation is taken into the calculation at the next step and meanwhile this cell is regarded as drying until the cell is sufficiently recharged or a neighbour having adequate water is identified [136].

3.5 Numerical Testing

In this section, several well-known benchmark cases are applied to validate the proposed scheme. All the tests are undertaken using the TVD-WAF/HLLC scheme described above. To demonstrate the proposed model's ability to deal with source terms as well as wetting/drying, the following benchmark tests and application cases were selected.

3.5.1 Still Water over Two Smooth Bumps

To verify that the proposed scheme can satisfy the *C*-property and is well-balanced between flux term and source term with wet/dry fronts, a test of still water over two smooth bumps test is reproduced. Similar tests with one submerged bump have been investigated in one dimension and two dimensions by other researchers [148-150]. In this test, two frictionless bumps are constructed, the centre of the submerged one is located at the (*x*=0.7 m, *y*=0.5 m), and the centre of the emerged one is located at (*x*=0.2 m, *y*=0.5 m). The whole container is 1m×1m square, with the bed elevation given by

$$z_b = \begin{cases} \max\{0, 0.25 - 5.0[(x - 0.7)^2 + (y - 0.5)^2]\} & x > 0.45m \\ \max\{0, 0.1 - 10.0[(x - 0.3)^2 + (y - 0.5)^2]\} & x \leq 0.45m \end{cases}$$

The initial water level is set as 0.15m; so the initial water depth h(*x*, *y*)=max(0, 0.15-z_b); both velocities in x and y direction are zero. Because there are no external forces, the water should keep still during the simulation period. The area is discretised by 100×100 cells ($\Delta x=\Delta y$=0.01 m), and the simulation is carried out for 500 s. Figure 3.6 demonstrates the simulated water surface over the two bumps. To show the difference between numerical and exact solutions, Figure 3.7 illustrates the water level and unit discharge comparison with the exact solutions at section *y*=0.5 m. The

results show that the proposed model maintains tranquil water and the water level and unit discharge are exactly reproduced whether in a wet domain or a dry domain. This test essentially verifies the well-balanced property of the proposed approach.
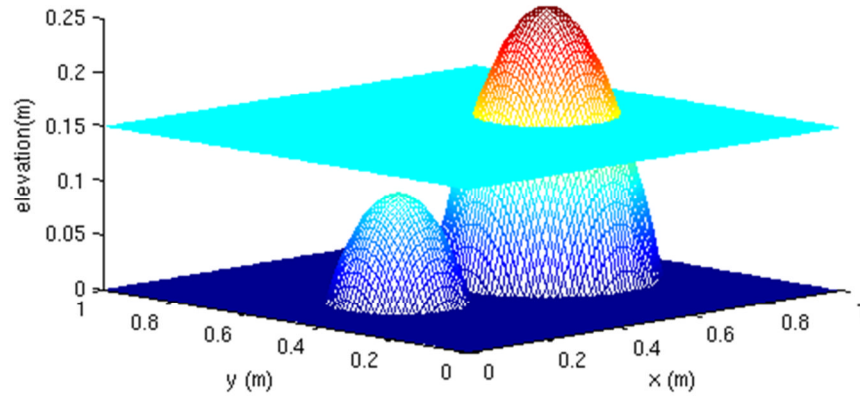
Figure 3.6 Still water over two smooth bumps: simulated water surface after 500s
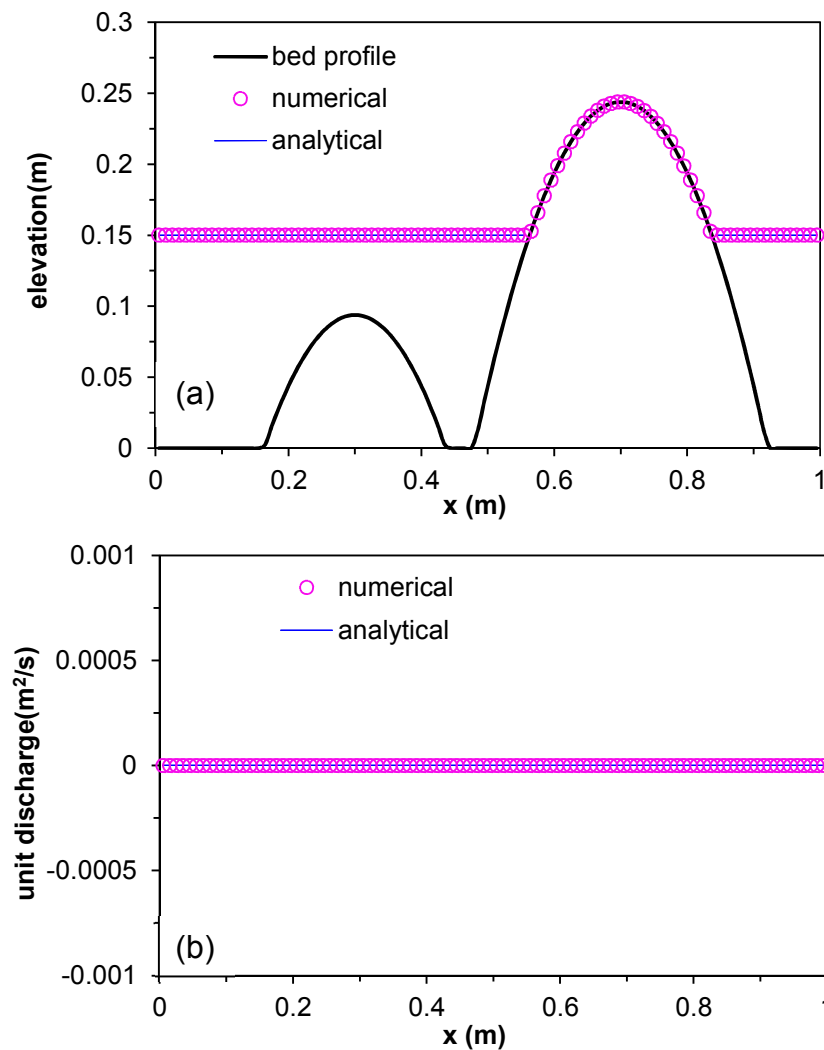
Figure 3.7 The comparison between numerical and analytical solutions at section y=0.5m after 500s; (a) water elevation; (b) unit discharge

3.5.2 Steady Flow over a Bump

This test has been used by a range of authors for validating bed-slope source term treatment [19, 78, 136, 151-153]. In order to verify that the proposed scheme achieves the correct balance between source flux and flux gradient, a non-stationary steady state case is also investigated. This is a one-dimensional test case but tested in two dimensions here, in which the spatial domain is represented by a 25 m×1 m rectangular, frictionless channel and then the computational domain is discretised into 250×10 cells. The bed profile is:

$$z_b = \begin{cases} 0.2 - 0.05(x-10)^2 & 8 \leq x \leq 12 \\ 0 & otherwise \end{cases}$$

For the convergence of numerical solution, the global relative error R<1×10^{-6} is defined here, where R is expressed by

$$R = \sqrt{\sum_i \left(\frac{h_i^n - h_i^{n-1}}{h_i^n} \right)^2}$$

where h_i^n and h_i^{n-1} are water depths at current and previous time steps at cell i.

Initial flow conditions for the transcritical flow case are defined as: upstream inflow is equal to 0.18 m^3/s and the downstream level is set equal to a constant 0.33 m. The initial water level is 0.33 m and the initial discharge is set to 0 m^3/s. To show how the proposed scheme performs, results are presented comparing: the method proposed here, which we will refer to as the Homogenous Flux method (HFM); the well-balanced scheme proposed by Song et al.(2011) [137] and the Surface Gradient Method (SGM) [11] which has been shown to handle this problem well and has been widely applied in solving the shallow water equations. The computed results are displayed in Figure 3.8 and show an excellent agreement between numerical results of water elevation, discharge and Froude number by HFM and analytical results. Errors are only apparent for discharge at one point, whilst at others values are as predicted analytically - something which is not achieved by any of the other methods for this test. HFM gives better results than those from the method of Song et al.(2011) and SGM for discharge.
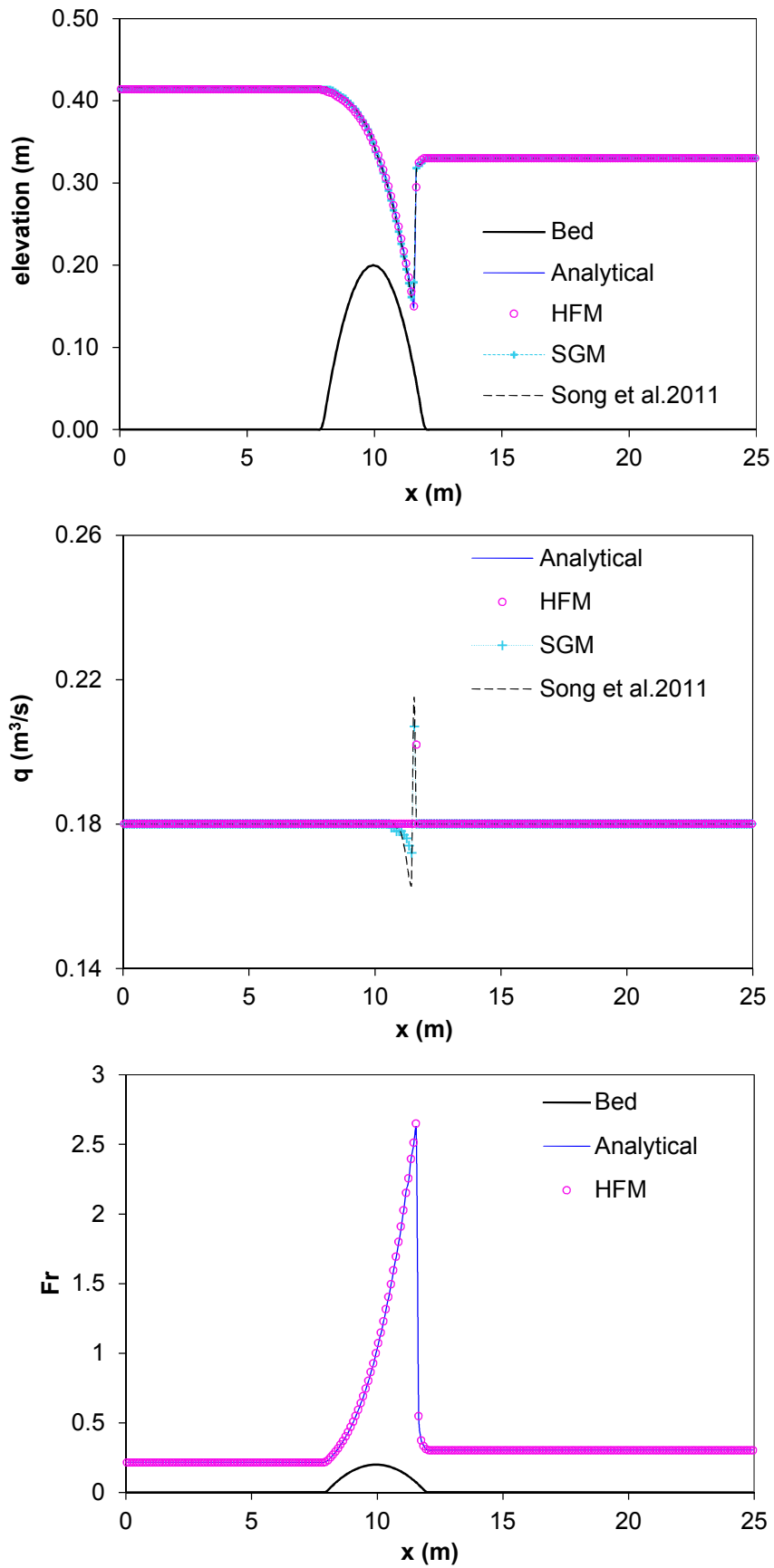
Figure 3.8 Transcritical flow over a bump

For the subcritical flow case, initial flow conditions are defined as: upstream inflow equal to 4.42 m³/s and downstream level equal to a constant 2 m. The computation results are shown in Figure 3.9. The comparisons between numerical solutions of HFM and analytical solutions show excellent (almost exact) agreement, both the SGM and the well-balanced method proposed by Liang and Borthwick (2009) [136] have a small oscillation in discharge around the bump [78] a similar or more severe oscillation also occurs on the test from other works [137, 154]. Figure 3.9(c) shows relative error R against iteration number, demonstrating the convergence history of subcritical flow over a bump. The comparison highlights the capability of the proposed method in maintaining the balance between flux gradient and bed slope for non-stationary steady state flow.
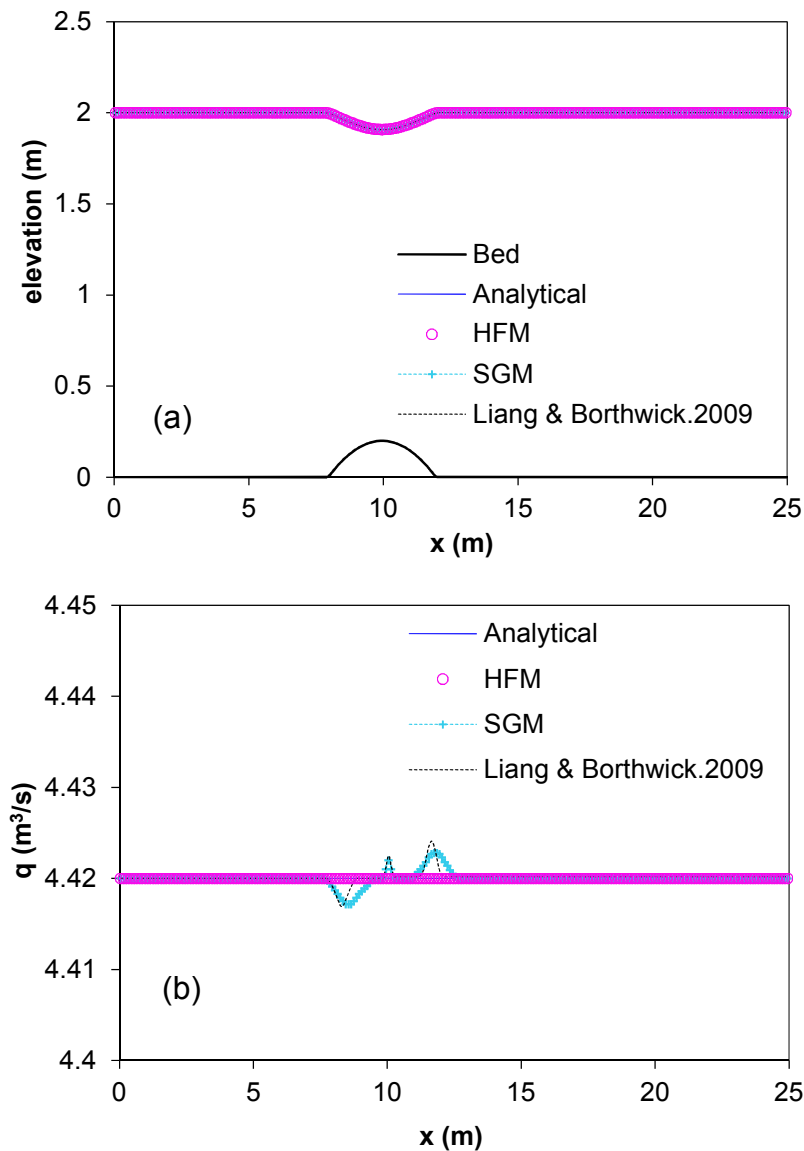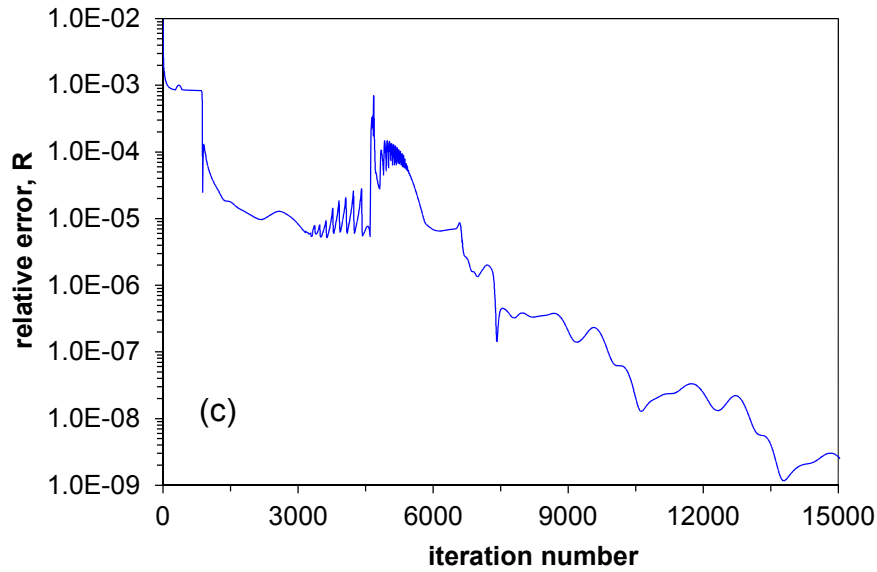
Figure 3.9 Subcritical flow over a bump: (a) water elevation; (b) discharge; (c) convergence history

3.5.3 Surge Wave Propagation Crossing a Vertical Step

This case has been proposed and implemented by a number of researchers [134, 155] to test source term treatments with a vertical or discontinuous bed step. Although some treatment approaches of bed slope have been proposed, few involve treatment of vertical bed step where significantly inaccurate results can occur. The flow conditions are defined as follows: the flow is unsteady; the channel length is 10,000 m and the bed step is 2 m in height at $x \geq 5,000$ m, otherwise the bed level is zero; and water surface elevation is 5.0 m in the channel; at the entrance, the water depth is imposed as a constant 10m and the surge velocity is defined as

$$u(t) = (\eta_u - \eta_d)\sqrt{\frac{g(\eta_u - \eta_d)}{2\eta_u\eta_d}}$$

where η_u is the upstream water level of 10 m; and η_d represents the downstream water level of 5 m. The simulation was undertaken with 1,000 uniform cells (Δx=10 m). As before, I compare the numerical results with SGM, without additional special treatment at the vertical step. Figure 3.10 shows the comparisons of water surface and velocity between numerical solutions and analytical solutions [155] at t=600.5 s. The comparisons show that the proposed method achieves good agreement with the analytical solution. However, there is an oscillation in the location of vertical step for SGM if it is not specially treated as described by Zhou et al. (2002). The

oscillation causes the water elevation to be too large before the step location and smaller just after the step location when compared to the analytical solution (see Figure 3.10). Correspondingly, the velocity is smaller than HFM and analytical solutions. However, there is not a big discrepancy in the surge wave and water front position. The comparison indicates that the treatment in this study is more accurate and performs better than SGM for a discontinuous bed.
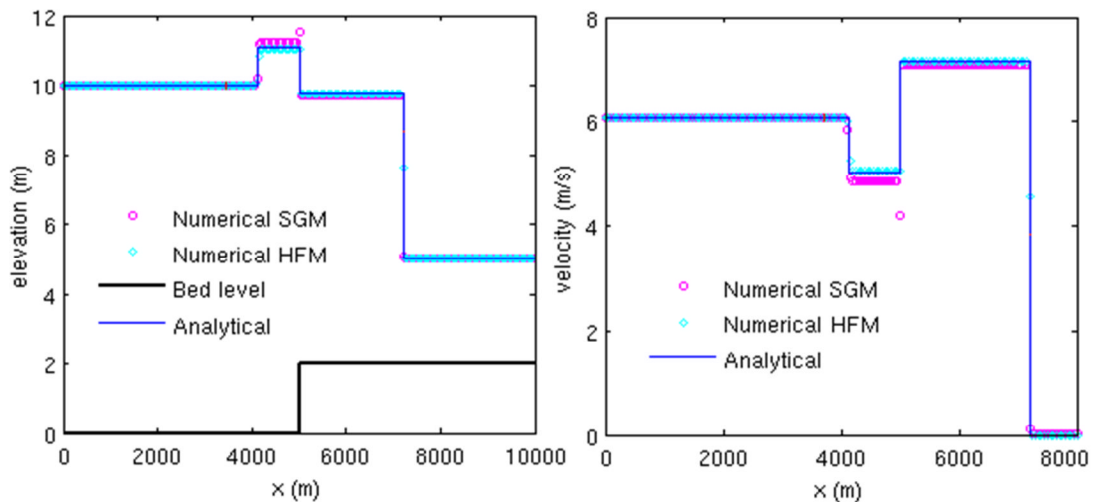
Figure 3.10 Comparisons of water surface and velocity between numerical and analytical solutions at t =600.5 s

3.5.4 Dam-break Flow over Channel with a Triangular Bump

This case is used to test the numerical model with irregular bed topography for the wetting/drying problem. The laboratory dam-break flow over a triangular hump is reproduced in this section, as investigated by the EU CADAM project [73]. The experimental setup is depicted in Figure 3.11 in which the lengths of bed profile and dam location are shown in which a symmetric triangular hump of 0.4 m is present. The still water surface elevation of the reservoir is 0.75 m upstream of the dam, while it is initially dry in the downstream floodplain of dam location. The downstream outlet of the domain is an open free outfall. Seven monitoring gauges were set up which are located at 2 m, 4 m, 8 m, 10 m, 11 m, 13 m and 20 m downstream of the dam, respectively. The Manning coefficient n was set equal to 0.0125 throughout the domain, and the domain was discretised by Δx=0.04 m.

The simulation was run for 90 s and the comparisons between numerical results and experimental data at Gauge 1, 3, 4, 5, 6 and 7 are given in Figure 3.12. The comparisons show that the predictions of arrival time and

water depth agree with the measured data fairly well at Gauge 1 to 6. However, at Gauge 7 after the bump, a discrepancy of water depth appears, but the arrival time is still a reasonably good prediction. Similar results were also obtained by other researchers [148, 154]. This discrepancy is thought to be due to a combination of numerical errors and measurement errors. Furthermore, the SGM approach is also implemented to reproduce this case and the comparisons are also shown in Figure 3.12. It can be seen that at Gauge 1, 3, 4, 5 and 7, the water depths from the two simulations are very close. However, at Gauge 6 where the irregular bed is located, the simulated water depth by HFM is slightly larger than that by SGM. In comparison with the measured data, both results have a fairly well agreement with that. This test shows the excellent stability and efficiency of proposed numerical model when modelling flow over an irregular bed in a wetting/drying case.
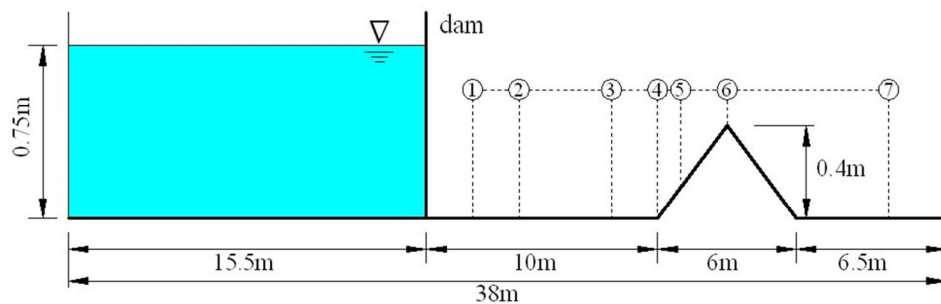
Figure 3.11 Dam-break flow over a triangular hump
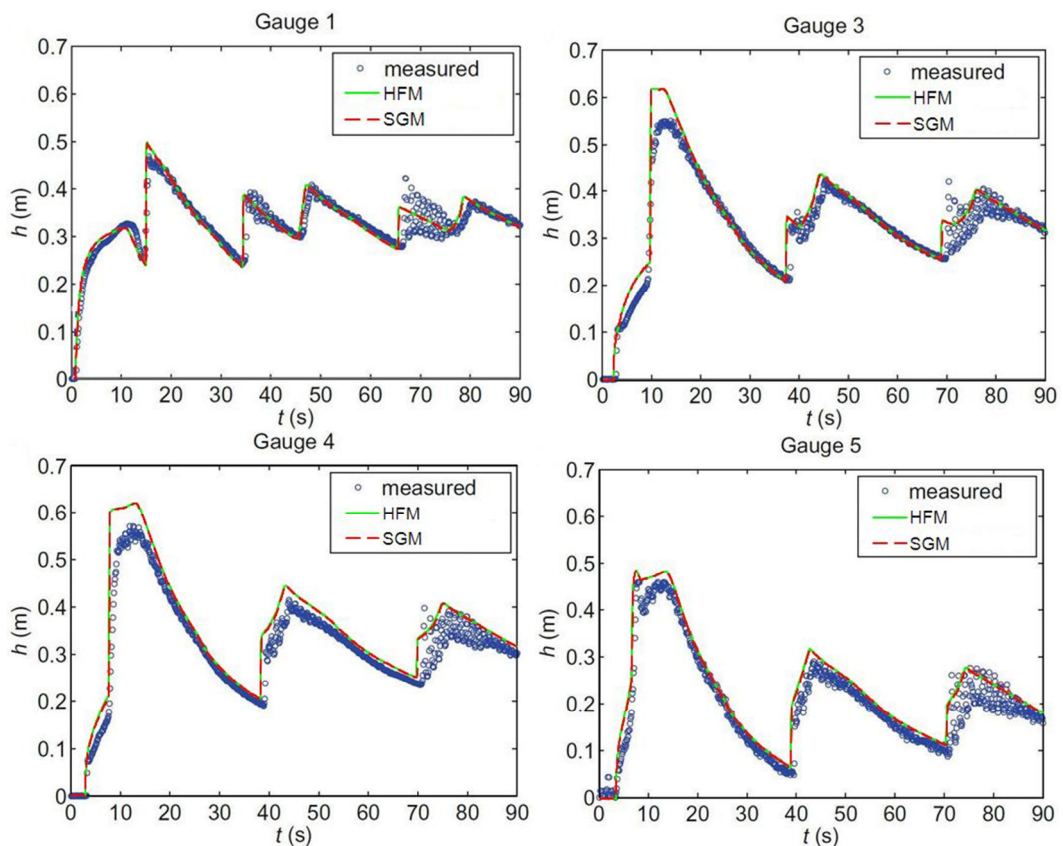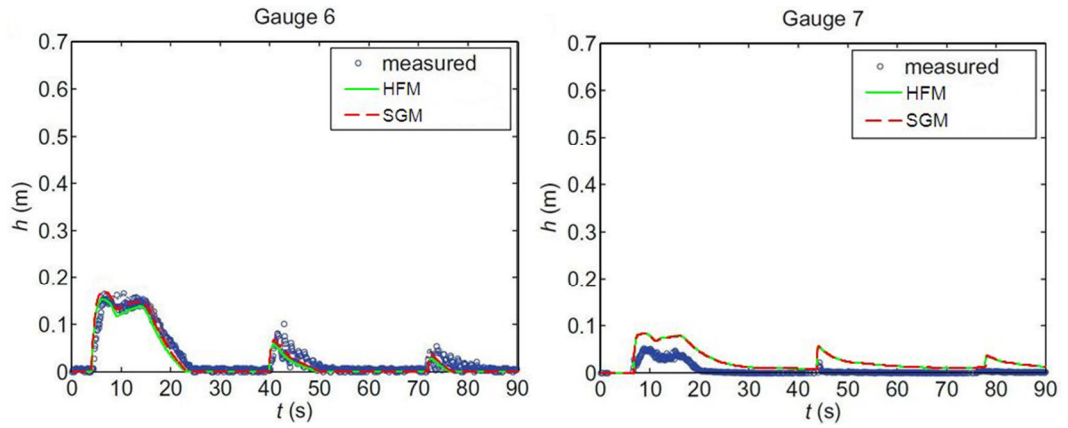
Figure 3.12 Dam-break over a hump: time histories of water depth at different gauges, in which the solid line represents simulation results and cycle points for experimental measures

3.5.5 2D Shallow Water Sloshing in Parabolic Basin

This test was proposed by Thacker [156] who presented several analytical solutions to time-dependent periodic oscillations in parabolic basins. This benchmark is in two-dimensions, and represents a complex test case for the verification of a moving boundary problem solver with 2D wetting/drying fronts. In this case, a planar water surface profile circulates inside a parabola of revolution. The bed elevation of two-dimensional parabolic basin can be expressed by

$$z_b(x,y) = \frac{h_0}{a^2}(x^2 + y^2) \quad -10\,000m \le x, y \le 10\,000m$$

where h_0 is the water depth at the centre of the basin and a is the distance from the centre to the shoreline with zero elevation. h_0=10 m; a=8,025.5 m in this study. The exact periodic solution can be expressed as the following water surface and velocity profile [156]:

$$z_w(x,y,t) = \frac{\eta h_0}{a^2}[2x\cos(wt) + 2y\sin(wt) - \eta] + h_0$$

$$u = -\eta w \sin(wt)$$

$$v = -\eta w \cos(wt)$$

where η is a constant that determines the amplitude of the motion, η=a/10=802.55; w=$(2gh_0)^{0.5}/a$=$2\pi/T$ is the frequency with periodic T=3,600 s. The parameter settings proposed by Liang [21] are applied here.

The computational domain is discretised as 200×200 uniform cells with mesh size of Δx=Δy=100 m. The initial water surface profile at t=0 is determined according to the above-equation. The proposed model was

applied to this test case for three wave periods. Figure 3.13 illustrates the 3D view of water surface at t=T+T/2 which is relatively smooth in the two-dimensional parabolic basin. The numerical solutions are compared to analytical solutions at t=T, T+T/2, 2T+T/3 and 2T+3T/4 respectively, which are depicted in Figure 3.14. The comparisons show good agreement, with the proposed HFM approach able to track the wet/dry front interface well. The velocity component in x-direction against time at point (5,050, -50) and point (7950, -50) over the three periods is illustrated in Figure 3.15 which displays the comparisons between analytical solution and second-order TVD-WAF solution. It is clear that good agreement is achieved. Furthermore, at t=2T+3T/4, the velocity u in x direction and v in y direction is also compared against Thacker's analytical solutions (see Figure 3.16). In general the agreement is good, although some error points still occur. These small errors mainly appear around the wet/dry interface area but they are accurate up to mass balance error. In conclusion, this benchmark verifies the capability of the proposed numerical model and indicates that the model can cope well with unsteady flow and 2D wetting and drying over complex bed topography.
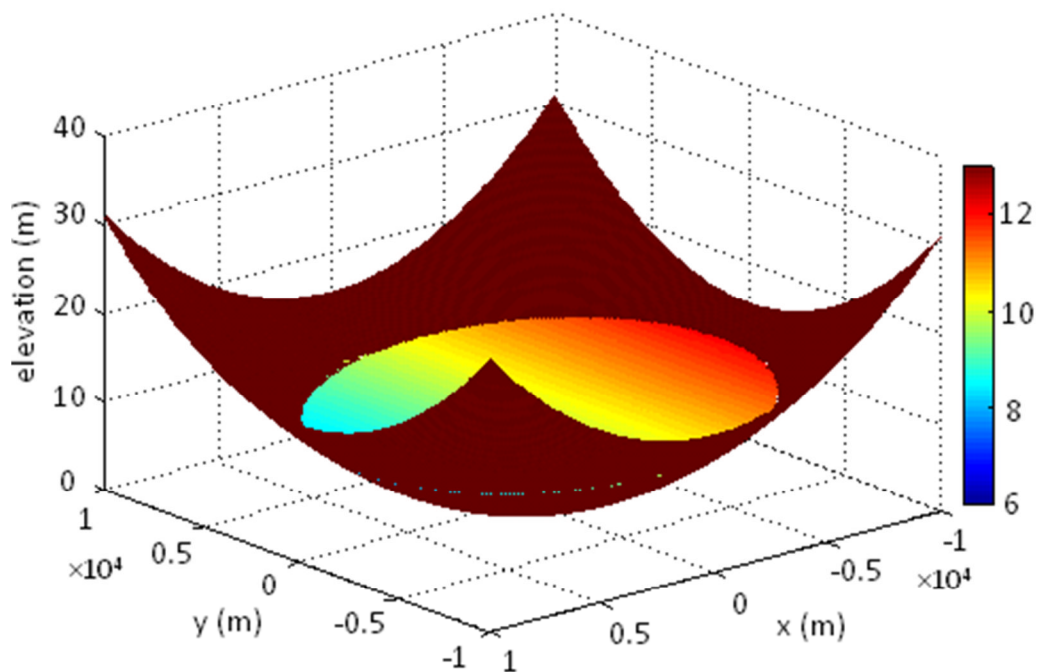
Figure 3.13 3D view of water surface and bed profile at t=T+T/2
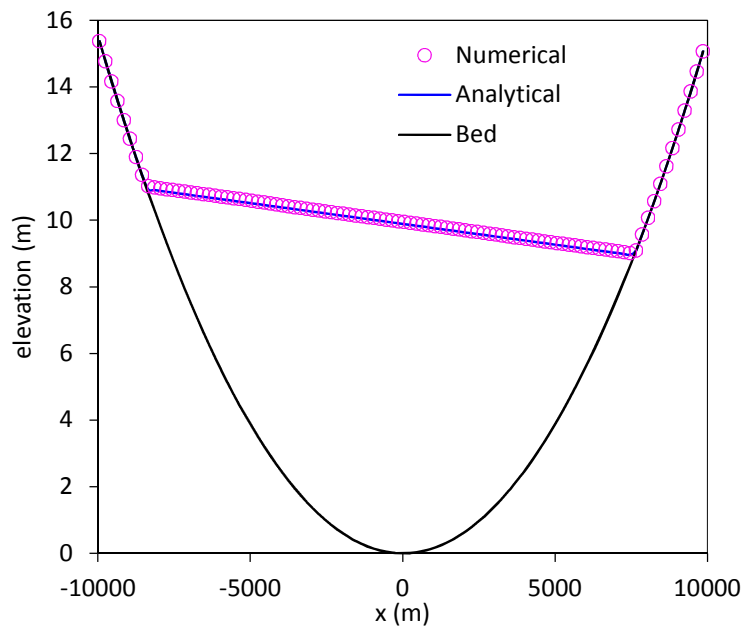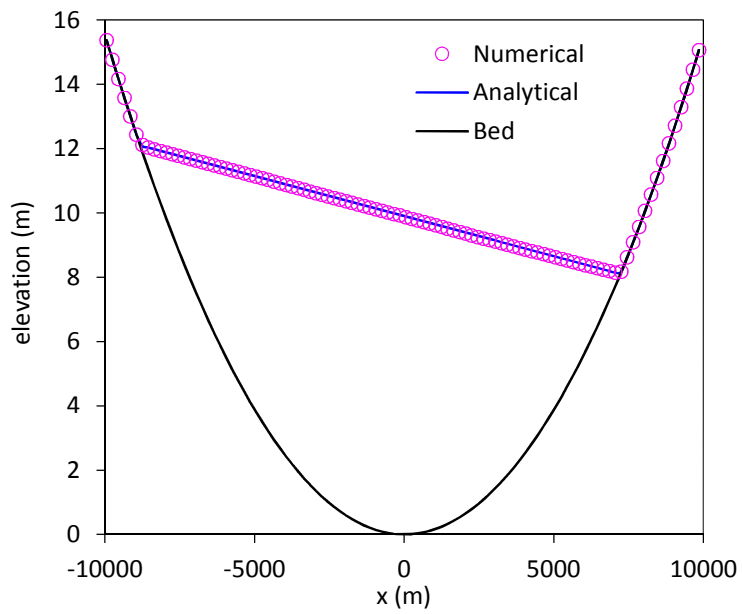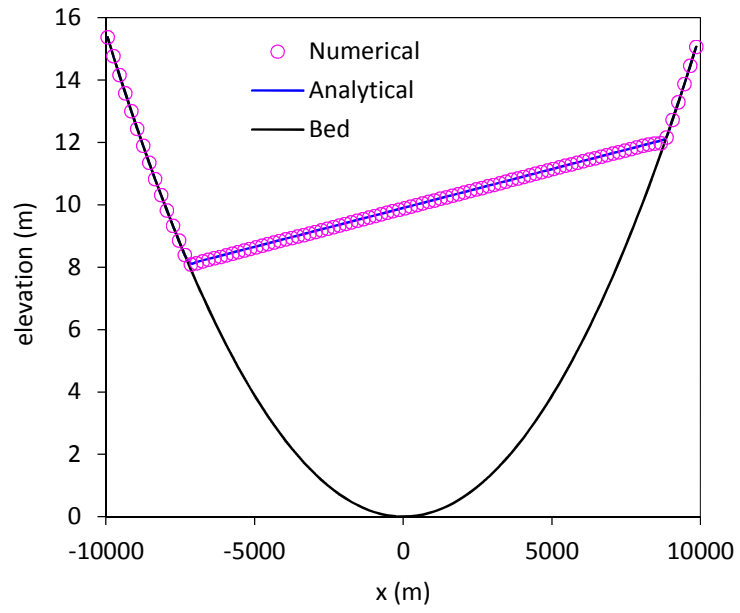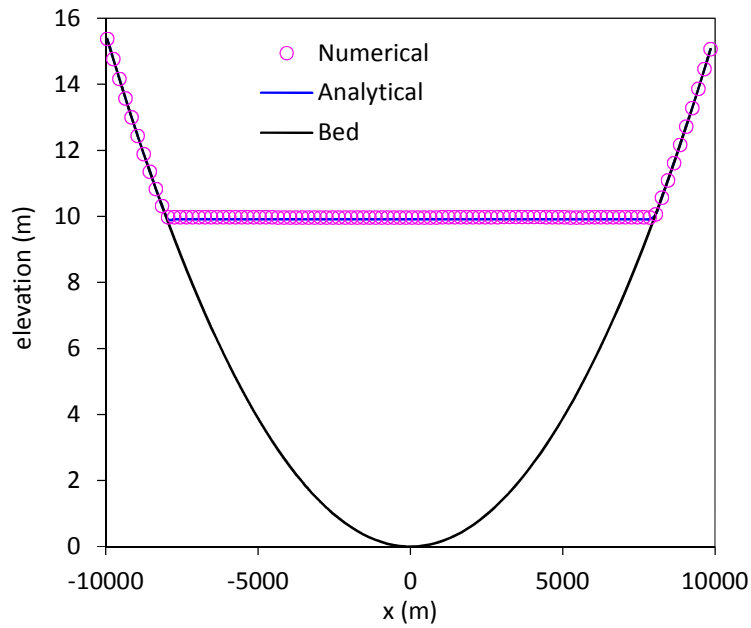
Figure 3.14 Comparisons between numerical solution by HFM and analytical solution proposed by Thacker (1981) (The time is T, T+T/2, 2T+T/3 and 2T+3T/4, respectively)
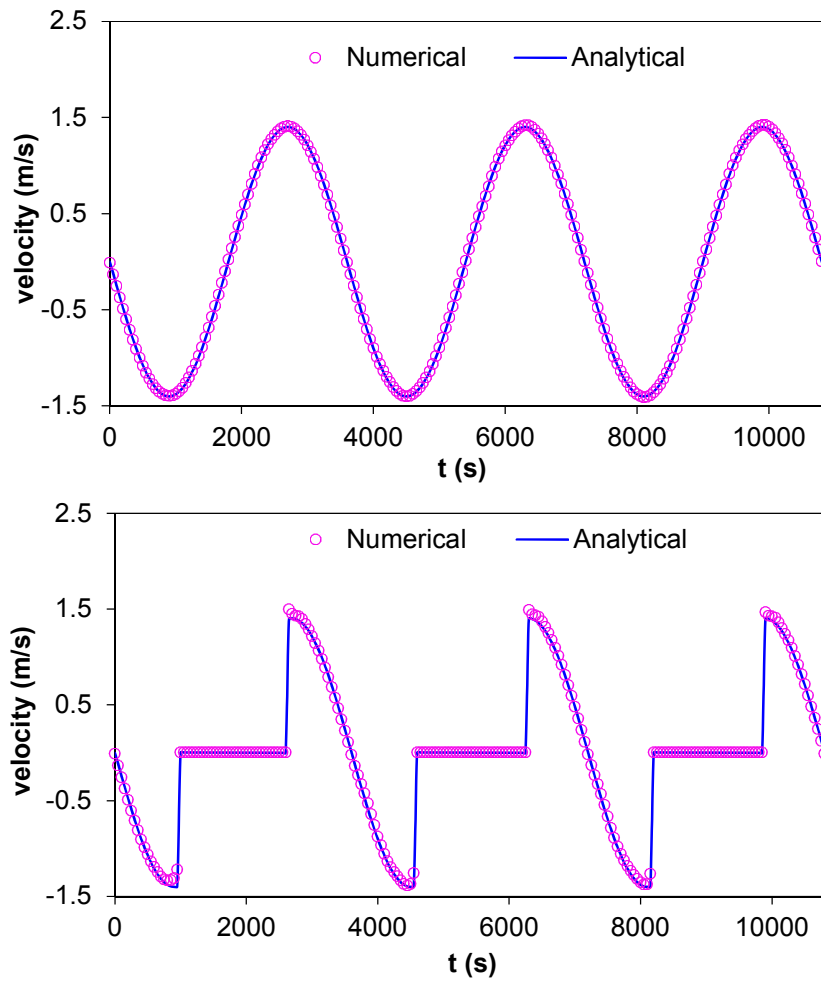
Figure 3.15 Comparison between numerical and analytical velocity in *x* direction at point (5050, -50) and (7950, -50).
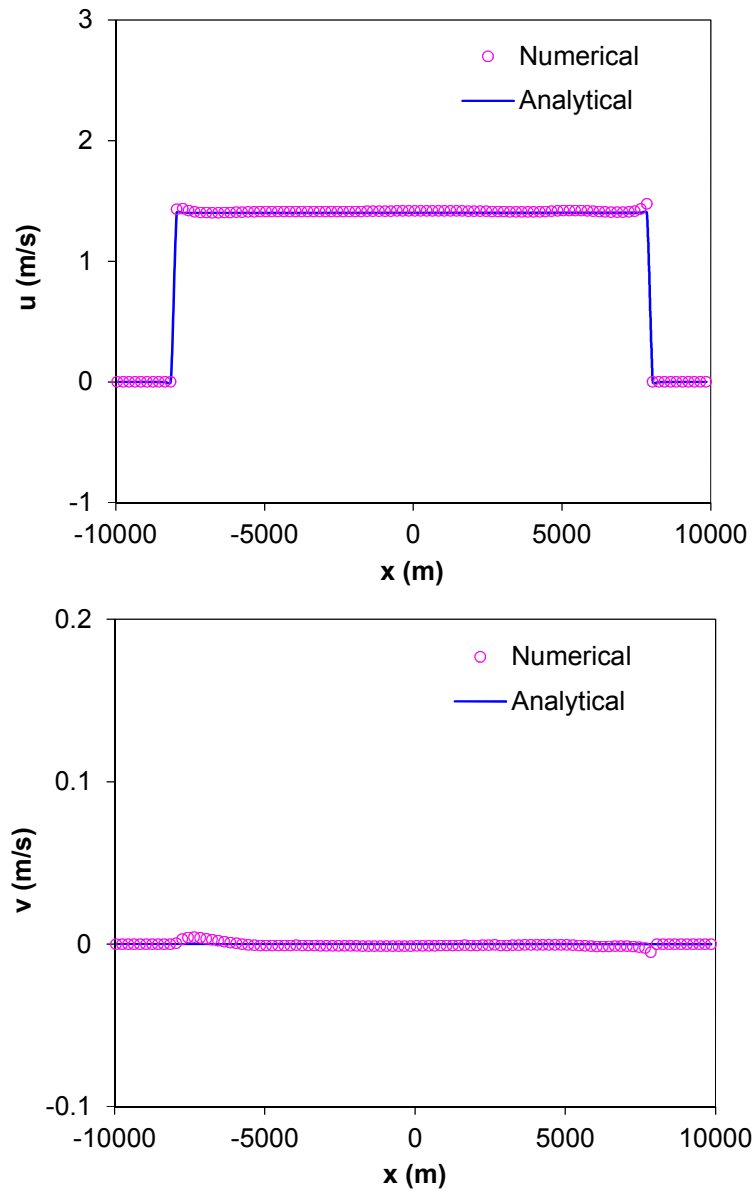
Figure 3.16 Comparison between numerical and analytical solutions of velocity in *x* direction and *y* direction against *x* distance.

3.5.6 Dam-break Flow around a 90º Bend

The EU CADAM project conducted experiments [157] of dam-break flow through a 90^0 bend. The experimental facilities consisted of a square reservoir of 2.44 m×2.39 m and an L-shaped channel which is depicted in Figure 3.17; in the *L*-shaped channel, bed level is set up to 0 m, however, the bed level of the reservoir is -0.33 m which forms a vertical step at the entrance to the channel. In the experiments, the initial water level in the reservoir is 0.2 m; in terms of water level in L-shaped channel, dry bed and wet bed cases in the L-shaped channel are taken into consideration; the water level for dry bed case is 0 m while it is 0.01 m for wet bed case; the six

measurement points are located at G1 (1.19 m, 1.21 m), G2 (2.74 m, 0.69 m), G3 (4.24 m, 0.69 m), G4 (6.56 m, 1.51 m), G6 (6.56 m, 3.01 m) taking the lower left corner as the origin. Manning's friction coefficient for the bed was set to 0.013.
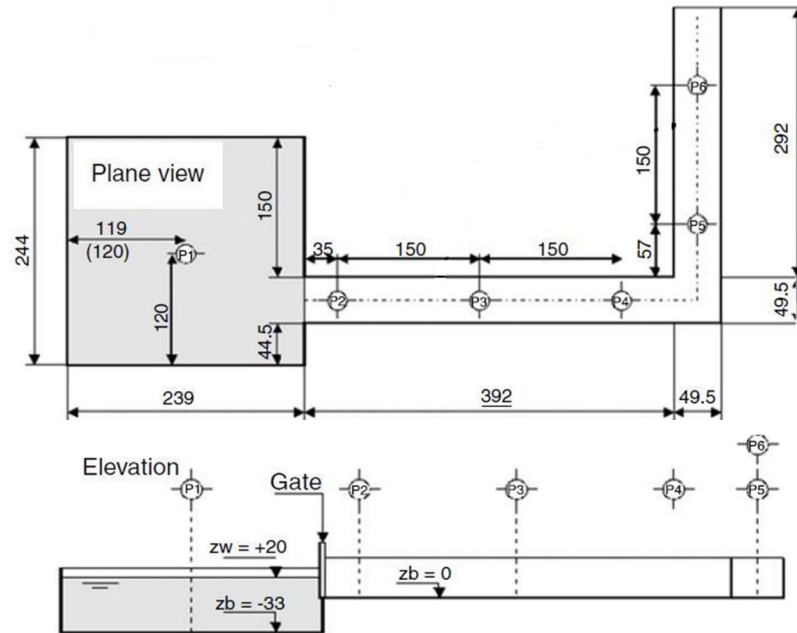
Figure 3.17 Geometry of the reservoir and L-shaped channel

With respect to the numerical model for this case, the second-order TVD-WAF numerical scheme is applied here and the computational grid is discretised as (Δx=0.04 m, Δy=0.02 m). For the flow process, the water flow arrives at the bend at approximately 3 s after dam-break; then the water is reflected from the wall to form a bore which propagates back towards the reservoir; while the water flow after the bend travels further downstream, multiple reflections on the walls can be observed and an eddy forms at bend of channel. The comparisons between numerical results and measured data for dry and wet bed case at the measurement gauges are presented in Figure 3.18 which shows that the arrival time of the flow agrees well at all the gauges, and water level at gauge 3, 4 and 6 shows good agreement. However, the numerical water level at gauge 5 after 20 s shows a bigger difference against experiment data. Such behaviour is also observed by other researchers. The disagreement is likely, on the one hand, to be due to additional head loss not accounted for in the numerical model cause higher numerical results; while on the other hand, measurement error may also be a cause. Overall, the agreement is good demonstrating the capability and accuracy of the method for predicting dam-break flows over a vertical step.

(a) dry case at gauge 3   (b) wet case at gauge 3

(c) dry case at gauge 4   (d) wet case at gauge 4

(e) dry case at gauge 5   (f) wet case at gauge 5

(g) dry case at gauge 6   (h) wet case at gauge 6
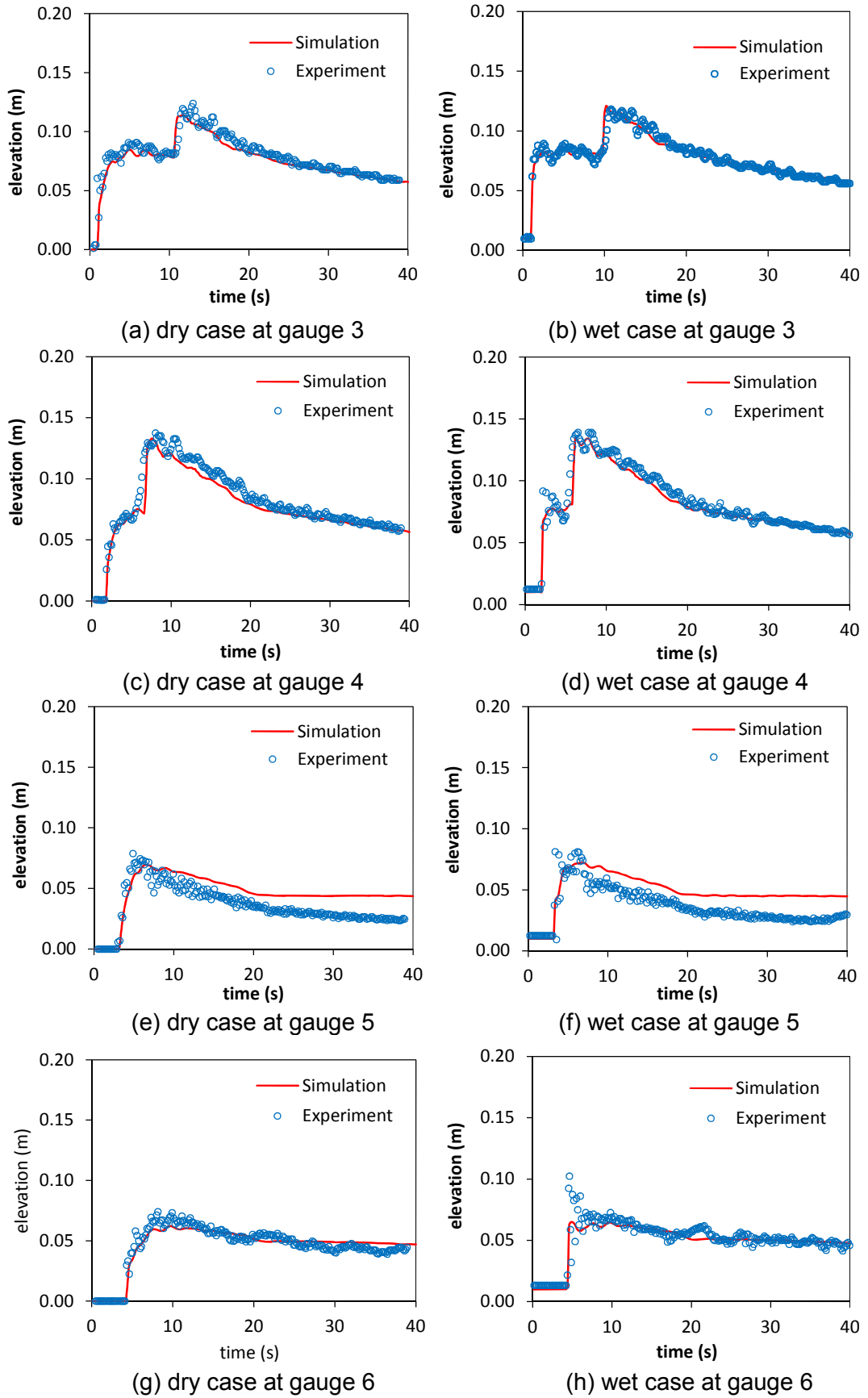
Figure 3.18 Comparisons between numerical and experimental data for dry and wet cases at Gauge 3 to 6; circular points represent experiment data and red lines are simulation results

3.5.7 Dam-break Flow in a Channel with Three Mounds

This case was initially proposed by Kawahara and Umetsu [158] and has been used by many researchers to evaluate the stability of numerical methods for dealing with wetting/drying problems [136, 148]. This test simulates dam-break flow propagation over a complicated channel geometry consisting of three mounds. The channel geometry is defined thus: the channel is 75 m long and 30 m wide with three mounds; the big mound is located at (x=47.5 m, y=15 m) with a radius of 10m and the side slope is 0.3; two smaller, identical ones and a side slope of 1/8, which are located at (x=30 m, y=6 m), (x=30 m, y=24 m), respectively. The channel geometry with initial water level is shown in Figure 3.19.
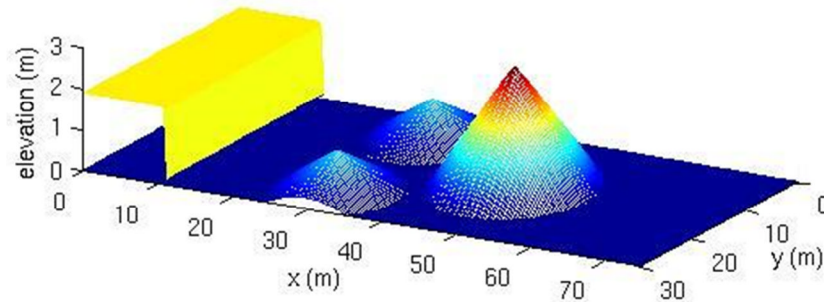
Figure 3.19 The initial water level at the channel geometry with three mounds

The bed geometry is given by

$$
\begin{cases}
z_{b1} = 0.3\left[10 - \sqrt{(x-47.5)^2 + (x-15)^2}\right] & (x-47.5)^2 + (x-15)^2 \le 100 \\
z_{b2} = \dfrac{1}{8}\left[8 - \sqrt{(x-30)^2 + (x-6)^2}\right] & (x-30)^2 + (x-6)^2 \le 64 \\
z_{b3} = \dfrac{1}{8}\left[8 - \sqrt{(x-30)^2 + (x-24)^2}\right] & (x-30)^2 + (x-24)^2 \le 64
\end{cases}
$$

The dam is located at x=11 m and the initial upstream water depth is set up to 1.875 m, and the downstream area is regarded as a dry bed with a Manning's roughness coefficient of 0.018. The computational grids are discretised with Δx=Δy=0.3 m. Figure 3.20 illustrates water surface profiles and water surface contour at t=3 s, 6 s, 12 s, 30 s and 100 s, respectively. From the pictures shown, dam failure makes the flow propagate downstream immediately; at 3s after dam-break, the flood waves arrive at the two smaller dry mounds and rise over them; then the flood waves completely submerge the initial two mounds, which initiate reflection shock waves that propagate back upstream. At 6 s, wetting/drying fronts reach the bigger mound but the high elevation causes flood waves to run around two sides of the mound

leaving a dry top area at 12 s. The principal wave and reflection waves interact with each other and as time increases, the flow gradually withdraws from the top of smaller mounds and water surface reaches a steady state after 100 s. Visual comparison with similar tests in the literature [136, 148, 159], Figure 3.20 shows that the flood inundation is well reproduced. The test verifies the stability of the proposed numerical model in terms of dealing with challenging wetting/drying over complex bed topography.
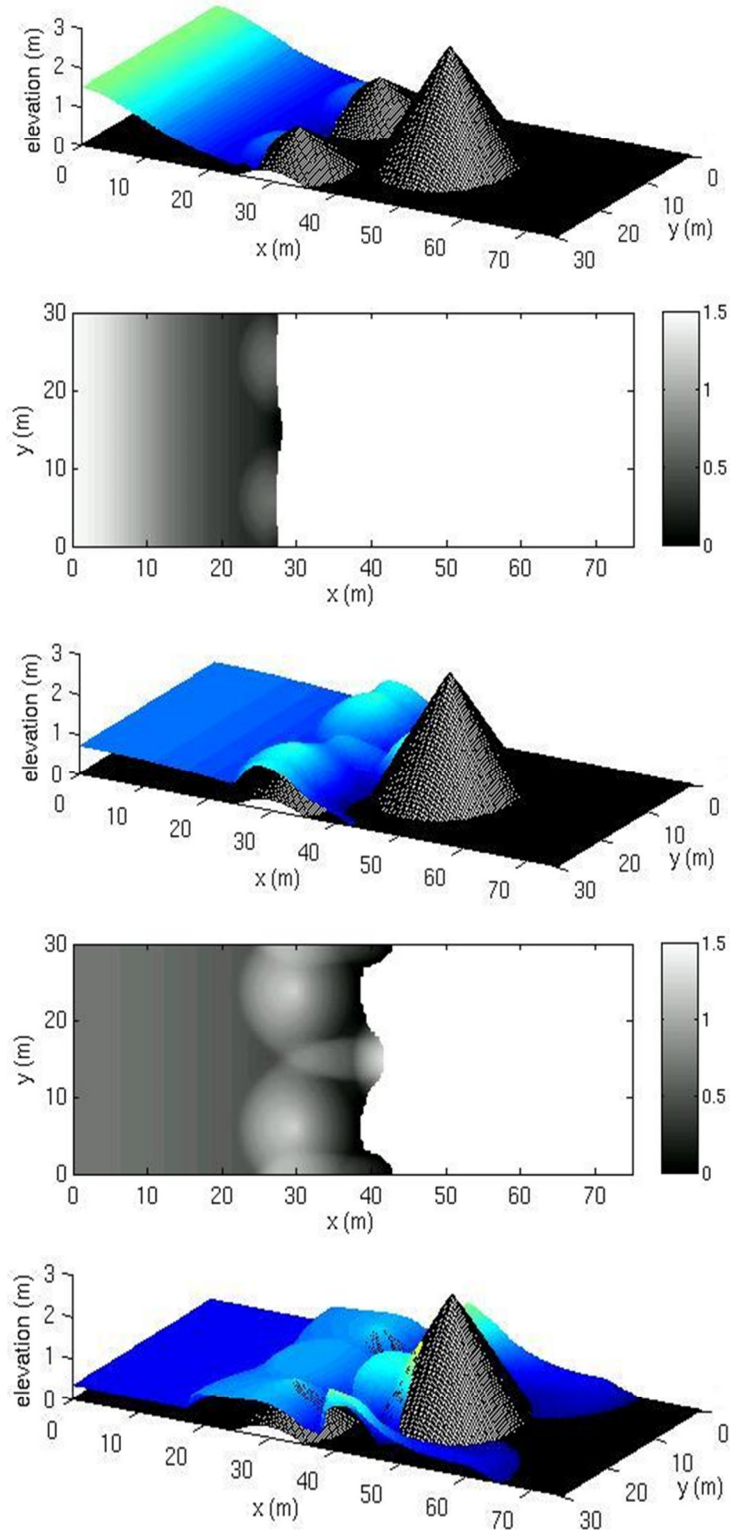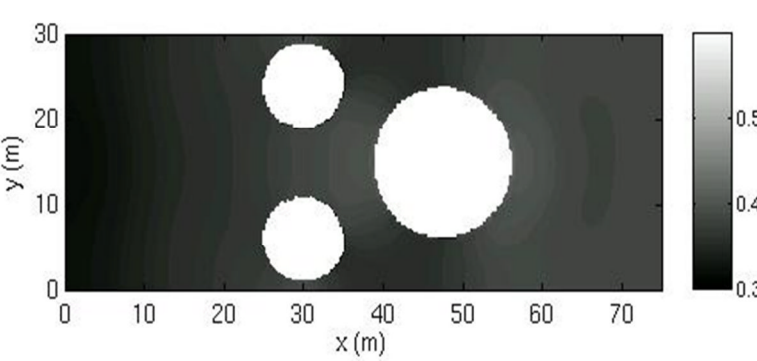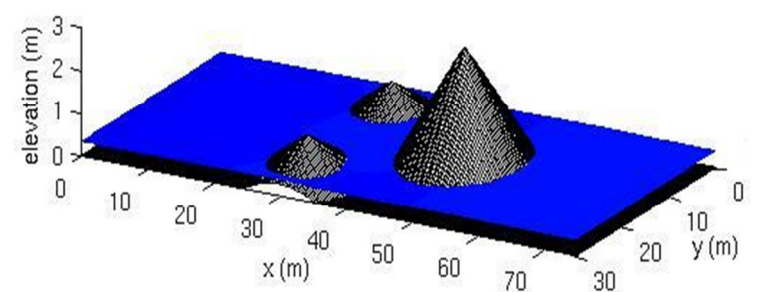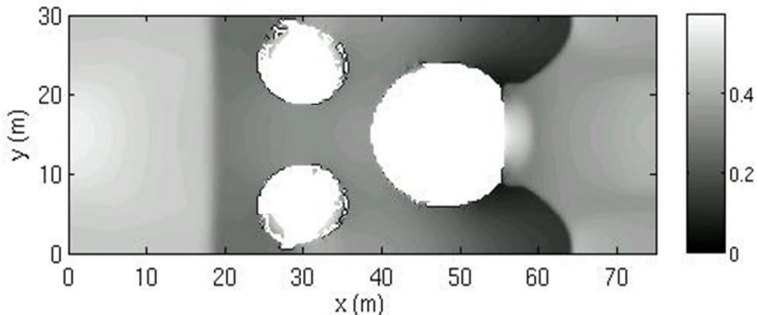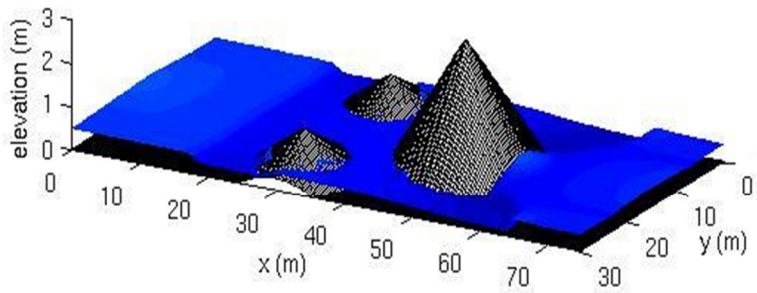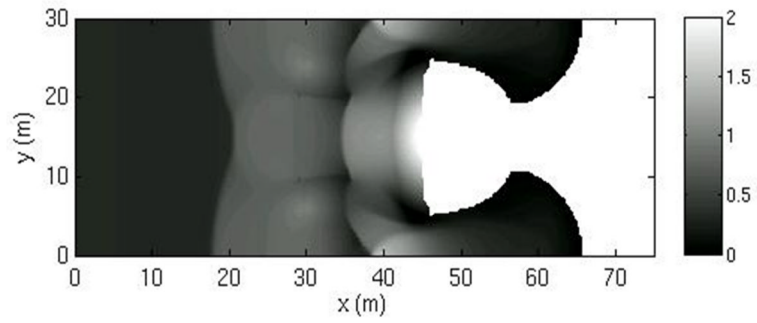
Figure 3.20 3D water surface and water contour at t=3 s, 6 s, 12 s, 30 s and 100 s

3.6 Concluding Remarks

This Chapter presents a 2D shallow water model with a robust HFM source term treatment and an easy-implemented wetting/drying method for flows over irregular bed topography. The HFM source term treatment method incorporates the bed slope term into the flux gradient, which automatically maintains the flux balance. A second-order TVD-WAF finite volume scheme is applied to solve the governing equations. The proposed model is verified by several benchmark tests and experimental results from the EU CADAM project. The proposed numerical scheme has the following advantages and robust characteristics:

- it is straightforward to implement,
- it copes with discontinuous or vertical bed topography as a matter of course without any special treatment,
- it is applicable to both steady and unsteady shallow water flow problems over complex irregular topography.

Chapter 4
One-dimensional Hydro-Morphodynamic Model

This chapter is the core of the thesis. A layer-based hydro-morphodynamic model in one dimension is built on the robust hydrodynamic model proposed in Chapter 3. A series of experimental tests is used to validate the model.

4.1 Model System

4.1.1 Introduction

As discussed earlier, in general, sediment transport is catalogued into three modes: wash load transport, suspended load transport and bed load transport. However, in reality, the sediment transport regime is closely related to flow properties and the type of sediment material [27], and the complexity of the flow and the bed makes them hardly independent; it is also a big challenge to distinguish between them. Which mode of sediment transport is dominant continually changes with the magnitude of flow intensity. Thus, a commonly-seen mode is so-called 'mixed load' [11, 15] which further involves suspended dominant load and sheet flow load. The sheet flow load is conventionally referred to as bed-load transport at high bottom shear stress for which sediment transport occurs in a layer near the bed with a thickness of several times sediment grain size. The mechanisms for each modes are different. Several types of morphodynamic models that attempt to describe sediment transport mechanism have appeared in the literature. These can be divided into four types:

(1) The first type is the capacity model. The most representative being the SWE-Exner-based model [47, 48, 80]. This approach is based on the assumption that the sediment transport rate is equal at any time to the sediment transport capacity. This method is inherently likely to cause issues with modelling accuracy because there are spatial and temporal lags for sediment transport to adapt to the local flow conditions [53, 88, 89]. In other words, the equilibrium conditions are not found until the fluid shear stress at the bed reaches the threshold value, but when the entrainment rate of bed particles into the sheet flow layer equals the deposition rate of sediment particles onto the bed, which is a dynamic equilibrium process at the bed rather than a static one.

(2) The second type is the two-layer transport model. The initial two-layer model [45] assumes the velocity of the clear water layer and sheet flow layer to be unique and sediment concentration in sheet flow layer to be constant. Later, the two-layer model was improved by assuming two distinct velocities and treating the two layers separately by use of two groups of mass and momentum equations [37, 160]. The two-layer model provided new insights into sediment transport in outburst flows: however, the limitation of them is that they assume the concentration in the sheet flow layer to be constant and in applications solving for several governing equations in two-dimensions is rather complex.

(3) The third type is the two-phase sheet flow model [95, 100, 161]. The two-phase model is attractive for predicting wave-generated sediment transport characteristics in the coastal zone, such as sediment flux, sediment concentration and sediment/fluid velocity variations. Yet, the development of two-phase morphodynamic model are still in the infancy; and the solution time of practical sediment problems for the two-phase flow model is quite expensive even in the not-so-near future [94].

(4) The fourth type is non-capacity model [12, 16, 53, 88] which is increasingly attractive and appropriate for predicting the morphological change caused by flows, but for some situations of sheet flow, a conventional empirical bedload equation is usually used without consideration of bed slope effects or unstable bed slope avalanching. Many models have not been sufficiently validated and nor tested against a large-scale flood event.

It is necessary to construct a reasonable conceptual model suitable for the application targets. According to the catalogue of sediment transport mentioned above, the corresponding sediment transport models are presented, including: STM1 layer-based sheet flow model which assumes bedload is the primary role inducing the morphological changes; STM2 suspended-load dominant model; STM3 coupled model of sheet flow and suspended load. The three sediment transport sub-models are packaged into the sediment transport module for the different application objectives and they are tested and validated by a series of laboratory experiments.

4.1.2 Layer-based Conceptual Model

The morphodynamic model is developed based on the shallow water theory. Therefore, the hydrodynamic module, the sediment transport module and the bed deformation module are packaged to form the model system.

- Hydrodynamic module: this is governed by the 2D shallow water equations. This considers the mass and momentum exchange of flow and bed.
- Sediment transport module: this module is the core of the whole model system since it determines the style of geomorphic change. As discussed above, sediment transport is a complex process with different regimes. Therefore, a flexible sediment transport model (STM1, STM2, STM3) is proposed to encapsulate various sediment transport modes.
- Bed deformation module: geomorphic change occurs due to the entrainment of deposition of bed material. Thus, the update of bed elevation is governed by an equation with various closure laws to describe sediment transport.
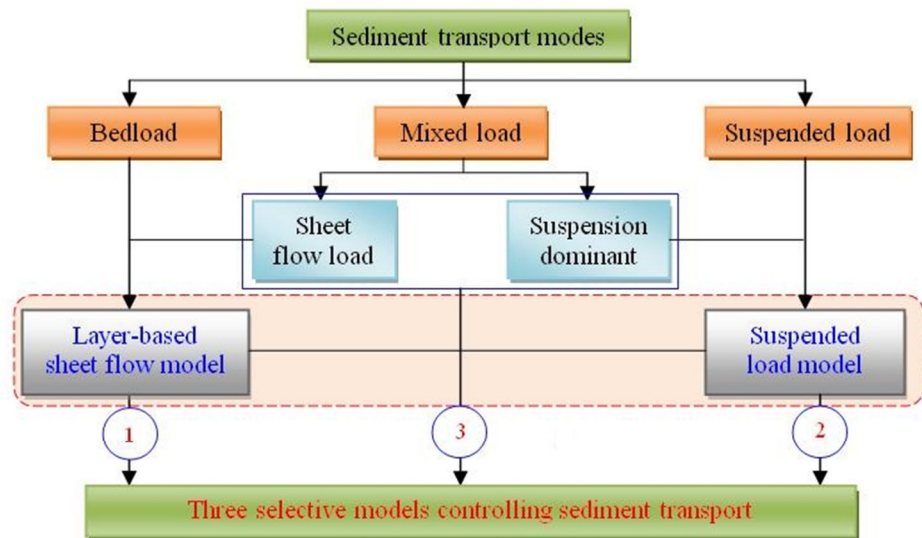
Figure 4.1 Model System of Multiple Object-oriented Application
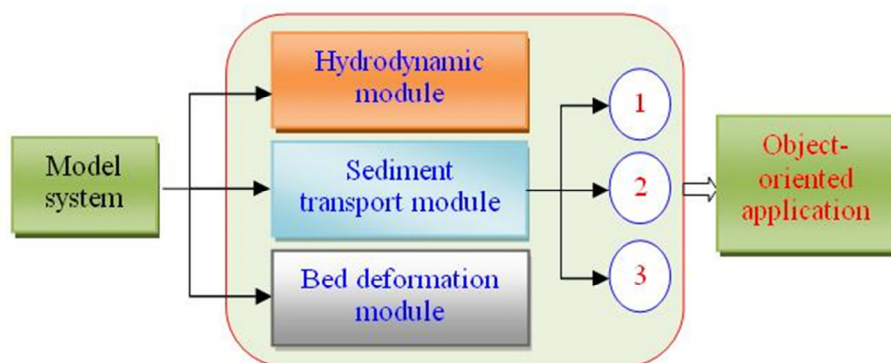
Figure 4.2 Model system framework

For rapid outburst floods, bedload seldom occurs solely as a result of the high bed shear stress, but bed material load which interacts with bed imposes a significant impact on geomorphic changes. The bed material-

water mixture is considered as bedload dominant sheet flow which indicates a situation where the sediment flow in a layer near the bed has a thickness much larger than the grain size, where bedload plays a significant role [40]. Following the research discussed in previous chapters, it was highlighted by several small-scale experimental and field observations [12, 40, 41] that bedload dominant sheet flow usually occurs in a separate layer within the flow. In order to represent the flow characteristics as real as possible, a layer-based conceptual model is adopted in this model system.
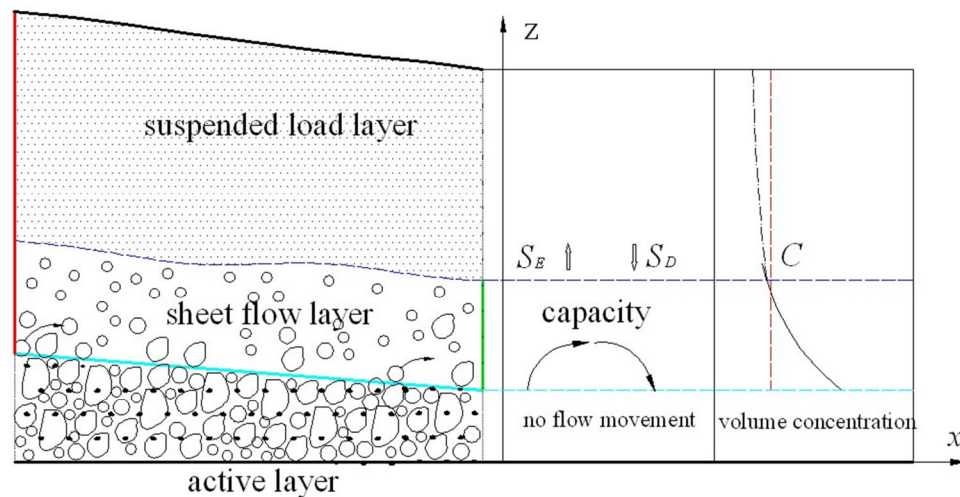
Figure 4.3 Schematic drawing longitudinal direction with movable layer

The lowest layer is called the active layer. In this layer, no flow or sediment movement longitudinally occurs. However, this layer is the active bed which provides bed material to move and accepts the settling sediment particles. The final geomorphic change is also represented by the bed deformation of this layer. In this layer, only mass exchange is considered, so the volume concentration of sediment is assumed to be a constant which does not vary in time or space.

Above the active layer, the bed material load entrained from bed transports in a certain layer near the bed which has a thickness much larger than several times the grain size. It is known as the sheet flow layer where the hydraulic features are different from those of conventional bed load transport. In this layer, the sediment particles move longitudinally by sliding, rolling and hopping over the bed, and some transport temporarily in suspension in case of very high energy flows. The collisional effects between particles and oscillation of flow are very intense in this layer. As the bed material is entrained from the active layer, the volumetric concentration

of sediment in this layer is lower than the sediment porosity. Also in this layer, sediment particles are mainly comprised of coarse particles together with an amount of fine sediment.

In the upper layer, there is a region with clear water or relatively low concentration of sediment and where flow stresses dominate over collisional ones between sediment particles. In this layer, sediment particles are usually fine, so that they are being conveyed in suspension and the longitudinal motion of the sediment is prevailing over the vertical motion due to turbulence fluctuation and particle fall-velocity. We call this the suspended load layer, in which sediment concentration is smaller than that of sheet flow layer. However, the velocity of suspension layer is approximately equal to flow velocity, which is larger than that of sheet flow layer. It is not straightforward to determine a clear interface boundary between sheet flow and suspended load layer. However, the entrainment and deposition of sediment particles do occur between the interface of the two layers. In general, the sediment of the suspension layer is mainly composed of fine particles and light sediment which are supported in suspension by buoyancy force and turbulence drag.

Based on the consideration outlined above, a model framework with three sediment transport models will be presented, such that for applications it would be possible to select an appropriate model that could be reasonable be expected to simulate the application targets.

4.1.3 Model Assumptions

The flow-sediment interaction in practical engineering problems is a rather complex process which is characterized by turbulence, free surface variation, bed change, phase interaction, etc.; therefore it is impossible to include all the hydraulic and sedimentary effects accurately in the model. It is claimed here that several assumptions are adopted when developing the model system.

1) The objective is to solve the geomorphic change caused by flooding, so the sediment transport mode is considered as non-cohesive bed material load (sheet flow) including bedload and a portion of suspended transport. For the cases including fine particles at high bottom shear stress, a suspended load model is further added. As wash load of very fine particles does not have significant influence on geomorphic change, it is neglected in this work.

2) The bulk effects of sediment collision, and the interactions among different gain-size classes are ignored.

3) The turbulence terms in the governing equations is ignored because of the effects of them on morphological change are not significant.

4) The flow is calculated assuming a "fixed" bed at each time step, as the time scale of bed change is much larger than that of flow motion.

5) Empirical functions for sediment transport capacities, channel roughness coefficients, entrainment and deposition rate of sediment, etc. are adopted to close the computational model.

4.2 Construction of 1D Morphodynamic Model

4.2.1 STM1: Bedload Dominant Sheet Flow Model

The governing equations of hydrodynamic model include: mass conservation and momentum conservation equations of the whole mixture flow region and mass conservation equation for sediment in the sheet flow layer; morphological changes are governed by the bed evolution equation. Therefore, the hydrodynamic model is given by the 1D shallow water equations including the mass conservation equation and momentum conservation equation. As sediment transport can influence flow propagation, the mass and momentum exchange between flow phase and sediment phase and bed level change are accounted for in the hydrodynamic equations. These are

$$\frac{\partial \rho h}{\partial t} + \frac{\partial \rho h u}{\partial x} = -\rho_0 \frac{\partial z_b}{\partial t} \tag{4.1}$$

$$\frac{\partial \rho h u}{\partial t} + \frac{\partial}{\partial x} \rho \left(h u^2 + \frac{1}{2} g h^2 \right) = \rho g h (S_{ox} - S_{fx}) \tag{4.2}$$

$$\frac{\partial h_b C_b}{\partial t} + \frac{\partial (h_b u_b C_b)}{\partial x} = -\frac{(q_b - q_{b*})}{L} \tag{4.3}$$

$$(1 - p) \frac{\partial z_b}{\partial t} = \frac{(q_b - q_{b*})}{L} \tag{4.4}$$

where, p= the porosity of sediment material

ρ_w = the density of water (kg/m^3)

ρ_s = the density of sediment particle (kg/m^3)

$\rho = \rho_w(1-S_b) + \rho_s S_b$ = the density of sediment and water mixture (kg/m^3)

$\rho_0 = \rho_s(1-p) + \rho_w p$ = the density of saturated bed (kg/m^3)

C_b=the volumetric concentration in sheet flow layer

u= average flow velocity (m/s)

h_b = the thickness of sheet flow layer (m)

q_b = real sediment transport rate (m²/s)

q_{b*} = sediment transport capacity (m²/s)

L = non-equilibrium adaptation length of sediment transport (m)

In the whole flow region, the real transport rate can be expressed by

$$h_b u_b C_b = hu S_b \ \rightarrow \ h_b C_b = \frac{u}{u_b} h S_b = \beta h S_b \tag{4.5}$$

where $\beta = u/u_b$ is flow-to-sediment velocity ratio; S_b= bedload volumetric concentration in total depth. Eq.(4.5) is substituted into Eq.(4.3) which is then expanded. Eq.(4.3) is replaced by

$$\frac{\partial h S_b}{\partial t} + \frac{1}{\beta} \frac{\partial hu S_b}{\partial x} = -\frac{1}{\beta} \frac{(q_b - q_{b*})}{L} - h S_b \frac{1}{\beta} \frac{\partial \beta}{\partial t} \tag{4.6}$$

Here, the change of the β is insignificant, so it is considered to be zero. Thus $\partial \beta / \partial t \approx 0$. Also, the relationship $\rho = \rho_w(1-C) + \rho_s C$ and $\rho_0 = \rho_s(1-p) + \rho_w p$ are substituted into Eq.(4.1) which is then expanded. Then, Eq.(4.4) and Eq.(4.6) are substituted into the expansion of Eq.(4.1), the following approximate equation can be derived.

$$\frac{\partial h}{\partial t} + \frac{\partial hu}{\partial x} = -\frac{\partial z_b}{\partial t}$$
$$\frac{\partial \eta}{\partial t} + \frac{\partial hu}{\partial x} = 0 \tag{4.7}$$

where $\eta = h + z_b$ = water elevation (m).

Eq.(4.2) is expanded and re-formulated by substituting Eq.(4.6) and Eq.(4.7) into it. The converted approximate momentum conservation equation is rewritten as

$$\frac{\partial hu}{\partial t} + \frac{\partial}{\partial x}\left(hu^2 + \frac{1}{2}gh^2\right)$$
$$= gh(S_{ox} - S_{fx}) + \frac{\Delta\rho u}{\rho} \frac{\partial z_b}{\partial t}\left(\frac{1-p}{\beta} - S_b\right) - \frac{\Delta\rho gh^2}{2\rho} \frac{\partial S_b}{\partial x} - S_A \tag{4.8}$$
$$S_A = \frac{\Delta\rho u}{\rho}\left(1 - \frac{1}{\beta}\right)\left[S_b \frac{\partial hu}{\partial x} - hu \frac{\partial S_b}{\partial x}\right]$$

where $\Delta\rho = \rho_s - \rho_w$

S_A = additional momentum transfer term related to the velocity difference between sediment and flow.

The last three source terms represent the interaction effects of sediment and water flow and momentum transfer due to sediment exchange. For non-uniform sediment, the bed consists of several sediment size classes. Hence, the mass conservation equation of the ith size class in sheet flow layer Eq.(4.6) is rewritten as follows

$$\frac{\partial h S_{bi}}{\partial t} + \frac{1}{\beta}\frac{\partial h u S_{bi}}{\partial x} = -\frac{1}{\beta}\frac{(q_{bi} - F_i q_{b*i})}{L_i} \qquad (4.9)$$

where F_i = the proportion of the ith fraction bedload grain-size fraction

q_{bi} =the real transport rate of ith size fraction

q_{b*i} = the bed load transport capacity of ith size fraction

S_{bi} =the volumetric concentration of ith size fraction

Likewise, the bed deformation for the ith size class is rewritten as

$$\frac{\partial z_b}{\partial t} = \sum_{i=1}^{N}\left(\frac{\partial z_b}{\partial t}\right)_i = \frac{1}{(1-p)}\sum_{i=1}^{N}\frac{(q_{bi} - F_i q_{b*i})}{L_i} \qquad (4.10)$$

4.2.1.1 Determination of Closure Relationships

For the model system, the four governing equations Eq.4.7, Eq.4.8, Eq.4.9 and Eq.4.10 have 8 variables; therefore, it is necessary to close the system with appropriate relationships. The closure variables are: friction slope, velocity ratio of flow and sediment; non-equilibrium adaptation length and sediment transport rate. The frictional slope is usually determined by the empirical equation based on Manning's roughness n which is expressed as

$$S_f = \frac{n^2 u|u|}{h^{4/3}}$$

Usually, a spatial and temporal lag between water and sediment exists, so the sheet flow velocity is smaller than mixture flow velocity, $\beta \geq 1$, which has also been observed through small-scale experiments. Indeed, it is difficult to determine the ratio coefficient. In this Chapter, the approximate velocity ratio β is estimated according to the equation proposed by [115] for the weak sediment transport; for severe sediment transport, β is set to be equal to 1. The equation used in this paper is expressed by

$$\frac{1}{\beta} = \begin{cases} \dfrac{u_b}{u} = \dfrac{u_*}{u}\dfrac{1.1(\theta/\theta_{cr})^{0.17}[1 - exp(-5\theta/\theta_{cr})]}{\sqrt{\theta_{cr}}} & \theta/\theta_{cr} < 20 \\ 1 & \theta/\theta_{cr} \geq 20 \end{cases} \qquad (4.11)$$

where θ = the dimensionless bed shear stress

θ_{cr} = the critical bed shear stress

The non-equilibrium adaptation length L of sediment transport has been investigated by many researchers [28, 31, 89, 114, 115] and still warrants further study. In this paper, the following equation is used to calculate the adaptation length based on previous research [28, 31, 115].

$$L = \frac{hu}{\gamma\omega}$$

where ω is the setting velocity of a single sediment particle, which is determined by van Rijn's equation [123]; γ is an empirical coefficient which is proposed semi-empirically by some authors [28, 115]. Physically, γ represents the ratio of near-bed concentration and depth-average concentration, and the near-bed concentration must not be larger than (1-p), thus, according to Eq. 5, γ is expressed by

$$\gamma = \min\left(\frac{C_b}{C}, \frac{1-p}{C}\right) = \min\left(\frac{u}{u_b}\frac{h}{h_b}, \frac{1-p}{C}\right) = \min\left(\frac{1}{\beta}\frac{h}{h_b}, \frac{1-p}{C}\right)$$

Several researchers have investigated the height of the sheet-flow layer [40, 162, 163], which leads to the conclusion that $h_b=\mu\theta D_{50}$; where μ is a dimensionless coefficient ranging from 6 to 12 that is related to sediment material and that depends on sediment setting velocity; its value is determined here based on previous results in the literature. Therefore, the non-equilibrium adaptation length L is finally calculated by

$$L = \frac{hu}{\gamma\omega} = \max\left[\frac{\beta h_b u}{\omega}, \frac{huC}{(1-p)\omega}\right] \tag{4.12}$$

The sediment transport rate in the sheet flow layer is mainly based on the bottom shear stress. In other words, when bottom shear stress exceeds the threshold value, sediment particles start to move. The bedload transport rate is represented as a function of the non-dimensional Shields parameter θ; many relationships have been proposed for the bedload transport rate, one of which is the commonly used relationship of Meyer-Peter & Müller [26] (denoted as *MPM* in the following) which is expressed by:

$$q_{b*} = 8(\theta - \theta_{cr})^{1.5}\sqrt{(s-1)gd_{50}^3} \tag{4.13}$$

The application ranges of the *MPM* equation are: bedload transport; bed slope ranges from 0.0004 to 0.02 and Shields number smaller than 0.25 [26], therefore, it might be open to question for application to outburst flow

cases or steep bed slope cases. In this study, *MPM* is applied only for bed slope of <0.03. With respect to a bed slope of ≥0.03, Smart and Jäggi (1983) (denoted as MJ in the following) expanded the database obtained by MPM for the steep slope range 0.03-0.20. They performed flume experiments to estimate the maximum transport capacity of mountain streams by the equation below. Therefore, for the case of bed slope>0.2, It is approximately assumed that the maximum bed slope S_{max} to be 0.2 in the equation to avoid the calculated transport rate becoming unphysically large due to passing beyond the bed slope limit. The slightly modified equation is written as:

$$q_{b*} = 4\left(\frac{d_{90}}{d_{30}}\right)^{0.2} \frac{h^{1/6}}{n\sqrt{g}} \min(S_o, 0.2)^{0.6} \theta^{0.5}(\theta - \theta_{cr})\sqrt{(s-1)gd_{50}^3} \qquad (4.14)$$

However, both transport equations are for bedload transport, and some authors [14, 54] suggested or modified the "8" in original *MPM* by increasing or multiplying a factor for application at high shear stress conditions (e.g. larger than 1), where the entrainment rate of sediment particles is larger than estimated by use of the *MPM* empirical equations. Therefore, a calibrated coefficient η is added to the original *MPM* Eq.(11) which is a Shields stress-dependent coefficient (approximately 1.0~4.0). Further, for the cells of hard beds where bed materials are non-erodible, the transport rate is assumed to be zero, so only deposition occurs in such cells.

4.2.1.2 Multiple-size Fractional Transport Rate

For refined sediment transport investigations, sediment transport rate in sheet flow layer is calculated by size fractions instead of the whole sediment mixture. Therefore changes in the grain size distribution due to selective transport equation are considered. Further, based on the description in Section 4.2, the sediment transport rate in each size fraction is calculated by the following modified version of Eq.(4.11) and (4.12), which are applied in this study (abbreviated as *M_MPM* and *M_SJ* in the following).

$$q_{b*i} = \psi 8\left(\theta_i - \theta_{cr,i}\right)^{1.5}\sqrt{(s-1)gd_{50}^3} \quad 0 \le S_o < 0.03 \ (M\_MPM)$$

$$q_{b*i} = \frac{4}{s-1}\left(\frac{d_{90}}{d_{30}}\right)^{0.2} \min(S_o, 0.2)^{0.6} \theta_i^{0.5}\left(\theta_i - \theta_{cr,i}\right)\sqrt{(s-1)gd_{50}^3} \ S_o \ge 0.03 \ (M\_SJ)$$

where $d_{50,i}$ = the median sediment diameter of *i*th fraction (m)

$\theta_{cr,i}$ = a critical Shields parameter of *i*th fraction

θ_i = the dimensionless bed shear stress of ith fraction.

The total bedload transport rate is calculated by

$$q_{b*} = \sum_{i=1}^{N} F_i q_{b*i} \tag{4.15}$$

4.2.2 STM2: Suspended Load Transport

For the fine particles at high bottom shear stress, sediment particles may be entrained into suspension if the lift forces exceed the grain weight or bed shear stress exceeds the suspension critical stress, e.g. suspension occurs for silt or fine sand, and for relatively coarse sand under the condition of high-energy outburst flows. The governing equation is simplified advection-diffusion equation expressed by

$$\frac{\partial h S_i}{\partial t} + \frac{\partial h u S_i}{\partial x} = G_i S_{E,i} - S_{D,i} \tag{4.16}$$

where S_i = volumetric suspended load concentration of the i th class

G_i = the proportion of the i th suspension grain-size fraction

$S_{E,i}$ = entrainment flux of sediment of the i th class

$S_{D,i}$ = deposition flux of sediment of the i th class

As mentioned above, for the suspended load dominant transport, the entrainment rate and deposition rate of sediment are vital; however, a complete theoretical expression does not exist (and is probably impossible to determine precisely). When the interface between the sheet flow layer and suspended-load layer is assumed to be at a reference level a, then the deposition flux is represented as the product of effective sediment settling velocity and the near-bed concentration at reference level $S_D=\omega_f C_a$. Therein $C_a =\delta C$ is the near-bed concentration at the reference level a. The coefficient δ definition of Cao et al. (2004) [11] is used as $\delta = \min\{2.0, (1-p)/C\}$. The entrainment rate of sediment is assumed as $S_E=\omega_f C_{ae}$, where C_{ae} is the near bed equilibrium concentration at the reference level determined by using the empirical equation of van Rijn (1984) [123].

$$C_{ae} = 0.015 \frac{d_{50}}{a} \frac{T^{1.5}}{d_*^{0.3}}$$

$$T = \frac{(u_*^2 - u_{*,cr}^2)}{u_{*,cr}^2}; a = \min[\max(\mu \theta_i d_{50}; 2 d_{50}; 0.01h), 0.2h]$$

where $d_*=d_{50}[(s-1)g/v^2]^{1/3}$ is the dimensionless particle diameter; $u_* = (g^{0.5}/C')u$ is bed-shear velocity related to grain; C' is the Chézy-coefficient related to grain; $u_{*,cr}$ is the critical bed-shear velocity.

4.2.3 STM3: Total Sediment Transport

For total sediment transport where both sheet flow and suspended load are equally important, a mass governing equation for total sediment transport (Eq.4.17) is used based on reformulating Eq.(4.9) and Eq.(4.16). The sediment concentration on the left hand of Eq.(4.17) is replaced by a total volumetric sediment concentration T. The external sediment source terms on the right hand are calculated by the entrainment flux and deposition flux for bedload and suspended load.

$$\frac{\partial hT_i}{\partial t} + \frac{\partial huT_i}{\partial x} = -\frac{(q_{bi} - F_i q_{b*i})}{L_i} + G_i S_{E,i} - S_{D,i} \qquad (4.17)$$

4.2.4 A Flexible Mode

The three models of Eq.(4.9), Eq.(4.16) and Eq.(4.17) could be integrated into a flexible mode as

$$\frac{\partial hC_i}{\partial t} + \alpha \frac{\partial huC_i}{\partial x} = -\alpha \frac{(q_{bi} - F_i q_{b*i})}{L_i} + G_i S_{E,i} - S_{D,i} \qquad (4.18)$$

where

$$C_i = \begin{cases} S_{bi} & for\ \text{STM1} \\ S_i & for\ \text{STM2} \\ T_i & for\ \text{STM3} \end{cases}; \quad \alpha = \begin{cases} 1/\beta & for\ \text{STM1} \\ 1 & for\ \text{STM2} \\ 1 & for\ \text{STM3} \end{cases}$$

C_i is the volumetric sediment concentration, α is the velocity ratio. $S_{E,i}$, $S_{D,i}$ will be calculated as zeros in absence of suspended load, and q_{bi}, q_{b*i}, L_i are zeros in absence of bedload.

The mass and momentum conservation equations (4.7) and (4.8) are re-written by replacing the flexible sediment concentration $C = \sum_{i=1}^{N} C_i$.

$$\frac{\partial \eta}{\partial t} + \frac{\partial hu}{\partial x} = 0 \qquad (4.19)$$

$$\frac{\partial hu}{\partial t} + \frac{\partial}{\partial x}\left(hu^2 + \frac{1}{2}gh^2\right)$$

$$= gh(S_{ox} - S_{fx}) + \frac{\Delta\rho u}{\rho}\frac{\partial z_b}{\partial t}[\alpha(1-p) - C] - \frac{\Delta\rho gh^2}{2\rho}\frac{\partial C}{\partial x} - S_A \qquad (4.20)$$

$$S_A = \frac{\Delta \rho u}{\rho}(1-\alpha)\left[C\frac{\partial hu}{\partial x} - hu\frac{\partial C}{\partial x}\right]$$

4.2.4 Morphological Change Model

The erosion and deposition is calculated per grid cell at each time step to update the new bed elevation on the basis of the results from the previous hydrodynamic model and sediment transport models. So the morphological evolution for non-uniform sediment material is calculated by the following equation which is reformulated by the bed deformation equation (4.9).

$$\frac{\partial z_b}{\partial t} = \sum_{i=1}^{N}\left(\frac{\partial z_b}{\partial t}\right)_i = \frac{1}{(1-p)}\sum_{i=1}^{N}\left[\frac{(q_{bi} - F_i q_{b*i})}{L_i} + \left(S_{D,i} - G_i S_{E,i}\right)\right] \qquad (4.21)$$

For STM2, the first term in the left of Eq.(4.18) will be diminished, the second term is treated as zero for bedload model STM1. Both are kept for STM3.

4.2.5 Bed Material Gradation

As above, the coefficients F_i, G_i represents the proportions of ith bedload and suspension grain-size fraction in total moving sediment. They vary with time. So the coefficients should be updated at each time step. This is so-called bed material gradation which is an essential process for non-uniform bed aggradation and degradation. Among to the classified layers, the active layer participates in the exchange with moving sediment. There are several bed material sorting models available in the literature. The approach presented by [31, 164] was adopted to address the sorting of bed material.

4.2.6 Threshold for Incipient Motion

As mentioned in Section 3.2 of Chapter 3, with consideration of hiding and exposure effects of coarse particles and bed slope effects, the critical Shields stress is calculated by

$$\theta_{cr} = k_1 k_2 \theta_c \qquad (4.22)$$

where $k_1 = (d_{90}/d_m)^{2/3}$ = the coefficient corresponding to hiding/exposure effect

k_2 = the coefficient related to bed slope effect determined by Eq.(3.13)

The critical dimensionless bed shear stress is calculated by the relationship of Soulsby (1997) [27].

$$\theta_c = \frac{0.30}{1 + 1.2d^*} + 0.055[1 - \exp(-0.02d^*)] \qquad (4.23)$$

4.2.7 Bed Avalanching Model

If the slope angle of a non-cohesive bed becomes larger than the critical angle of bed slope, the bed material will slide or avalanche to form a new slope approximately equal to the critical value. The unstable bed avalanching model proposed in section 2.4 of Chapter 2 is applied in the morphodynamic model.

4.3 Numerical Solution

Eqs. (4.7), (4.8) and (4.18) constitute a nonlinear hyperbolic system. Currently, a range of numerical schemes has been proposed and can be utilised to solve such hyperbolic system [138]. Here an upwind Godunov-type scheme with a HLL Approximate Riemann Solver is applied to solve the coupled model. The governing equations are rewritten in compact form as follows

$$\frac{\partial \mathbf{U}}{\partial t} + \frac{\partial \mathbf{F}}{\partial x} = \mathbf{S}$$

where $\mathbf{U}$ = a vector of the conservative variables

$\mathbf{F}$ = the flux vector which is the function of conservative variables

$\mathbf{S}$ = the vector of source terms

$$\mathbf{U} = \begin{bmatrix} \eta \\ hu \\ hC_i \end{bmatrix} \quad \mathbf{F} = \begin{bmatrix} hu \\ hu^2 + \frac{1}{2}gh^2 \\ \alpha huC_i \end{bmatrix}$$

$$\mathbf{S} = \begin{bmatrix} 0 \\ gh(S_{ox} - S_{fx}) + \frac{\Delta \rho u}{\rho} \frac{\partial z_b}{\partial t}[\alpha(1-p) - C] - \frac{\Delta \rho gh^2}{2\rho} \frac{\partial C}{\partial x} - S_A \\ -\alpha \frac{(q_{bi} - F_i q_{b*i})}{L_i} + G_i S_{E,i} - S_{D,i} \end{bmatrix}$$

With respect to the discretisation of conservative variables, the shallow water equations are discretised conservatively by using the finite volume method (FVM).

$$\mathbf{U}_i^{n+1} = \mathbf{U}_i^n - \frac{\Delta t}{\Delta x}\left(\mathbf{F}_{i+1/2}^* - \mathbf{F}_{i-1/2}^*\right) + \Delta t \mathbf{S}_i$$

The interface fluxes between the two neighbouring cells are calculated by the HLL scheme expression as follows:

$$\mathbf{F}_{i+1/2}^* = \begin{cases} \mathbf{F}_i & if\ S_L \geq 0 \\ \mathbf{F}_{i+1} & if\ S_R \leq 0 \\ \mathbf{F}^* & otherwise \end{cases}$$

where $\mathbf{F}_i = \mathbf{F}(\mathbf{U}_i)$, $\mathbf{F}_{i+1} = \mathbf{F}(\mathbf{U}_{i+1})$ are the flux and conservative variable vectors at the left and right sides of each cell interface; the S_L, S_R denote two wave speeds which must be selected carefully to avoid any entropy violation; $\mathbf{F}^*$ is the numerical flux in the star region, calculated in two dimensions by

$$\mathbf{F}^* = \frac{S_R \mathbf{F}_i - S_L \mathbf{F}_{i+1} + S_R S_L (\mathbf{U}_{i+1} - \mathbf{U}_i)}{S_R - S_L}$$

The S_L and S_R are estimated by the so-called "two expansion" including dry-bed options. They are expressed by

$$S_L = \begin{cases} \min\left(u_i - \sqrt{gh_i}, u^* - \sqrt{gh^*}\right) & if\ h_i > 0 \\ u_{i+1} - 2\sqrt{gh_{i+1}} & if\ h_i = 0 \end{cases}$$

$$S_R = \begin{cases} \min\left(u_{i+1} + \sqrt{gh_{i+1}}, u^* - \sqrt{gh^*}\right) & if\ h_{i+1} > 0 \\ u_i + 2\sqrt{gh_i} & if\ h_{i+1} = 0 \end{cases}$$

where

$$u^* = \frac{1}{2}(u_i + u_{i+1}) \cdot \mathbf{n} + \sqrt{gh_i} - \sqrt{gh_{i+1}}; \quad \sqrt{gh^*} = \frac{1}{2}\left(\sqrt{gh_i} + \sqrt{gh_{i+1}}\right) + \frac{1}{4}(u_i - u_{i+1})$$

To calculate the inter-cell numerical fluxes, a weighted average flux (WAF) total variation diminishing (TVD) method is employed with a flux limiter function.

$$\mathbf{F}_{i+1/2}^* = \frac{1}{2}(\mathbf{F}_i + \mathbf{F}_{i+1}) - \frac{1}{2}\sum_{k=1}^{N} sign(c_k)\Phi_{i+1/2}^k \Delta \mathbf{F}_{i+1/2}^k$$

where c_k is the Courant number for wave k, $c_k = \Delta t S_k / \Delta x$; S_k is the speed of wave k and N is the number of waves in the solution of the Riemann problem. $N=2$ when applied in conjunction with the HLL approximate Riemann solver. $\Delta \mathbf{F}^{(k)}_{i+1/2} = \mathbf{F}^{(k+1)}_{i+1/2} - \mathbf{F}^{(k)}_{i+1/2}$, which is the flux jump across wave k; $\mathbf{F}^{(k)}_{i+1/2}$ is the value of the flux vector in the interval k; herein $\mathbf{F}^{(1)}_{i+1/2} = \mathbf{F}(\mathbf{U}_L)$, $\mathbf{F}^{(2)}_{i+1/2} = \mathbf{F}(\mathbf{U}^*)$, and $\mathbf{F}^{(3)}_{i+1/2} = \mathbf{F}(\mathbf{U}_R)$ which are estimated by the HLL approximate Riemann solver, $\Phi(r)$ is the WAF limiter function. The WAF limiter used here is the *minmod* limiter expressed by $\varphi(r)$:

$$\Phi(r) = 1-(1-|c|)\varphi(r)\ with\ \varphi(r) = \max[0, \min(1, r)]\ \ (minmod\ limiter)$$

where $r^{(k)}$ is the ratio of the upwind change to the local change in scalar quantity q. It can be written by:

$$r^{(k)} = \begin{cases} \Delta q_{i-1/2}^{(k)} / \Delta q_{i+1/2}^{(k)} = \left(q_i^{(k)} - q_{i-1}^{(k)}\right) / \left(q_{i+1}^{(k)} - q_i^{(k)}\right) & if\ c_k > 0 \\ \Delta q_{i-3/2}^{(k)} / \Delta q_{i+1/2}^{(k)} = \left(q_{i+2}^{(k)} - q_{i+1}^{(k)}\right) / \left(q_{i+1}^{(k)} - q_i^{(k)}\right) & if\ c_k > 0 \end{cases}$$

$q=\eta$ is chosen (water surface elevation) for the left wave S_L (k=1) and the right wave S_R (k=2). For the bed slope source term treatment, the homogenous flux approach is applied here [79]. Figure.4.4 shows the computation procedure at each time step for the morphodynamic model:

(1) input initial hydraulic and sediment information, including flow depth, flow velocity, sediment concentration and bed elevation;
(2) calculate the dimensionless bed shear stress using the information from step (1);
(3) estimate the weight coefficient of bedload transport;
(4) calculate the bedload transport capacity according to the empirical functions and the entrainment/deposition fluxes of suspended load;
(5) solve the model system of Eq.(4.18)(4.19)(4.20) based on the information from above-steps and to update the hydraulic and sediment information;
(6) update the bed elevation calculated by Eq.(4.21);
(7) update the proportions for ith fraction in the total moving sediment;
(8) evaluate the stability of the newly formed bed;
(9) return the step (1) and repeat step (1) to (8).
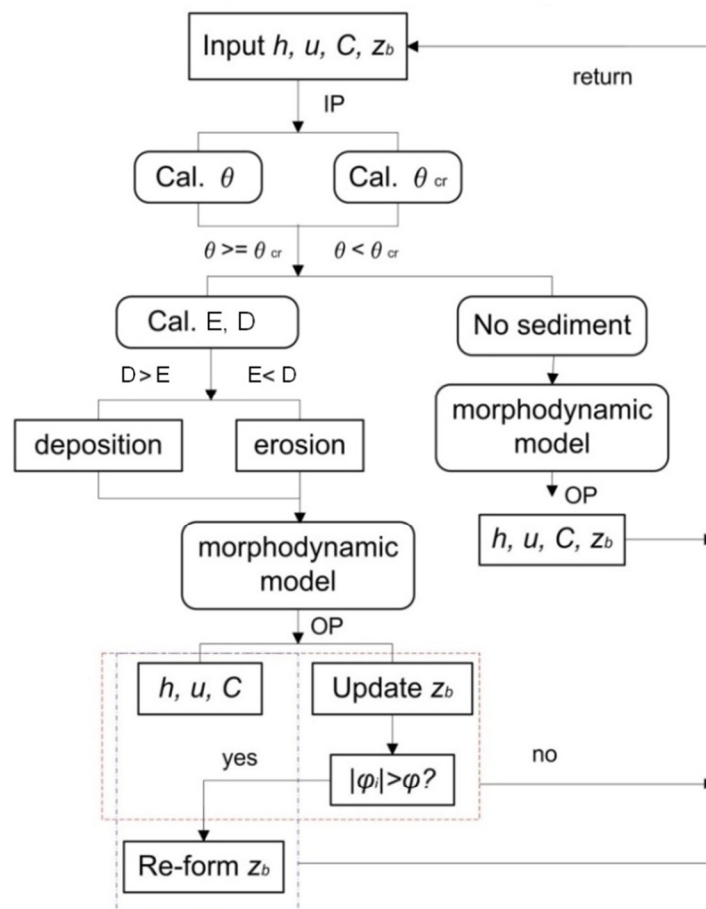
Figure 4.4 Framework of computational procedures

4.4 Validation of 1D Morphodynamic Model

As described above, three sediment transport models were presented in order to solve issues with corresponding sediment transport modes. However, it is really difficult to define a criteria for choosing an appropriate model to use. Here, the models are selected according to the eye evidence of the target experimental events. For a large-scale event, the model is chosen based on an experienced assessment of historic floods, sediment composition and flood velocities.

4.4.1 Sediment Transport in a Trench

This test is to verify the applicability of the suspended load model (STM2). The experiments were originally conducted at the Delft Hydraulics Laboratory to investigate the movable bed evolution caused by steady open channel flow. In the experiments, three tests were investigated with different initial trench profiles in a rectangular flume of 30 m long, 0.5 m wide and 0.7 m deep. Test 3 with a side slope of 1:10 was reproduced here. Figure 4.5(a) illustrates the initial configurations of the trench profiles of Test 3. Furthermore, the initial hydraulic conditions were: the mean inflow velocity was 0.51 m/s at the inlet and the water depth were kept constant as 0.39 m. As for sediment material, the erodible bed was constituted by fine sand with d_{10}=0.115 mm, d_{50}=0.16 mm and d_{90}= 0.2 mm. The sand density was 2,650 kg/m^3; the sand porosity was 0.4; and the settling velocity of sediment particle was 0.013 m/s with a relative error of ±25%; Manning's coefficient n was set to be 0.0124. In addition, to maintain the sediment equilibrium conditions in upstream of the channel (no scour or deposition), sand with the same size and composition was fed at a constant rate of 0.03±0.006 kg/s/m. In this case, the fine sand is only considered to transport as suspended load. The measured data of bed evolution was provided after 7.5 hours and 15 hours. The whole domain was discretised with a space interval Δx=0.2 m and the time step is Δt=0.06 s. In the test, the setting velocity ω_0=0.017. For the reference level in entrainment equation (1), a=0.01 m is verified to be good for maintaining the sediment equilibrium in upstream of the channel. To make the flow to be steady flow, the model is run in 900 s, keeping bed profile to be unchanged. After 900 s, sand is fed and bed evolution starts to occur. Two runs with and without bed slope effects (BSE) were implemented in order to elucidate the effects of bed slope on bed change. Figure 4.5(b)(c) demonstrates the comparisons between the measured and simulated bed profiles after 7.5 hours and 15 hours. It can be seen that the predicted bed

profiles with bed slope effects agree better with the measured bed those without BSE. The bed is overestimated slightly at the bottom for the scenario without BSE. Overall, this reveals that the model system can predict the morphological evolution effectively caused by sediment-laden flow with suspended load dominant transport, and bed slope effects make the model more accurate.
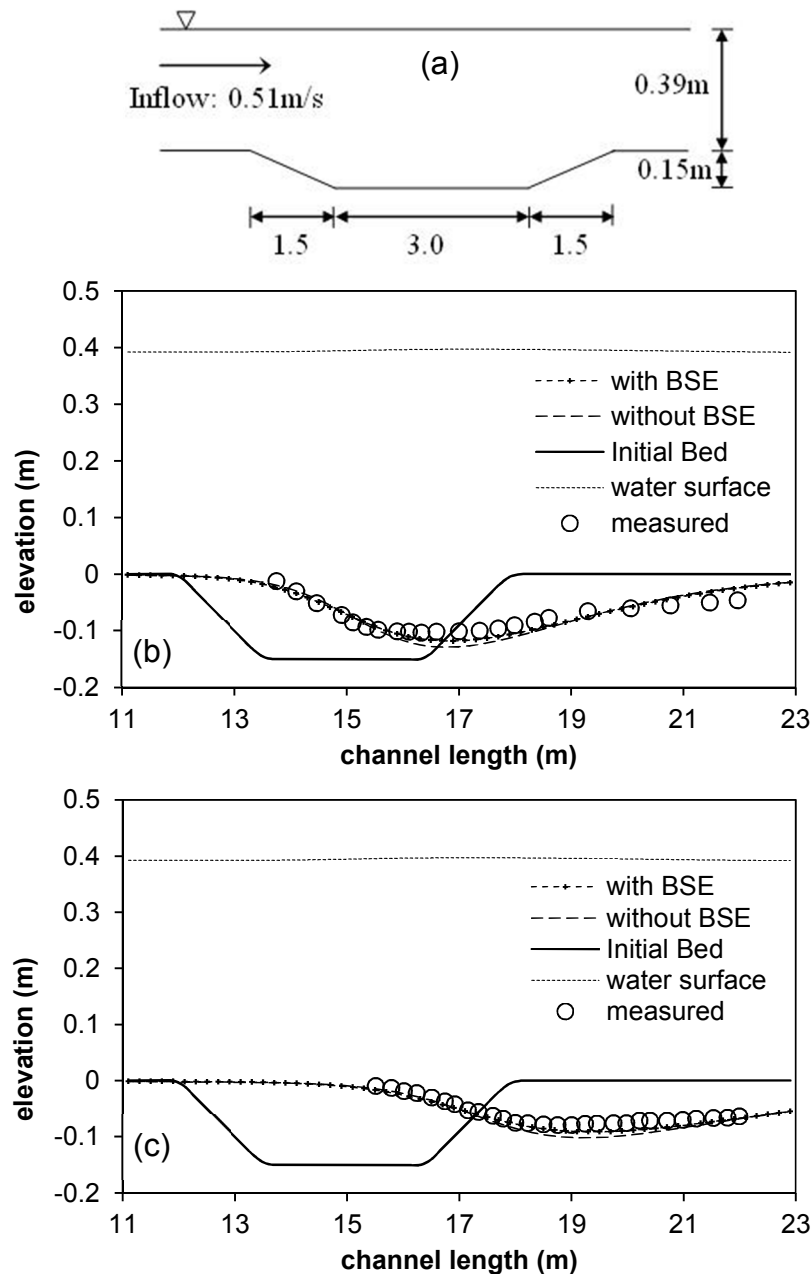
Figure 4.5 (a) initial setup; (b) the measurement and simulation at 7.5 hours; (c) the measurement and simulation at 15 hours

4.4.2 Dam-break Flow over a Movable Bed

In this section, the erosion and deposition processes induced by unsteady outburst flow are reproduced in order to validate the applicability of the

proposed bedload model (STM1). A sand bed and a bed of PVC particles are tested and the simulated results are compared with the measured data.

4.4.2.1 Sand Particles

Dam-break flow over movable bed experiments were conducted in the laboratory of the Civil and Environmental Engineering Department at UCL in Belgium [37, 41]. A horizontal glass-walled flume of 6 m × 0.25 m × 0.70 m rectangular cross-section was used. A thin gate was located at the middle of the flume. The bed material was water-saturated sand with a diameter of 1.82 mm, density of 2,683 kg/m^3, porosity of 0.47 and repose angle of 30°. Different initial conditions were tested by adjusting the initial water depth and the thickness of movable bed upstream and downstream of the gate. In this test, three configurations are simulated. The first one is a dam-break flow over a flatbed with a thickness of 0.125 m for the movable bed, and the water depths before and after the gate are 0.35m and 0m respectively. The second and third configurations consider a dam-break over a movable bed with a downward bed step of 0.1 m and upstream water depth of 0.25 m. Downstream water depth for the second configuration is 0m and for the third configuration it is 0.10 m, see Figure 4.6.
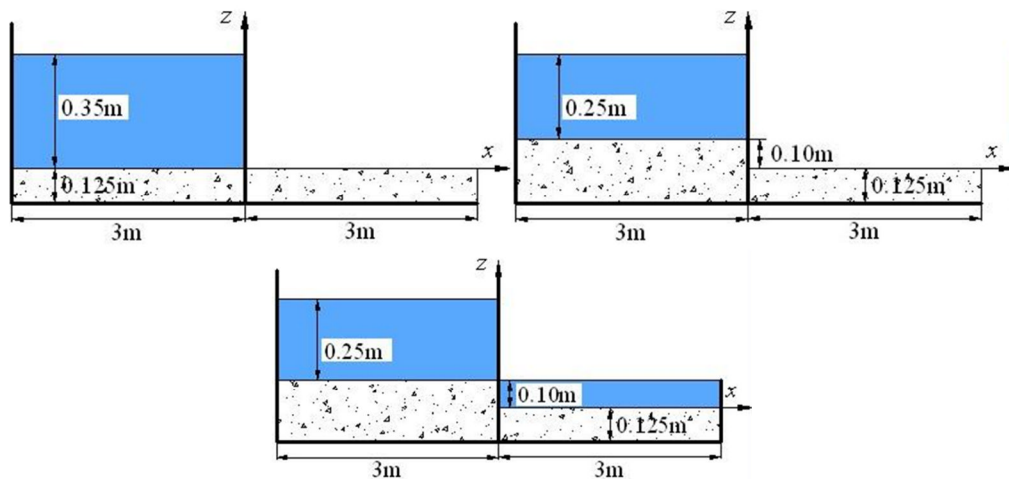
Figure 4.6 Initial experimental dam-break configurations

The channel is discretised with 600 cells in one dimension (dx=0.01m); the Manning's coefficient is set as 0.018 in line with the experimental work. Simulations with and without the inclusion of bed avalanching model are carried out in order to explain the role the unstable bed avalanching plays in the morphodynamic model. The simulated results at t=6.6t_0 are shown in Figure 4.7, where t_0=0.189 s and H_0=0.35 m. The simulated water surfaces and bed profiles are compared with the measured data in Figure 4.7. The comparisons show that the three key factors, water front, water surface and

bed level, are predicted effectively with the inclusion of bed slope avalanching and the simulated results agree well with the measured results. Secondly, from the results with and without the inclusion of bed avalanching model, it can be seen that the simulated bed profiles without bed slope avalanching are underestimated and the erosion and deposition are less severe than the measured bed profiles. This verifies that the reformation of the unstable bed is necessary when carrying out morphodynamic modelling. As demonstrated in Figure 4.7(b, c), the simulated water surface and bed profile without bed slope avalanching are predicted poorly at the vertical step. Finally, there are some small discrepancies in water surfaces and bed change. This is likely to be due to uncertain empirical parameters and energy loss in the experimental case not captured in the model. In summary, the avalanching of an unstable bed slope is vital in a morphodynamic model, the simulated results with the inclusion of bed slope avalanching are acceptable and satisfactory; and the proposed model predicts the morphological process induced by outburst flow with good agreement.
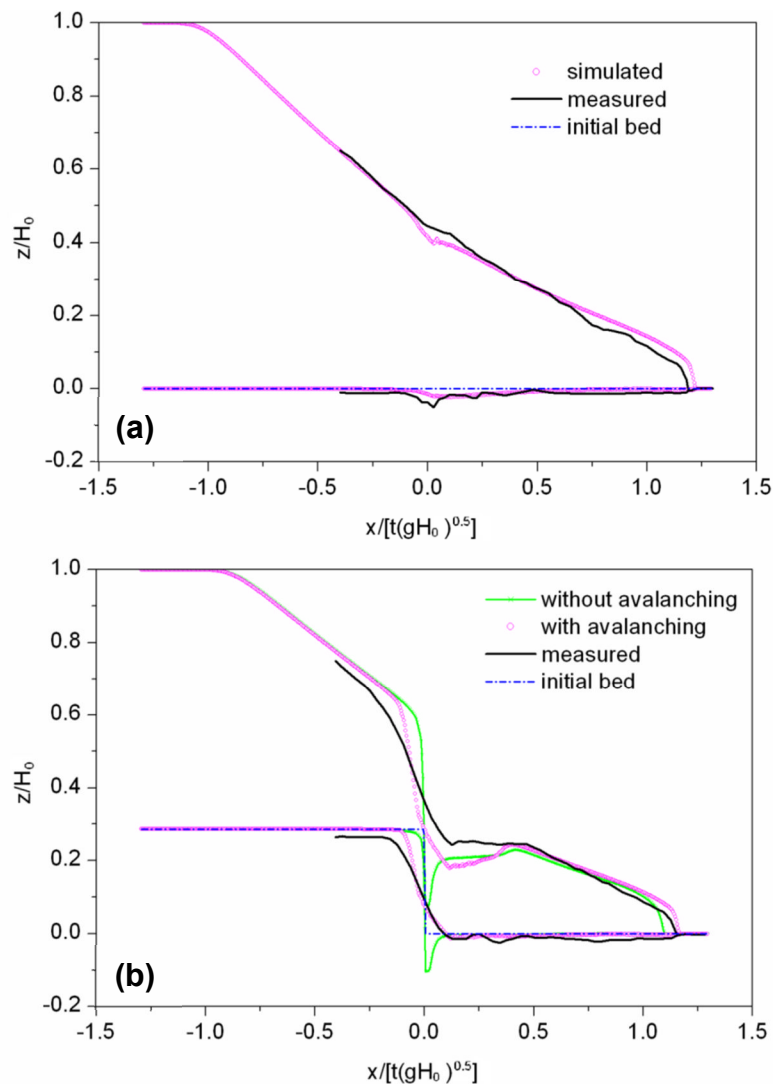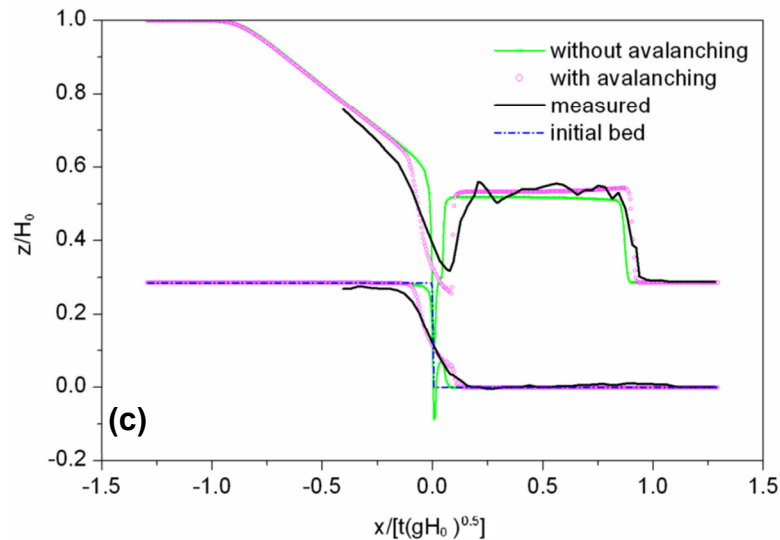
Figure 4.7 Comparison between the simulated results and the experimental data at t=6.6t_0 for the three configurations

4.4.2.2 PVC Particles

In this experiment, also carried out at UCL [13], the sediment particles were cylindrical PVC pellets having an equivalent spherical diameter of 3.5 mm, density of 1,540 kg/m^3 and settling velocity of about 18 cm/s. The experiments were performed in a horizontal prismatic flume with a rectangular cross section of 2.5m×0.1m×0.25m. In this test, bedload is the dominant mode of sediment transport. For the simulation the sediment porosity p is taken as 0.47.

For this test case the 1D solver is used and the computational area is discretised with 200 cells in one dimension (dx=0.0125 m). The experiment was run for 2 s. When the gate is removed, the water front moves rapidly downstream and erodes the bed progressively. A hydraulic jump occurs at the location of the gate where the maximum eroded depth is generated. The comparisons of simulated and measured results are given in Figure 4.8. It is seen that (1) the trend of water surfaces and bed profiles agree well with the measured data; (2) the maximum eroded depth of bed is simulated well; and (3) the hydraulic jump is observed numerically; although the simulated water front is slightly faster than measured data and there is a discrepancy in terms of quantitative comparisons; the reasons are similar to those in the sand bed case. This test shows that the model can address rapid transient bed deformation with good results.
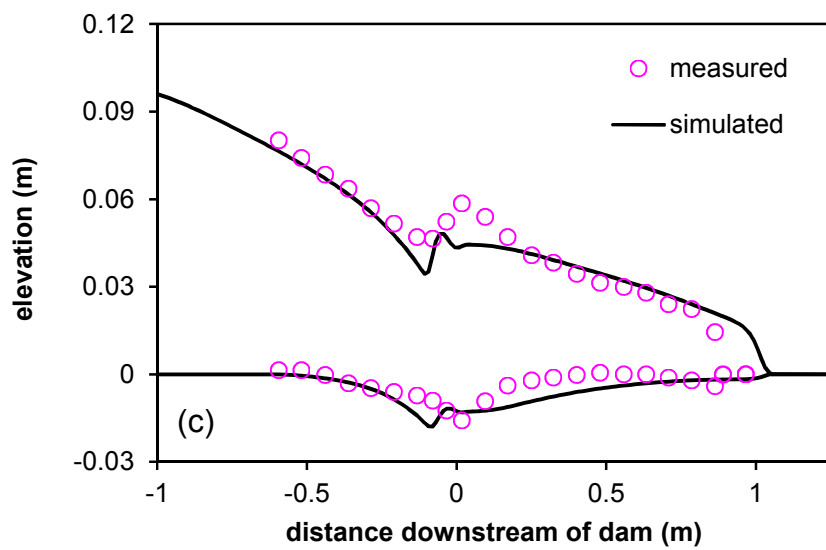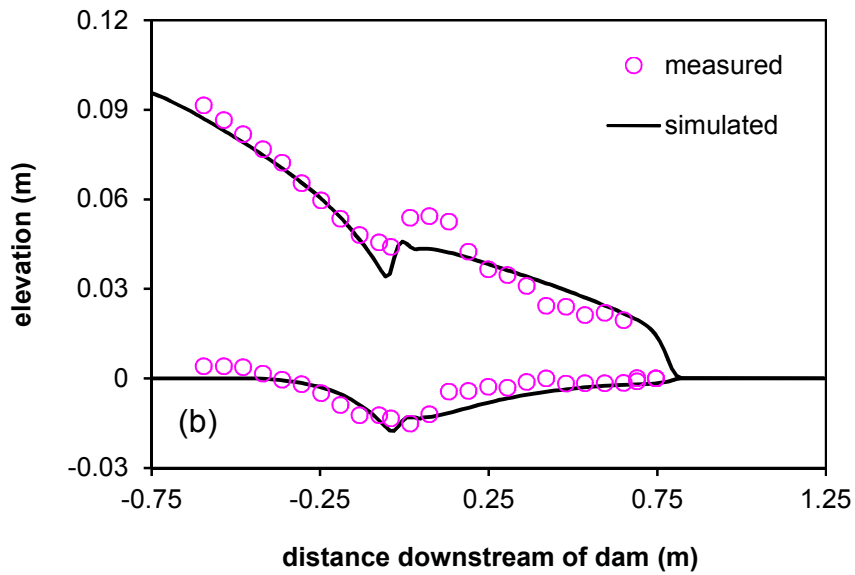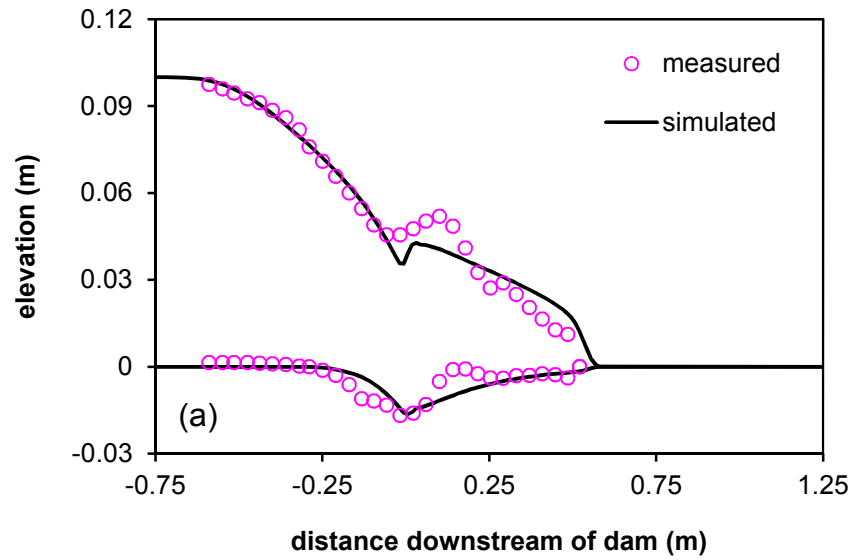
Figure 4.8 Comparison between the simulated and measured data; (a) $t=5t_0$ (b) $t=7.5t_0$ and (c) $t=10t_0$; here $t_0=0.101$s

4.4.3 Sediment Aggradations under Transcritical Flows

This test aims to validate the applicability of the bedload sheet flow model (STM1) in a case where deposition severely occurs. Experiments on wedge aggradation caused by sediment overloading have been performed at the St. Anthony Falls Laboratory by Seal et al. [165]. Compared to the test in Section 4.1, this test is not under conditions of rapid outburst flow and the sediment deposition takes a more important role during the entire experiment. Therefore, this test is considered in order to verify that the model can represent sediment transport in transcritical flow and predict sediment deposition effectively. Run1 from the experiment is reproduced with the model (see Fig.4.9). The experiment was conducted in a rectangular channel of 45 m × 0.305 m, with an initial bed slope of 0.002; the inflow discharge was a constant as 0.049 m^3/s with a sediment feed rate of 0.19 kg/s at 1m downstream of the head gate of the flume. To obtain transcritical flow over the wedge, the tailgate was kept at a constant height as 0.4 m so that a hydraulic jump or a shock wave was produced at the downstream end of the main gravel deposit. The material fed in was a gravel and sand mixture comprising a wide range of sizes from 0.125 to 64 mm and d_{50} = 6 mm; the mixture porosity is 0.3. In line with the experiment, the Manning's n is set as 0.028 and the angle of repose is 32°.
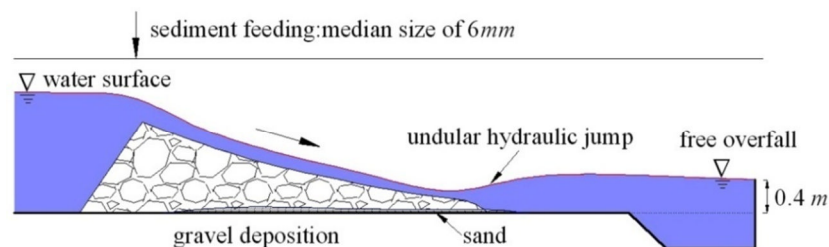
Figure 4.9 Schematic of experiment setup of Seal et al. (1995)

The computational model is run for 16.8 hours of simulated time and the results are illustrated in the following figures. From the point of view of numerical simulation, the whole process includes three stages: (1) at the initial stage, the flow runs into the channel; and then with the feeding of sediment, most parts of gravel are deposited progressively at inlet of channel because they are not easily entrained by the weak slow inflow; (2) after a period, a wedge is formed with a steeper slope which results in an undular hydraulic jump at the end of wedge (see Figure 4.10); (3) with increasing of time, more and more sediment is increasingly deposited, causing the elevation of the wedge and water surface to increase gradually,

and meanwhile the hydraulic jump moves downstream progressively along with the moving wedge front, but the water surface after hydraulic jump remains constant at 0.4 m. In this case, the water surface and deposited bed has a significant feature that a hydraulic jump occurs in the wedge front where the flow transits from Froude number <1 to Froude number>1 and in this location a steeper slope bed is formed. Figure 4.10(a, b, c) shows the comparisons between the measured and predicted bed profiles at t=2 h, 8 h and 16.8 h, as well as a comparison of the water surface at t=16.8 h. It can be seen that the simulated beds and water surfaces agree very well with the measured results, particularly in the early stages; but the simulated bed and water surface profiles at 16.8 h are slightly higher than the measured results. This is likely to be due to energy and momentum losses in the experiment which are neglected by the numerical model; also, the uncertain empirical parameters can cause errors. However, overall, it is clearly shown that the proposed model is capable of predicting the sediment deposition with good agreement and capturing of the hydrodynamic and morphodynamic characteristics in the case of sediment transport under transcritical flow.
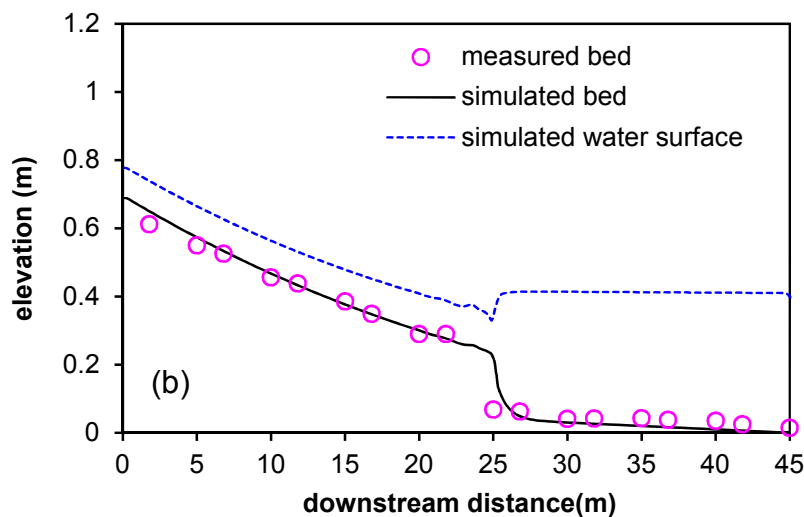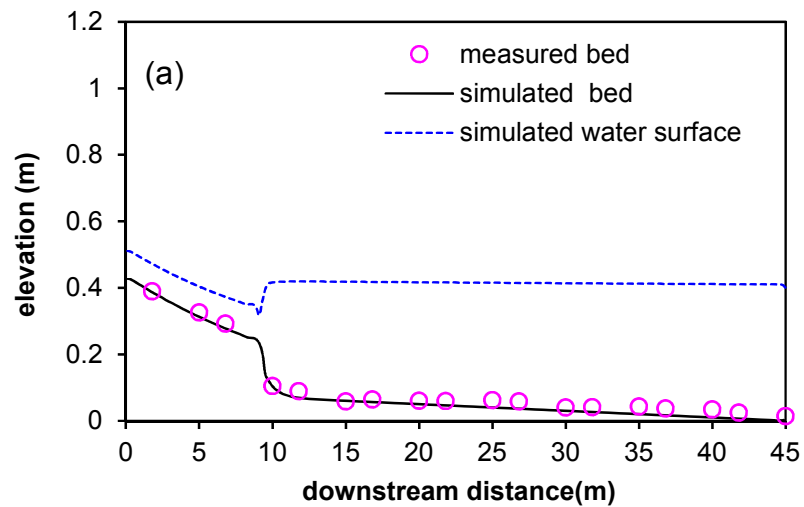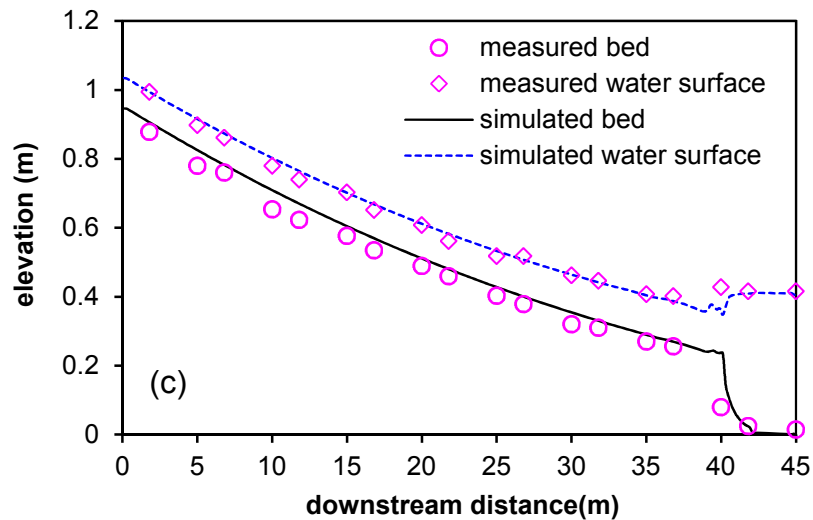
Figure 4.10 Comparisons between simulated results and measured data; (a) t = 2 h; (b) t = 8 h; (c) t = 16.8 h

4.4.4 Dike Erosion due to Flow Overtopping

Dike erosion due to flow overtopping is a complex flow process involving outburst flow, supercritical flow, subcritical flow and steady flow. Further, in this situation bed slope effects occur due to the existence of upstream and downstream slopes. Additionally, it is also important to predict the flow propagation and dike erosion processes to inform risk management. Therefore, this test is undertaken to verify that the bedload dominant sheet flow model (STM1) can solve this sediment transport problem under complex hydraulic conditions while at the same time predicting the morphological change. Here the experimental Run2 of Chinnarasri et al.(2003) [166] is reproduced. A dike was located in the middle of a flume of 35m×1m×1m being 0.8 m in height, 1 m wide with a crest width of 0.3 m (see Figure 4.11). The upstream and downstream slope of the dam was 1V:3H and 1V:2.5H, respectively. The dike is composed of sand with a median diameter of 1.13 mm, d_{30} = 0.52 mm, d_{50} = 0.86 mm, d_{90} = 3.8 mm and the density of $2.65×10^3$ kg/m^3. The initial reservoir level is 0.83m and the downstream water level is 0.03 m; the inflow discharge has a constant value of $1.23×10^{-3}$ m^3/s; the bed material porosity is taken as 0.25 and the Manning coefficient n is set as 0.015 for non-uniform sediment mixture bed. The sediment-to-flow velocity ratio α is calculated by Eq.(4.11) and the adaptation length L is calculated by Eq.(4.12).

For the simulation the 1D solver is used and the domain is discretised into 700 cells in one dimension (dx = 0.05 m) and the sheet flow transport rate is

calculated by the equation of *M_SJ* or *M_MPM* according to the bed slope. As reviewed in the introduction, the Shallow Water-Exner coupled model has been frequently investigated by other researchers. To demonstrate the improvements in the model presented here, a Shallow Water-Exner coupled model proposed by Murillo and Garcia-Navarro (2010) [80] is applied to simulate this case in order to provide comparison. Figure 4.12 illustrates a good agreement between the simulated and measured dam profiles at *t*=30*s*. The comparisons of the reservoir level and overtopping discharge are demonstrated in Figure 4.13. It shows that the proposed model achieves better results than the Shallow Water-Exner model, which underestimates the peak discharge and overestimates the arrival time significantly. The Manning's coefficient *n*=0.015 and 0.018 are used to investigate its sensitivity. It was seen that the larger Manning's *n* generates faster erosion, resulting a higher outflow discharge. This is due to the larger *n* value elevating the bed shear stress, resulting in more severe scour. Better results are obtained for *n* = 0.018, but the arrival time of peak discharge is slightly earlier than the measured data. Figure 4.13(c) compares the predicted outflow discharge with the method proposed here, *M_MPM* (ψ = 2.0), Nielsen [105] and Ribberink [106]. It can be seen that these three formulations underestimate the erosion process significantly and the combined sediment transport formulations achieve better results.
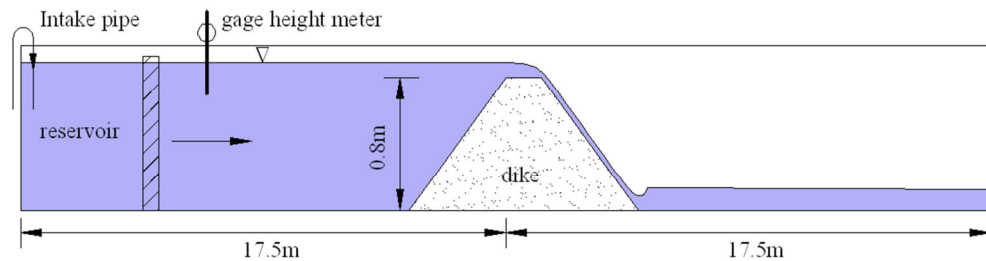
Figure 4.11 Schematic diagram of experiment of Chinnarasri et al. (2003)
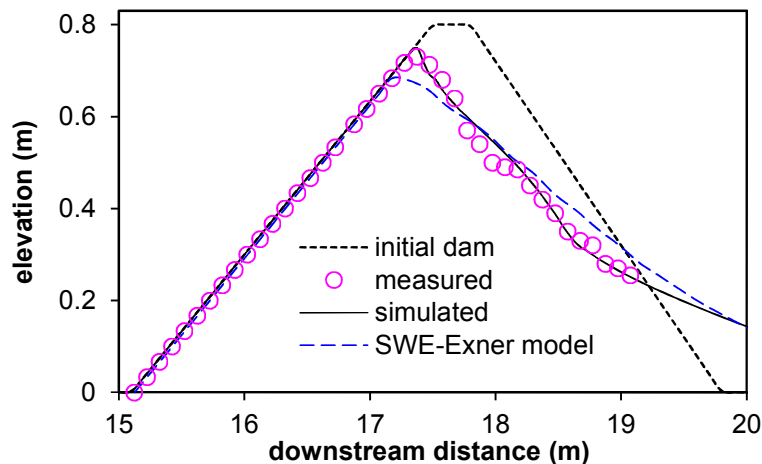
Figure 4.12 Dam profiles at t=30 s
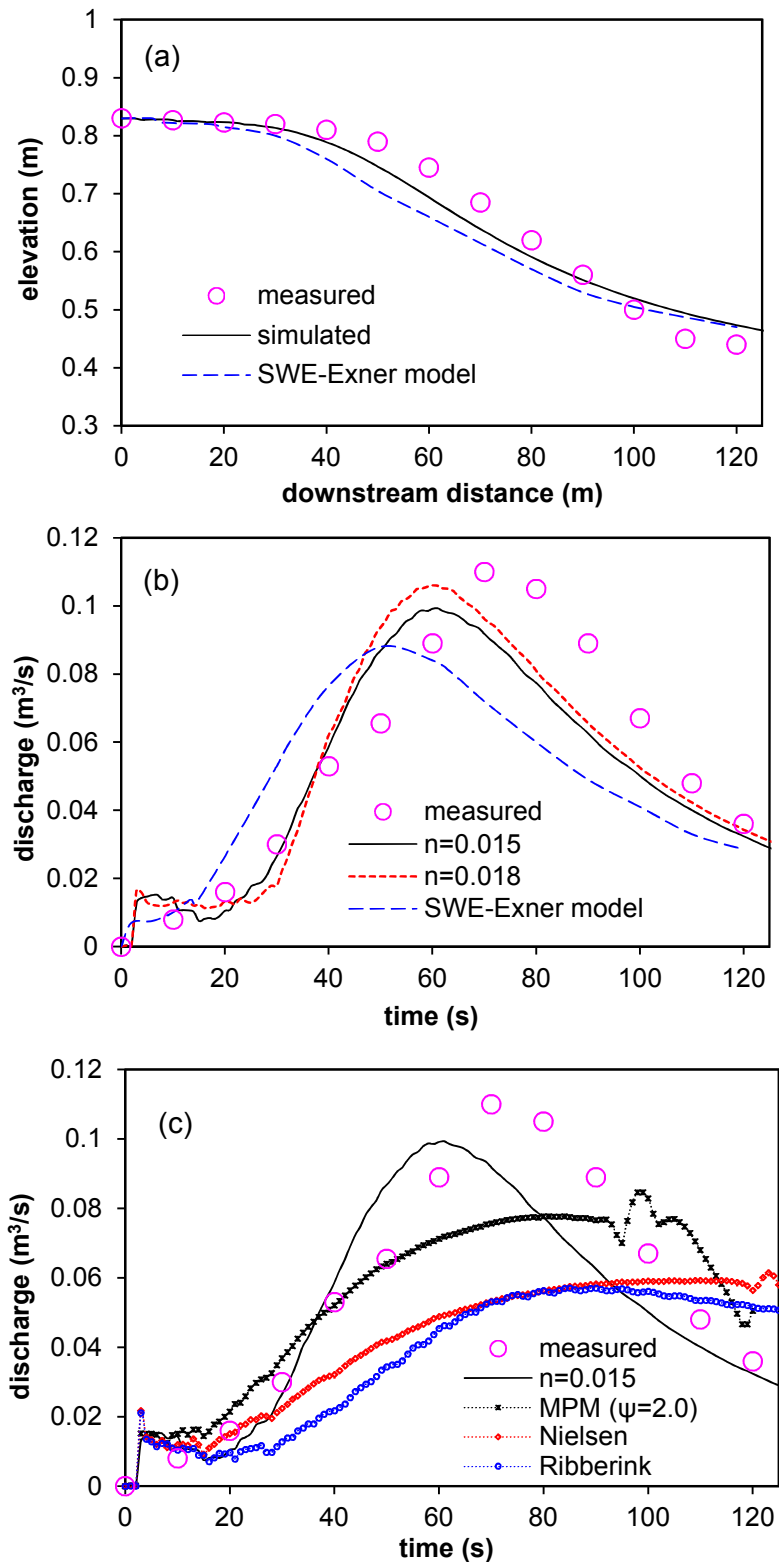
Figure 4.13 The simulated results and measured data (a) reservoir water level and (b) overtopping discharge (c) discharge for different sediment transport equations

Figure 4.14 shows the dike erosion processes at t=30 s, 100 s, 150 s and 200 s. At the beginning, the overtopping flow is small due to a low water height above the crest, erosion starts at the front edge of the dam crest, and

a small head cut forms downstream of the dam crest, and a hydraulic jump is formed in the downstream water. After a certain period, the overtopping flow discharge and erosion rate increase rapidly, and sediment particles deposit in the downstream of the dam and move downward gradually. With the time increasing, the overtopping discharge after arriving at a peak value decreases and erosion rate also slows down. After a long period, the deposition edge in the downstream does not move downward anymore, even the sediment is eroded again, and the water level in the downstream reservoir steadily increases backward to upstream, see Figure 4.14 (b, c, d). At the final stage, a large wedge is formed.
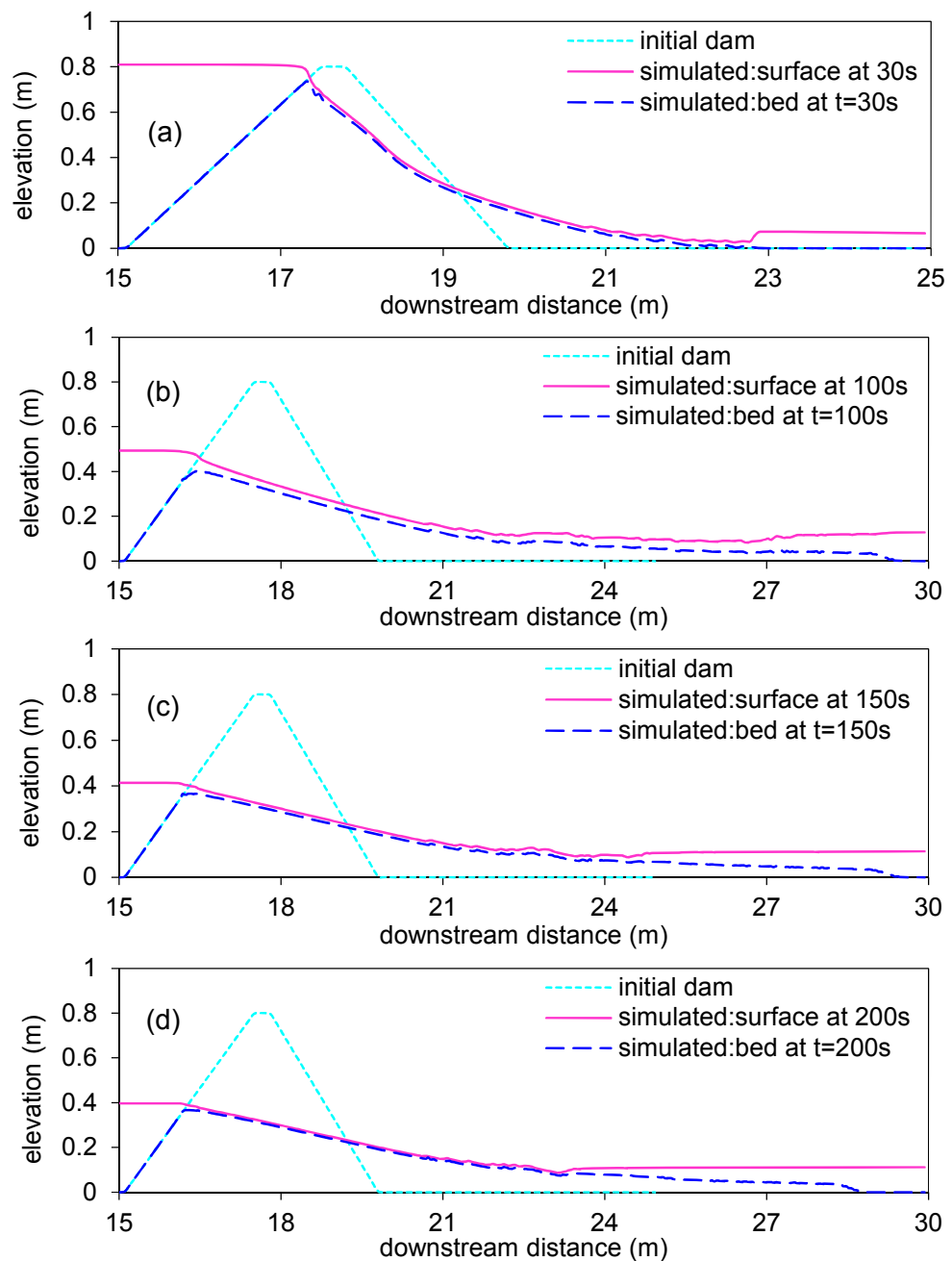
Figure 4.14 Simulated dike breach at t=30 s, 100 s, 150 s and 200 s

In addition, compared to the Shallow Water-Exner model, the layer-based sheet flow model can predict the spatial and temporal distribution of sediment concentration which is an important factor in understanding the erosion and deposition process. Figure 4.15 illustrates the sediment concentration at t=30 s, 100 s, 150 s, 200 s and 1000 s. It is clear that the sediment concentration is larger at 30 s, before decreasing and moving downward. As the flow becomes weak and tends towards steady state, the sediment concentration diminishes progressively in the erosion and deposition area. Furthermore, in Figure 4.16, the effects of the sediment-to-flow velocity ratio α ($\alpha=1/\beta$) are compared to the simulated results at 200s when the sediment transport is weaker. It is seen that the ratio α is smaller than 1 signifying that the velocity of sediment transport is smaller than flow velocity. The comparisons also indicate that the simulation without α apparently overestimates the water depth. Yet, an equivalent velocity ratio $\alpha=1$ is usually assumed in morphodynamic models. The ratio α has been studied and formulated by previous research, but here a sensitivity analysis was conducted. It is found that the results for using the equation from [109, 115, 159] have no significant difference. The test emphasizes the implication
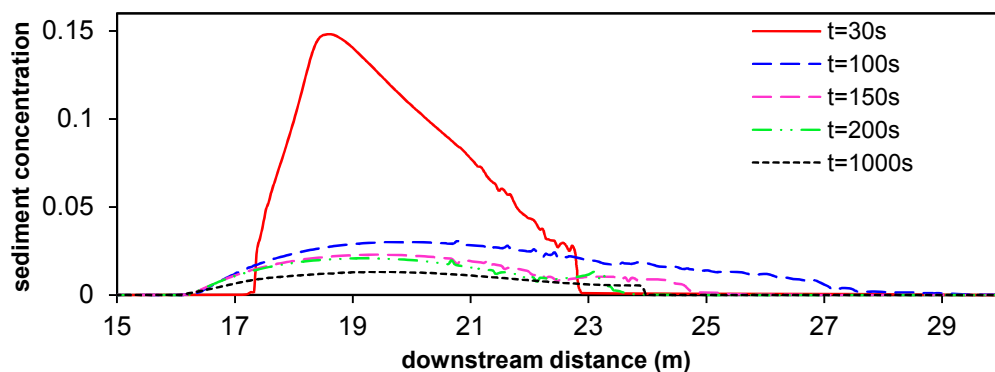
Figure 4.15 Volume-averaged sediment concentration at t=30s, 100s, 150s and 200s, respectively
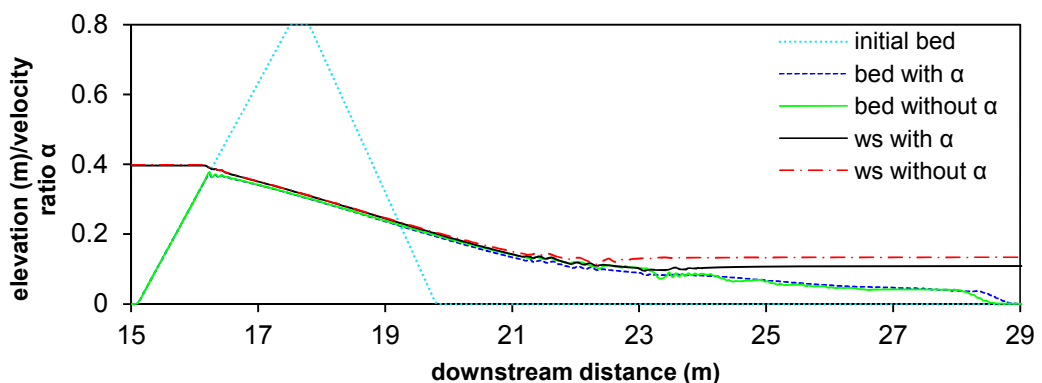
Figure 4.16 Comparisons between simulated results with and without velocity ratio α at t = 200 s; *ws*= water surface

of the sediment-to-flow velocity ratio α in morphodynamic models and demonstrates that it should not be ignored for morphodynamic events, particularly for weaker sediment transport. The assumption that the velocity of sediment transport is always equal to the clear water velocity is shown to be inappropriate.

4.4.5 Dam-break flow over an inclined movable bed

The bed slope can impose an impact on incipient motion of sediment and sediment transport capacity. Geomorphic flows commonly occur in the natural environment, not only in flat channels, but in steep mountain rivers. The proposed model takes these effects into consideration comprehensively. To demonstrate the applicability of the 1D model (STM1) to an inclined bed and analysis of bed slope effects, a case of dam-break flow over a movable bed with an inclined bed is modelled here. The purpose of this test is to emphasise the bed slope effects on sediment movement and meanwhile give some understandings on sediment transport in the case of rapid outburst flows. The initial conditions are set up as follows: the initial bed slope is 1-in-10 in a 100 m channel; the water level is 10 m in a reservoir which is separated by a gate located at 0m. The bed material is composed of sands with median diameter of 1mm; the bed porosity is 0.45; and the Manning's coefficient of bed is set as 0.025.

For these sands bed with diameter of 1 mm, the flow belongs to outburst sheet flow with bedload being dominant. The process is simulated for 8s. Figure 4.17 shows the water surfaces and bed profiles at t = 2 s, 4 s, 6 s and 8 s after the dam-break. The flow process is described as: when the gate is instantaneously removed, the outburst flow runs rapidly downward over the erodible bed; due to the intense water flow and thus bed shear stress, sand particles are entrained and start moving downward so that a scour hole is formed in the bed. In order to show bed profile change clearly, the relative elevation of water surface and bed profile with initial bed are depicted in Figure 4.18 which shows the water surface and bed profile evolution. It can be clearly seen that the scour hole deepens and expands progressively with increasing time, while the location of the deepest point does not change. Figure 4.19 illustrates water velocity and sediment concentration from which It can be seen that the high concentration sediment mainly accumulates in the wave front and propagates downstream along with the water flow, but the value of concentration does not have a large variation with increasing time; it remains around 0.25 for this case. The sediment concentration has a

close relationship with flow velocity (e.g. magnitude, range). This phenomenon is similar to the theoretical analysis and experimental observations for water front described by other research [13]. Theoretically, bedload concentration has a constant maximum.
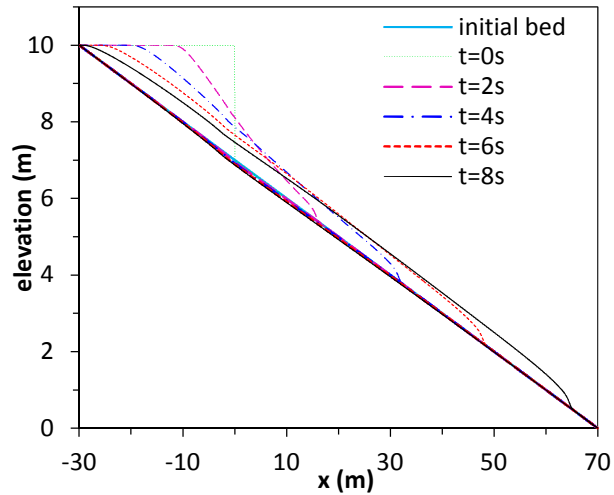
Figure 4.17 schematic graphic of dam-break flow over movable bed with an inclined bed at t = 2 s, 4 s, 6 s and 8 s
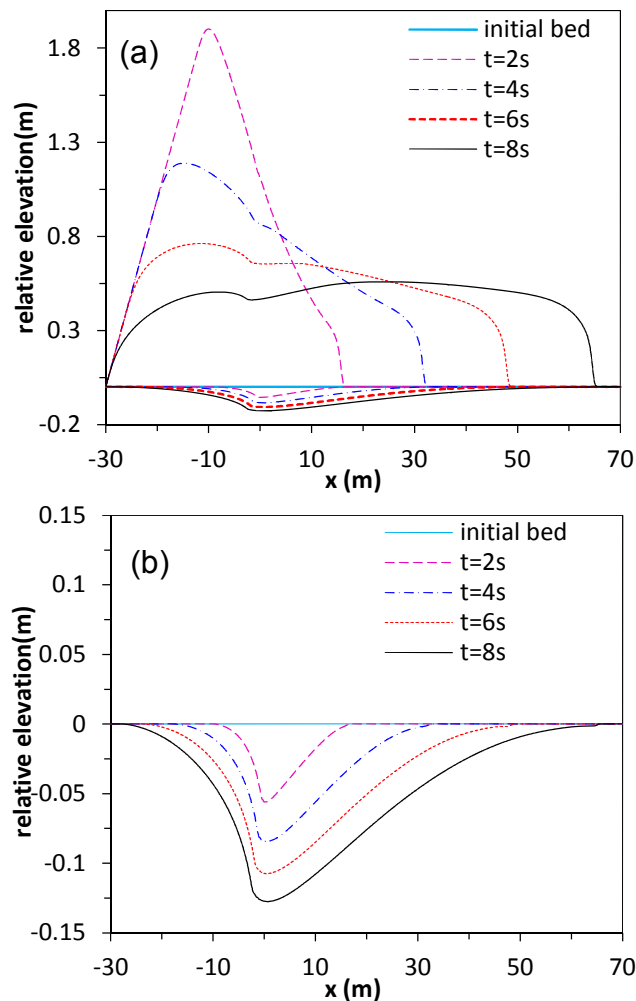
Figure 4.18 the relative elevation of (a) water surface and (b) bed profile with initial bed at t = 2 s, 4 s, 6 s and 8 s
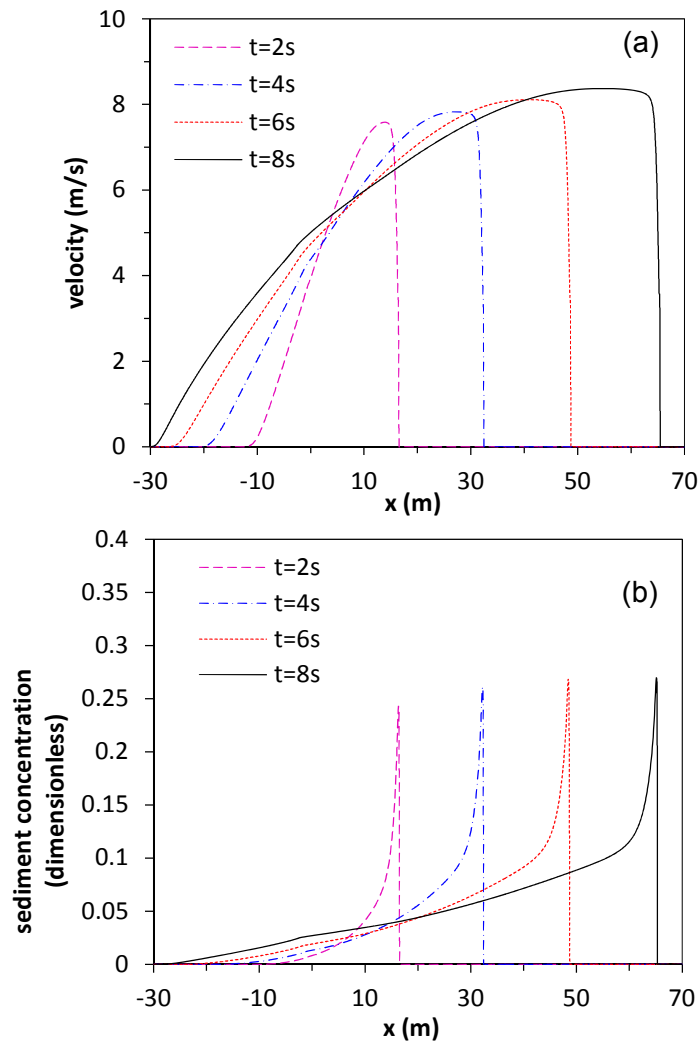
Figure 4.19 the velocity (a) and sediment concentration (b) profiles at t = 2 s, 4 s, 6 s and 8 s, respectively

The proposed model is applied to simulate outburst geomorphic flow process with and without bed slope effects. The runs without bed slope effects adopts the *M_MPM* transport equation; while the runs with bed slope effects uses the transport equation *M_SJ* which is obtained by extending the *MPM* database to cover these steep slopes. Moreover, the critical bed shear stress is calculated by using bed slope influenced Eq.(15) for the run with bed slope effects. Firstly, Figure 4.20(a) shows that the difference mainly focuses on the depth of scour hole but the water front has a similar velocity. Secondly, the scour hole is deeper with *M_SJ* with bed slope effects than with *M_MPM* without bed slope effects, that is to say, the bed slope increases the erosion rate in the downstream direction. Further, the sediment concentration is also larger; however, the maximum value in water front has no significant difference. The differences between the two runs are not very large; only slight differences in water surface, bed scour and sediment concentration are evident. However, the proportion of the

difference in total change emphasises how much the bed slope influences the bed scour. For example, at the location 0*m*, the bed scour depth with bed slope effects can reach 7 m-6.87 m=0.13 m, while the bed scour depth without bed slope effects is 7 m-6.9 m=0.1 m; therefore, the difference proportion can reach (0.13 m-0.1 m)/0.1 m =30%. In summary, for the morphodynamic events in channels with steep slopes, the bed slope effects on sediment transport rate and critical bed shear stress should be considered.
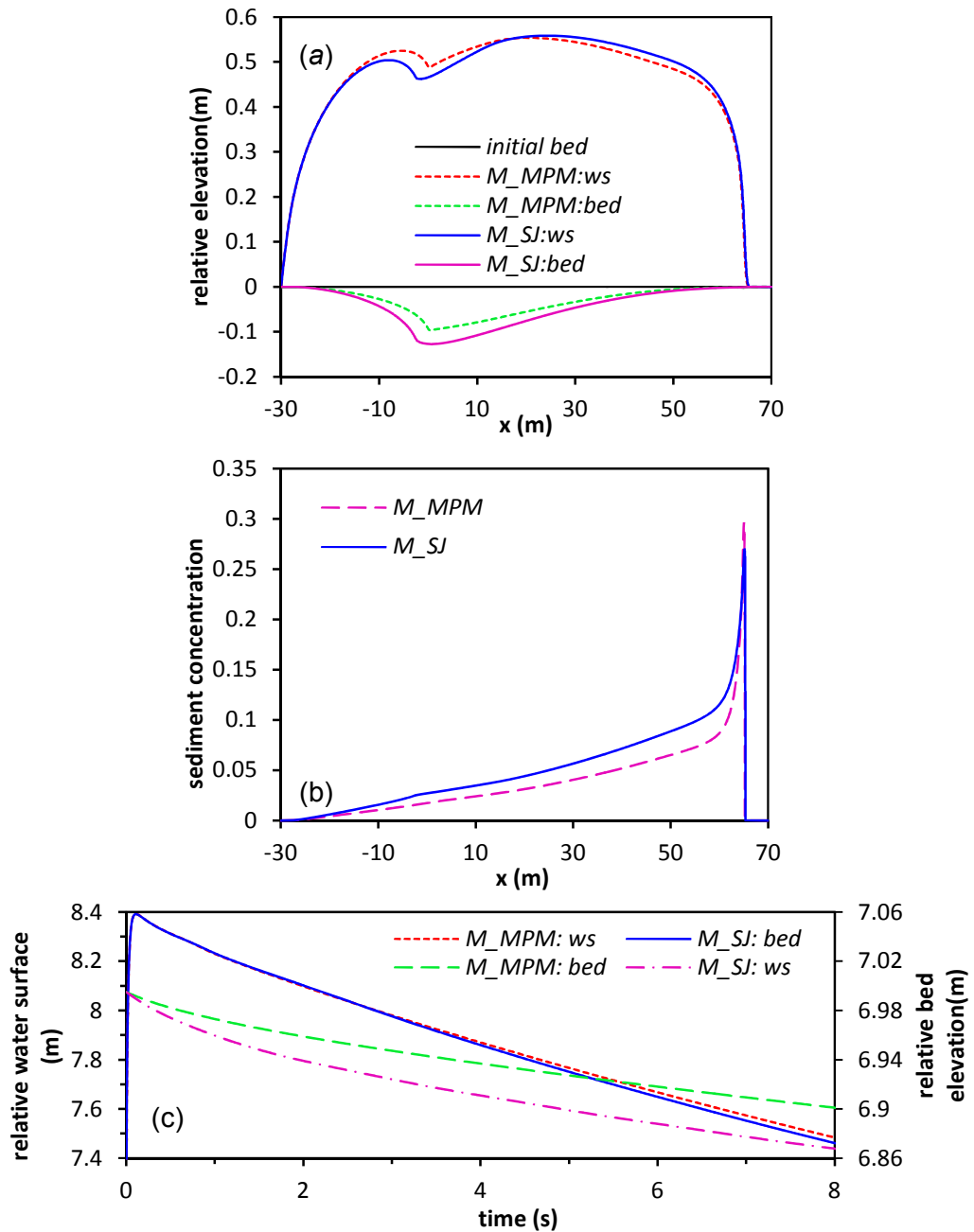
Figure 4.20 the comparisons between the results of SJ with bed slope effects and MPM without bed slope effects at t = 8 s; a) is the comparison of relative elevation; b) is the comparison of water and bed elevation at location 0 m against time; c) for sediment concentration

4.5. Concluding Remarks

In summary, a one-dimensional multi-purpose morphodynamic model system based on shallow water theory and non-equilibrium sediment load assumptions has been developed. The chapter proposed three sediment transport models which can be chosen according to the simulated objects. This makes the model system not only applicable to solely bedload transport or suspended load transport, but also suitable for total sediment transport. Some key sediment parameters or relationships are identified for simulation of applicability to real hydraulic features. A bed slope avalanching model is included in the model system, so this improves the predicted results, particularly the bed changes. Also, the inclusions of bed slope effects, hiding/exposure effects enhance the applicability of the proposed model in complex physical conditions. As shown by comparisons with experimental investigations, good agreements have been achieved, revealing that the model system presented is capable of effectively simulating flow-sediment transport events under steady or unsteady flow conditions over a flat bed or steep bed.

Chapter 5
Extension to a 2D Morphodynamic Model

5.1 Construction of 2D Morphodynamic Model

5.1.1 Hydrodynamic Module

In this Chapter, the hydrodynamic process is calculated by solving the 2D shallow water equations using Godunov-based finite volume method technologies. Based on the derivation of the 1D model in Chapter 4, the 2D hydrodynamic model can be easily extended as expressed by:

$$\frac{\partial \eta}{\partial t} + \frac{\partial hu}{\partial x} + \frac{\partial hv}{\partial y} = 0 \tag{5.1}$$

$$\frac{\partial hu}{\partial t} + \frac{\partial}{\partial x}\left(hu^2 + \frac{1}{2}gh^2\right) + \frac{\partial huv}{\partial y}$$
$$= gh(S_{ox} - S_{fx}) + \frac{\Delta\rho u}{\rho}\frac{\partial z_b}{\partial t}[\alpha(1-p) - C] - \frac{\Delta\rho gh^2}{2\rho}\frac{\partial C}{\partial x} - S_A \tag{5.2a}$$

$$\frac{\partial hv}{\partial t} + \frac{\partial huv}{\partial x} + \frac{\partial}{\partial y}\left(hv^2 + \frac{1}{2}gh^2\right)$$
$$= gh(S_{oy} - S_{fy}) + \frac{\Delta\rho v}{\rho}\frac{\partial z_b}{\partial t}[\alpha(1-p) - C] - \frac{\Delta\rho gh^2}{2\rho}\frac{\partial C}{\partial y} - S_B \tag{5.2b}$$

where h= flow depth (m)

  u, v = average flow velocity in x and y direction (m/s)

  z_b = the bed level (m)

  p = the sediment material porosity

  C = the flexible volumetric sediment concentration $C = \sum_{i=1}^{N} C_i$.

  ρ_s, ρ_w = the density of sediment and water flow respectively (m³/s)

  $\Delta\rho$ = ρ_s-ρ_w (m³/s)

  ρ = the density of sediment and flow mixture (m³/s)

  $S_{ox} = -\partial z_b/\partial x$, $S_{oy} = -\partial z_b/\partial y$ = bed slope in x and y direction

  S_f, S_{fy} = frictional slope in x and y components

  α is the sediment-to-flow velocity ratio

  S_A, S_B = the additional velocity ratio related terms determined as

$$S_A = \frac{\Delta\rho u}{\rho}(1-\alpha)\left[C\left(\frac{\partial hu}{\partial x} + \frac{\partial hv}{\partial x}\right) - \left(hu\frac{\partial C}{\partial x} + hv\frac{\partial C}{\partial y}\right)\right] \tag{5.3a}$$

$$S_B = \frac{\Delta\rho v}{\rho}(1-\alpha)\left[C\left(\frac{\partial hu}{\partial x} + \frac{\partial hv}{\partial x}\right) - \left(hu\frac{\partial C}{\partial x} + hv\frac{\partial C}{\partial y}\right)\right] \tag{5.3b}$$

The frictional slopes S_{fx}, S_{fy} are calculated based on Manning's roughness coefficient n by

$$S_{fx} = \frac{n^2 u \sqrt{u^2 + v^2}}{h^{4/3}}; \ S_{fy} = \frac{n^2 v \sqrt{u^2 + v^2}}{h^{4/3}} \tag{5.4}$$

The last three source terms of Eq.(5.2) represent the interaction effects of sediment and water flow and momentum transfer due to sediment exchange.

5.1.2 STM1: Sheet Flow Model

As for the bed load model, the governing equation is the 2D non-equilibrium transport equation which is the extended version in two dimensions of Eq.(4.9). It is written by

$$\frac{\partial h S_{bi}}{\partial t} + \frac{1}{\beta} \frac{\partial h u S_{bi}}{\partial x} + \frac{1}{\beta} \frac{\partial h v S_{bi}}{\partial y} = -\frac{1}{\beta} \frac{(q_{bi} - F_i q_{b*i})}{L_i} \tag{5.5}$$

where S_{bi} = volumetric concentration of the ith size fraction by bed load

q_{bi} = real bed load transport rate of the ith fraction (m^2/s)

q_{b*i} = bed load capacity of the ith fraction (m^2/s)

F_i = the proportion of i th size fraction in total moving sediment

L_i = non-equilibrium adaptation length of sediment transport (m)

A number of empirical relationships have been proposed on the bed load transport rate, one of which, the commonly-used relationship, Meyer-Peter & Müller equation [26], is adopted here. However, Meyer-Peter & Müller equation was derived based on the conditions: sediment with diameter <29mm, only for bed slope of <0.03 and the Shields parameter in that hydraulic condition is smaller than 0.25 [26]. Therefore, it might be open to question for application to high shear stress flow over extra-coarse clasts or channels with steep bed slopes. In this study, a calibrated coefficient η is introduced independent on application. Smart and Jäggi [112] expanded the database obtained by Meyer-Peter & Müller and estimated the maximum transport capacity of mountain streams for the steep slope range up to 0.03-0.20. As for bed slope>0.2 surpassing its derived range, a limitation of maximum for S to be 0.2 is implemented in the equation to avoid the calculated transport capacity becoming unphysical large.

$$q_{b*i} = \psi 8 (\theta_i - \theta_{cr,i})^{1.5} \sqrt{(s-1)g d_{50}^3} \quad 0 \le S_o < 0.03 \ (M\_MPM)$$

$$q_{b*i} = 4 \left(\frac{d_{90}}{d_{30}}\right)^{0.2} \frac{h^{1/6}}{n\sqrt{g}} \min(S_o, 0.2)^{0.6} \theta_i^{0.5} (\theta_i - \theta_{cr,i}) \sqrt{(s-1)g d_{50,i}^3} \ S_o \ge 0.03 (M\_SJ)$$

where ψ = the calibrated coefficient

$s = \rho_s/\rho_w - 1$

S_o = bed slope

θ_{cri} = the critical bed shear stress of i th fraction

θ_i = the dimensionless bed shear stress of i th fraction

The non-equilibrium adaptation length L of bed material load was derived in Section 4.2.2. In two-dimensions, it is calculated by

$$L = \frac{hU}{\gamma\omega_{fi}} = \frac{h\sqrt{u^2+v^2}}{\gamma\omega_{fi}} = \frac{\beta h_b\sqrt{u^2+v^2}}{\omega_{fi}} \tag{5.6}$$

where $\gamma = \min\left(\frac{C_b}{C}, \frac{1-p}{C}\right) = \min\left(\alpha\frac{h}{h_b}, \frac{1-p}{C}\right)$

β = the ratio of sediment-to-flow velocity

ω_f = effective setting velocity of sediment particle (m/s)

μ = a dimensionless coefficient related to the sediment material

The effective settling velocity is determined by the equation of Soulsby [27] considering the hindered settling effect.

$$\omega_{fi} = \frac{\nu}{d_i}\left[\sqrt{10.36^2 + (1-C)^{4.7}1.049d_{i*}^3} - 10.36\right] \tag{5.7}$$

5.1.3 STM2: Suspended load transport

For the fine particles at high bottom shear stress, sediment particles may be entrained into suspension if the lift forces exceed the grain weight or bed shear stress exceeds the suspension critical stress, e.g. suspension occurs for silt or fine sand, and for relatively coarse sand under the condition of high-energy outburst flows. Similarly, the governing equation is a simplified advection-diffusion equation extended from Eq.(4.16)

$$\frac{\partial hS_i}{\partial t} + \frac{\partial huS_i}{\partial x} + \frac{\partial hvS_i}{\partial y} = G_iS_{E,i} - S_{D,i} \tag{5.8}$$

where S_i = volumetric concentration of the i th class by suspended load

G_i = the proportion of the i th suspension grain-size fraction

$S_{E,i}$ = entrainment flux of sediment of the i th class

$S_{D,i}$ = deposition flux of sediment of the i th class

According to Section 4.2.2, the erosion and deposition fluxes are also calculated by using the following relationships.

$$S_D = \omega_f C_a; \quad S_E = \omega_f C_{ae} \tag{5.9}$$

where $C_a = \delta C$ is the near-bed concentration at the reference level a.

C_{ae} is the near bed equilibrium concentration at the reference level a.

$$\delta = \min\{2.0, (1-p)/C\}.$$

$$C_{ae} = 0.015 \frac{d_{50}}{a} \frac{T^{1.5}}{d_*^{0.3}}$$

$$T = \frac{(u_*^2 - u_{*,cr}^2)}{u_{*,cr}^2}; \quad a = \min[\max(\mu\theta_i d_{50}; 2d_{50}; 0.01h), 0.2h]$$

where $d_* = d_{50}[(s-1)g/v^2]^{1/3}$ is the dimensionless particle diameter; $u_* = (g^{0.5}/C')u$ is bed-shear velocity related to grain; C' is the Chézy-coefficient related to grain; $u_{*,cr}$ is the critical bed-shear velocity.

5.1.4 STM3: Total Sediment Transport

As presented in section 4.2.3, for both sheet flow and suspended load are equally important, Eq.(4.17) could be extended to two dimensions as

$$\frac{\partial hT_i}{\partial t} + \frac{\partial huT_i}{\partial x} + \frac{\partial hvT_i}{\partial y} = -\frac{(q_{bi} - F_i q_{b*i})}{L_i} + G_i S_{E,i} - S_{D,i} \qquad (5.10)$$

5.1.5 A Flexible Mode in Two dimensions

The integrated flexible form of Eq.(5.5), Eq.(5.8) and Eq.(5.10) is written by

$$\frac{\partial hC_i}{\partial t} + \alpha \frac{\partial huC_i}{\partial x} + \alpha \frac{\partial hvC_i}{\partial y} = -\alpha \frac{(q_{bi} - F_i q_{b*i})}{L_i} + G_i S_{E,i} - S_{D,i} \qquad (5.11)$$

where

$$C_i = \begin{cases} S_{bi} & for\ \text{STM1} \\ S_i & for\ \text{STM2} \\ T_i & for\ \text{STM3} \end{cases}; \quad \alpha = \begin{cases} 1/\beta & for\ \text{STM1} \\ 1 & for\ \text{STM2} \\ 1 & for\ \text{STM3} \end{cases}$$

C_i is the volumetric sediment concentration, α is the velocity ratio. $S_{E,i}$, $S_{D,i}$ will be calculated as zeros in absence of suspended load, and q_{bi}, q_{b*i}, L_i are zeros in absence of bedload.

5.1.6 Morphological Evolution Model

The purpose of this module is to update the new bed elevation caused by flood. Morphological evolution is decided by the volume of sediment entrained and deposited in the flood process which is calculated per grid cell

at each time step. The equation used to calculate the morphological evolution is written by

$$\frac{\partial z_b}{\partial t} = \sum_{i=1}^{N} \left(\frac{\partial z_b}{\partial t}\right)_i = \frac{1}{(1-p)} \sum_{i=1}^{N} \left[\frac{(q_{bi} - F_i q_{b*i})}{L_i} + (S_{D,i} - G_i S_{E,i})\right] \qquad (5.12)$$

Similar to 1D model, the first term in the left of Eq.(5.12) will be diminished for STM2, the second term is treated as zero for bedload model STM1. Both are kept for STM3.

5.1.7 Bed Slope Collapse

To maintain the stability of the bed profiles, the stability analysis of bed slope should be assessed. In this section, the 2D bed slope avalanching model Eq.(2.27) proposed in Chapter 3 is used.

5.2 Numerical Solution

The Eq.(5.1), Eq.(5.2) and Eq.(5.10) constitute a shallow water non-linear system. In compact form, the governing equations can be expressed by

$$\frac{\partial \mathbf{U}}{\partial t} + \frac{\partial \mathbf{F}}{\partial x} + \frac{\partial \mathbf{G}}{\partial y} = \mathbf{S} \qquad (5.12)$$

$$\mathbf{U} = \begin{bmatrix} \eta \\ hu \\ hv \\ hC_i \end{bmatrix}; \ \mathbf{F} = \begin{bmatrix} hu \\ hu^2 + \frac{1}{2}gh^2 \\ huv \\ \frac{1}{\beta}huC_i \end{bmatrix}; \ \mathbf{G} = \begin{bmatrix} hu \\ huv \\ hv^2 + \frac{1}{2}gh^2 \\ \frac{1}{\beta}hvC_i \end{bmatrix}$$

$$\mathbf{S} = \begin{bmatrix} 0 \\ gh(S_{ox} - S_{fx}) + \frac{\Delta\rho u}{\rho}\frac{\partial z_b}{\partial t}\left(\frac{1-p}{\beta} - C\right) - \frac{\Delta\rho gh^2}{2\rho}\frac{\partial C}{\partial x} - S_A \\ gh(S_{oy} - S_{fy}) + \frac{\Delta\rho v}{\rho}\frac{\partial z_b}{\partial t}\left(\frac{1-p}{\beta} - C\right) - \frac{\Delta\rho gh^2}{2\rho}\frac{\partial C}{\partial y} - S_B \\ -\frac{1}{\beta}\frac{(q_{bi} - F_i q_{b*i})}{L_i} + F_i S_{E,i} - S_{D,i} \end{bmatrix}$$

Similar to the algorithm of the 1D model, the fluxes at the interface of two adjacent cells for the model system (5.12) is solved by inserting a middle contact discontinuity waves S_*, and the sediment flux is determined based on the concentration at right cell or left cell through the assessment of S_*.

Firstly, the first three flux term can be expressed by basic HLL scheme expression as follows:

$$\mathbf{E}^*_{LR\ 1,2,3} = \begin{cases} \mathbf{E}_L & if\ S_L \geq 0 \\ \mathbf{E}_R & if\ S_R \leq 0 \\ \mathbf{E}^* & otherwise \end{cases} \tag{5.13}$$

where $\mathbf{E}_L = E(U_L)$, $\mathbf{E}_R = E(U_R)$ are the flux and conservative variable vectors at left and right side of each cell interface. $\mathbf{E}^*$ is the numerical flux in the star region. It is calculated in two dimensions by

$$\mathbf{E}^* \cdot \mathbf{n} = \frac{S_R \mathbf{E}_L \cdot \mathbf{n} - S_L \mathbf{E}_R \cdot \mathbf{n} + S_R S_L (\mathbf{U}_R - \mathbf{U}_L)}{S_R - S_L} \tag{5.14}$$

in which, R and L represent the right and the left side of the cell interface respectively; $\mathbf{n} = [n_x, n_y]^\mathsf{T}$; the S_L and S_R denote two wave speeds which are supposed to be selected carefully to avoid entropy violation. The so-called "two expansion" approach [65] was adopted here including dry-bed options to estimate S_L and S_R. They are expressed by

$$S_L = \begin{cases} \min\left(\mathbf{q}_L \cdot \mathbf{n} - \sqrt{gh_L}, u^* - \sqrt{gh^*}\right) & if\ h_L > 0 \\ \mathbf{q}_R \cdot \mathbf{n} - 2\sqrt{gh_R} & if\ h_L = 0 \end{cases}$$

$$S_R = \begin{cases} \min\left(\mathbf{q}_R \cdot \mathbf{n} + \sqrt{gh_R}, u^* - \sqrt{gh^*}\right) & if\ h_R > 0 \\ \mathbf{q}_L \cdot \mathbf{n} + 2\sqrt{gh_L} & if\ h_R = 0 \end{cases}$$

where

$$u^* = \frac{1}{2}(\mathbf{q}_L + \mathbf{q}_R) \cdot \mathbf{n} + \sqrt{gh_L} - \sqrt{gh_R},\ \sqrt{gh^*} = \frac{1}{2}\left(\sqrt{gh_L} + \sqrt{gh_R}\right) + \frac{1}{4}(\mathbf{q}_L - \mathbf{q}_R) \cdot \mathbf{n}$$

In which, $\mathbf{q} = [u, v]$. The middle wave speed S_* is determined using the following form which is proposed by Toro [138].

$$S_* = \frac{S_L h_R(\mathbf{q}_R \cdot \mathbf{n} - S_R) - S_R h_L(\mathbf{q}_L \cdot \mathbf{n} - S_L)}{h_R(\mathbf{q}_R \cdot \mathbf{n} - S_R) - h_L(\mathbf{q}_L \cdot \mathbf{n} - S_L)}$$

To calculate the intercell numerical fluxes, the weighted average flux (WAF) method is employed. However, the basic WAF scheme without TVD modification is seldom used in practice because of its unphysical or spurious oscillations so to avoid such oscillations, a total variation diminishing (TVD) constraint is enforced on the WAF scheme with a flux limiter function. The TVD-WAF scheme is second-order accurate in space and time by solving the conventional Riemann problem associated with the first-order Godunov scheme. A detailed description can be found in [138]. As introduced in

Section 4.3 of Chapter 4, The TVD-WAF flux in the x direction is calculated by:

$$\mathbf{F}^*_{i+1/2,(1,2,3)} = \frac{1}{2}(\mathbf{F}_i + \mathbf{F}_{i+1}) - \frac{1}{2}\sum_{k=1}^{N} sign(c_k)\Phi^k_{i+1/2}\Delta\mathbf{F}^k_{i+1/2} \qquad (5.15)$$

in which, $\mathbf{F}_i= \mathbf{F}\,(\mathbf{U}_i)$, $\mathbf{F}_{i+1}= \mathbf{F}\,(\mathbf{U}_{i+1})$ are the flux and conservative variable vectors at left and right side of each cell interface; c_k is the courant number for wave k, $c_k=\Delta t S_k/\Delta x$; S_k is the speed of wave k and N is the number of waves in the solution of the Riemann problem, N=2 in conjunction with HLL approximate Riemann solver; $\Phi(r)$ is WAF limiter function.

Based on the solution of the previous three flux terms, the fourth flux term-the sediment flux at the interface of two adjacent cells is determined by virtue of the relationships of the middle waves S_* and zero. Specifically, the fourth sediment flux component is calculated by

$$F^*_{i+1/2,4} = \begin{cases} F^*_{i+1/2,1}C_L & S_* \geq 0 \\ F^*_{i+1/2,1}C_R & S_* < 0 \end{cases} \qquad (5.16)$$

where C_L and C_R represent volumetric sediment concentration in the left and right cells; $F_{i+1/2,1}$ is the first flux component calculated by Eq.(5.15); $F_{i+1/2,4}$ is the sediment flux component. The numerical scheme is explicit, so in order to restrict the instability of numerical model, the well-known Courant-Friedrichs-Lewy (*CFL*) stability condition is applied. For two-dimensional structure cell, the time step Δt is determined by

$$\Delta t = CFL \min\left(\min\frac{dx_i}{|u_i| + \sqrt{gh_i}}, \min\frac{dy_j}{|v_j| + \sqrt{gh_j}}\right) \qquad (5.17)$$

where *CFL* is known as the Courant number and satisfies 0<*CFL*<1.

5.3 Testing 2D Model

5.3.1 A Partial Dam-breach Flow over a Mobile Channel

This case is to verify and validate the performance of suspended load model (STM2) by reproducing partial dam-breach flow experiments over a mobile bed, which is carried out at the Hydraulics Laboratory of Tsinghua University, China [16]. A thin dam was located at 2.0 m downstream of a 18.5 m × 1.6 m rectangular flume, and a 0.2 m wide dam-breach centred at y = 0.8 m; the region of 4.5 m after dam site was covered by fine non-uniform

coal ash with a median diameter of 0.135 mm, and its natural and dry density were measured approximately as 2248 kg/m^3 and 720 kg/m^3 respectively; the water depth was initially set to be 0.4 m in the reservoir and 0.12 m downstream of the dam. In this experiment, the bed levels at two cross sections CS1 (x = 2.5 m) and CS2 (x = 3.5 m) after 20 s were measured. During the whole experiment, only suspended load transport occurs due to the particles being so fine.

For the simulation, the domain is discretised by 370 × 80 cells, and the time interval Δt = 0.005 s. The Manning's coefficient n = 0.02; and the entrainment equation (2) is chosen to apply according to the experimental conditions; the sediment porosity is set as 0.35. The suspended load model is run in 20 s. Figure 5.1 shows a comparison between the observed and calculated cross-sectional profiles after 20 s. It is shown that the trend of the predicted bed profiles is similar to that of the measured profiles. Erosion occurs in the middle of the cross sections. The bed erosion quantity is less than the measurement at CS1 where the predicted bed is underestimated, particularly in terms of the erosion width. However, a similar maximum scour depth and location are predicted here. At CS2, the bed simulated and measured profiles have a good agreement with each other. The simulated and measured scour depths are very close and the erosion areas agree very well with each other, but the measured range of bed profile is about 20 cm wider than the simulated range. The bed deposition is underestimated by the model here. This is possibly due to either the experimental errors or the neglected turbulence term, which means the model may not be able to generate the rapid formation of horizontal circulating flow at the downstream of the dam. Figure 5.2 illustrates the view of bed topography predicted by suspended model in the system.
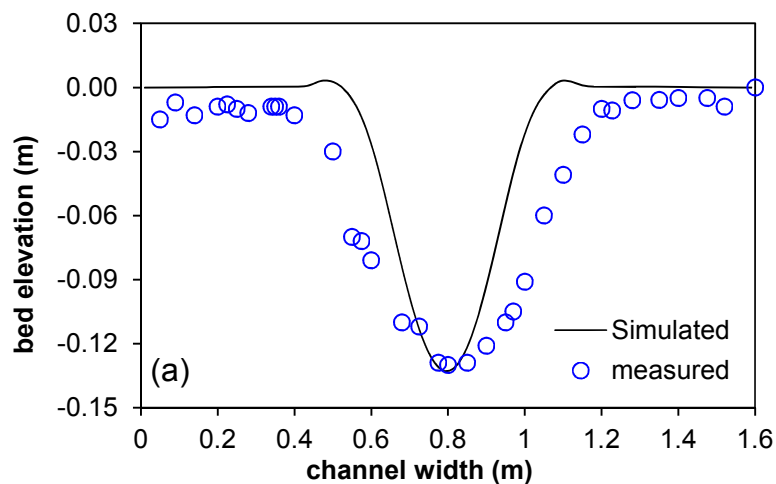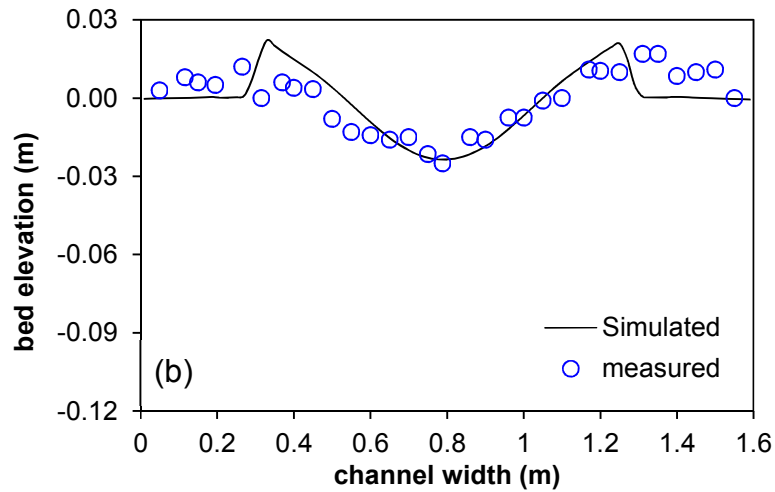
Figure 5.1 Comparison between measured and simulated bed profile at CS1 and CS2
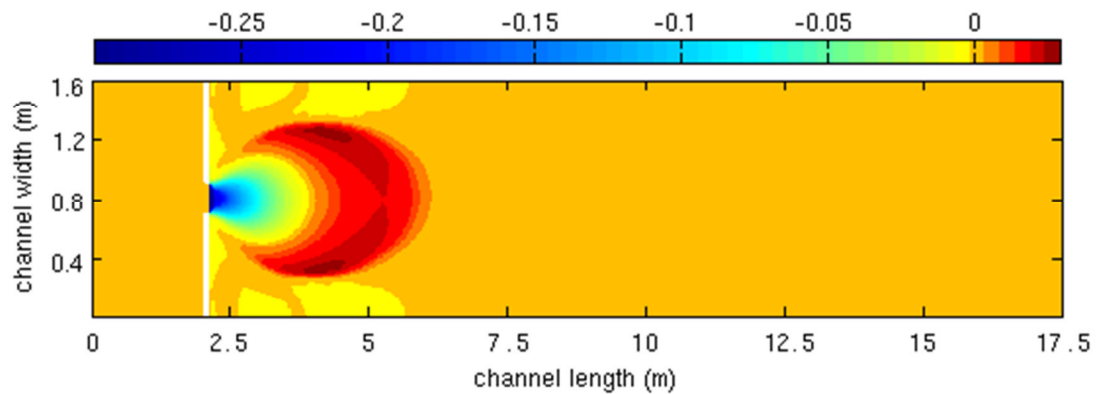
Figure 5.2 Bed topography contour after 20s

5.3.2 Erosion in a Basin due to Clear-Water Inflow

The experiment was conducted to investigate the erosion process in a rectangular basin due to clear water inflow from a narrow channel by Thuc (1991). In this test, both suspended load and bedload are considered to verify the fully suspended and bedload model (STM3). The initial setup involves an inlet rectangular channel of 2.0 m long and 0.2 m wide, a rectangular movable basin with 5.0 m long and 4.0 m wide, and a 1.0m long and 1.2 m wide channel in the downstream. Therein, the movable basin consists of fine sand with median diameter of 0.6 mm, with a movable bed layer was 0.16 m thick. For the initial hydraulic conditions, initial water depth was specified as 0.15 m; the inflow velocity at the inflow boundary was kept constant at 0.6 m/s, and the water depth at the outlet was a constant value of 0.15 m. A fixed bed is prescribed during the experiment period.

The length of channel is discretised with a constant interval $\Delta x = 0.1$ m, but in width direction, the grid spacing around the centreline (±0.6m) is set to be finer ($\Delta y_1 = 0.02$ m) than that in other parts ($\Delta y_2 = 0.05$ m). The computational mesh in the basin consists of 80×116 cells. The time step for flow and sediment calculation is set the same at 0.009 s. The Manning's roughness coefficient n in the basin is given a value of 0.03. The model was run for 2 hours of experiment time. Eq.(5.9) is used to calculated the entrainment and deposition fluxes in this case, with the coefficient $\delta = \min(4.0, (1-p)/C)$ adopted. Figure 5.3 shows the simulated bed change pattern around the inflow region at the centre part of the basin after 4 hours. Erosion occurs due to the inflow of clear water, and the eroded sediment moves downstream and deposits forming a hill. Figure 5.4 shows the comparison of the measured and simulated bed changes along the longitudinal centreline. Overall, the simulated morphological evolution tendency at 1 hour and 2 hours are in good agreement with the measured results. However, the maximum deposition heights are slightly under-predicted, about 13.4% difference at 1 hour and 30.6% at 2 hours. Furthermore, it can be seen that the model overestimates the erosion depth at the inlet of the basin. There the simulated erosion is much more severe than the measured erosion. This is most likely because secondary flow plays an important role here, however, these non-hydrostatic flows are neglected in the current model.
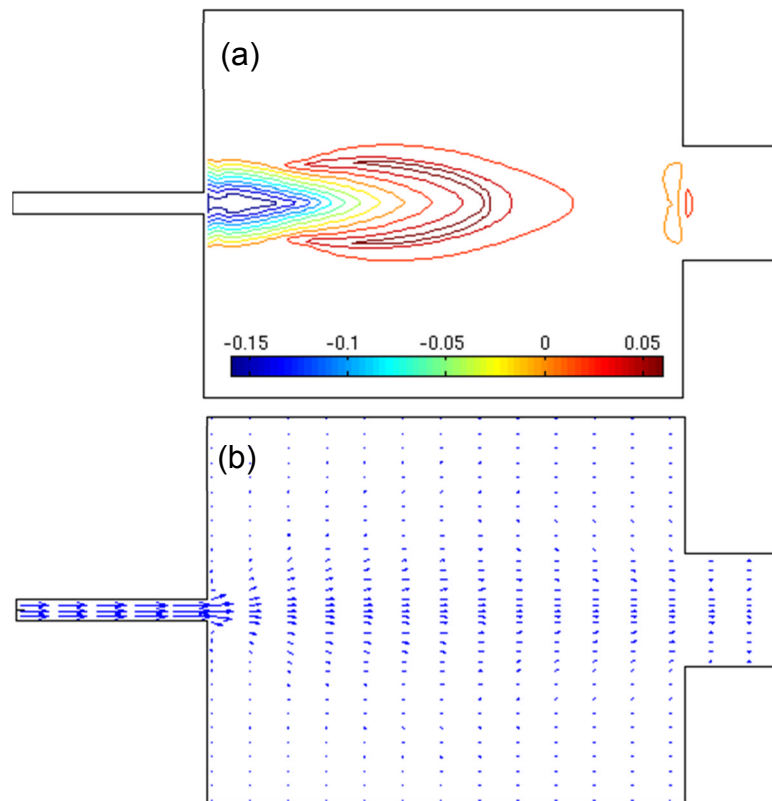
Figure 5.3 (a) bed topography contour after 2hrs; (b) velocity field after 2hrs
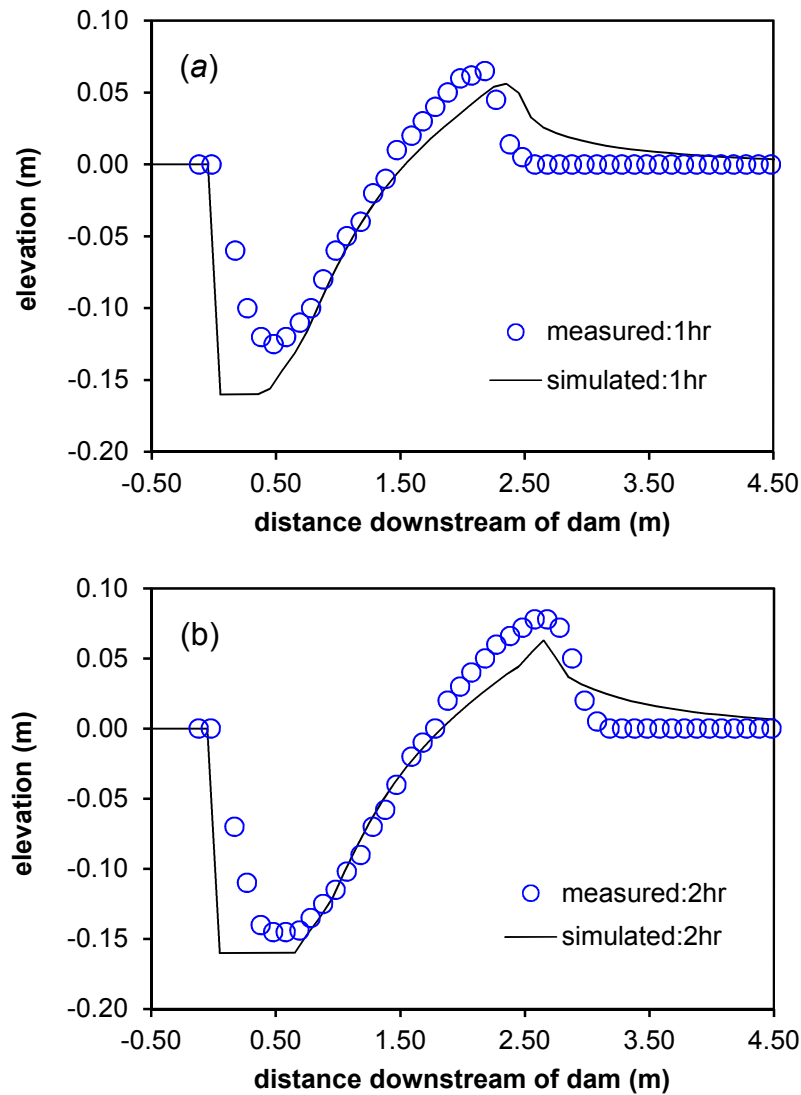
Figure 5.4 Comparison between the measured and simulated bed profile at the centreline at 1hour and 2hours

5.3.3 Dam-break Flow over an Erodible Channel with Sudden Enlargement

To verify the capability of the proposed 2D bedload dominant sheet flow model (STM1), another experiment test is reproduced here. The experiment was undertaken in the laboratory of UCL in Belgium [167]. The experimental conditions are: the length of flume is 6 m long; a thin gate is located at the middle of the flume; the width is sudden enlarged from 0.25 m to 0.5 m at 1.0 m downstream of the gate; the initial experiment setup is shown in Figure 5.5. The initial water depth before and after the gate is 0.25m and 0m respectively; the erodible bed layer of 0.1m thick consists of fully saturated sand over the whole flume. The sediment material used was almost uniform coarse sand with an uniformity index $d_{84}/d_{16}=1.96$ and a median diameter of

1.72mm; the special density of the sand was equal to $\rho_s/\rho_w=2.63$, and the porosity after deposition was equal to 39%. The boundary condition at the downstream outlet was free outflow over the sediment bed maintained at the initial elevation by a vertical plate presenting the same height as the bed layer. For simulation, the model domain is discretised by 300 × 100 uniform cells ($\Delta x=0.02$ m; $\Delta y=0.005$ m).The Manning n value is set equal to 0.023 which is set according to the value used in the experimental work [167].
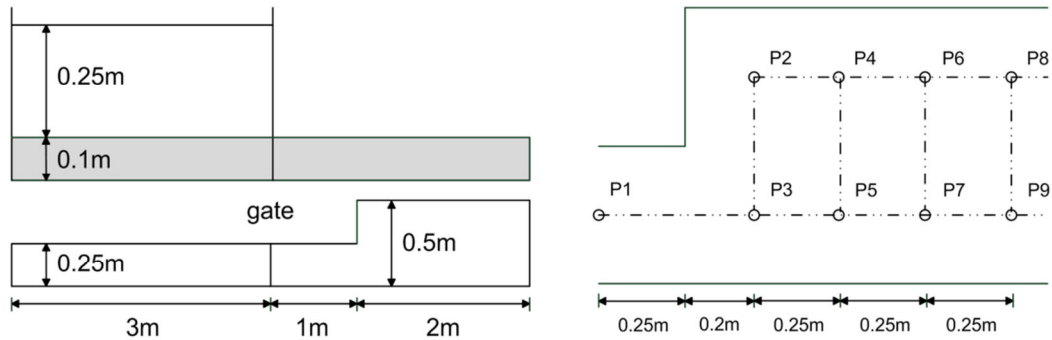
Figure 5.5 Sketch of a dam-break flow experiment over a mobile bed

For this case the bedload transport is considered to be the dominant role. Firstly, we illustrate the spatial flow state at 1 s and 1.5 s and compare simulated water surface and experimental imagine in Figure 5.6. We can see that similar flow features are reproduced. More specifically, at t=1 s the water flow runs into the enlarged channel from the enlargement outlet and the water front has nearly arrived at the left side wall of the flume; at 1.5 second reflective wave bores are generated at the side wall of the flume, notice a dry area without water flow is presented in the corner to the left of the expansion (shown in Figure 5.6).
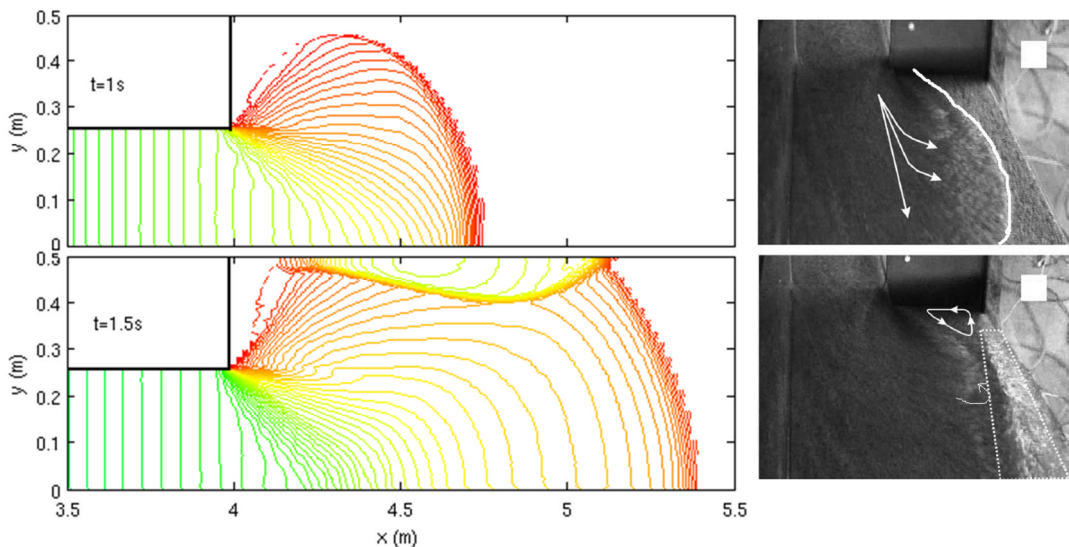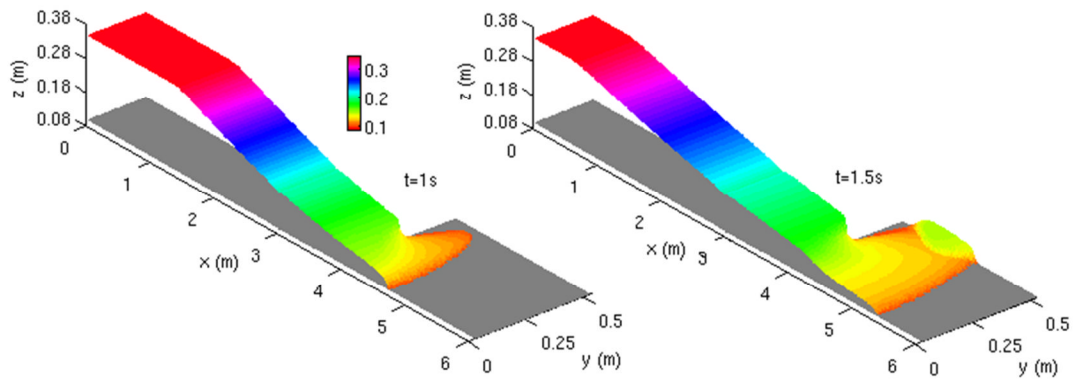
Figure 5.6 Simulated results at t=1 s and 1.5 s; the upper shows a comparison between simulated water contours and experimental observations; the lower map shows a 3D views of the simulated results.

The simulated temporal evolution of water level over ten seconds are compared against measured results at seven gauges (sketched in Figure 5.5) P1, P2, P3, P5, P6 and P7 in Figure 5.7. It can be seen that the simulated water levels agree fairly well with measured data. Although there are some slight differences at some gauges, e.g.at P3, the more severe erosion renders the water level slightly lower than measured; the temporal simulation of the flow inundation process is well reproduced. Furthermore, the spatial simulation of the bed change is examined. The sediment-flow process is completed, reaching a steady state after around 50 s. In Figure 5.8(a), the simulated final bed topography is illustrated. The experimental and simulated final bed terrain can both be seen in Figure 5.8(b). Two strong features can be seen on both: the first an eroded hole that is generated at the enlargement location area where the most severe scour occurs; the second is a deposited mound located at near the left side wall behind the expansion outlet. This area is also the main deposition zone in the sediment-flow process (see Figure 5.8). In terms of the change of bed cross sections, the simulated bed profiles at the four cross sections (CS1: 4.2 m, CS2: 4.3 m, CS3: 4.4 m, CS4: 4.5 m downstream from inlet respectively) are sketched to compare with measured data in Figure 5.9. In addition, we also compare the simulated results by SWE-Exner model proposed by Soares-Frazão and Zech [81]. Therein, at CS4 (x=4.5 m), the simulated bed profile by the proposed model agrees well with measured bed profile and simulated results by SWE-Exner model. However, at the other three cross sections, the simulated results do not estimate the bed profiles accurately in terms of quantitative assessment; the scour hole moves faster than experimental observation and the maximum height of deposited mound is a little bit larger than measured bed. However the trend of erosion and deposition and bed profile shape at every cross section is similar to the experimental

observations, which is qualitatively better than the simulated results by the coupled SWE-Exner model. With respect to the quantitative discrepancy, the following reasons are suggested: firstly, the effect of secondary currents is neglected in the 2D model, which most likely plays a significant role in this case with a sudden enlargement channel; secondly, in the physical process, the flow movement is accompanied by particle-particle collision which is not accounted for in the numerical model and such causes the simulated erosion and deposition processes to be more severe.
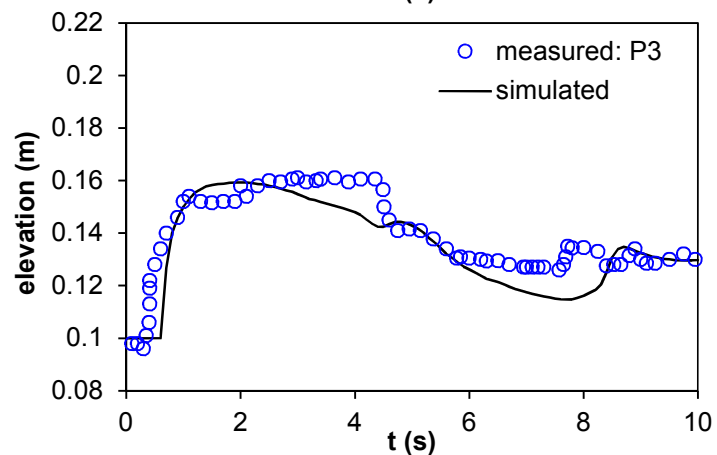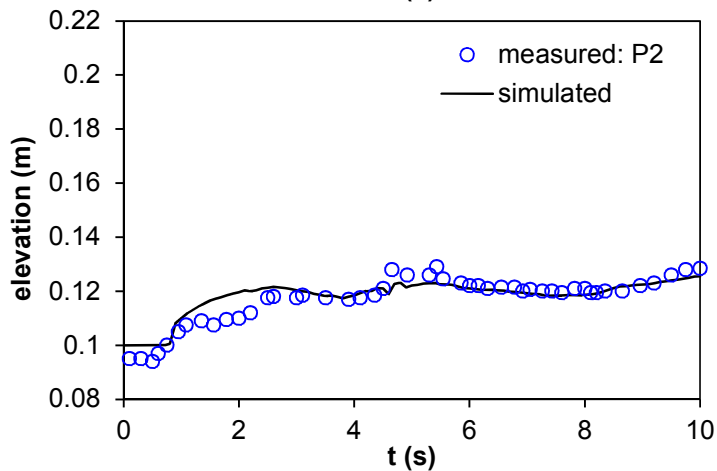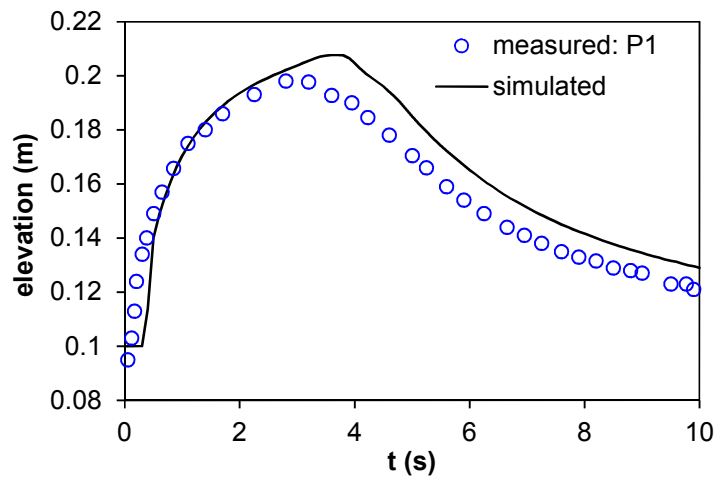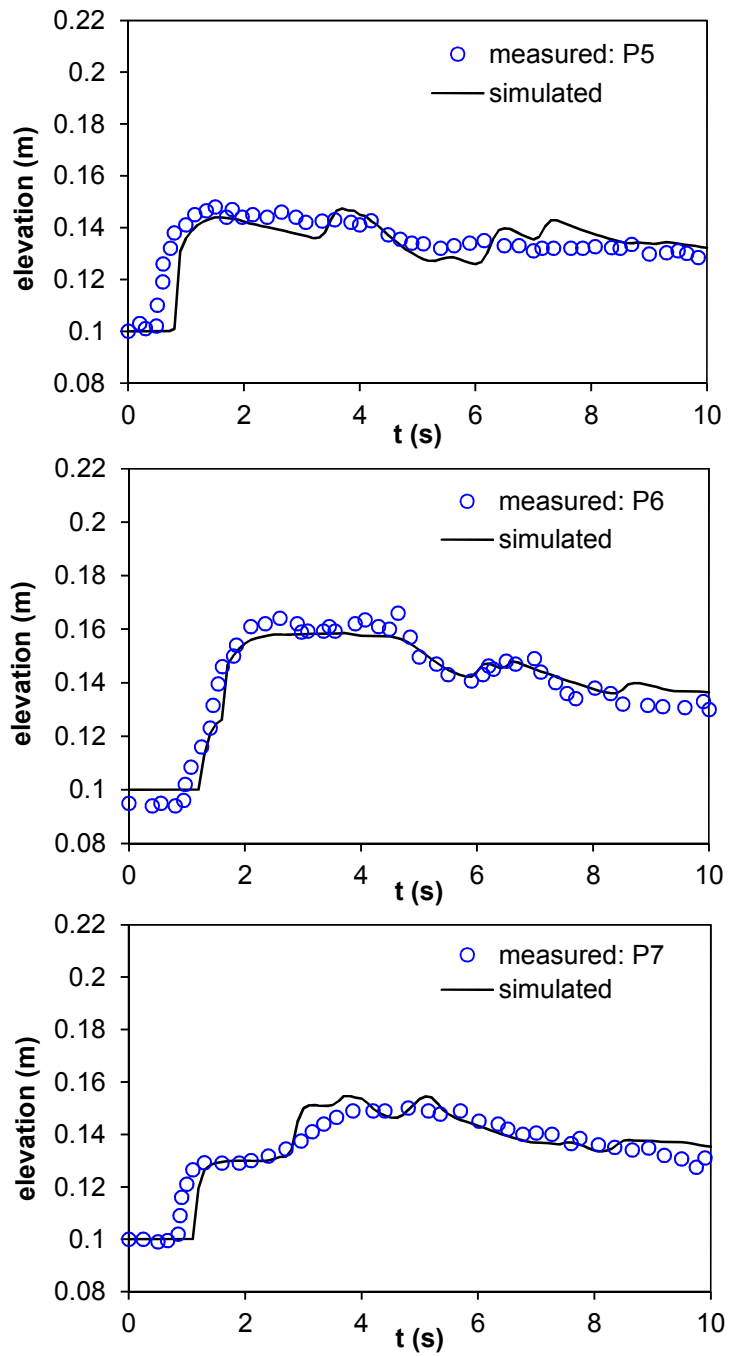
Figure 5.7 Comparisons between simulated and measured water levels at P1, P2, P3, P5, P6 and P7
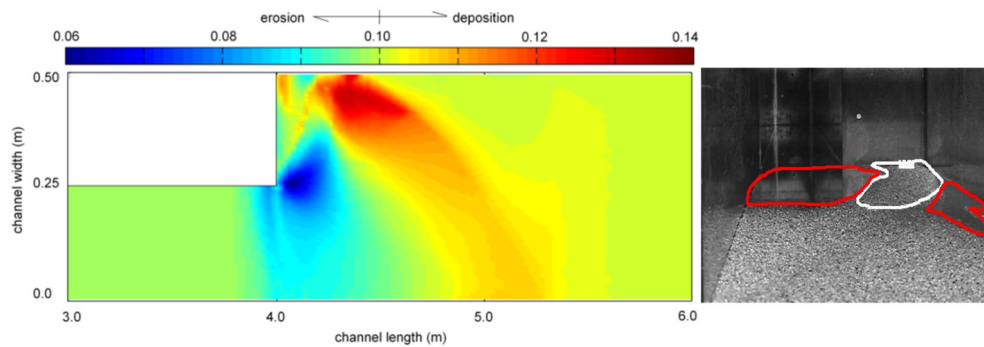
Figure 5.8 Final bed topography; left is simulated bed and right is experimental observation
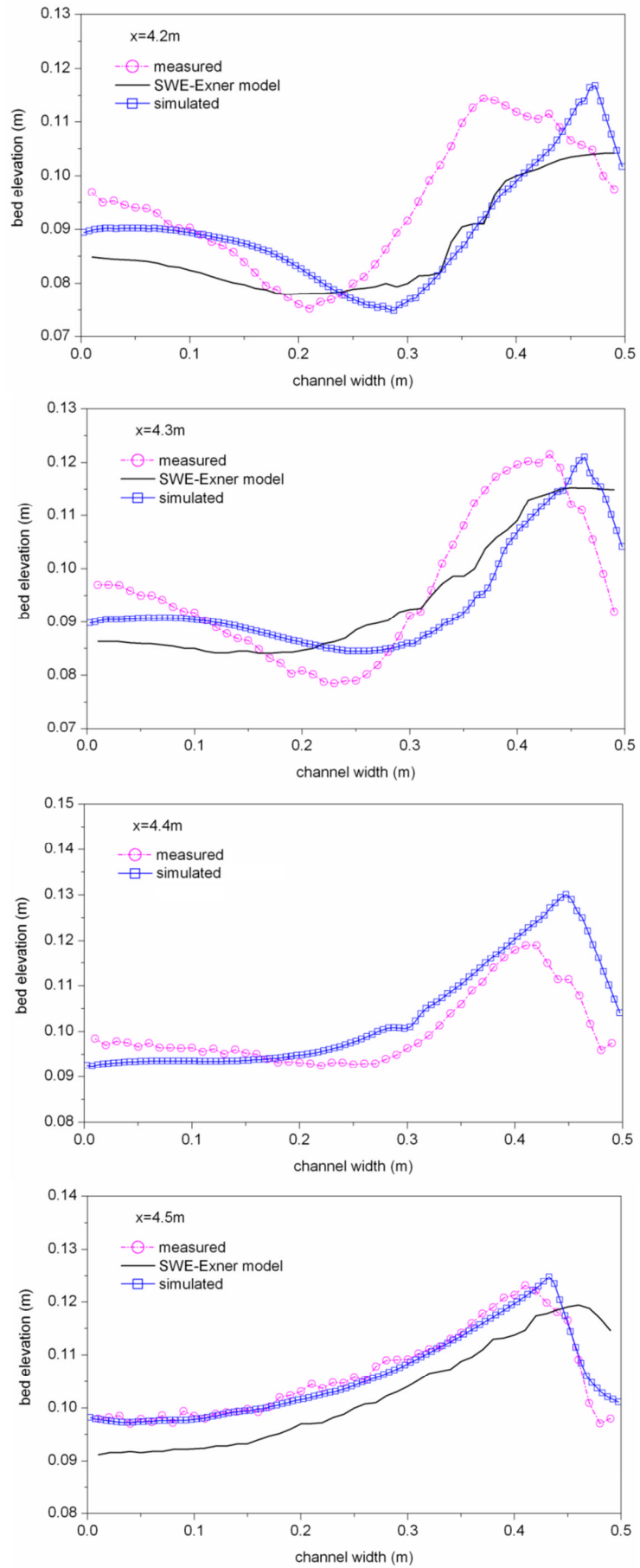
Figure 5.9 Comparisons between the simulated and measured bed profiles

5.3.4 Dam Erosion due to Flow Overtopping

Dam erosion due to flow overtopping is a complex flow process involving outburst flow, transition from supercritical flow to subcritical flow and eventually steady flow. This test is presented to verify that the 2D bedload model (STM1) can predict the erosion and deposition under complex hydraulic conditions. The experiment Run2 conducted by Chinnarasri et al. [166] is reproduced here. A dike was located in the middle of a flume of 35 m × 1 m × 1 m being 0.8 m in height, 1m wide with a crest width of 0.3 m. The upstream and downstream slope of the dam was 1V:3H and 1V:2.5H, respectively. The dike was composed of sand with a median diameter of 1.13 mm, and the density of $2.65×10^3$ kg/m³. The initial reservoir level was 0.83m and the downstream water level is 0.03m; the inflow discharge had a constant value of $1.23×10^{-3}$ m³/s; the bed material porosity was measured as 0.35; the Manning's coefficient n was determined as 0.018; the coefficient ψ=1.5 and μ=9.0 for this case.

For the simulation, the whole area is discretised by 700×10 cells (dx=0.05 m, dy=0.1 m); the sediment transport rate is calculated by the equation of *M_SJ* and *M_MPM* according to the extent of bed slope. Figure 5.10 illustrates the comparison between simulated dike bed profiles and measured data at t=30 s and t=60 s. It indicates that the comparison at 30 s show fairly good agreement, but at t=60 s, a significant discrepancy can be observed, in particular at the top of the dam where a scour hole occurs in the experiment, while the predicted bed profile is smooth. In fact, the measured scour hole occurs with randomness. Therefore, overall, the model can predict the dam erosion caused by the overtopping flow very well. Figure 5.11 illustrates the comparisons between the simulated results and the measured data: the water level and the outflow discharge. The agreements are reasonably good, but it is also found that the simulated water level is slightly smaller than the measured data before 90 s and the arrival time of peak discharge is a bit earlier. There is hitherto no one universal sediment transport equation available. Most of the empirical functions are derived based on the certain experimental data; nonetheless, they cannot be completely applicable to all the complex flow conditions. A simulation on a finer mesh has been performed and it is found that the mesh size is not a major reason causing the inaccuracies.
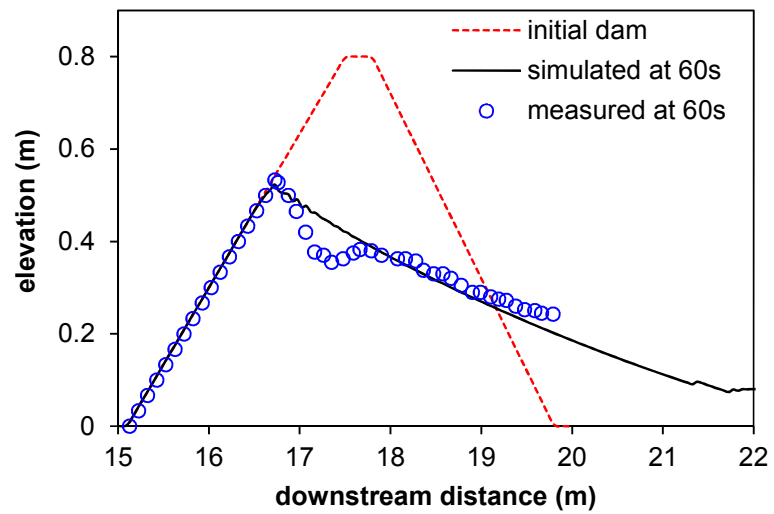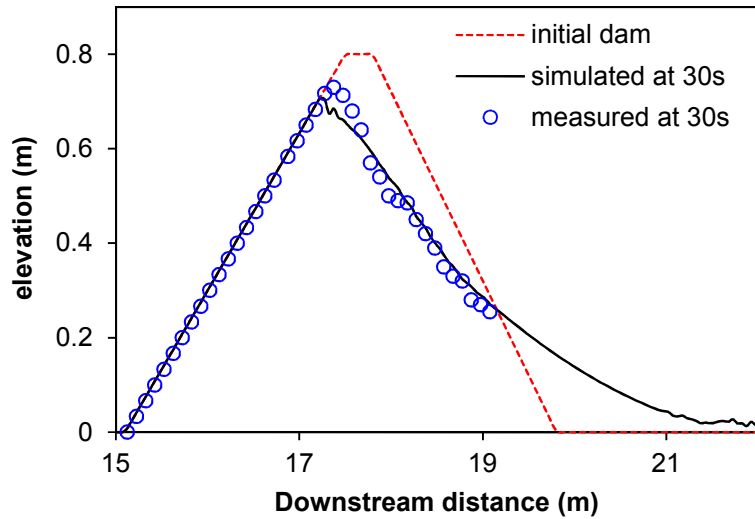
Figure 5.10 Comparisons between the simulated and measured dam profiles at t=30 s and t=60 s
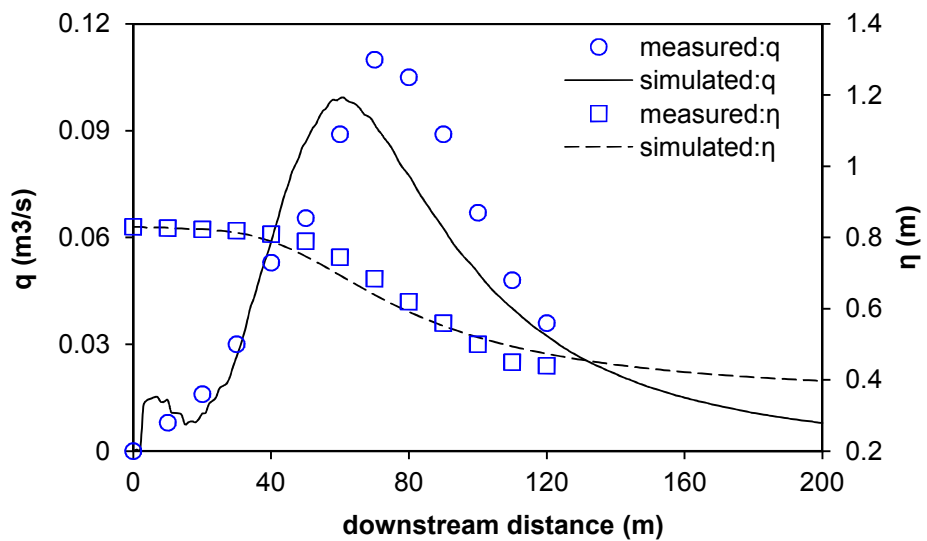
Figure 5.11 Comparisons between the simulated and measured reservoir water level and overtopping discharge

5.3.5 Applied to Dike Breach by Partially Flow Overtopping

An regular dike breach is usually treated as a sudden-break of constant breach width or area; however, in reality, it is usually a complex flow-sediment interaction process. In this section, a partial dike breach process is reproduced by the validated morphodynamic model. The predicted outflow hydrograph and the change of water level in reservoir are compared with experimental results. The complicated flow-sediment process is simulated reasonably well by the proposed numerical model.

5.3.5.1 Experimental Conditions

Breach formation experiments have been carried out by a number of research institutes in recent years [168, 169]. In this section, the experiment conducted by Université Catholique de Louvain [169] is simulated and results presented. As shown in Figure 5.12(a), the experimental conditions include: the channel flume dimensions were 36.2 m ×3.6 m; a 2.4 m wide and 0.47 m high in it sand dike was built in the location of 11.8 m along the flume, two fixed blocks were placed on the left and right sides of the dike; the upstream and downstream slopes of sand dike were 1:2 and 1:3 respectively, and there was a 10 cm thick sand layer in the downstream of the dike; the dike and downstream layer was constituted by sand with median diameter d_{50}=1.80 mm, the specific gravity of sand s=2.615, the loose bed porosity p=0.42 after compaction. The upstream reservoir was separated by a gate in front of which the water was stored. On starting the experiment, the gate was gradually lifted so the water filled the second part of the reservoir until water level arrives to 0.45 m in both parts. Based on that, a trapezoidal breach was dug on the top middle of dike and the size of breach is illustrated in Figure 5.12(b). Then, flow overtopping occurred and the dike breach enlarged gradually with time.
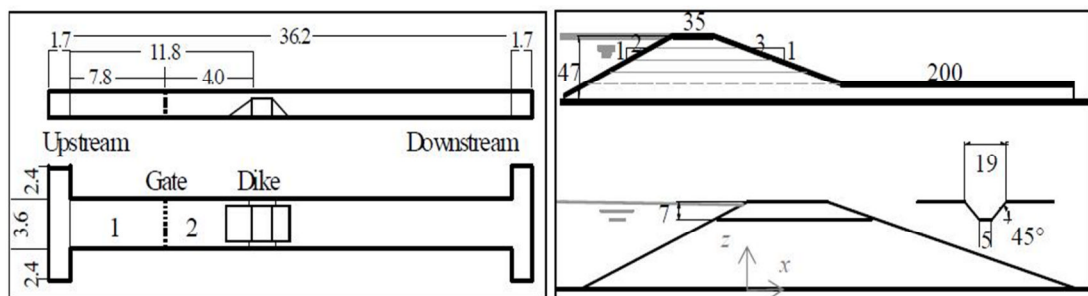
Figure 5.12 (a) dike position in the flume (m); (b) dike and trapezoidal breach initiation size (cm) [170]

5.3.5.2 Measured data

The measured data in the investigation of [169] is used, including:

(1) the water level change against the time in the upstream reservoir;

(2) the outflow discharge against the time; the outflow discharge was estimated by using the measured water level, which can therefore cause a large uncertainty; the estimated outflow hydrographs [169, 170] shows that the uncertainty range is very significant; the average of estimated discharges is used in the following;

(3) full digital terrain models (DTMs) of the breach topography interpolated from laser-observed transverse profiles.

5.3.5.3 Predicted Hydrograph

For simulation, the whole dike and channel are discretised with dx=0.035m and dy=0.03m. The coefficients ψ=1.5 and μ=9.0 are used for this case. For such kind of flood events, the outflow peak discharge is a vital hydraulic parameter that needs to be predicted. Traditional methods often estimate the peak outflow discharge by use of empirical relations or physical-based model with a lot of simplifying assumptions [171-173]. However, the present morphodynamic model is constructed from the viewpoint of fluid dynamics and sediment transport mechanisms. The spatial and temporal evolution of the entire flood process can be well simulated in this simple and effective approach, including the outflow hydrograph, the peak outflow discharge, the change of water level, as well as the evolution of breach size etc. Manning's coefficient n has a direct influence on the bed shear stress which decides the quantification of flow-induced sediment transport; therefore, four different Manning's coefficients (n=0.017, 0.018, 0.019, 0.02) are used for evaluating and analysing its sensitivity in the modelling of the dike breach process. For the measured results, Figure 5.13 illustrates the comparisons between the predicted results and the measured data, involving the outflow hydrograph (Figure 5.13a) and the water level in the reservoir (Figure 5.13b). It can be seen that the Manning's coefficient changes the value and the occurrence time of the peak outflow discharge, consequently the water level in the reservoir is also changed. More specifically, the larger Manning's coefficient leads to more water outflow from the reservoir, thus the outflow peak discharge becomes larger and occurs in earlier time; conversely, for smaller Manning's coefficient, the peak outflow discharge is smaller and occurs later. This is primarily because the increasing of Manning's coefficient increases the calculated bed shear stress, which induces more sediment to move, so the dike is eroded more severely and thereby the breach process is

accelerated. Furthermore, some small oscillations occur at the simulated outflow hydrograph, particularly at the peak stage. This is because the lateral bed avalanching erodes the sediment material into the breach, which raises the elevation of the breach temporarily and plays a blockage role there; then the further erosion occurs based on the previous updating of the bed. Overall, the present model predicts the outflow hydrograph and the temporal change of water level in the reservoir effectively with good agreement. In the following simulation, n=0.018 is chosen because the model reproduces the peak discharge accurately at this value.
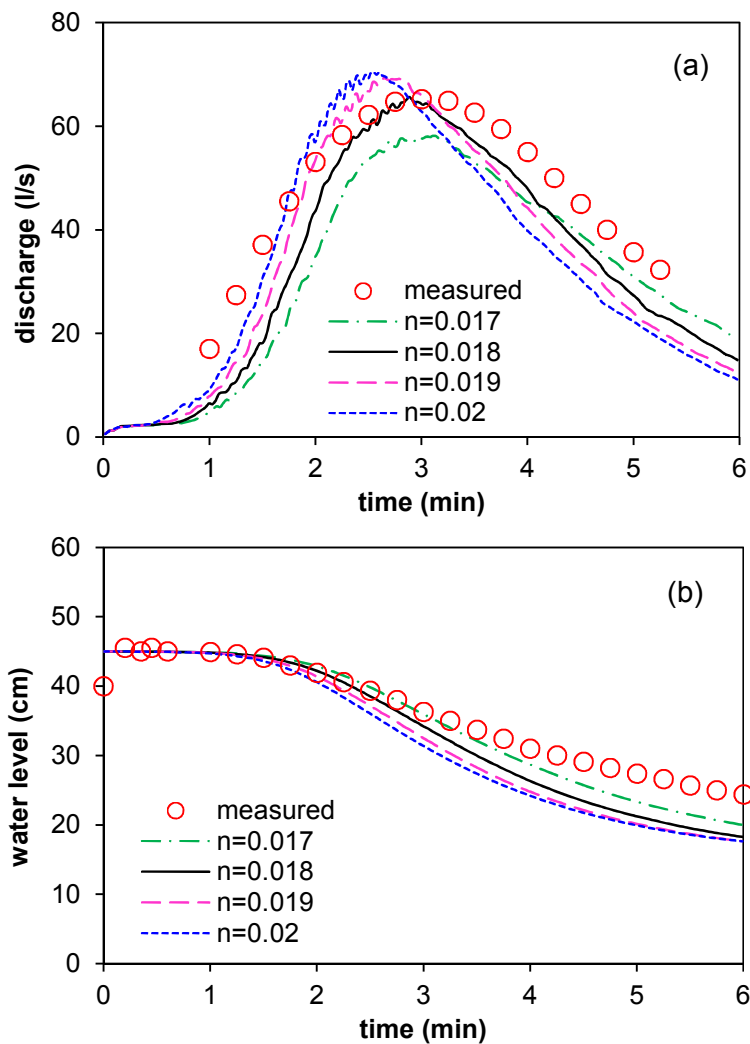
Figure 5.13 (a) outflow discharge; (b) water level against with time

5.3.5.4 Simulated dike breach

As mentioned above, the DTMs [169, 170] are used to compare with the simulated dike terrain in order to show the capability of the present model and the bed slope avalanching model to predict the breach size. It needs to be clarified that the DTMs suffer from a lack of precision because of the distinct refractive indexes of the laser in water and air which are not

considered. Figure 5.14 demonstrates the digital terrain for measurement and the simulated dike breach at the initial stage t=20s and the final stage t=370s. The breaching process is reasonably well reproduced by the numerical model and the bed slope avalanching model. However, the numerical model predicts slightly more severe erosion at the downstream toe of the dike at t=20s; obviously more deposition occurs there than observed in the experiment. At t=370s, it is shown that the more severe erosion can be observed at the middle area of the dike, whilst the weaker lateral erosion occurs at both sides of the breach. In other words, the numerical model overestimates the vertical erosion, but the bed slope avalanching model slightly underestimates the lateral erosion, presenting a narrower breach.
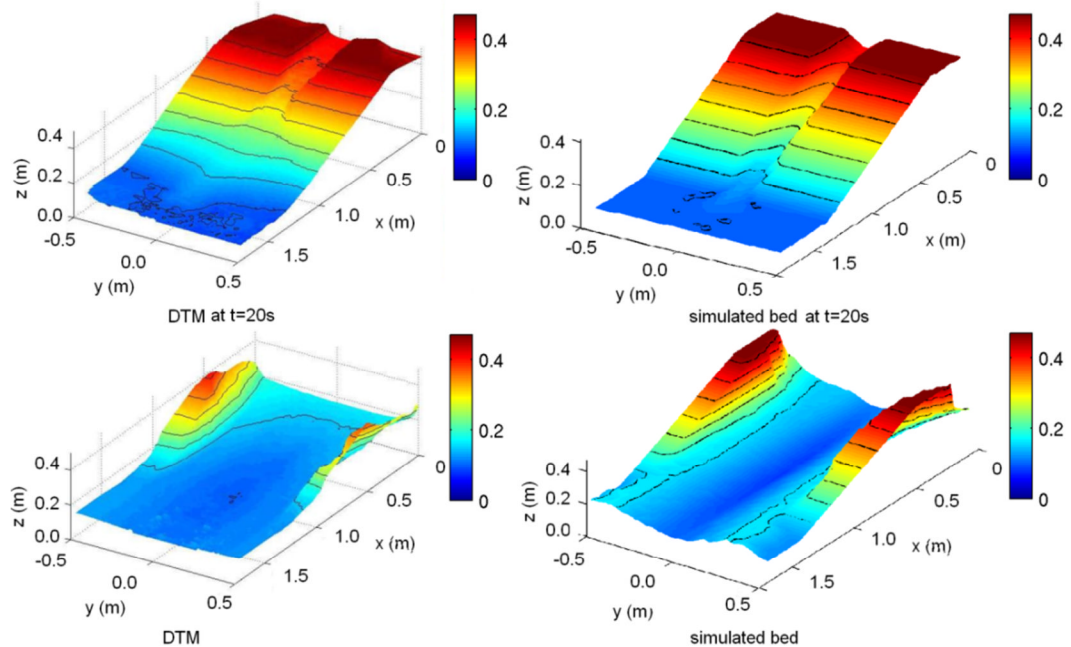
Figure 5.14 Dike breach due to flow overtopping at t=20s and 370s

Furthermore, from a wider view, Figure 5.15 shows the simulated spatial distribution of bed and water, as well as the experimental figure at the final equilibrium stage. It is found that the present model reproduces the characteristic erosion, deposition and wet/dry area well; more specifically, the eroded sediment from the breach primarily deposits behind the dike and a secondary channel along the centreline is formed. In summary, the present model can reproduce the dike breach process effectively, however the model also presents some shortcomings which need to be addressed when being applied: (1) the empirical parameters related to sediment transport affect the modelling results to different extents; an appropriate calibrated parameter is very important for the evolution of the breach size and also for the outflow hydrograph; (2) the criterion of bed slope avalanching is based

on the consideration of the relationship between the real bed slope and the critical angles, however, the randomness of lateral erosion in a dike collapse is difficult to predict and the present bed slope avalanching model probably is not applicable once this occurs, as it would cause bias for the predicted breach profiles; (3) as mentioned above, the failure time step depends closely on the sediment material properties; two different failure time steps have been tested for this case, although the final breach size is hardly influenced by them, the arrival time of the discharge has a slight difference, thus, the failure time step should be also paid attention to.
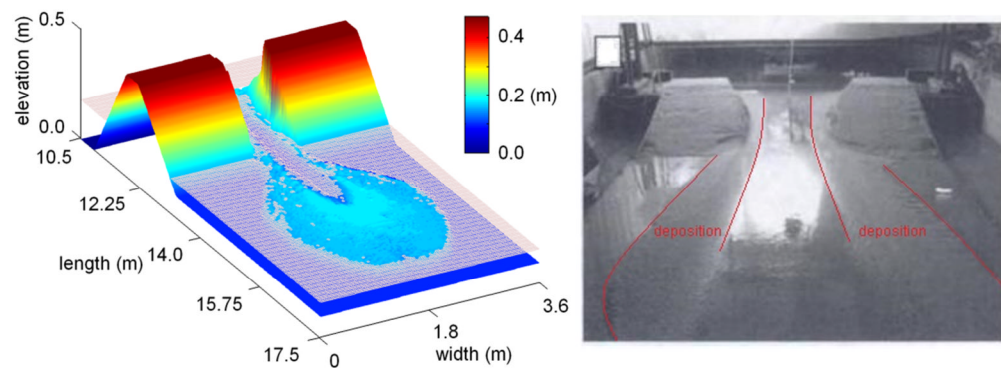
Figure 5.15 Simulated final dike breach and water surface

5.3.5.5 The role of bed slope avalanching

As mentioned above, the main purpose of the bed slope avalanching model in this case is to simulate the later erosion of the dike. We can postulate that the dike breach will stay constant in the horizontal direction and that erosion can only occur in vertical direction if no bed slope avalanching is implemented. Although the different critical angles and re-formation angles above and below the water are suggested for use [169], the values of these angles are still ambiguous which directly influences the breach size and the outflow hydrograph. Also for the dike breach process, it has been investigated that the apparent cohesion represented by the pore-water pressure influences the stability of the breach slide slopes and thereby the whole breach process [174]. To further investigate the effects of these angles, four runs with four different pairs of angles are implemented: run1 (82°, 34°) means the critical angles above and below the water are 82° and 34° respectively, it is similar for run2 (72°, 34°), run3 (82°, 30°) and run4 (62°, 30°); the re-formation angles are equal to the critical angles minus 2°. For the breach cross-section profiles, the comparisons for the four runs at the upstream slope of the dike, the dike top and the downstream slope of the dike are demonstrated in Figure 5.16. It is shown that the breach width is obviously influenced by the angles; more specifically, the smaller the critical

angles, the wider the breach size, but the side slope of the breach is steeper for the larger critical angles. These effects can be easily explained by the fact that bed slope avalanching can occur at the earlier time, also more lateral erosion occurs for the smaller critical angles. The comparisons of the simulated results by the four runs show that the bed slope avalanching model is extremely important for the dike breach process and the critical angles used play a crucial role in the final breach size.
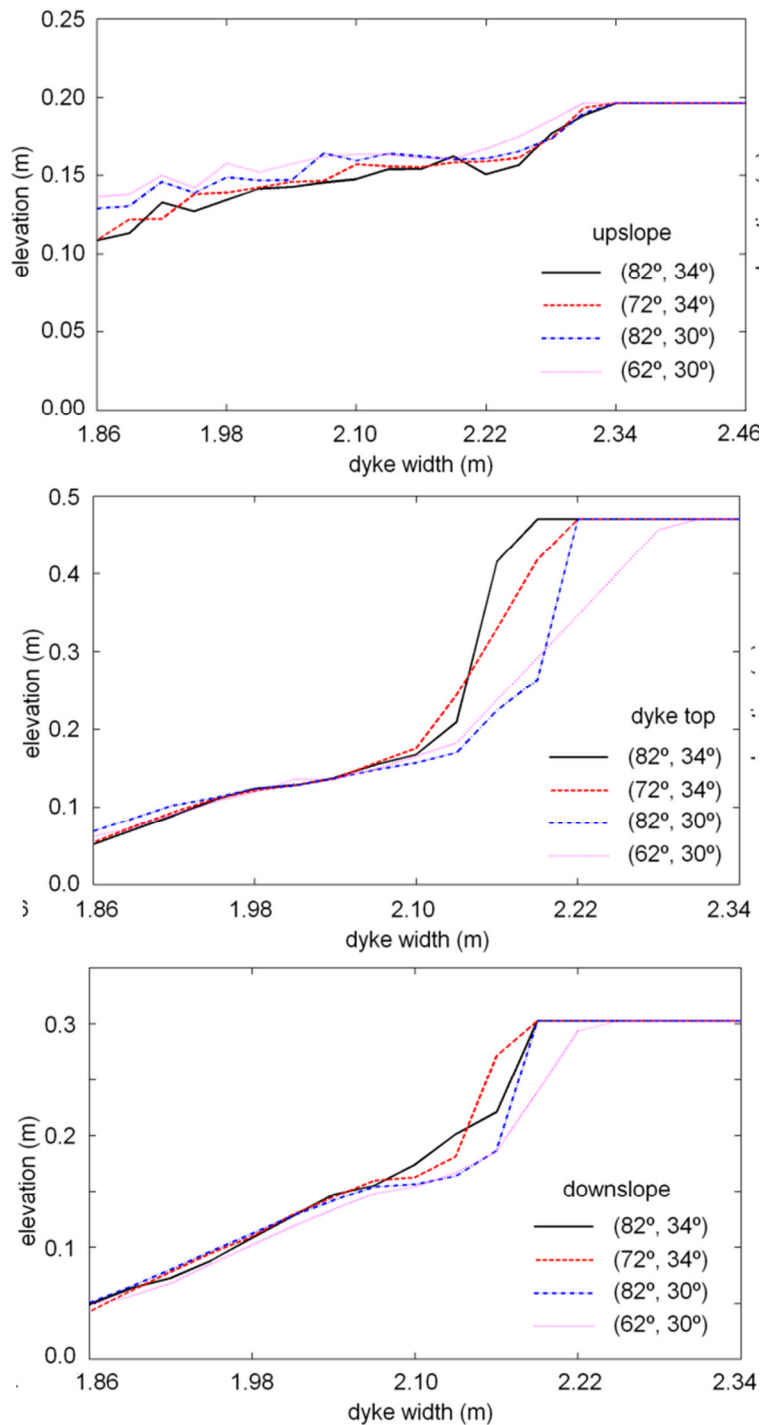
Figure 5.16 Comparisons between predicted bed cross-sections for the four pairs of angles at the upslope, top and downslope of the dike

5.4 Concluding Remarks

In conclusion, a 2D non-uniform morphodynamic model has been built on 1D model proposed in Chapter 4 based on shallow water theory and non-equilibrium sediment load assumptions. Also a 2D bed slope avalanching model is incorporated. The 2D model is solved by a robust numerical scheme based on the research output of Chapter 3, including handling the wetting/drying issues and addressing the bed slope term. The model is validated by several experimental benchmark tests, presenting good agreement with the measured data in terms of both hydrodynamic and morphodynamic aspects. The results show that the proposed 2D hydro-morphodynamic model is capable of predicting both hydraulic information and geomorphic impacts effectively. In addition, the proposed model can predict the flood event caused by dike breach due to partial flow overtopping, in terms of not only hydrograph, but also dike breach evolution.

Chapter 6
Application to a Full-scale Rapid Outburst Flood

6.1 Introduction

Outburst floods are one of the most catastrophic natural hazards for populations and infrastructure, including man-made dam break floods, glacial outburst floods and sudden release of meltwater from ice sheets caused by volcanic activity etc. [3-8]. Such high-magnitude, sudden onset floods generally comprise an advancing, intense kinematic water wave which can induce considerable geomorphic change rapidly. Therefore, the exploration and investigation of this kind of flood cannot be limited to water flow solely, but also flow-induced sediment transport. Glaciers and ice sheets are important sediment carriers so that sediment transport caused by glacial outburst floods is usually orders of magnitude larger than those in regular fluvial processes [175, 176]. One of a variety of mechanisms initiating glacial outburst floods is that due to the volcanic activity as the high temperature of the volcano results in the glaciers and ice sheets melting rapidly, and thereby causing large volumes of meltwater and erupted material to be released abruptly [9, 10, 177, 178]. Such flooding can cause damage to property and communications in glaciated areas. In recent decades, attention has increasingly been paid to numerical modelling of such flood events [5, 56, 177] because it is money-saving and convenient to implement. The problem though is that the exact predication of sediment transport is unattainable entirely, they can, however, enhance and improve our insights into the rapid sediment-laden floods.

To date, a variety of morphodynamic models have been developed to emphasise the erosion and deposition by outburst floods [11-18]. However, most of them have been limited to investigations of theoretical analysis or testing small-scale laboratory experiments, and have not been tested on the events of large-scale rapid flooding, so there is a danger that they might not work as expected on rapid geomorphic change in large-scale outburst floods, and the understandings obtained from small-scale experiments may not be applicable to large-scale flood events. According to the investigations [4, 9, 10, 179, 180], sediment transport is one highly transient aspect of the sudden onset floods where sediment is entrained by intense flow and then affects flow hydraulics in return; and the deposition of sediment occurs when the flow energy is not enough to support sediment material in motion.

Furthermore, in such kind of glaciated areas, sediment material is constituted by coarse-particle gravel with several or tens of centimetres and some fine sand. From the views of laboratory observations [37, 42, 44], the gravel sediment in sudden onset floods is generally transported in bedload dominant mode in a specific layer, a so-called sheet flow layer. While suspended load of fine particles is usually transported in upper suspension layer. In such circumstances, a layer-based morphodynamic model is more appropriate to use for simulation and thereby gain better understanding of the complex flow-bed interactions in sediment-laden outburst floods.

In historical time, glacial outburst floods induced by volcanic activity have frequently occurred in Iceland and one of them is a well-documented volcanically-generated flood bursts from Sólheimajökull southern Iceland in July 1999 [9, 10, 179]. In this chapter, such a flood is reproduced by the proposed 2D hydro-morphodynamic model in previous chapters based on shallow water theory. As mentioned above, the existing numerical models emphasising the within-channel erosion and deposition by sudden onset floods have seldom tested against real large-scale flooding data. It is necessary to take such concerns into consideration and gain the further insights obtained from modelling these extreme flow will be important for hazard management. Consequently, the motivations of this chapter are: (1) to verify the applicability of the proposed hydro-morphodynamic model in complex full-scale outburst flood event; (2) to improve the insights and understandings of the unsteady fluvial hydraulics and flow-sediment interactions in large-scale outburst floods from the consequential numerical results.

6.2 Study Area and Floodwater Routing

A volcano-induced glacial outburst flood occurred unexpectedly at Sólheimajökull, Iceland in July, 1999. It was well documented and has been physically investigated in detail [10, 179]. Sólheimajökull is an 8km long temperate, non-surging outlet glacier draining the Mýrdalsjökull ice cap belonging to the southern volcanic zone in southern Iceland (see Figure 6.1). The surface area of the glacier is 78km^2 [181] with a snout 1 km wide, and is slightly over deepened. There is a river channel called Jökulsá á Sólheimasandi draining Sólheimajökull and it has three main inflow sources (See Figure 6.2) [10]: (1) the first exits Jökulsárgilsjökull, an outlet glacier 3km to the north of Sólheimajökull; (2) the glacial meltwater from

Sólheimajökull itself via a 1km long subglacial tunnel; and (3) the river Fjallgilsá, converging the Jökulsá approximately 2km downstream of the glacier snout. Furthermore, several small streams are converged into the main river before flowing under the road bridge approximately 5km downstream of the glacier terminus.
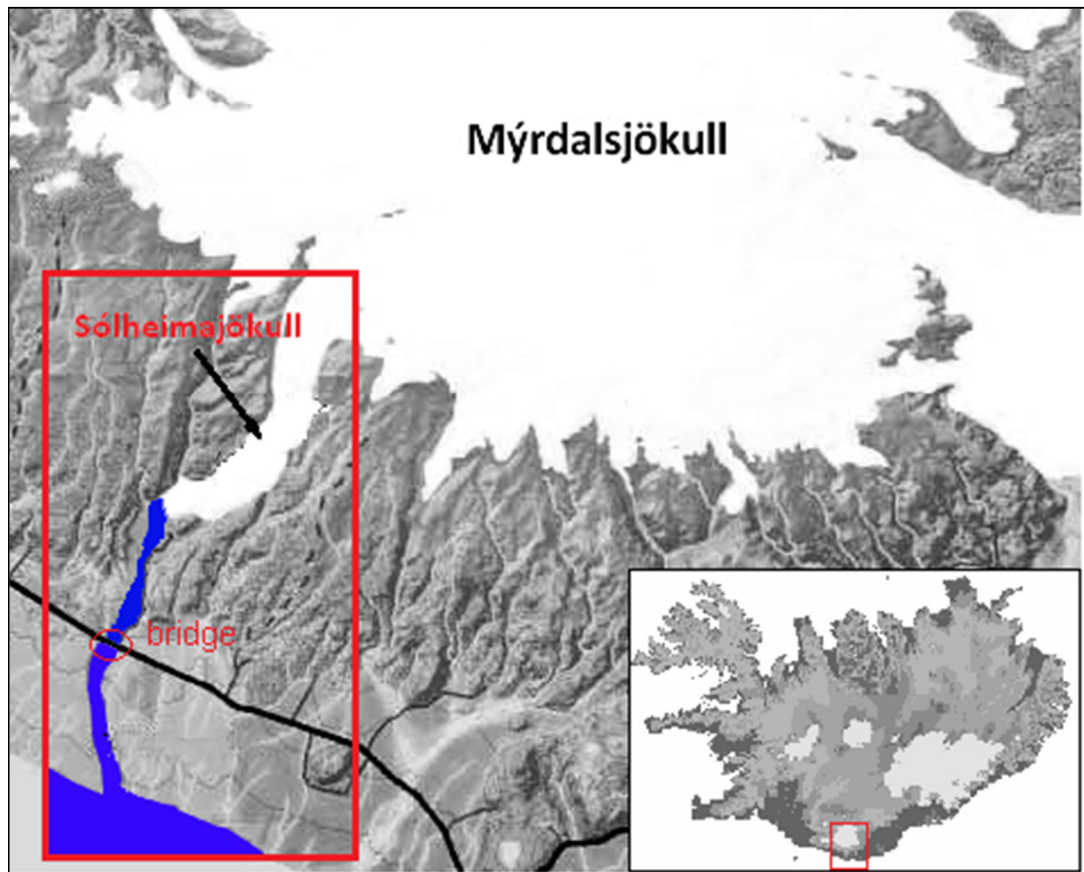
Figure 6.1 Location of Sólheimajökull and Mýrdalsjökull in southern Iceland

The glacier is located in volcanic zone so that the eruption of volcano can result in the ice sheet melt rapidly because of the high temperature to generate outburst flooding. In July 1999, an unexpected glacial outburst flood occurred at Sólheimajökull [182, 183]. The flooding process was sudden, short-lived and high discharge. The high discharge lasted approximately 6h and after about 24h the discharge in the Jökulsá á Sólheimasandi was back to normal. The flood burst initially from the western margin of Sólheimajökull. On exiting the glacier via a series of ice fractures and conduits, the flows drained ice-marginally into a former ice-dammed lake basin, approximately 3.7km from the glacier snout and filled it (Figure 6.2a location). Then the meltwater over spill from this lake basin flowed into a lower tributary valley, Jökulsárgil, whose storage capacity was approximately 1×10^6 m^3 ± 0.05×10^6 m^3 (Figure 6.2b location). Additional floodwater converged to enhance the discharge into Jökulsárgil along the

western margin of the glacier between the upper basin and Jökulsárgil. Meanwhile an amount of shattered glacial ice entered into Jökulsárgil with meltwater caused by ice fracturing. Supra-glacial fracture outlets about 3km from the glacier snout also carried quantities of sediment-laden floodwater [182, 184]. This routing in the Western Conduit of 150m wide is the biggest floodwater source, and the other flood source is the Central Conduit that opened up in the centre of the snout draining the majority of waning stage and post-outburst flooding flow. The floodwater in the two conduits was accumulated into the river channel, Jökulsá á Sólheimasandi. Moreover, there were some smaller flows exit the eastern margin of the snout from a small, newly-cut, steep-sided channel and from a series of minor outlets flowing across vegetated hillslopes.

Part A
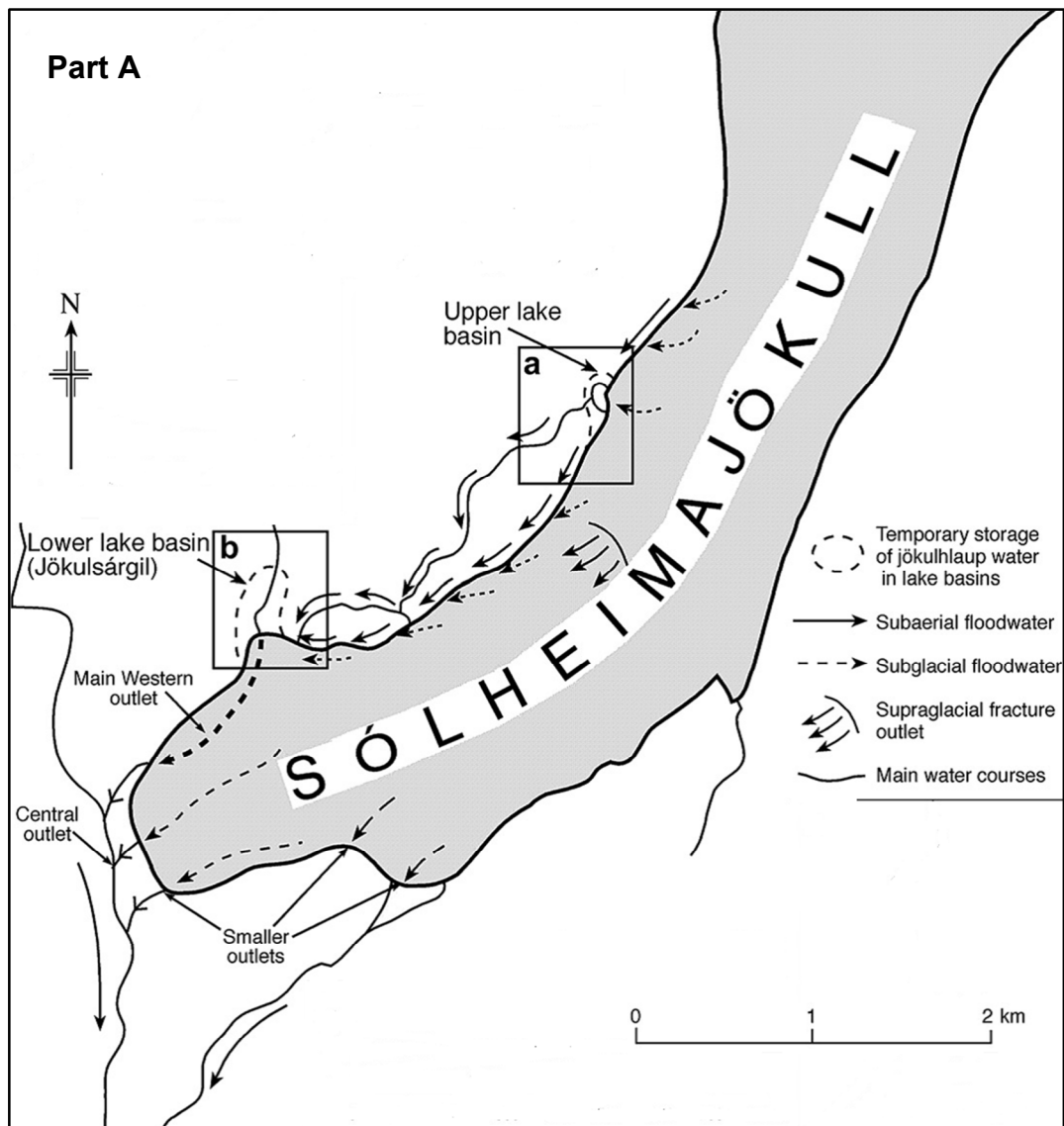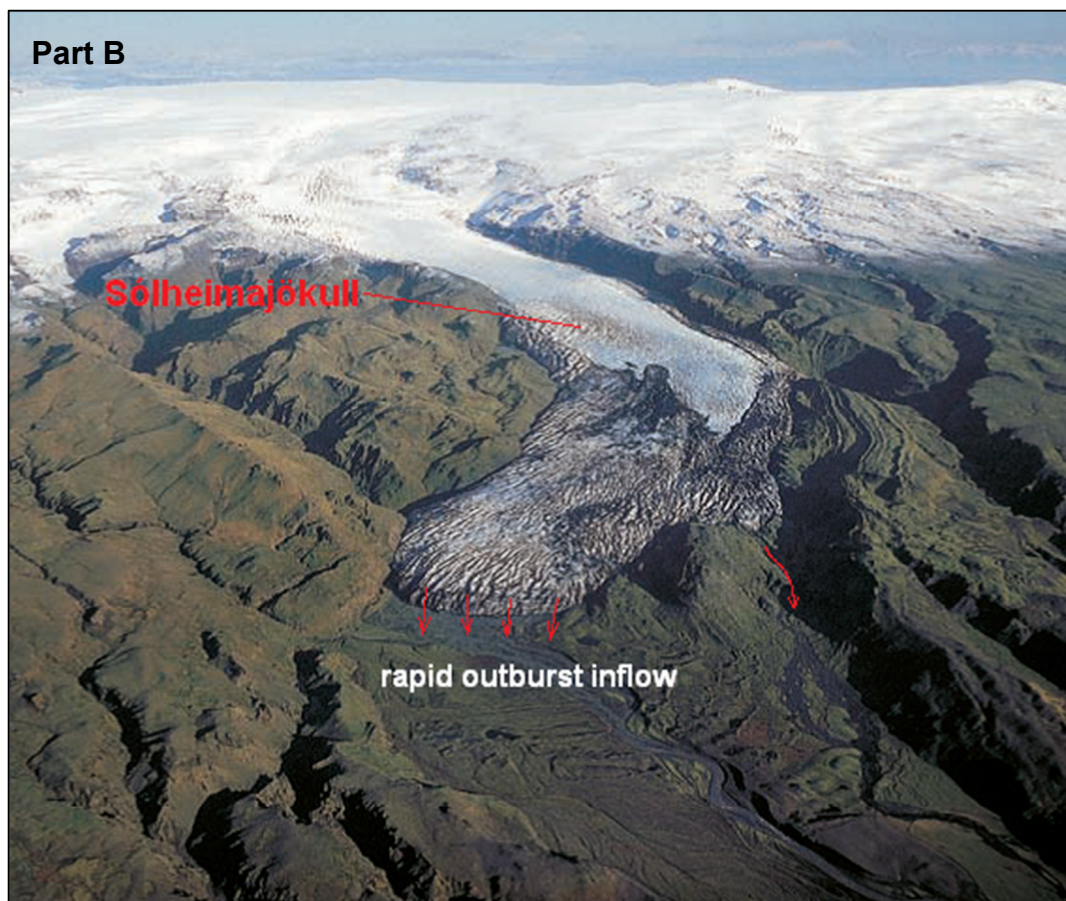
Figure 6.2 the July 1999 flood routeways and temporary floodwater storage locations [10]

6.3 Data Collection and General Considerations

The dataset used in this study is shown in Table 6.1. Measurement of topography was made using airborne LiDAR before the flood occurred. This study utilises two constructed DEM datasets with different resolutions (8 m × 8 m and 4 m × 4 m) in order to elucidate the balance of computational efficiency and accuracy. The whole research river channel is approximately 9km long and around hundreds meters wide. The reconstructed flow hydrograph of the sudden onset flood is used as the inflow boundary, and the outflow boundary is set as open free because the flow enters into the sea. Figure 6.3 illustrated the inflow hydrograph from the two conduits ignoring the flow from smaller outlets at the eastern margin.

In reality, the river channel is generally composed of different sediment grain size fractions. According to the field observations (Figure 6.5) [10], the sediment material is constituted by different grain-size particles from fine gravel to coarse boulder. The properties of the sediment fractions are

summarised in Table 6.2. It can be seen that the median diameters for the three fractions differ significantly. In fact, the estimation of grain-size in a 9km full-scale channel is fairly ambiguous and difficult. The sediment diameter is therefore considered to be an uncertainty factor for the modelling. As the water depth is only approximately 2m-5m in most area for this jökulhlaup, the coarse boulder with a median diameter of 0.4m seems relatively very large. Importantly, there are not hitherto any sediment transport functions suitable enough that could be appropriated for the transport of such coarse boulders. Also, the proportion of the coarse boulders is small. Consequently, an appropriate simplification is assumed in that the sediment fractions of granules and cobbles are only considered in the morphodynamic modelling.
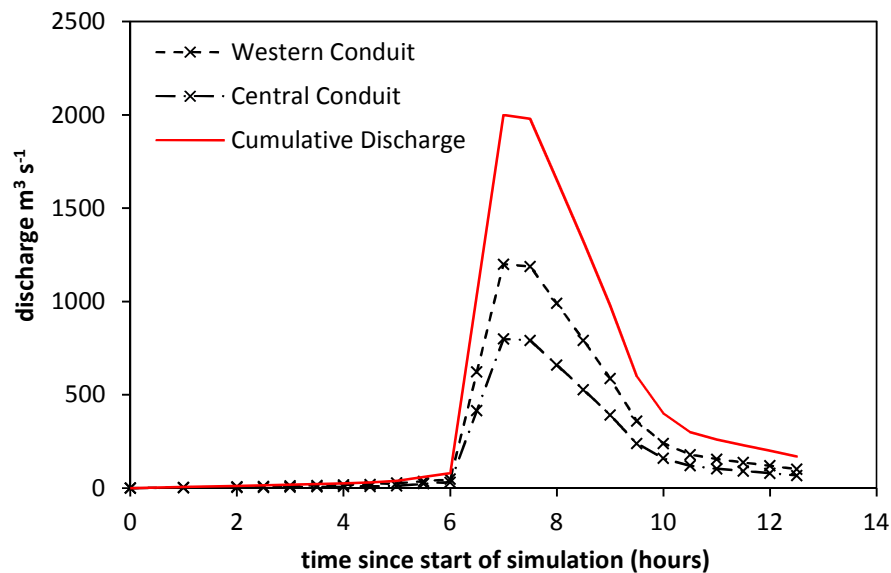
Figure 6.3 The hydrograph from Western Conduit, Central Conduit and cumulative inflow discharge

Table 6.1 Data used in the study

Data collection	Explanations
Pre-flood DEM topography (Figure 6.4)	Resolution1: 4m×4m Resolution2: 8m×8m
Inflow hydrograph	Cumulative discharge from western and central conduit is input to the hydro-morphodynamic model (Figure 6.3)
Sediment composition	The sediment information was documented (Figure 6.5, Table 6.2). The non-uniform grain-sizes are input to the model.
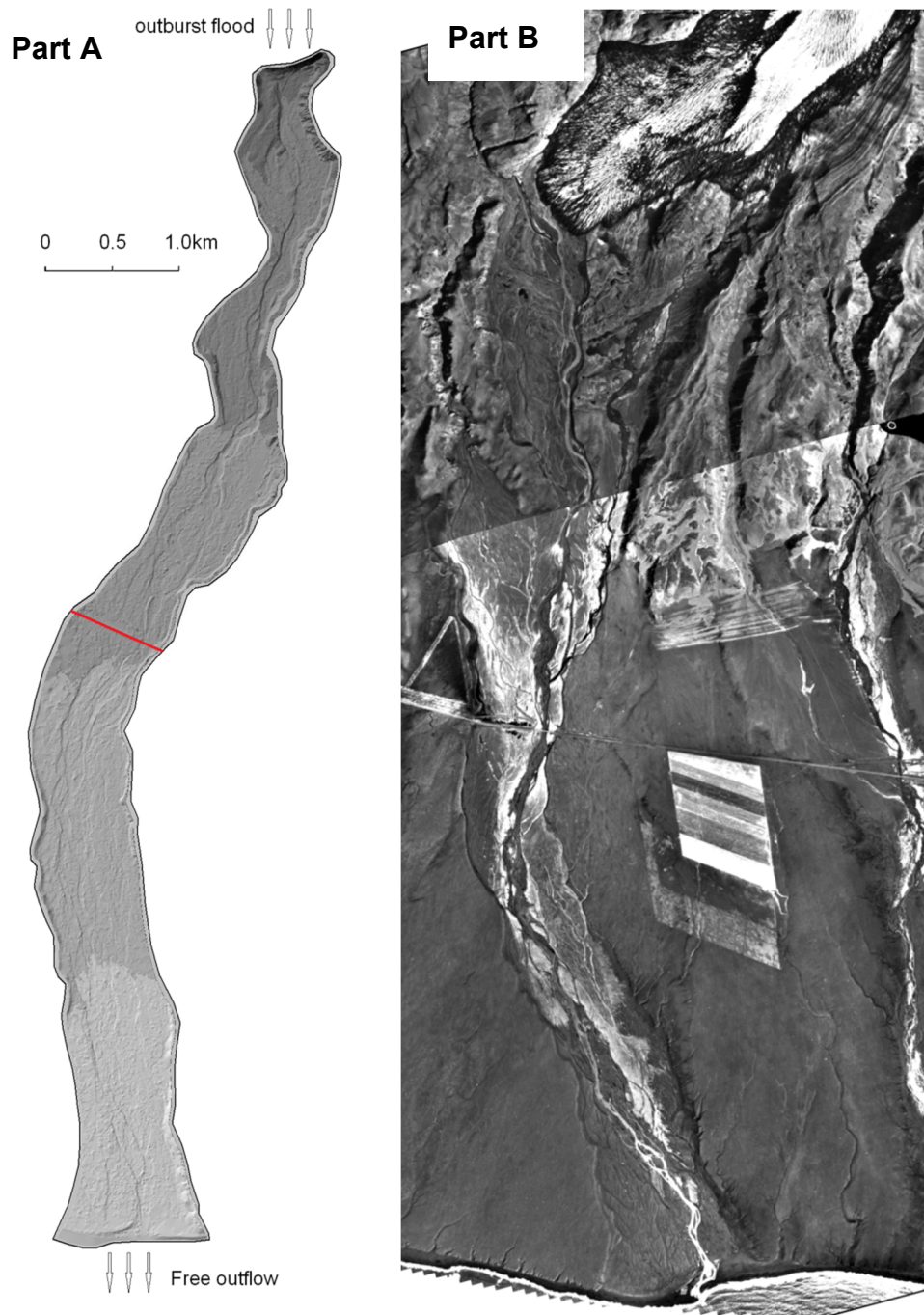
Figure 6.4 Input DEM topography
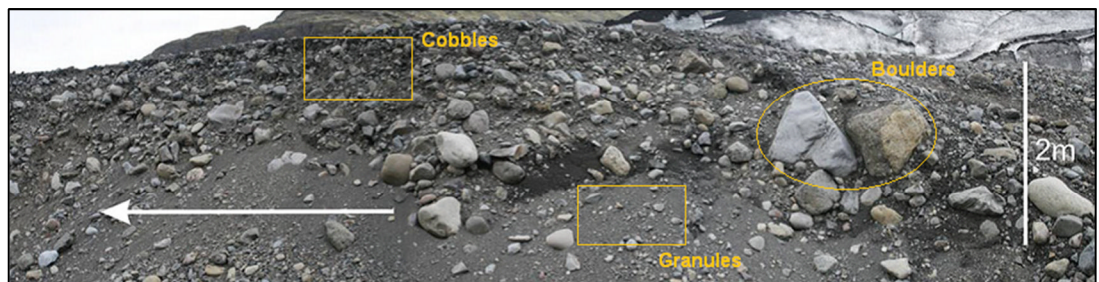
Figure 6.5. Sediment composition of the river channel

Table 6.2 Properties of sediment grain size fractions

Sediment grain size fractions	1	2	3
	Granules	Cobbles	Boulders
Median diameter (mm)	2.8	105	400
Specific density (kg/m^3)	2680	2680	2680

In addition, the inflow discharge before 6 hours is the base flow and the outburst flood that occurred from the 6th hour until the 12th hour (see Figure 6.3), thus the simulation is carried out mainly over this period, so we define the start-time of the flood as zero and the end-time as 6 hours when the transient outburst flood finished. Moreover, a bridge is located near to x=332908.86, so this cross section (x=332908.86) is chosen to be a typical one in order to analyse the flow-sediment process. As for the estimation of Manning roughness, many empirical relationships have been proposed [185, 186], in this study, the Manning's coefficient n is estimated according to $n = 0.038d_{90}^{1/6}$, where d_{90} is the 90th percentile grain-size values.

6.4 Model Setup

6.4.1 Computational Model Equations

For this sudden onset flood, the discharge reaches about 2000 m^3/s and also the bed includes fine granules of about 2.8mm. Therefore, a combined model of sheet flow and suspended load is applied to simulate it. As described in Chapter 5, the computational model contains hydrodynamic model (Eqs.(5.1) (5.2)), a flexible sediment transport model (Eq.(5.11)), as well as morphological evolution model (Eq.(5.12)). The model system is solved by the numerical scheme proposed in Section 5.2.

6.4.2 Closure relationships

The closure parameters for the model are determined by the relationship introduced in above-sections. They include the frictional slopes S_{fx}, S_{fy}; bedload transport capacity; the non-equilibrium adaptation length L of bed material load; the setting velocity of sediment particles; the entrainment rate and deposition rate of sediment etc.

6.5 Modelling Results and Discussion

6.5.1 Inundation for Flood Without Sediment

In order to explain the role of sediment transport in the rapid flood, a run of the flood with clear water was first conducted. Figure 6.6 illustrates the maximum water surface and minimum bed elevation at each cross section. Figure 6.7 shows the simulated spatial change of the flood water depth. The bridge and a gauge exist at the position of (332908.86, 480099.78). It is shown that the arrival time of water front at the bridge location is about 32.4 minutes and the peak discharge arrives there after approximately 82.1 minutes after the flood occurs; moreover, the maximum water depth was calculated as being about 2.98 m. As the water is released suddenly, the water level increases to a maximum depth very rapidly, and it then decreases progressively as the level in the volcanic lake is reduced. The extent of the flood inundation reduces correspondingly as shown in Figure 6.7. There, at about 2 hours the flood waters cover a significant portion of the domain.
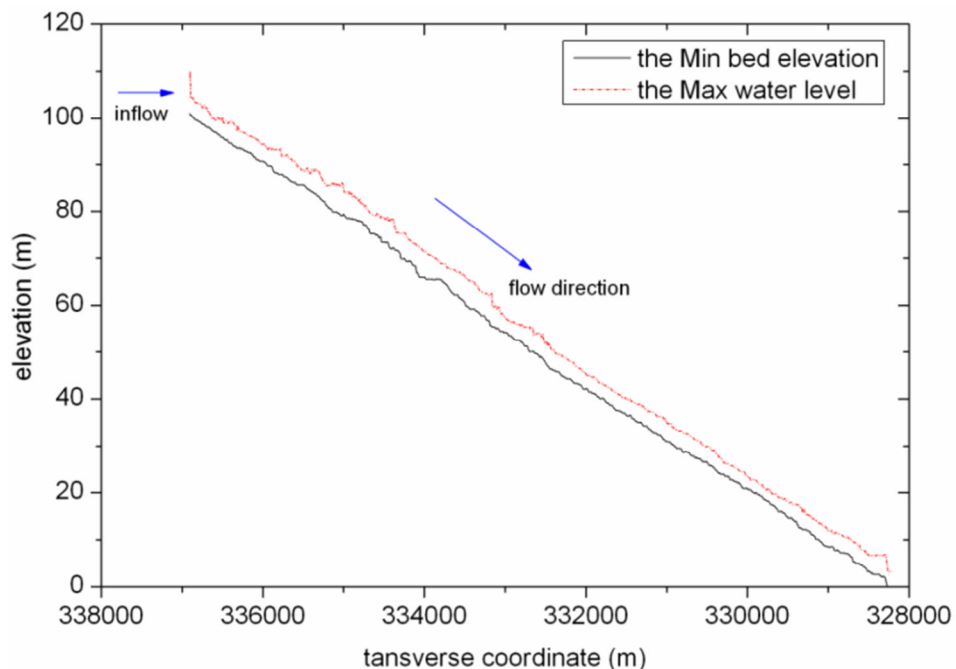
Figure 6.6 The maximum water surface and the minimum bed level in the entire river channel.
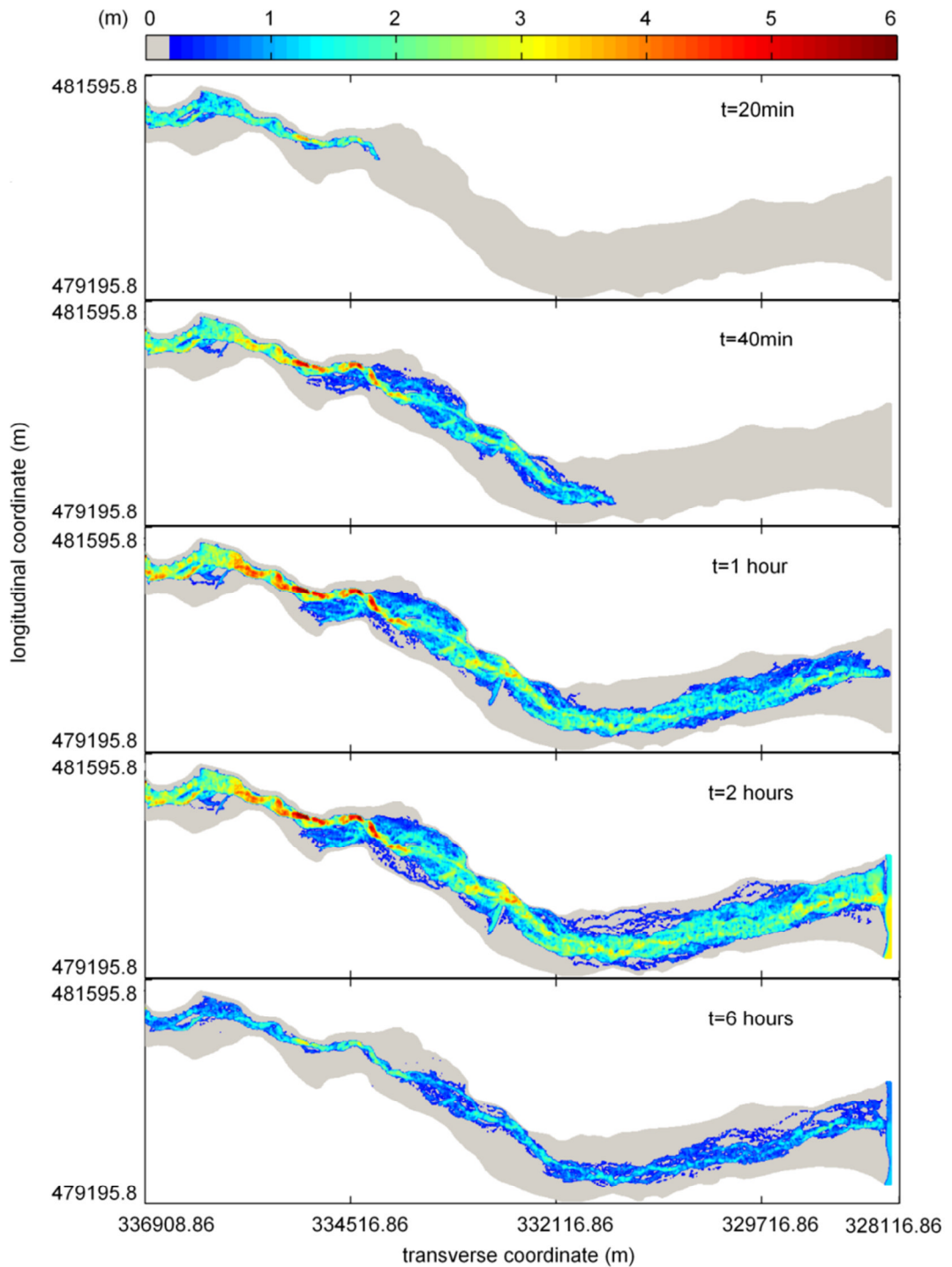
Figure 6.7 The spatial and temporal change of the flood water depth at t=20 min, 30 min, 1 hour, 2 hours and 6 hours after the flood occurred.

6.5.2 Effects of Sediment Grain Size

A sensitivity analysis of sediment grain size is carried out in this section in order to elucidate the role sediment grain size plays in the rapid flow-sediment process. The single size fraction of d_{50}=40 mm and the single size of d_{50}=80 mm are also used as a input parameter for this rapid outburst

flood. Firstly, the hydraulic parameters are compared for the different sediment grain sizes, involving the temporal changes of flow discharge at the cross section nearby the bridge and the water surface elevation at the gauge (332908.86, 480099.78), which is shown in Figure 6.8. It can be seen that the difference is insignificant for the arrival time of flood front; it is approximately 30.5 minutes after the flood occurred for mixed diameter and d_{50}=40 mm, while it is about 32.5 minutes for d_{50}=80 mm, 2 minutes later than other two cases. Likewise, the arrival time and the amount of the peak flow discharge are slightly different for the three sediment grain sizes. As for the difference for water surface elevation at the selected gauge, it is observed that the simulated water level for mixed diameter is larger than that for single size of d_{50}=40 mm and d_{50}=80 mm, particularly in the subsiding period of the flood.
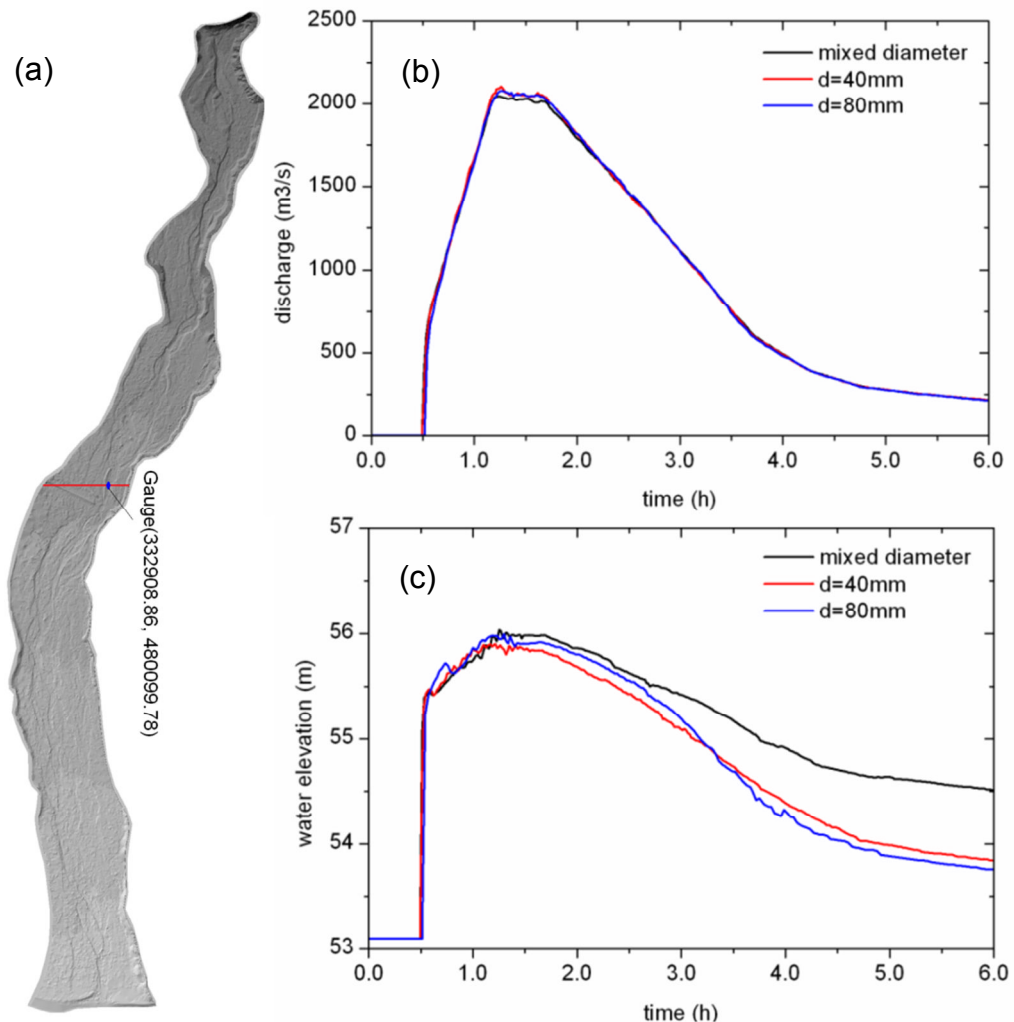
Figure 6.8 (a) bed terrain; (b) the temporal change of flow discharge at the typical cross section near the bridge (x=332908.86) and (c) water depth at the gauge (332908.86, 480099.78) for the different sediment grain sizes

Secondly, Figure 6.9 illustrates the simulated spatial change of the typical cross section near the bridge, as well as the temporal change of scour depth at the gauge (332908.86, 480099.78). It is clearly shown that the changes of the cross section and the scour depth for the three grain sizes are very different, i.e. the deposition occurs at 30.5 minutes immediately when flood front reaches the gauge (332908.86, 480099.78), then the bed is eroded and the sediment is deposited here progressively again for the mixed diameter, but for the coarse particle d_{50}=80mm, the bed change process only includes the deposition in the first period and then the erosion until the end; and the start-time of bed scour is about 44 minutes, 13.5 minutes later than that for the mixed diameter and d_{50}=40 mm. This can be attributed to the flood water not having enough energy to induce the coarser sediment particles to move when it just reaches the location because of the properties of the coarser particles. Yet, in the flood subsiding period, the deposition occurs there for the mixed diameter because the higher concentration of sediment exceeds the sediment transport capacity. The differences of the bed scour depth are also the reason that the water level is different among the three gain sizes in Figure 6.8. As shown in Table 6.3, the total bed change area is 2.51 km^2 for the mixed gain-size which is larger than the bed change area of 2.08 km^2 for d_{50}=40 mm; the extent of bed change for d_{50}=80 mm is the smallest for the three cases, it is only 1.60 km^2. Figure 6.10 demonstrates the spatial distribution of the simulated bed erosion and deposition in the river channel. Likewise, from the spatial-scale point of view, the extent of bed change for d_{50}=80 mm is much smaller than that the other two. While the extent of bed changes for the mixed grain-size input is the broadest in the three cases. Overall, the amount and extent of the bed erosion and deposition are significantly influenced by the sediment grain size. More specifically, the finer sediment particles can be induced to move more easily, even in the case of weak flows, resulting in the geomorphic change being more severe; whilst the converse is true for coarser sediment particles.

Table 6.3. Extent of bed change for the three inputs of grain size

resolutions	erosion area (km^2)	deposition area (km^2)	total area (km^2)
d_{50}=80 mm	1.15	0.45	1.60
d_{50}=40 mm	1.35	0.73	2.08
mixed grain-size	1.36	1.15	2.51
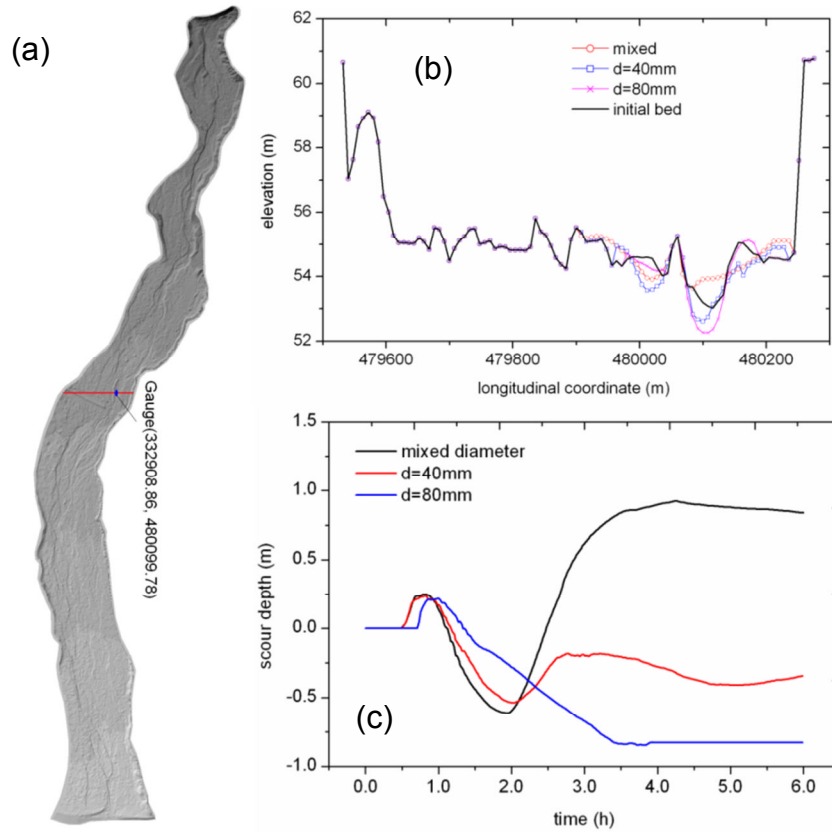
Figure 6.9 (a) bed terrain; (b) the simulated spatial change of the typical cross section near the bridge (x=332908.86) and (c) the temporal change of scour depth at the gauge (332908.86, 480099.78) for the different grain sizes
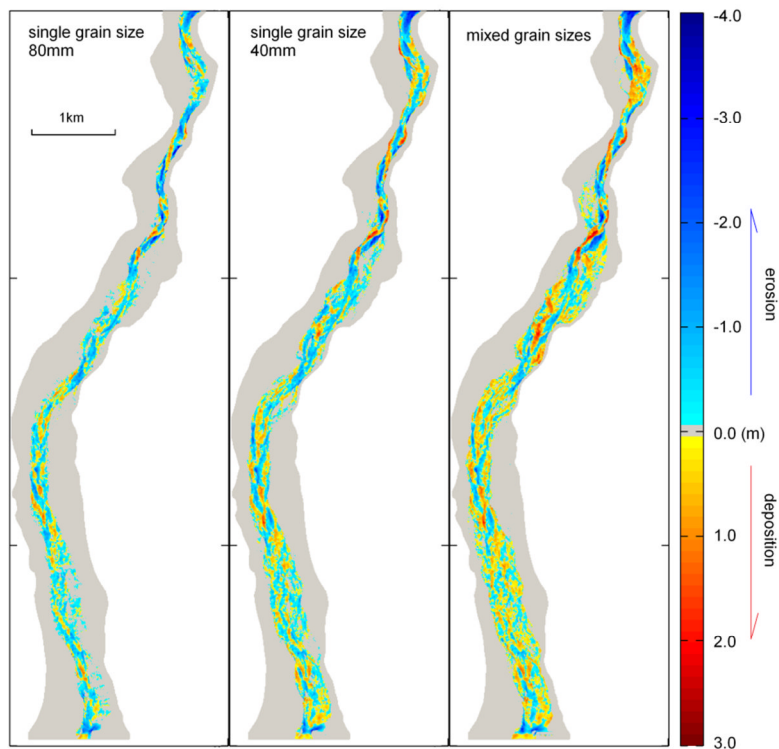
Figure 6.10 Simulated spatial change of bed topography for the different sediment grain sizes

6.5.3 Implications of Topography Resolution

The topography of high resolution can reflect the real conditions more accurately but at the expense of increasing the computational time. Therefore, it is necessary to balance the computational accuracy and the computational time, because there is no doubt that quicker computation with similar accuracy is much more attractive. Thus, two resolution datasets of bed topography (Run.1 with 8m×8m spaced data and Run.2 with 4m×4m spaced data) are used as input in the computational model in order to elucidate how the topography resolutions affect the simulation and the simulated outputs. As shown in Figure 6.11, in terms of hydrodynamic aspects, the flow hydrograph at the cross section x=332908.86 is almost the same between the two runs, including the peak discharges and arrival time. Also, the water level has a similar modelling result with just a slight difference. As shown in Table 6.4, the simulated total erosion and deposition volume are $7.81×10^5$ m^3 and $5.91×10^5$ m^3 respectively for the 4m×4m DEM, while for the 8m×8m DEM they are $7.47×10^5$ m^3 and $5.57×10^5$ m^3; the differences are approximately 4.32% and 5.75%. At the cross section x=332908.86, it can be found that the difference of the maximum water level is insignificant, just 0.08m. In Figure 6.12, it can be seen that both the simulated outputs for the 4m×4m resolution and 8m×8m resolution have the similar trend of increasing and then tending towards a constant value. Also before 1.5 hours, both total erosion and deposition volume are very close, but after that time, the total erosion volume and the total deposition volume simulated for the 4m×4m resolution are slightly larger than those for the 8m×8m resolution.
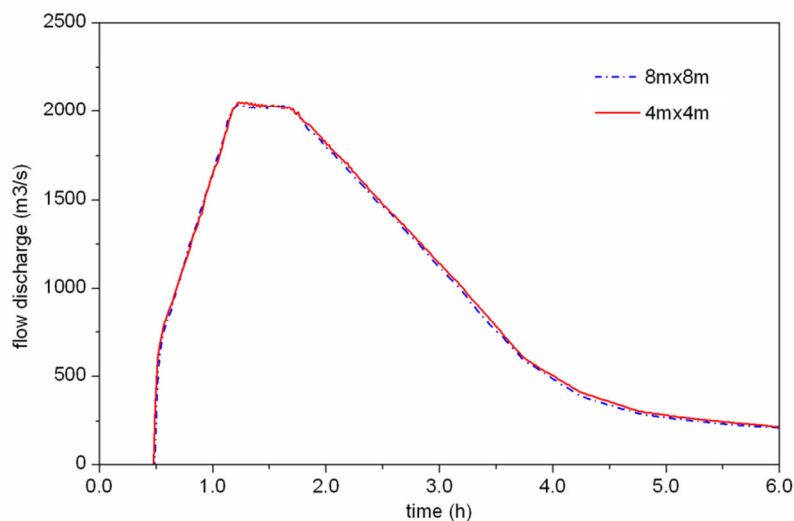
Figure 6.11 The flow hydrograph at the cross section x=332908.86

Table 6.4 Comparison of characteristic factors between the two resolutions

resolutions	max. water level (m)	final scour volume ($\times 10^5 \, m^3$)	
		erosion	deposition
r1. 4m×4m	55.96	7.81	5.91
r2. 8m×8m	56.04	7.47	5.57
diff. (r1-r2)	-0.08	0.34	0.34
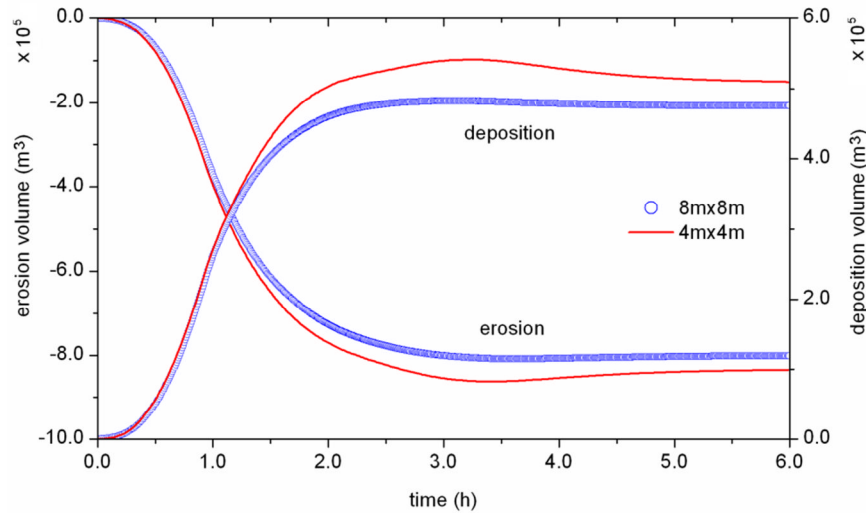
Figure 6.12 the simulated temporal change of total sediment erosion volume and deposition volume after 6 hours since the flood occurred for the two topography resolutions

Furthermore, from the spatial-scale point of view, Figure 6.13 demonstrates a very similar spatial distribution of the final erosion and deposition caused by the rapid flood for the two resolutions. For comparison, Figure 6.14 illustrates the simulated bed profiles at the 8 selected cross sections by the two resolutions. Firstly, it is found that the distribution of erosion area and deposition area is not influenced significantly by the resolutions; both have a similar distribution feature. Taking the 8 selected cross sections as examples to compare the differences caused by the topography resolutions, the features of geomorphic change can be summarised as: (1) the bed erosion and deposition primarily occur in the main channel for both simulations; (2) the simulated bed profiles are very close at some cross sections, e.g. cs2-2, cs7-7 and cs8-8; however, (3) at other cross sections, the bed elevations have some differences under the premise of similar erosion and deposition feature, e.g. cs1-1, cs3-3, cs4-4, cs5-5 and cs6-6; commonly at these cross sections the bed scour simulated by fine resolutions of 4m×4m is more severe than that calculated by 8m×8m topography, in other words, the erosion is more severe and the deposition, too; this feature is also explained indirectly by the total erosion and deposition volumes shown in Figure 6.12.

In summary, for the implications of input topography resolutions, we conclude that (1) flow discharge and water level are not affected significantly, including the values and inundation time; but (2) the simulated bed erosion and deposition by fine resolution is more severe than those by coarse resolution, yet with a slight difference; (3) for both resolutions the bed scour results have a similar distribution; however, (4) the computational time by fine 4m×4m resolution is approximately 4 times than that by coarse 8m×8m resolution; (5) so the coarse resolution of 8m×8m is enough for the outburst flood case.
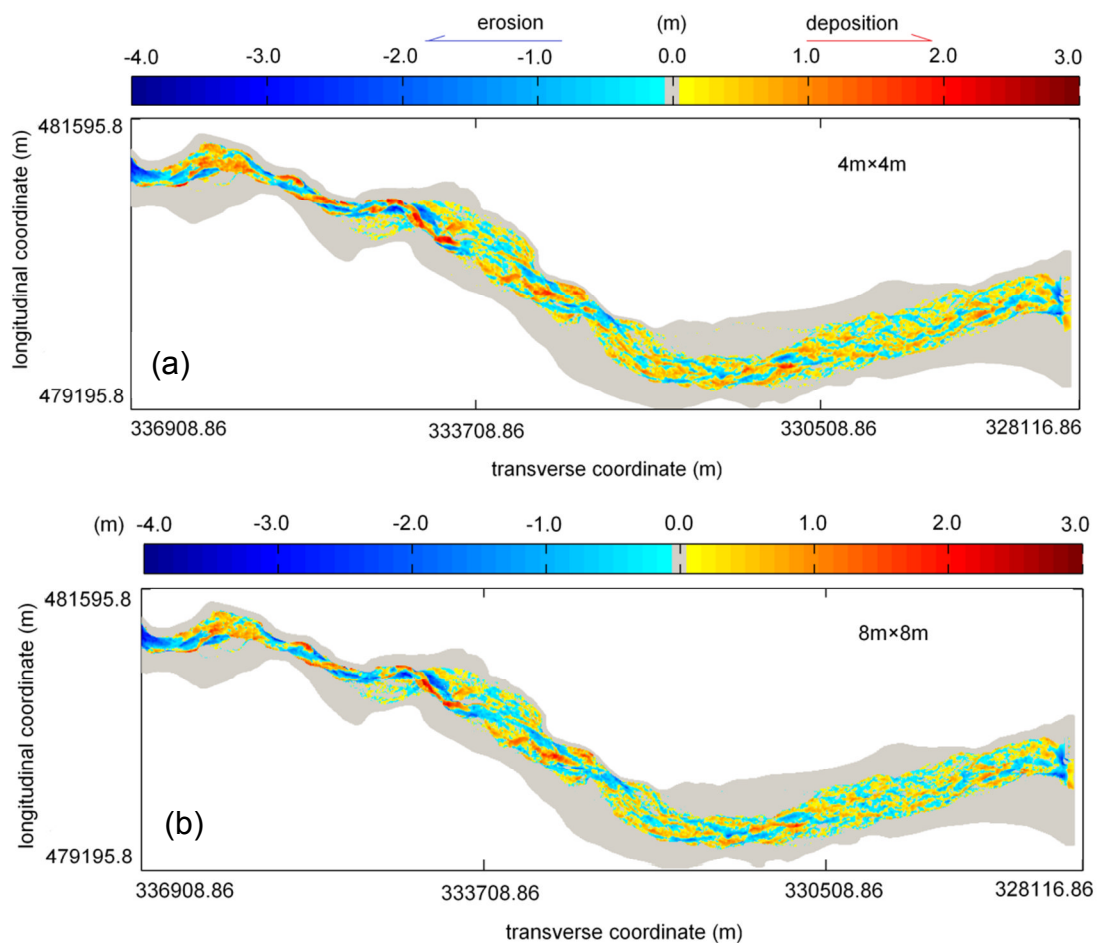
Figure 6.13 the distributions of bed erosion and deposition for (a) 4m×4m resolution and (b) 8m×8m resolution
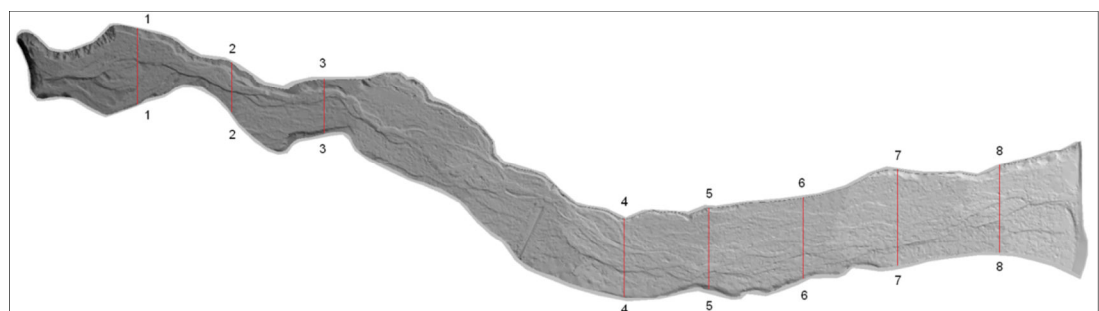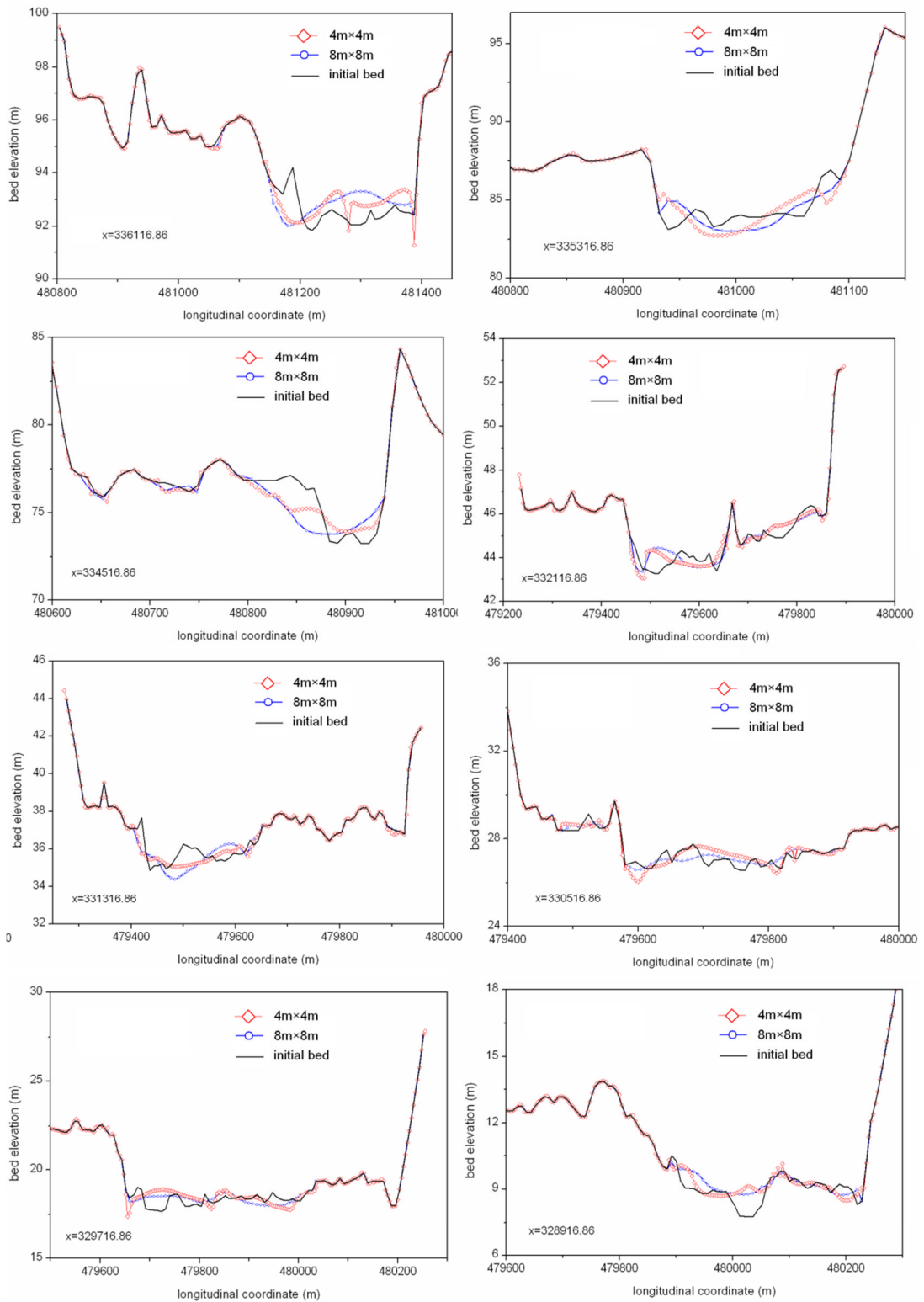
Figure 6.14 The final cross sections simulated by use of the two resolution datasets

6.5.4 Hydraulic Effects of Sediment Transport

Sediment entrained by sudden onset flood affects the hydraulics by modifying flow density, flow viscosity and the turbulence regime; hence, the

frontal wave speed, flow velocity and flow depth will be altered considerably due to the incorporation of sediment transport [13, 14, 42, 44, 187]. Most existing investigations were carried out based on small-scale experiments or modelling works on small-scale flood, e.g. simple dam-break flow over movable bed. In this section, the effects of sediment load in the large-scale flood event are discussed and analysed from the numerical point of view. In order to answer the question, two runs are conducted: i) modelling of clear flood water without sediment transport (the simulated outputs in section 6.5.1); ii) water-sediment mixed flood modelling with the incorporation of sediment transport. As in the previous test, the flow discharge at the cross section (x=332908.86) near the bridge is selected as a typical one to compare between the two runs and the water surface at the gauge (332908.86, 480099.78) is also illustrated in Figure 6.15. It shows that: (1) the peak flow discharge is not affected significantly by the incorporation of sediment transport, it is only slightly different; however, (2) the water depth history at the gauge is altered significantly due to the existence of sediment transport; the maximum water depth with sediment is 3.45 m, almost half a meter larger than that without sediment at 2.98 m; and the water depth becomes smaller after the peak flow discharge as a result of the bed elevation changes during the flood process; (3) as shown in Table 6.5, the arrival time of peak discharge for flooding with sediment is considerably earlier than that without sediment transport, the time difference of this arrival is 7.2 minutes; further, the arrival time of the water front is also decreased by about 2.6 minutes due to sediment transport.
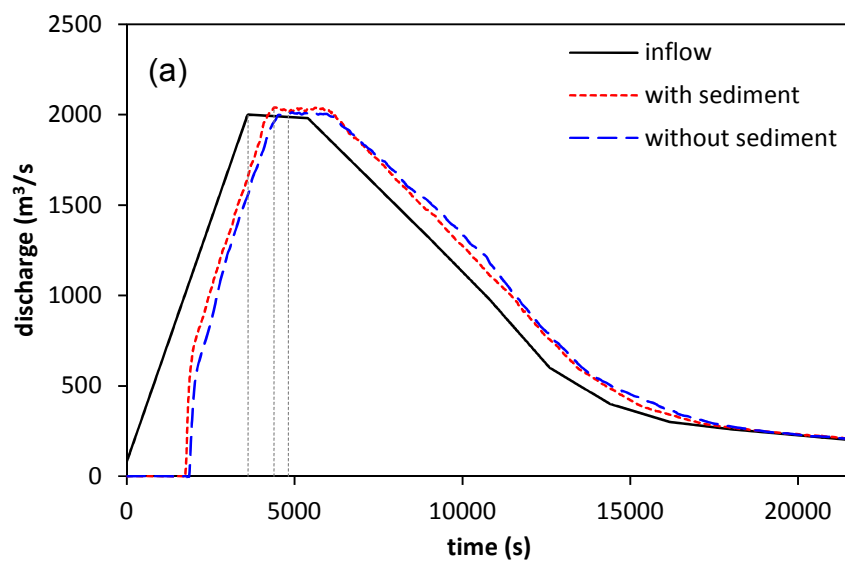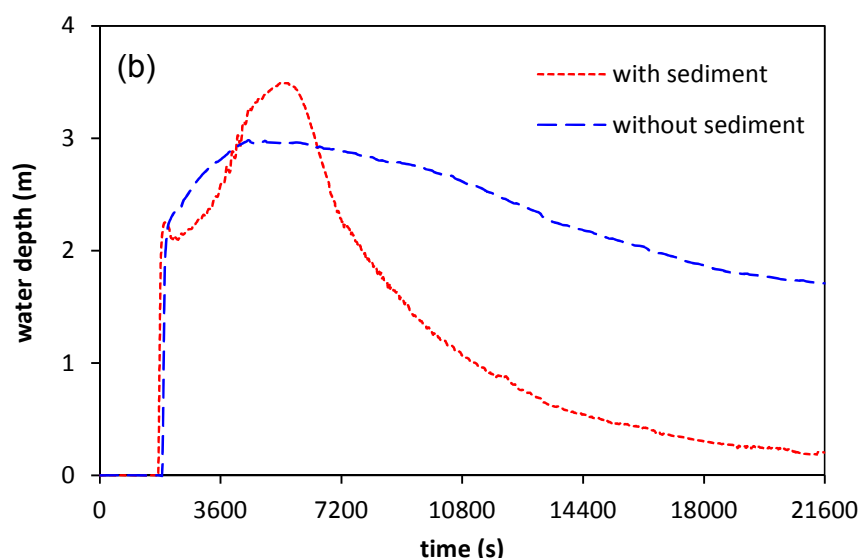
Figure 6.15 (a) the temporal change of flow discharge at the cross section x=332908.86 and (b) water depth at the gauge (332908.86, 480099.78)

Table 6.5 Statistics of flooding parameters at the cross section x=332908.86

flood types	water front arrival time (min)	peak flow arrival time (min)	max. water depth (m)
inflow discharge	0.0 (+0.0)	61.0 (+0.0)	0.00
1. with sediment	29.1 (+29.1)	73.2 (+12.2)	3.45
2. without sediment	31.7 (+31.7)	80.4 (+19.4)	2.98
difference (type.1-type.2)	-2.6	-7.2	0.47

Moreover, the incorporation of sediment transport changes the bed topography, which is bound to alter the hydraulic properties, such as water level, water depth and flow velocity field etc. From the spatial-scale viewpoint, Figure 6.16 illustrates the differences of simulated results at 2 hours by the two runs with and without sediment transport, including the maximum water level, the maximum water depth, the minimum of final bed elevation, as well as the spatial differences of water level and water depth. From the illustration, it can be seen that: the differences of the minimum bed elevations have both positive values and negative values, because of the erosion and deposition process caused by the rapid outburst flood; however, the maximum water surface and maximum water depth for the run with sediment is significantly smaller than those for the run without sediment at most cross sections; only a few cross sections are increased due to the incorporation of sediment transport; in other words, a primary spatial effect of sediment transport is to reduce the maximum water level and water depth at most cross sections. As shown in Figure 6.16, the water surfaces with sediment transport are smaller in most areas of the whole channel. Table 6.6

shows the statistics of simulated results by the two runs. The plan area where the water level becomes smaller due to sediment transport reach approximately 3.03 km^2 which is approximately 2.27 km^2 larger than the area (~0.76 km^2) where the water levels become larger; moreover, for the water depth in the channel, the area where the water depth becomes smaller and larger due to sediment transport are approximately 2.68 km^2 and approximately 1.11 km^2 respectively with a difference of about 1.57 km^2. Moreover, the flood submerged area simulated by the run without sediment transport is apparently larger than that with sediment transport. From the comparison and analysis for the two runs, we conclude that the incorporation of sediment transport reduces the water level and water depth in the most areas of the river channel, which shows a beneficial role of sediment transport in the outburst flood process.
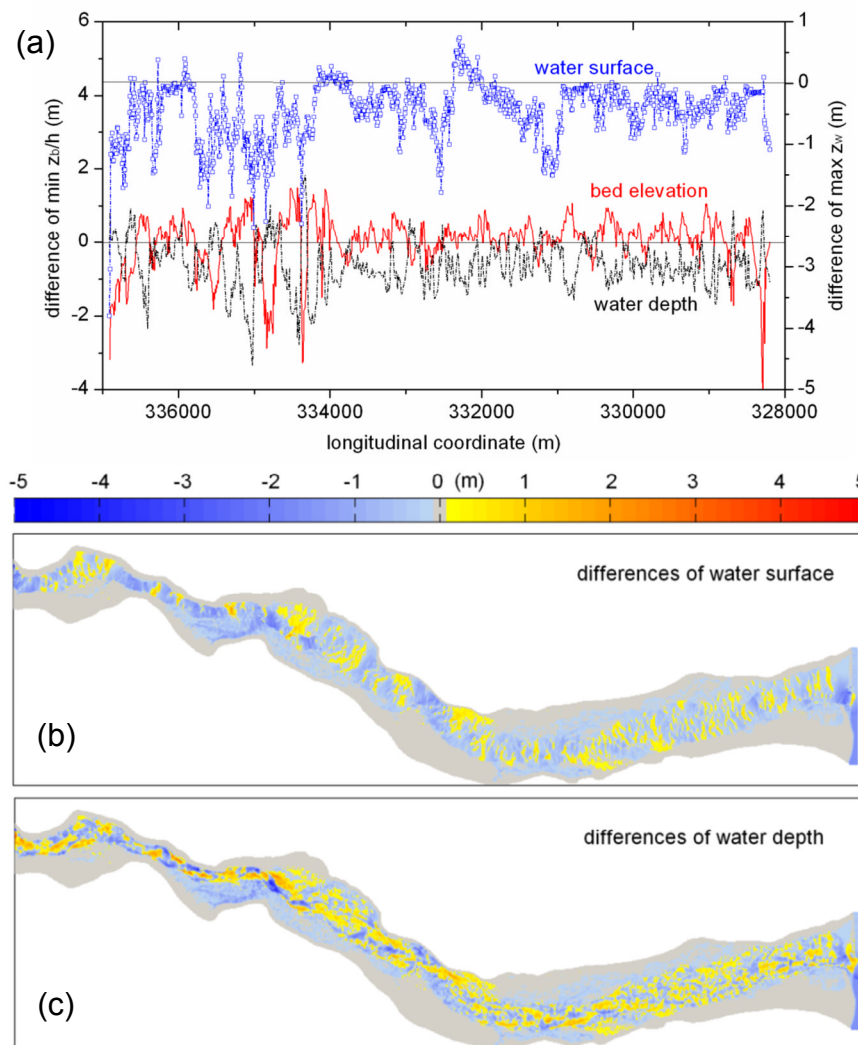
Figure 6.16 the differences of the results by the two runs with and without sediment transport; (a) differences of maximums; (b) differences of water surfaces; (c) differences of water depths; (note: $\Delta\eta = \eta_{sed} - \eta_{no\,sed}$, $\Delta h = h_{sed} - h_{no\,sed}$, $\Delta z = z_{sed} - z_{no\,sed}$)

Table 6.6 Statistics of simulated results by the two runs

	differences Δ (m)	area (km^2)	flood submerged area (km^2)	
water surface	>0	~0.76	with sediment	no sediment
	<0	~3.03	~3.44	~3.78
	area<0 – area>0	~2.27		
water depth	>0	~1.11	~0.34	
	<0	~2.68		
	area<0 – area>0	~1.57		

In addition, Figure 6.17 illustrates the flow velocity field at 2 hours when the flow there is approximately at the peak stage. Intuitively, it is clear that the flow velocity fields have different contour distribution but with the similar feature of higher velocity in the main channel than that in the surrounding channel. More specifically, the surface of flow velocity field for flood with sediment transport shows a smooth contour distribution; conversely, the contour distribution without sediment transport has obvious oscillations in the surface compared to that with sediment, which is also observed in the spatial distribution of the water depth in the river channel as shown in Figure 6.18. These is attributed to that the high intense rapid flow scours the protruding bed and deposits the depressed topography, so making the irregular topography smoother. In summary, we infer that the flood water induces sediment transport, creating a smoother topography and thereby improves the flow capacity of each cross section, which in return leads to the flood propagation being accelerated. It is also considered that the incorporation of sediment transport is the reason of the earlier arrival time of water front and peak flow. To show the inundation process, Figure 6.19 illustrates the water depth at the different time.
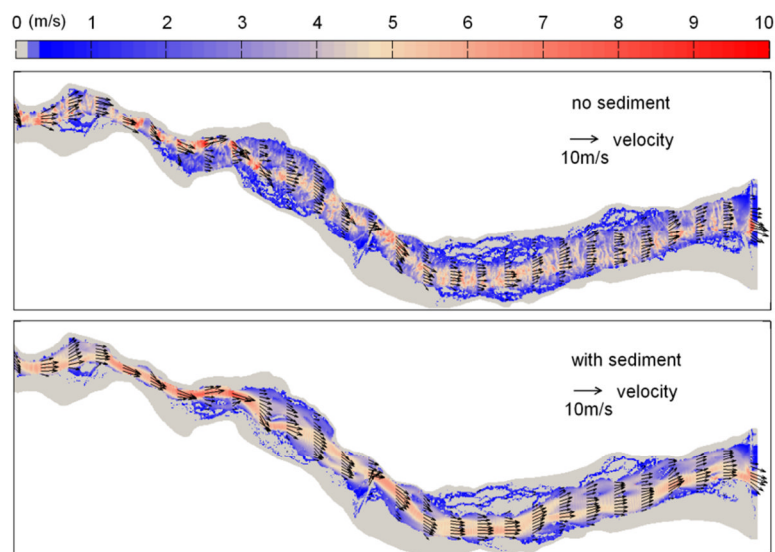
Figure 6.17 the contour distribution of the flow velocity field at t=2 hours
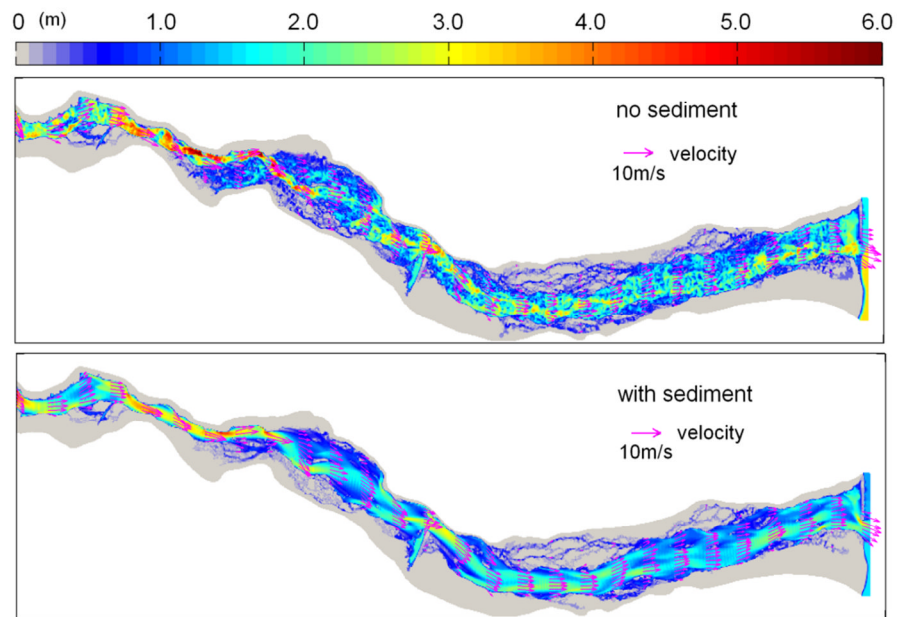
Figure 6.18 the contour plot of water depth with and without sediment in the river channel at 2 hours
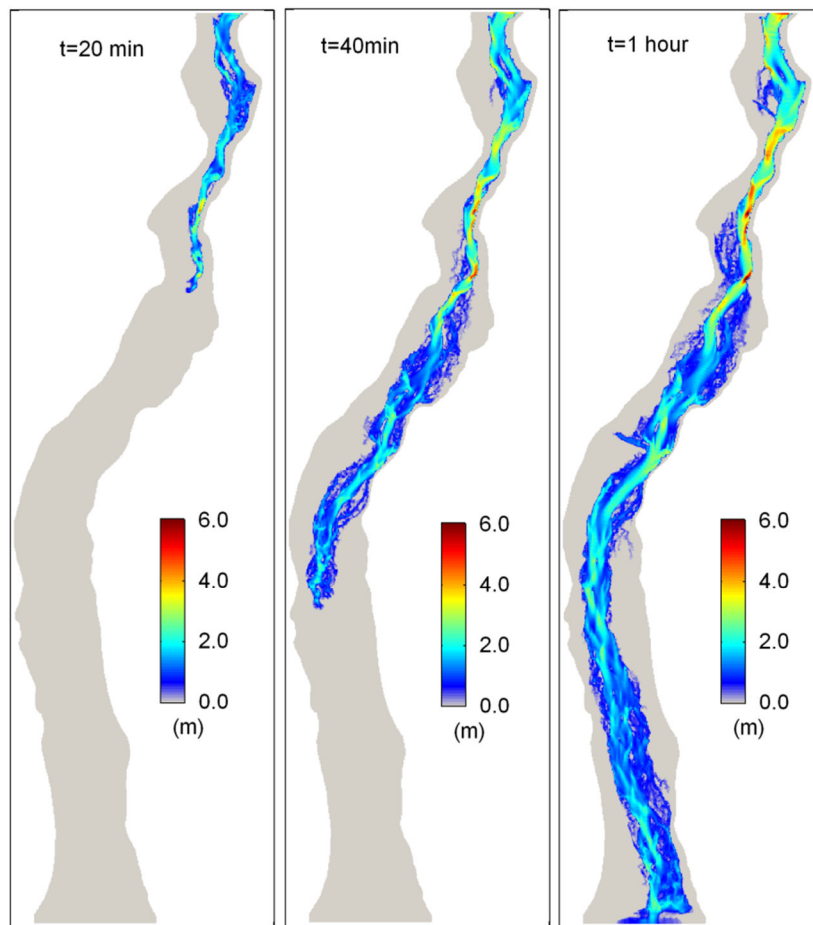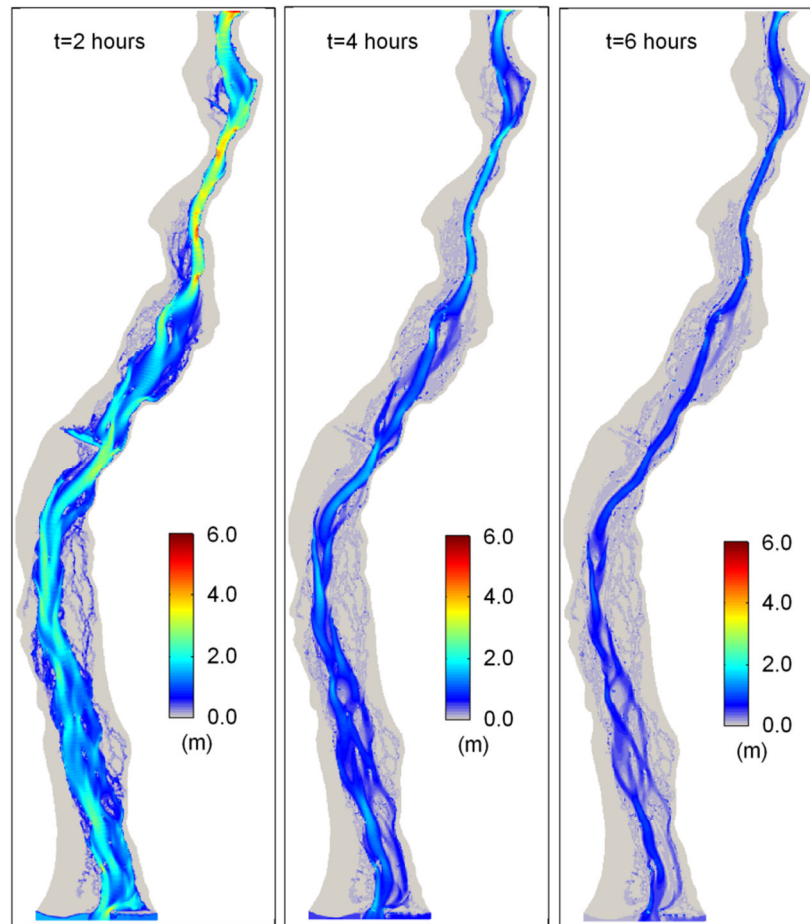
Figure 6.19 The simulated water depths for the scenarios with sediment transport

6.5.5 Erosion and Deposition

The short-lived, transient outburst flood induced considerable sediment load, causing the geometry change rapidly. However, it is quite complex to quantify the volume of the erosion and deposition in temporal-scale and spatial-scale using the physical measurement. The temporal and spatial changes of the outburst flood are modelled by using the layer-based morphodynamic model with the input of mixed sediment particles. The simulated final topography scour is illustrated in Figure 6.20 showing the spatial distribution of the erosion depth and the deposition depth, as well as the scour extent. It is found that the volcano-induced flood causes the erosion and deposition to occur in the main channel, and both erosion and deposition are more severe in the narrower reach of the river (e.g. part A as shown in Figure 6.20), because the narrow channel deepens the water depth and meanwhile elevates the value of velocity, which induces more sediment into movement and correspondingly re-deposition within a

- 157 -

transport distance. In part A, the maximum erosion depth reaches 4.99 m, while the maximum deposition depth is up to 2.71 m. Figure 6.21 shows the bed topography of part A in Figure 6.20 before flood, at the peak stage and after flood. It can be seen that the main channel is obviously expanded due to erosion and deposition. The increase of the capacity is bound to influence the flood propagation. The temporal changes of the total erosion volume and deposition volume are also simulated and shown in Figure 6.22(a). As the inflow discharge is characterised by increasing suddenly to the peak stage and then decreasing progressively for 6 hours, the total erosion and deposition volume is closely related to the degree of inflow discharge. More specifically, (1) in the first period, the inflow discharge increases to peak value rapidly in one hour during which the total erosion volume of sediment accumulates rapidly as a result of the intense bed shear stress, also, the entrained sediment in water body is then re-deposited within a calculated transport distance; (2) during the peak flow stage, the total erosion and deposition of sediment accumulate continually, and at about t=3.5 hours, the total erosion and deposition volume tend to reach a constant value; (3) in the final flood subsiding period, the smaller discharge causes bed shear stress to be weak, resulting in the sediment no longer being induced in motion, correspondingly, the total erosion volume and deposition volume do not significantly change, either. In this volcano-induced outburst flood, the deposition volume is determined to be approximately 5.57×10^5 m^3 and the total erosion volume of sediment to be approximately 7.47×10^5 m^3 which is more than 1.5 times the total deposition volume. In addition, in order to understand the erosion and deposition against the inflow discharge more clearly, the erosion rate and deposition rate are calculated and illustrated in Figure 6.22(b). It is clearly shown that the erosion rate and deposition rate have quite a similar pattern of change, in other words, the erosion rate and the deposition rate occur simultaneously for this case, and the rates are closely related to the magnitude of the inflow discharge. The peak values of both erosion rate (approximately 638.9 m^3/s) and deposition rate (approximately 618.9 m^3/s) occurs in about 1.5 hour when the inflow discharge is at its peak stage. The erosion rate and deposition rate increase rapidly before the time of maximum, and after that they decrease progressively. It is also noted that the majority of erosion and deposition occurs in approximately 2-3 hours which is the main inundation time, and conversely, little scour occurs during the flood subsiding period. To demonstrate the sediment-laden flood inundation process, Figure 6.23 illustrates the water depth and the resulting bed change pattern in the river

channel at the different stages. In summary, it can be conclude that (1) the rapid outburst flood can induce a rapid geomorphic change, occurring in 2-3 hours in this case; and (2) the erosion rate and deposition rate is closely related to the degree of inflow discharge; (3) the narrower the channel, the more severe the bed scour.
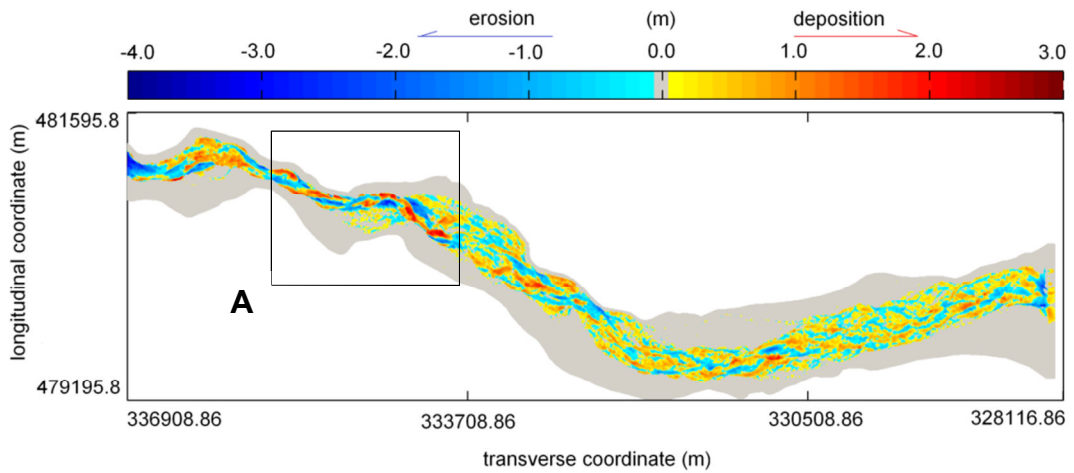
Figure 6.20 The depth and extent of erosion and deposition caused by the transient outburst flood at 6 hour
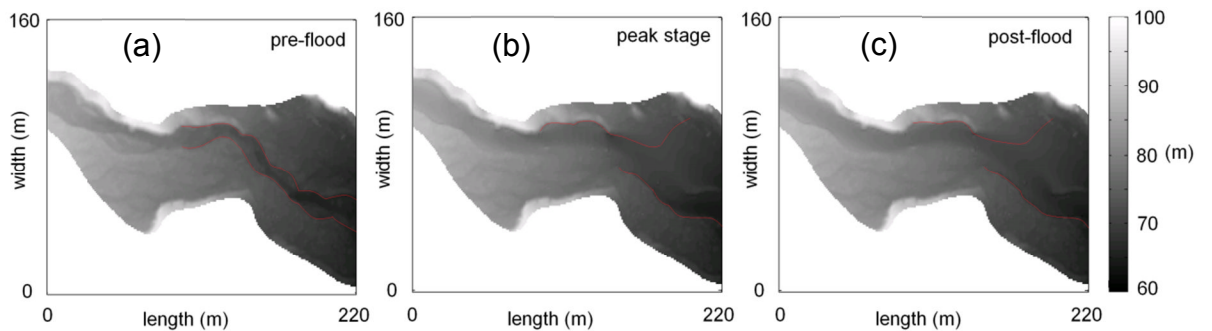
Figure 6.21 Bed terrains of part A (a) before flood; (b) at peak stage; (c) after flood.
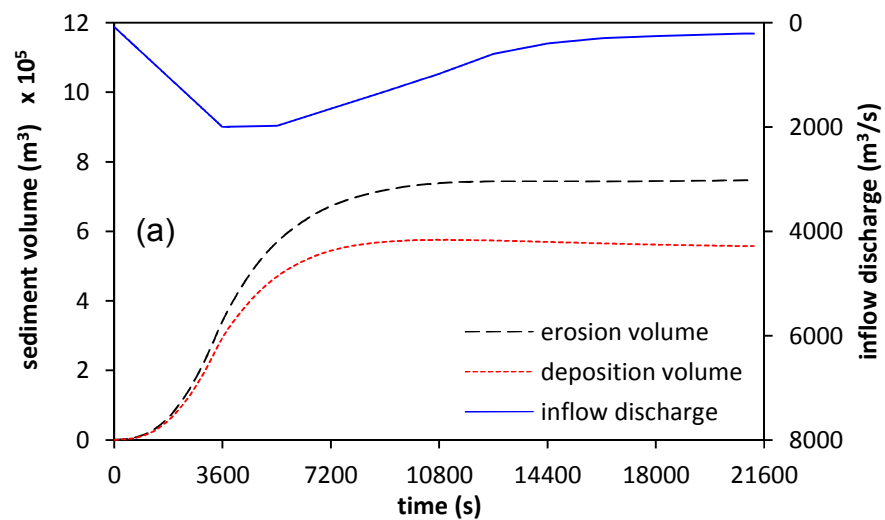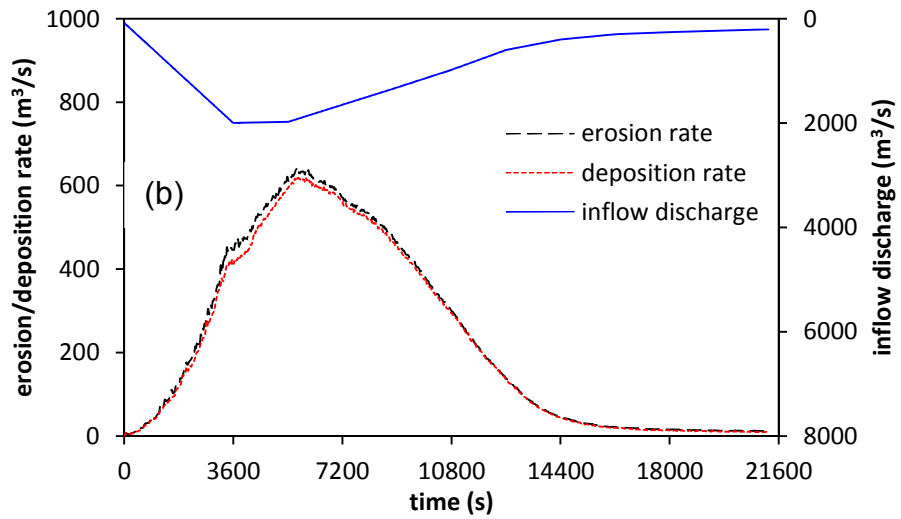
Figure 6.22 Temporal evolution of total erosion and deposition volume; the erosion rate and deposition rate
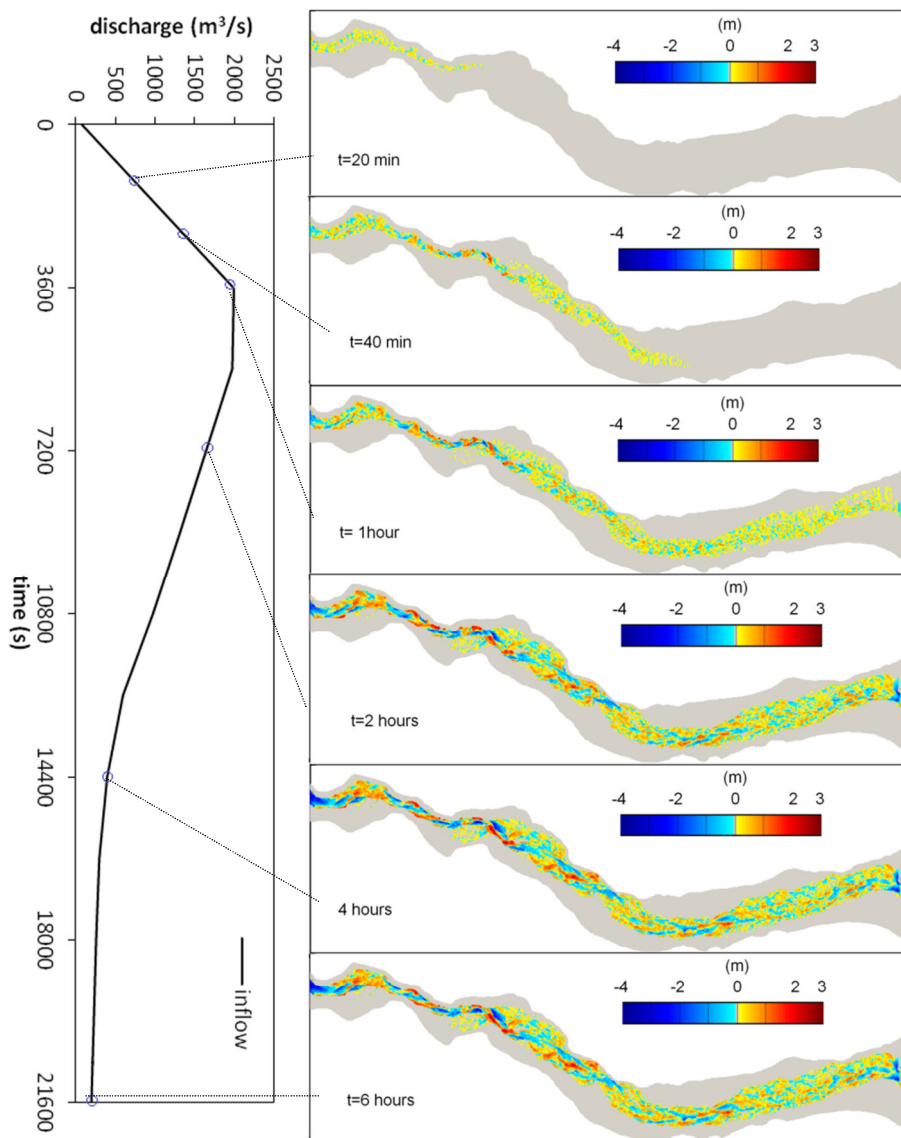
Figure 6.23 The spatial distribution of erosion and deposition caused by the rapid outburst flood.

6.5.6 More Discussion

According to the investigations of the GLOF carried out by Russell et al.(2010), the flood hydrograph and peak flow discharge was reconstructed by using the slope-area technique, but still with a deviation of the order of $10^3 m^3/s$; moreover, the channel bed is quite complex with all kinds of sediment size fractions from several millimetres to meters which might result in regular sediment transport equations losing effectiveness. Therefore, the complexities of real conditions led to a lot of difficulties in quantifying the bed change through numerical modelling; complete confidence in the quantification of bed erosion and deposition is still unattainable. In the present morphodynamic model, non-equilibrium adaption length for sediment transport is found a sensitive parameter, because it directly influence how far sediment particles can transport. The existing empirical expressions based on laboratory data might be problematic when applied to a large-scale event because they are inappropriate. The commonly-used relationship of Eq.(4.12) based theoretical analysis would be recommend to use because it can reduce the errors caused by empirical functions and scale. Although a series of uncertainty of modelling results, the qualitative assessment through the quantitative analysis is beneficial to better understanding the complex sediment-laden flood process. Of course, the modelled values do have a lot of uncertainties, but those are not the major concerns in this study, our motivations are to elucidate the applicability of the hydro-morphodynamic model and to seek the understandings of the sediment-laden outburst flood in reality. Some data which cannot be gained in fieldwork was calculated to help understanding the events further. They include:

(1) The arrival time to the bridge of flood fronts is approximately 29.1 minutes, 2.6 minutes faster than that without sediment; and the arrival time of peak stage is approximately 12.2 minutes, 7.2 minutes faster than that without sediment (19.4 minutes), accelerated by about 37.1%.

(2) The total deposition volume is approximately 5.57×10^5 m^3, while the total erosion volume of sediment is approximately 7.47×10^5 m^3.

(3) The peak erosion rate is approximately 638.9 m^3/s and the peak deposition rate is approximately 618.9 m^3/s, which takes place at the peak stage of about 1.5 hours.

(4) The maximum erosion depth is more than about 5 m, while the maximum deposition depth reaches to about 2.7 m.

6.6 Concluding Remarks

Although a plethora of hydraulic-sediment transport models have been presented by many authors in the past, they have only been focused on theoretical analysis or small-scale experiments. They have seldom been applied to large-scale sudden onset flood from real case studies. In this chapter, an unsteady sediment transport induced by a huge rapid outburst flood has been considered and simulated a novel hydro-morphodynamic model. The model is well applied to a large-scale volcano-induced glacial outburst flood and the model has been demonstrated that it is capable of simulating the spatial and temporal change of the rapid hydraulic-morphological phenomenon. Importantly, through the simulations and results of analysis of several scenarios, more insights and further understandings towards unsteady sediment transport behaviours in large-scale outburst floods have been gained, which were impossible to be obtained in small-scale experimental works. In conclusion, some key points from this chapter are summarised as:

(1) The rapid unsteady outburst flood results in a rapid significant landscape change by the erosion and deposition process the majority of which occur in approximately the first 2-3 hours for this simulated case; and the erosion rate and deposition rate are closely related to the magnitude of the flow discharge, because the intensity of flood water directly decides the quantity of sediment that is entrained and re-deposited.

(2) Compared to the clear-water flood without sediment transport, the sediment-laden flood is accelerated significantly. The arrival time of peak discharge is much smaller. The fundamental reason is the entrained sediment makes the density of the flow higher than that of clear water, so both mass and momentum of the sediment-laden flow are increased. Also, it is found that the high intense rapid flood scours the protruding bed and deposits the depressed topography, so making the irregular topography smoother, which conversely enhances the capacity of the river channel conveyance.

(3) The most significant implications of sediment grain size are determined as the water depth, the flow velocity, the quantity of sediment transport and the features of bed erosion and deposition. Nonetheless, it does not have significant influences on the flow discharge, water surface elevation and inundation extent.

(4) The inclusion of sediment transport in the model complicates the calculation process, so consuming more computational time.

(5) The fine topography resolution might improve the accuracy of the simulated results, but at the expense of increasing computational time. At least, for the case in this paper, the computational time increases by nearly 4 times but the simulated flow-sediment parameters, i.e. flow discharge, water level, as well as landscape erosion and deposition, are not significantly influenced. i.e. for this particular case study 8m×8m is sufficient resolution.

Furthermore, the layer-based hydro-morphodynamic model simulated the rapid morphological change of a full-scale flood event fairly well, and evaluated the outburst flow hydraulics and unsteady sediment transport qualitatively. The understandings are instructive for flood risk management and flood hazard mitigation.

Chapter 7
Conclusions and Future Work

7.1 Conclusions

The main contributions of this work are the development of a robust layer-based hydro-morphodynamic model system based on shallow water theory and the non-equilibrium sediment transport assumption, and the application of the model leading to a better understand of outburst flood hydraulics and geomorphic impacts of large-scale sudden onset floods. The model's development is thoroughly and methodically demonstrated and it is extensively tested in a wide range of circumstances. In summary, the following conclusions are drawn out from the work in this thesis:

7.1.1 Fully 2D Hydrodynamic Model

A robust 2D hydrodynamic model without sediment was presented. In order to avoid the imbalance of computation caused by irregular bed topography, a homogenous flux method (HFM) was proposed to solve the bed slope term. A series of test results indicated that the 2D hydrodynamic model is robust to apply and runs well for real-world flood events. The proposed numerical scheme has the following advantages and robust characteristics:

- it is straightforward to implement,
- it copes with discontinuous or vertical bed topography as a matter of course without any special treatment,
- it is applicable to both steady and unsteady shallow water flow problems over complex irregular topography.

7.1.2 Layer-based Hydro-Morphodynamic Model

A layer-based hydro-morphodynamic model system was developed to predict flood events with rapid geomorphic change. A multi-purpose sediment transport model system was proposed incorporating bedload, suspended load and total sediment load mode. Through the testing of a series of 1D and 2D benchmark cases, it is shown that the model can simulate the cases with different sediment transport regimes according to the application objects; the use of a layer-based conceptual model leads to the model to simulate well the temporal and spatial change of rapid outburst

flood events, including the hydraulic aspects and the aspects of geomorphic change caused by sediment-laden flows.

7.1.3 Applications in Full-scale Outburst Floods

The 2D hydro-morphodynamic model was applied to a volcano-induced geomorphic outburst flood at Sólheimajökull, Iceland, a selected appropriate representation of large-scale real-case flood events which differs from the long-term fluvial process by perennial flows in rivers or coastal areas. It is shown that the model is appropriate for large-scale rapid flood events and can simulate them well. Therefore, many rapid, sediment-laden floods can be predicted by the proposed model.

7.1.4 Understanding of Rapid Sediment-laden Floods

From the numerical point of view, some insights and further understanding included in this thesis have been obtained to advance flood hydraulics and unsteady sediment transport in large-scale outburst floods, many of which are impossible to be gained in small-scale experimental work. Such insights involve: what role does sediment grain size play in the flow-sediment interactions? what are the implications of sediment transport on flood propagation? and how does the rapid floods affect the river bed? According to the investigation presented in Chapter 6, it can be concluded that:

(1) The rapid unsteady outburst flood results in a rapid significant landscape change by the erosion and deposition process; and the erosion rate and deposition rate are closely related to the magnitude of flow discharge.

(2) Comparing the clear water floods, the sediment-laden flood could be accelerated significantly, especially for the arrival time of peak discharge. This is because, on one hand, the entrained sediment increases the mass and momentum of the flow; on the other hand, it is found the river bed is changed to smooth, so increasing the capacity of river channel conveyance.

(3) The sediment grain size can influence water depth, flow velocity, sediment load quantity as well as the range of bed erosion and deposition. Nonetheless, it does not have significant influence on the flow discharge, water surface elevation and inundation extent.

(4) The inclusion of sediment transport in the model complicates the calculation process, so consuming more computational time by roughly 5

times. Fine topography resolution might improve the accuracy of the simulated results, but at the expense of increasing computational time.

7.2 Future Work and Recommendation

7.2.1 Cohesive Sediment Transport

The present computational model is primarily focused on the non-cohesive sediment transport. However, fine-grained and cohesive suspended sediment transport is also usually seen in the natural environment. The mechanisms of cohesive sediment and non-cohesive sediment are quite different. The different aspects mainly include the entrainment and deposition of sediment, as well as the collapse mechanism of bedform. Thus the present model cannot be applied to solve the cohesive sediment transport issues. In order to increase the applicability of the computational model, a module incorporating cohesive sediment transport could be included.

7.2.2 Modelling of Debris Flows

Debris flows are fast moving, liquefied landslides of mixed and unconsolidated water and debris that look like flowing concrete. They are defined by their non-newtonian flow dynamics, and behave as Bingham plastics. Debris flow occurs in many different environments and scales. In general, debris flows are generated when unconsolidated material becomes saturated and unstable, either on a hillslope or in a stream channel. Such kind of flows involve the motion of large rocks and debris characterised by destructive frontal impact surging and flow cessation on steep slopes, and the mixture contain high concentrations of non-cohesive coarse material. The differences between this and regular sediment transport include: the exchange of flow momentum and energy dissipation is controlled by the dispersive stress arising from the collision of large particles; debris flows attain high velocities and they are exceedingly destructive. Therefore, it is important and necessary to model such flows for diasater management. Although the present model is shown to function well when applied to outburst floods, it still leaves much room for improvement before being applied to debris flows.

7.2.3 Numerical Methods

Numerical meshes include structured grids and unstructured grids. Both of them have advantages and disadvantages. The structured grids are simple to generate, but one limitation of them is that geometric surfaces are usually approximated by blocking out entire elements, which leads to boundaries having discrete steps which introduce flow losses and produce other undesirable effects. Unstructured grids have the advantage of generality in conforming to nearly any desired geometry but they come with a price. The disadvantages of unstructured grids involve: it is complicated to produce grids with acceptable degrees of local resolution; it requires more information to be stored and recovered than structured grids; it is not straightforward to get an efficient parallelization; and changing element types and sizes can increase numerical approximation errors.

The computational model presented here is solved numerically with rectangular grids. These are easy to implement and have good efficiency with relatively little effort. However, there is still work to be done to improve their use for handling complex geomortry. In further research, it would be helpful to make use of cut rectangular meshes or adaptive mesh refinement according to the topography. In addition, to save the time of computation, a parallel computation should be implemented for the model based on the grids.

7.2.4 Two-phase Flow Model

Most of existing morphodynamic models for the fluvial process including the proposed model in this thesis stem from single-phase flow theory. In recent years, the conceptual model of two-phase flow has been investigated and suggested for sediment-laden flows and hyperconcentrated flows in open channels or coastal zones [95-101]. The two-phase flow model is increasingly attractive because it can reflect the fluid phase and solid phase in sediment-laden flow process more accurately. Yet, its use and even the formulation of the governing equations in flow-sediment problems are still in the infancy; and the solution time for practical sediment problems using the two-phase flow model is significantly more expensive even for the not-so-near future [94]. The two-phase concept for complete morphodynamic models has hardly been seen in the open literature. In future research, two-phase morphodynamic model is recommended to be examined.

7.2.5 Morphological Evolution in Meandering Channels

In meandering channels, the situation will become much more complex because the secondary, non-hydrostatic, flow occurs where strong spiral characteristic play a significant role in the morphological evolution. The present model in this research considered the complex irregular topography and the rapid outburst flows, but the issue in terms of sediment transport in strongly curved channels has not been paid attention. In further research, the secondary flow should be incorporated in order to handle the effects of strong bends and thus to widen the applicability of the computational model.

List of References

[1] Zong Y, X Chen. The 1998 Flood on the Yangtze, China. Natural Hazards. 22 (2000) 165-84.

[2] Miller JD, TR Kjeldsen, J Hannaford, DG Morris. A hydrological assessment of the November 2009 floods in Cumbria, UK. Hydrology Research. 44 (2013) 180-97.

[3] Alho P, AJ Russell, JL Carrivick, J Käyhkö. Reconstruction of the largest Holocene jökulhlaup within Jökulsá á Fjöllum, NE Iceland. Quaternary Science Reviews. 24 (2005) 2319-34.

[4] Carrivick JL, EL Rushmer. Understanding high-magnitude outburst floods. Geology Today. 22 (2006) 60-5.

[5] Carrivick JL, V Manville, A Graettinger, SJ Cronin. Coupled fluid dynamics-sediment transport modelling of a Crater Lake break-out lahar: Mt. Ruapehu, New Zealand. Journal of Hydrology. 388 (2010) 399-413.

[6] Manville V, JDL White, BF Houghton, CJN Wilson. Paleohydrology and sedimentology of a post-1.8 ka breakout flood from intracaldera Lake Taupo, North Island, New Zealand. Geological Society of America Bulletin. 111 (1999) 1435-47.

[7] Dai FC, CF Lee, JH Deng, LG Tham. The 1786 earthquake-triggered landslide dam and subsequent dam-break flood on the Dadu River, southwestern China. Geomorphology. 65 (2005) 205-21.

[8] Huggel C, A Kaab, W Haeberli, P Teysseire, F Paul. Remote sensing based assessment of hazards from glacier lake outbursts: a case study in the Swiss Alps. Canadian Geotechnical Journal. 39 (2002) 316-30.

[9] Russell AJ, MJ Roberts, H Fay, PM Marren, NJ Cassidy, FS Tweed, et al. Icelandic jökulhlaup impacts: Implications for ice-sheet hydrology, sediment transfer and geomorphology. Geomorphology. 75 (2006) 33-64.

[10] Russell AJ, FS Tweed, MJ Roberts, TD Harris, MT Gudmundsson, Ó Knudsen, et al. An unusual jökulhlaup resulting from subglacial volcanism, Sólheimajökull, Iceland. Quaternary Science Reviews. 29 (2010) 1363-81.

[11] Cao Z, G Pender, S Wallis, P Carling. Computational dam-break hydraulics over erodible sediment bed. Journal of Hydraulic Engineering-ASCE. 130 (2004) 689-703.

[12] Capart H, DL Young. Formation of a jump by the dam-break wave over a granular bed. J Fluid Mech. 372 (1998) 165-87.

[13] Fraccarollo L, H Capart. Riemann wave description of erosional dam-break flows. J Fluid Mech. 461 (2002) 183-228.

[14] Zech Y, S Soares-Frazao, B Spinewine, NL Grelle. Dam-break induced sediment movement: Experimental approaches and numerical modelling. Journal of Hydraulic Research. 46 (2008) 176-90.

[15] Wu WM, SSY Wang. One-dimensional Modeling of dam-break flow over movable beds. Journal of Hydraulic Engineering-ASCE. 133 (2007) 48-58.

[16] Xia J, B Lin, RA Falconer, G Wang. Modelling dam-break flows over mobile beds using a 2D coupled approach. Advances in Water Resources. 33 (2010) 171-83.

[17] Emmett M, TB Moodie. Dam-break flows with resistance as agents of sediment transport. Physics of Fluids. 20 (2008).

[18] Pritchard D, AJ Hogg. On sediment transport under dam-break flow. J Fluid Mech. 473 (2002) 265-74.

[19] Begnudelli L, BF Sanders. Unstructured grid finite-volume algorithm for shallow-water flow and scalar transport with wetting and drying. Journal of Hydraulic Engineering-ASCE. 132 (2006) 371-84.

[20] Bradford SF, BF Sanders. Finite-volume model for shallow-water flooding of arbitrary topography. Journal of Hydraulic Engineering-ASCE. 128 (2002) 289-98.

[21] Liang QH. Flood Simulation Using a Well-Balanced Shallow Flow Model. Journal of Hydraulic Engineering-ASCE. 136 (2010) 669-75.

[22] Sleigh PA, PH Gaskell, M Berzins, NG Wright. An unstructured finite-volume algorithm for predicting flow in rivers and estuaries. Computers & Fluids. 27 (1998) 479-508.

[23] Villanueva I, NG Wright. Linking Riemann and storage cell models for flood prediction. Proceedings of the ICE - Water Management. 159 (2006) 27-33.

[24] Bagnold RA. An approach to the sediment transport problem from general physics. Geological Suvey Professional Paper 422-I. (1966).

[25] Einstein H. The Bed-Load Function for sediment transportation in open channel flows. Tech Bull No 1026, US Dept of Agriculture, Washington, DC1950.

[26] Meyer-Peter E, R Müller. Formulas for bed load transport. Proc, 2nd Meeting, Stockholm, Sweden, 1948. pp. 39–64.

[27] Soulsby R. Dynamics of marine sands: a manual for practical applications. ThomasTelford, London, UK, 1997.

[28] Armanini A, G Di Silvio. A one-dimensional model for the transport of a sediment mixture in non-equilibrium conditions. Journal of Hydraulic Research. 26 (1988) 275-92.

[29] Spasojevic M, FM Holly. 2-D bed evolution in natural watercourses - new simulation approach. Journal of Waterway Port Coastal and Ocean Engineering-Asce. 116 (1990) 425-43.

[30] Wu WM, W Rodi, T Wenka. 3D numerical modeling of flow and sediment transport in open channels. Journal of Hydraulic Engineering-Asce. 126 (2000) 4-15.

[31] Wu WM. Depth-averaged two-dimensional numerical modeling of unsteady flow and nonuniform sediment transport in open channels. Journal of Hydraulic Engineering-ASCE. 130 (2004) 1013-24.

[32] Abderrezzak KE, A Paquier. One-dimensional numerical modeling of sediment transport and bed deformation in open channels. Water Resources Research. 45 (2009).

[33] Papanicolaou AN, M Elhakeem, G Krallis, S Prakash, J Edinger. Sediment transport modeling review - Current and future developments. Journal of Hydraulic Engineering-ASCE. 134 (2008) 1-14.

[34] Costa JE, RL Schuster. The formation and failure of natural dams. Geological Society of America Bulletin. 100 (1988) 1054-68.

[35] Fraccarollo L, H Capart. Riemann wave description of erosional dam-break flows. J Fluid Mech. 461 (2002).

[36] Abderrezzak KEK, A Paquier, B Gay. One-dimensional numerical modelling of dam-break waves over movable beds: application to

experimental and field cases. Environmental Fluid Mechanics. 8 (2008) 169-98.

[37] Spinewine B. Two-layer flow behaviour and the effects of granular dilatancy in dam-break induced sheet-flow. PhD thesis. (2005).

[38] Ferreira RML, JGAB Leal. 1D Mathematical modelling of the instantaneous Dam-break flood wave over mobile bed: Application of TVD and flux-splitting schemes. CADAM meeting, Munich, Germany. (1998).

[39] Morris M, M Hassan, K Vaskinn. Investigation of Extreme Flood Process and Uncertainty (IMPACT) WP2 - Breach formation: Technical reports. 2005.

[40] Sumer BM, A Kozakiewicz, J Fredsoe, R Deigaard. Velocity and concentration profiles in sheet-flow layer of movable bed. Journal of Hydraulic Engineering-ASCE. 122 (1996) 549-58.

[41] Spinewine B, Y Zech. Small-scale laboratory dam-break waves on movable beds. Journal of Hydraulic Research. 45 (2007) 73-86.

[42] Carrivick JL. Dam break - Outburst flood propagation and transient hydraulics: A geosciences perspective. Journal of Hydrology. 380 (2010) 338-55.

[43] Chen YH, DB Simons. An experimental study of hydraulic and geomorphic changes in an alluvial channel induced by failure of a dam. Water Resour Res. 15 (1979) 1183-8.

[44] Carrivick JL, R Jones, G Keevil. Experimental insights on geomorphological processes within dam break outburst floods. Journal of Hydrology. 408 (2011) 153-63.

[45] Capart H. Dam-break induced geomorphic flows and the transition from solid- to fluid-like behaviour across evolving interfaces. PhD thesis, University Catholique de Louvain, Belgium. (2000).

[46] Leal J, RML Ferreira, AH Cardoso. Geomorphic dam-break flows. Part I: conceptual model. Proceedings of the Institution of Civil Engineers-Water Management. 163 (2010) 297-304.

[47] Benkhaldoun F, S Sahmim, M Seaïd. A two-dimensional finite volume morphodynamic model on unstructured triangular grids. International Journal for Numerical Methods in Fluids. 63 (2010) 1296-327.

[48] Diaz MJC, ED Fernandez-Nieto, AM Ferreiro. Sediment transport models in Shallow Water equations and numerical approach by high order finite volume methods. Computers & Fluids. 37 (2008) 299-316.

[49] Duc BM, W Rodi. Numerical simulation of contraction scour in an open laboratory channel. Journal of Hydraulic Engineering-ASCE. 134 (2008) 367-77.

[50] Fagherazzi S. Numerical simulations of transportational cyclic steps. Computers & Geosciences. 29 (2003) 1143-54.

[51] Simpson G, S Castelltort. Coupled model of surface water flow, sediment transport and morphological evolution. Computers & Geosciences. 32 (2006) 1600-14.

[52] Sun T, G Parker. Transportational cyclic steps created by flow over an erodible bed. Part 2. Theory and numerical simulation. Journal of Hydraulic Research. 43 (2005) 502-14.

[53] Cao ZX, YT Li, ZY Yue. Multiple time scales of alluvial rivers carrying suspended sediment and their implications for mathematical modeling. Advances in Water Resources. 30 (2007) 715-29.

[54] Guan MF, NG Wright, PA Sleigh, JL Carrivick, K Staines. A layer-based morphodynamic model for unsteady outburst geomorphic floods: application in real world events. in: DR Parsons, PJ Ashworth, JL Best, CJ Simpson, (Eds.). 10th International Conference on Fluvial Sedimentology, Leeds, UK, 2013. pp. 130-1.

[55] Abderrezzak KE, A Paquier. Applicability of sediment transport capacity formulas to dam-break flows over movable beds. Journal of Hydraulic Engineering-ASCE. 137 (2011) 209-21.

[56] Carling P, I Villanueva, J Herget, N Wright, P Borodavko, H Morvan. Unsteady 1D and 2D hydraulic models with ice dam break for Quaternary megaflood, Altai Mountains, southern Siberia. Global and Planetary Change. 70 (2010) 24-34.

[57] Carrivick JL, AJ Russell, FS Tweed, D Twigg. Palaeohydrology and sedimentary impacts of jokulhlaups from Kverkfjoll, Iceland. Sedimentary Geology. 172 (2004) 19-40.

[58] Denlinger RP, DRH O'Connell. Simulations of ancient and cataclysmic glacial outburst floods from Glacial Lake Missoula. Geological Society of America Bulletin. (2010) 678-89.

[59] Alho P, VR Baker, LN Smith. Paleohydraulic reconstruction of the largest Glacial Lake Missoula draining(s). Quaternary Science Reviews. 29 (2010) 3067-78.

[60] Soares Fraz~ao S, S Sillen, Y Zech. Dam-break flow through sharp bends: physical model and 2D Boltzmann model validation. Proceedings of the CADAM Meeting, Wallingford, UK, 1998.

[61] Carrivick JL. Modelling coupled hydraulics and sediment transport of a high-magnitude flood and associated landscape change. in: GKC Clarke, J Smellie, (Eds.). Annals of Glaciology, Vol 45, 20072007. pp. 143-54.

[62] Fraccarollo L, H Capart, Y Zech. A Godunov method for the computation of erosional shallow water transients. International Journal for Numerical Methods in Fluids. 41 (2003) 951-76.

[63] Mingham CG, DM Causon. High-resolution finite-volume method for shallow water flows. Journal of Hydraulic Engineering-ASCE. 124 (1998) 605-14.

[64] Lomax H, T Pulliam, D Zingg. Fundamentals of computational fluid dynamics. 1999. pp. 275.

[65] Toro EF. Riemann problems and the WAF method for solving the two-dimensional shallow water equations. Philosophical Transactions of the Royal Society of London Series a-Mathematical Physical and Engineering Sciences. 338 (1992) 43-68.

[66] Alcrudo F, P Gacia-Navarro. A high-resolution Godunov-type scheme in finite volumes for the 2D shallow-water equations. International Journal for Numerical Methods in Fluids. 16 (1993) 489-505.

[67] Coussoe DLaP. Numerical modelling of mudflows. Journal of Hydraulic Engineering-ASCE. 123 (1997) 617-23.

[68] Singh VP. Dam Breach Modeling Technology. Kluwer Academic, the Netherlands, 1996.

[69] Rosatti G, L Fraccarollo. A well-balanced approach for flows over mobile-bed with high sediment-transport. Journal of Computational Physics. 220 (2006) 312-38.

[70] Rosatti G, J Murillo, L Fraccarollo. Generalized Roe schemes for 1D two-phase, free-surface flows over a mobile bed. Journal of Computational Physics. 227 (2008) 10058-77.

[71] Armanini A, L Fraccarollo, G Rosatti. Two-dimensional simulation of debris flows in erodible channels. Computers & Geosciences. 35 (2009) 993-1006.

[72] Benkhaldoun F, S Sahmim, M Seaïd. A two-dimensional finite volume morphodynamic model on unstructured triangular grids. International Journal for Numerical Methods in Fluids. (2009) n/a-n/a.

[73] Morris M. CADAM: Concerted action on dam break modeling—Final report. Report SR 571 HR Wallingford, 2000.

[74] Nujic M. Efficient implementation of non-oscillatory schemes for the computation of free-surface flows. Journal of Hydraulic Research. 33 (1995) 101-11.

[75] LeVeque RJ. Balancing source terms and flux gradients in high-resolution Godunov methods: The quasi-steady wave-propagation algorithm. Journal of Computational Physics. 146 (1998) 346-65.

[76] Bermudez A, E Vazquez. Upwind methods for hyperbolic conservation-laws with source terms. Computers & Fluids. 23 (1994) 1049-71.

[77] Garcia-Navarro P, ME Vazquez-Cendon. On numerical treatment of the source terms in the shallow water equations. Computers & Fluids. 29 (2000) 951-79.

[78] Zhou JG, DM Causon, CG Mingham, DM Ingram. The surface gradient method for the treatment of source terms in the shallow-water equations. Journal of Computational Physics. 168 (2001) 1-25.

[79] Lee S-H, NG Wright. Simple and efficient solution of the shallow water equations with source terms. International Journal for Numerical Methods in Fluids. 63 (2010) 313-40.

[80] Murillo J, P Garcia-Navarro. An Exner-based coupled model for two-dimensional transient flow over erodible bed. Journal of Computational Physics. 229 (2010) 8704-32.

[81] Soares-Frazão S, Y Zech. HLLC scheme with novel wave-speed estimators appropriate for two-dimensional shallow-water flow on erodible bed. International Journal for Numerical Methods in Fluids. 66 (2011) 1019-36.

[82] Liang Q. A coupled morphodynamic model for applications involving wetting and drying. Journal of Hydrodynamics, Ser B. 23 (2011) 273-81.

[83] Briganti R, N Dodd, D Kelly, D Pokrajac. An efficient and flexible solver for the simulation of the morphodynamics of fast evolving flows on coarse sediment beaches. International Journal for Numerical Methods in Fluids. 69 (2012) 859-77.

[84] Hudson J, PK Sweby. A high-resolution scheme for the equations governing 2D bed-load sediment transport. International Journal for Numerical Methods in Fluids. 47 (2005) 1085-91.

[85] Kubatko EJ, JJ Westerink, C Dawson. An unstructured grid morphodynamic model with a discontinuous Galerkin method for bed evolution. Ocean Modelling. 15 (2006) 71-89.

[86] Liu X, BJ Landry, MH García. Two-dimensional scour simulations based on coupled model of shallow water equations and sediment transport on unstructured meshes. Coastal Engineering. 55 (2008) 800-10.

[87] Mirabito C, C Dawson, EJ Kubatko, JJ Westerink, S Bunya. Implementation of a discontinuous Galerkin morphological model on two-dimensional unstructured meshes. Computer Methods in Applied Mechanics and Engineering. 200 (2011) 189-207.

[88] Cao ZX, P Hu, G Pender. Multiple Time Scales of Fluvial Processes with Bed Load Sediment and Implications for Mathematical Modeling. Journal of Hydraulic Engineering-ASCE. 137 (2011) 267-76.

[89] Phillips BC, AJ Sutherland. Spatial lag effects in bed-load sediment transport. Journal of Hydraulic Research. 27 (1989) 115-33.

[91] Li SC, CJ Duffy. Fully coupled approach to modeling shallow water flow, sediment transport, and bed evolution in rivers. Water Resources Research. 47 (2011).

[92] Wu WM, FD Shields, SJ Bennett, SSY Wang. A depth-averaged two-dimensional model for flow, sediment transport, and bed topography in curved channels with riparian vegetation. Water Resources Research. 41 (2005).

[93] Guan MF, NG Wright, PA Sleigh. A 2D Process-based Morphodynamic Model for Flooding by Non-cohesive Dyke Breach. Journal of Hydraulic Engineering-ASCE (in press) 101061/(ASCE)HY1943-79000000861. (2014).

[94] Spasojevic M, M Holly. Two- and Three-Dimensional Numerical Simulation of Mobile-Bed Hydrodynamics and Sedimentation. in: HG Marcelo, (Ed.). Sedimentation engineering: processes, measurements, modeling, and practice. American Society of Civil Engineers2008. pp. 683-761.

[95] Bakhtyar R, A Yeganeh-Bakhtiary, DA Barry, A Ghaheri. Two-phase hydrodynamic and sediment transport modeling of wave-generated sheet flow. Advances in Water Resources. 32 (2009) 1267-83.

[96] Dewals B, F Rulot, S Erpicum, P Archambeau, M Pirotton. Advanced Topics in Sediment Transport Modelling: Non-alluvial Beds and Hyperconcentrated Flows. in: SS Ginsberg, (Ed.). Sediment Transport. InTech, Janeza Trdine 9, 51000 Rijeka, Croatia, 2011. pp. 1-30.

[97] Cao Z, L Wei, J Xie. Sediment-Laden Flow in Open Channels from Two-Phase Flow Viewpoint. Journal of Hydraulic Engineering-ASCE. 121 (1995) 725-35.

[98] Jha SK, FA Bombardelli. Two-phase modeling of turbulence in dilute sediment-laden, open-channel flows. Environmental Fluid Mechanics. 9 (2009) 237-66.

[99] Greimann BP, M Muste, FM Holly. Two-phase formulation of suspended sediment transport. Journal of Hydraulic Research. 37 (1999) 479-500.

[100] Li M, S Pan, BA O'Connor. A two-phase numerical model for sediment transport prediction under oscillatory sheet flows. Coastal Engineering. 55 (2008) 1159-73.

[101] Amoudry L, TJ Hsu, PLF Liu. Two-phase model for sand transport in sheet flow regime. Journal of Geophysical Research-Oceans. 113 (2008).

[102] Wu FC, HW Shen, YJ Chou. Variation of roughness coefficients for unsubmerged and submerged vegetation. Journal of Hydraulic Engineering-ASCE. 125 (1999) 934-42.

[103] Green JC. Modelling flow resistance in vegetated streams: review and development of new theory. Hydrological Processes. 19 (2005) 1245-59.

[104] Sellin RHJ, TB Bryant, JH Loveless. An improved method for roughening floodplains on physical river models. Journal of Hydraulic Research. 41 (2003) 3-14.

[105] Nielsen P. Coastal bottom boundary layers and sediment transport. World Scientific, 1992.

[106] Ribberink JS. Bed-load transport for steady flows and unsteady oscillatory flows. Coastal Engineering. 34 (1998) 59-82.

[107] Rickenmann D. Comparison of bed load transport in torrents and gravel bed streams. Water Resources Research. 37 (2001) 3295-305.

[108] Smart G. Sediment Transport Formula for Steep Channels. Journal of Hydraulic Engineering-ASCE. 110 (1984) 267-76.

[109] van Rijn LC. Sediment transport part I, bed load transport. Journal of Hydraulic Engineering-ASCE. 110 (1984) 1431-56.

[110] Camenen B, M Larson. Phase-lag effects in sheet flow transport. Coastal Engineering. 53 (2006) 531-42.

[111] Rickenmann D. Hyperconcentrated flow and sediment transport at steep slopes. Journal of Hydraulic Engineering-ASCE. 117 (1991) 1419-39.

[112] Smart G, M Jäggi. Sediment transport on steep slopes. Mitteilung 64 Versuchsanstalt fu¨ r Wasserbau, Hydrologie und Glaziologie, ETH Zurich, Zurich. (1983).

[113] Yang C, S Wan. Comparisons of Selected Bed‐Material Load Formulas. Journal of Hydraulic Engineering-ASCE. 117 (1991) 973-89.

[114] Van Rijn LC. Mathematical modelling of morphological processes in the case of suspended sediment transport. Delft: Delft University of Technology; 1987.

[115] Greimann B, Y Lai, JC Huang. Two-dimensional total sediment load model equations. Journal of Hydraulic Engineering-ASCE. 134 (2008) 1142-6.

[116] Engelund F, J Fredsoe. Sediment transport model for straight alluvial channels. Nordic Hydrology. 7 (1976) 293-306.

[117] Garcia M, G Parker. Entrainment of bed sediment into suspension. Journal of Hydraulic Engineering-ASCE. 117 (1991) 414-35.

[118] Smith JD, SR McLean. Spatially averaged flow over a wavy surface. Journal of Geophysical Research-Oceans and Atmospheres. 82 (1977) 1735-46.

[119] Van Rijn LC. Sediment Pick-Up Functions Journal of Hydraulic Engineering-ASCE. 110 (1984) 1494-502.

[120] Zyserman JA, J Fredsoe. Date-analysis of bed concentration of suspended sediment. Journal of Hydraulic Engineering-ASCE. 120 (1994) 1021-42.

[121] Guan MF, NG Wright, PA Sleigh. Appicability of entrainment formulas to modelling of geomorphic outburst flows. in: R Hinkelmann, MH Nasermoaddeli, SY Liong, D Savic, P Fröhle, KF Daemrich, (Eds.). 10th International Conference on Hydroinformatics, Hamburg, GERMANY, 2012.

[122] Kouwen N, RM Li. Biomechanics of vegetative channel linings. Journal of the Hydraulics Division. 106 (1980) 1085-106.

[123] van Rijn LC. Sediment transport part II, suspended load transport. Journal of Hydraulic Engineering-ASCE. 110 (1984) 1613–41.

[124] Julien PY. Erosion and Sedimentation. Second ed. Cambridge University Press, Cambridge, UK, 2010.

[125] Hunziker RP, MNR Jäggi. Grain sorting processes. Journal of Hydraulic Engineering-ASCE. 128 (2002) 1060-8.

[126] Lamb MP, WE Dietrich, JG Venditti. Is the critical Shields stress for incipient sediment motion dependent on channel-bed slope? Journal of Geophysical Research-Earth Surface. 113 (2008).

[127] Parker C, NJ Clifford, CR Thorne. Understanding the influence of slope on the threshold of coarse grain motion: Revisiting critical stream power. Geomorphology. 126 (2011) 51-65.

[128] Cao ZX. Equilibrium near-bed concentration of suspended sediment. Journal of Hydraulic Engineering-ASCE. 125 (1999) 1270-8.

[129] Zhou J, J Li. Modeling Storm-Induced Current Circulation and Sediment Transport in a Schematic Harbor. Journal of Waterway, Port, Coastal, and Ocean Engineering. 131 (2005) 25-32.

[130] Wong M, G Parker. Reanalysis and Correction of Bed-Load Relation of Meyer-Peter and Müller Using Their Own Database. Journal of Hydraulic Engineering-ASCE. 132 (2006) 1159-68.

[131] Stelling GS. On the construction of computational methods for shallow water flow problems. Delft: TU Delft; 1983.

[132] Falconer RA. Mathematical modelling of jet-forced circulation in reservoirs and harbours. London: University of London; 1976.

[133] van Leer B. Towards the ultimate conservative difference scheme. V. A second-order sequel to Godunov's method. Journal of Computational Physics. 32 (1979) 101-36.

[134] Zhou JG, DM Causon, DM Ingram, CG Mingham. Numerical solutions of the shallow water equations with discontinuous bed topography. International Journal for Numerical Methods in Fluids. 38 (2002) 769-88.

[135] Brufau P, P Garcia-Navarro, ME Vazquez-Cendon. Zero mass error using unsteady wetting-drying conditions in shallow flows over dry irregular topography. International Journal for Numerical Methods in Fluids. 45 (2004) 1047-82.

[136] Liang QH, AGL Borthwick. Adaptive quadtree simulation of shallow flows with wet-dry fronts over complex topography. Computers & Fluids. 38 (2009) 221-34.

[137] Song L, J Zhou, J Guo, Q Zou, Y Liu. A robust well-balanced finite volume model for shallow water flows with wetting and drying over irregular terrain. Advances in Water Resources. 34 (2011) 915-32.

[138] Toro EF. Shock-Capturing Methods for Free-Surface Shallow Flows John Wiley &Sons, LTD, 2001.

[139] Fernández-Nieto ED, G Narbona-Reina. Extension of WAF Type Methods to Non-Homogeneous Shallow Water Equations with Pollutant. J Sci Comput. 36 (2008) 193-217.

[140] Toro EF. A Weighted Average Flux Method for Hyperbolic Conservation Laws. Proceedings of the Royal Society of London Series A, Mathematical and Physical Sciences. 423 (1989) 401-18.

[141] Einfeldt B. On Godunov-type methods for gas-dynamics. Siam Journal on Numerical Analysis. 25 (1988) 294-318.

[142] Audusse E, M-O Bristeau. A well-balanced positivity preserving "second-order" scheme for shallow water flows on unstructured meshes. Journal of Computational Physics. 206 (2005) 311-33.

[143] Gallardo JM, C Parés, M Castro. On a well-balanced high-order finite volume scheme for shallow water equations with topography and dry areas. Journal of Computational Physics. 227 (2007) 574-601.

[144] Vázquez-Cendón MaE. Improved Treatment of Source Terms in Upwind Schemes for the Shallow Water Equations in Channels with Irregular Geometry. Journal of Computational Physics. 148 (1999) 497-526.

[145] Sanders BF. Integration of a shallow water model with a local time step. Journal of Hydraulic Research. 46 (2008) 466-75.

[146] Crossley AJ, NG Wright. Time accurate local time stepping for the unsteady shallow water equations. International Journal for Numerical Methods in Fluids. 48 (2005) 775-99.

[147] Kramer T, J Jozsa. Solution-adaptivity in modelling complex shallow flows. Computers & Fluids. 36 (2007) 562-77.

[148] Brufau P, ME Vazquez-Cendon, P Garcia-Navarro. A numerical model for the flooding and drying of irregular domains. International Journal for Numerical Methods in Fluids. 39 (2002) 247-75.

[149] Brufau P, P García-Navarro. Unsteady free surface flow simulation over complex topography with a multidimensional upwind technique. Journal of Computational Physics. 186 (2003) 503-26.

[150] Kesserwani G, Q Liang. Well-balanced RKDG2 solutions to the shallow water equations over irregular domains with wetting and drying. Computers & Fluids. 39 (2010) 2040-50.

[151] Caleffi V, A Valiani, A Zanni. Finite volume method for simulating extreme flood events in natural channels. Journal of Hydraulic Research. 41 (2003) 167-77.

[152] Goutal N, F Maurel. Proceedings of the 2nd workshop on dam-break wave simulation. HE 43/97/016/B, Départment Laboratoire Nationald'Hydraulique, Groupe Hydraulique Fluviale Electricité de France, France. (1997).

[153] Rogers BD, AGL Borthwick, PH Taylor. Mathematical balancing of flux gradient and source terms prior to using Roe's approximate Riemann solver. Journal of Computational Physics. 192 (2003) 422-51.

[154] Liang Q, F Marche. Numerical resolution of well-balanced shallow water equations with complex source terms. Advances in Water Resources. 32 (2009) 873-84.

[155] Hu K, CG Mingham, DM Causon. Numerical simulation of wave overtopping of coastal structures using the non-linear shallow water equations. Coastal Engineering. 41 (2000) 433-65.

[156] Thacker W. Some exact solutions to the nonlinear shallow-water wave equations. J Fluid Mech. 107 (1981) 499-508.

[157] Soares Frazao S, Y Zech. Dam break in channels with 90 degrees bend. Journal of Hydraulic Engineering-ASCE. 128 (2002) 956-68.

[158] Kawahara M, T Umetsu. Finite-element method for moving boundary-problems in river flow. International Journal for Numerical Methods in Fluids. 6 (1986) 365-86.

[159] Wu W, M Altinakar, SSY Wang. Depth-average analysis of hysteresis between flow and sediment transport under unsteady conditions. International Journal of Sediment Research. 21 (2006) 12.

[160] Zech Y, S Soares-Frazao, B Spinewine, C Savary, L Goutiere. Inertia effects in bed-load transport models. Can J Civil Eng. 36 (2009) 1587-97.

[161] Dong P, K Zhang. Two-phase flow modelling of sediment motions in oscillatory sheet flow. Coastal Engineering. 36 (1999) 87-109.

[162] Pugh FJ, KC Wilson. Velocity and concentration distributions in sheet flow above plane beds. Journal of Hydraulic Engineering-ASCE. 125 (1999) 117-25.

[163] Jenkins JT, DM Hanes. Collisional sheet flows of sediment driven by a turbulent fluid. J Fluid Mech. 370 (1998) 29-52.

[164] Wu WM, SSY Wang. One-dimensional explicit finite-volume model for sediment transport with transient flows over movable beds. Journal of Hydraulic Research. 46 (2008) 87-98.

[165] Seal R, C Paola, G Parker, JB Southard, PR Wilcock. Experiments on downstream fining of gravel .1. Narrow-channel runs. Journal of Hydraulic Engineering-ASCE. 123 (1997) 874-84.

[166] Chinnarasri C, T Tingsanchali, S Weesakul, S Wongwises. Flow patterns and damage of dike overtopping. International Journal of Sediment Research. 18 (2003) 301-9.

[167] Goutiere L, S Soares-Frazão, Y Zech. Dam-break flow on mobile bed in abruptly widening channel: experimental data. Journal of Hydraulic Research. 49 (2011) 367-71.

[168] Morris MW, M Hassan, KA Vaskinn. Breach formation: Field test and laboratory experiments. Journal of Hydraulic Research. 45 (2007) 9-17.

[169] Spinewine B, A Delobbe, L Elslander, Y Zech. Experimental investigation of the breach growth process in sand dikes. Proceedings of the Second International Conference on Fluvial Hydraulics, Napoli, Italy, 2004.

[170] Van Emelen S, C Swartenbroekx, Y Zech, S Soares-Frazão. Numerical modelling of the breaching process in an earthen dike. Fifth International Conference on Advanced COmputational Methods in ENgineering, Liège, Belgium, 2011.

[171] Macchione F. Model for Predicting Floods due to Earthen Dam Breaching. I: Formulation and Evaluation. Journal of Hydraulic Engineering-ASCE. 134 (2008) 1688-96.

[172] Pierce MW, CI Thornton, SR Abt. Predicting Peak Outflow from Breached Embankment Dams. Journal of Hydrologic Engineering. 15 (2010) 338-49.

[173] Wahl TL. Prediction of embankment dam breach parameters—A literature review and needs assessment. Dam Safety Rep No DSO-98-004. U.S. Dept. of the Interior. Bureau of Reclamation, Denver, 1998.

[174] Pickert G, V Weitbrecht, A Bieberstein. Breaching of overtopped river embankments controlled by apparent cohesion. Journal of Hydraulic Research. 49 (2011) 143-56.

[175] Guymon GL. Regional Sediment Yield Analysis of Alaska Streams. Journal of the Hydraulics Division-Asce. 100 (1974) 41-50.

[176] Hallet B, L Hunter, J Bogen. Rates of erosion and sediment evacuation by glaciers: A review of field data and their implications. Global and Planetary Change. 12 (1996) 213-35.

[177] Carrivick JL. Hydrodynamics and geomorphic work of jokulhlaups (glacial outburst floods) from Kverkfjoll volcano, Iceland. Hydrological Processes. 21 (2007) 725-40.

[178] Alho P, J Aaltonen. Comparing a 1D hydraulic model with a 2D hydraulic model for the simulation of extreme glacial outburst floods. Hydrological Processes. 22 (2008) 1537-47.

[179] Russell AJ, FS Tweed, Ó Knudsen. Flash flood at Sólheimajökull heralds the reawakening of an Icelandic subglacial volcano. Geology Today. 16 (2000) 102-6.

[180] Carling PA. Morphology, sedimentology and palaeohydraulic significance of large gravel dunes, Altai Mountains, Siberia. Sedimentology. 43 (1996) 647-64.

[181] Lawler DM, H BjÖRnsson, M Dolan. Impact of subglacial geothermal activity on meltwater quality in the Jökulsá á Sólheimasandi system, southern Iceland. Hydrological Processes. 10 (1996) 557-77.

[182] Roberts MJ, FS Tweed, AJ Russell, Ó Knudsen, TD Harris. Hydrologic and geomorphic effects of temporary ice-dammed lake formation during jökulhlaups. Earth Surface Processes and Landforms. 28 (2003) 723-37.

[183] Soosalu H, K Jónsdóttir, P Einarsson. Seismicity crisis at the Katla volcano, Iceland—signs of a cryptodome? Journal of Volcanology and Geothermal Research. 153 (2006) 177-86.

[184] Roberts MJ, AJ Russell, FS Tweed, Ó Knudsen. Ice fracturing during jökulhlaups: implications for englacial floodwater routing and outlet development. Earth Surface Processes and Landforms. 25 (2000) 1429-46.

[185] Ryder JM, M Church. The Lillooet terraces of Fraser River: a palaeoenvironmental enquiry. Canadian Journal of Earth Sciences. 23 (1986) 869-84.

[186] Russell AJ. Subglacial jökulhlaup deposition, Jotunheimen, Norway. Sedimentary Geology. 91 (1994) 131-44.

[187] Iverson RM. The physics of debris flows. Rev Geophys. 35 (1997) 245-96.